BIOFILM-INDUCED CARBONATE PRECIPITATION

AT THE PORE-SCALE

by

James Martin Connolly

A dissertation submitted in partial fulfillment
of the requirements for the degree

of

Doctor of Philosophy

in

Engineering

MONTANA STATE UNIVERSITY
Bozeman, Montana

April 2015

©COPYRIGHT

by

James Martin Connolly

2015

All Rights Reserved

DEDICATION

This dissertation is dedicated to my parents, Jackson and Kathleen Connolly who made it all possible.

ACKNOWLEDGEMENTS

There are many people to acknowledge but first among them is my advisor and committee chair Dr. Robin Gerlach whose personal and professional guidance will shape my future and many of my colleagues' and friends' futures. Thanks Robin. Secondly, I would like to thank my people in no particular order: Kristen, Sophie, Carley, Jon, Davis, Annette, Jesse, Joe, Kris, Alex, Lauren, Heidi and all of the people who float rivers with me, strap skis to their feet with me or ride bikes with me. Thanks to the CBE which has generously provided me with a safe, supportive and collaborative environment to work in and thanks to Betsey Pitts, Ann Willis, Drs. Adie Philips, Ellen Lauchnor, Erin Field, Andrea Radu, Cristian Picioreanu and Phil Himmer who taught me what I needed to know. Thanks to Benjamin Jackson for thought-provoking discussion and for all of the mathematics help. Thanks to Adam Rothman who was an integral part of this work as a highly capable and independent undergraduate, and later graduate, researcher. Thanks to the National Science Foundation and the U.S. Department of Energy who provided my funding. Finally, thanks to my committee, Drs. Al Cunningham, Ross Carlson, Isaac Klapper, Warren Jones, and Binhai Zhu who have been nothing but supportive of my work and deserve much of the credit for it.

TABLE OF CONTENTS

1. INTRODUCTION 1

Background 1
Dissertation Overview 3

2. MICROBIALLY INDUCED CARBONATE PRECIPITATION IN THE SUBSURFACE: FUNDAMENTAL REACTION AND TRANSPORT PROCESSES 7

Contribution of Authors and Coauthors 7
Manuscript Information Page 8
Introduction 9
Biological Processes 12
Alkalinity Producing Metabolisms in the Subsurface 12
Urea Hydrolysis 16
Denitrification 17
Sulfate Reduction 18
Iron Reduction 21
Biofilms 22
Kinetics 24
Mineral Precipitation Theory 28
Carbonate Minerals and Polymorphs 28
Nucleation 30
Crystal Growth Models and Kinetics 36
Reactive Transport 44
Solute Transport 45
Biofilm-Catalyzed Reactions 47
Precipitation Reactions 56
Concluding remarks 58
Acknowledgements 60
Modeling Notes 60
Chapter 2 Nomenclature 61

3. CONSTRUCTION OF TWO UREOLYTIC MODEL ORGANISMS FOR THE STUDY OF MICROBIALLY INDUCED CALCIUM CARBONATE PRECIPITATION 65

Contribution of Authors and Coauthors 65
Manuscript Information Page 67
Abstract 68
Introduction 69

TABLE OF CONTENTS – CONTINUED

Materials and Methods 72
Bacterial Strains and Growth Conditions 72
Plasmid and Model Organism Construction 72
Urease Gene Sequencing 74
Test Tube Screening 74
Batch Kinetic Studies 75
Confocal Microscopy 77
Analytical Measurements 78
Biomass Quantification 78
Bulk GFP 78
Urea 79
pH 79
Kinetic Models 79
Results and Discussion 82
Construction of Urease Positive GFP Organisms 82
Test Tube Screening 86
Kinetic Studies 88
Growth and Ureolysis Characteristics 88
Kinetic Curve Fitting 90
Strain Comparison 93
Additional Parameters 94
Application in Flow Cell Reactors 95
Conclusions 97
Chapter 3 Glossary 98
Acknowledgements 99

4. ESTIMATION OF A BIOFILM-SPECIFIC REACTION RATE: KINETICS OF BACTERIAL UREA HYDROLYSIS IN A BIOFILM 100

Contribution of Authors and Coauthors 100
Manuscript Information Page 101
Abstract 102
Introduction 103
Materials and Methods 105
Biofilm Growth 105
Urea Quantification 109
Urea Hydrolysis Rate Determination 109
Results and Discussion 113
Analytical Results 113
Urea Measurement 113
Biofilm Thickness Profiles 113

TABLE OF CONTENTS – CONTINUED

Sources of Error 114
Reactive Transport Characterization 115
Kinetic Parameter Fitting 119
Practical Applications 123
Conclusions 124
Acknowledgements 125

5. REACTIVE TRANSPORT AND PERMEABILITY REDUCTION IN A SYNTHETIC 2D POROUS MEDIUM WITH BIOFILM-INDUCED CARBONATE PRECIPITATION 126

Contribution of Authors and Coauthors 126
Manuscript Information Page 127
Abstract 128
Introduction 129
Materials and Methods 131
Micromodel Fabrication 131
Strain and Growth Conditions 134
Micromodel Experiment 135
Confocal Microscopy and Image Analysis 138
Reactive Transport Simulations 140
Results and Discussion 142
Imaging and Image Processing 142
Porosity and Permeability Reduction 143
Preliminary Study of Long-Term Behavior 153
Pore-Scale Reactive Transport 157
Conclusions 160

6. INDIVIDUAL-BASED MODELING OF BIOFILM-INDUCED CALCIUM CARBONATE PRECIPITATION 162

Background, Rationale and Objectives 162
Background 162
Rationale and Objectives 163
Theoretical Basis 164
Carbonate Equilibrium 164
Finite Element Model 167
Individual-Based Biofilm and Precipitate Growth Model 170
Computational Procedure 171
2D Approximation 173
Results and Discussion 175

TABLE OF CONTENTS – CONTINUED

Conclusions and Outlook 177

7. CONCLUSIONS AND OUTLOOK 179

Conclusions and Impacts 179
Recommendations for Future Work 183

Concluding Remarks 185

REFERENCES CITED 186

APPENDICES 206

APPENDIX A: Nucleotide Sequences Referenced in Chapter 3 207
APPENDIX B: Supplemental Information for Chapter 4 211
APPENDIX C: Raw and Thresholded Images Relating to Chapter 5 226
APPENDIX D: Steady State PHREEQC Output Relating to Chapter 5 228
APPENDIX E: Model Parameters and Code Architecture Relating to Chapter 6 233
APPENDIX F: Surface Characterization and Depth Profiling of Bacterial Ureolysis-Driven $CaCO_3$ Precipitates Using XPS 243
APPENDIX G: Supplemental Data and Images for Surface Characterization and Depth Profiling of Bacterial Ureolysis-Driven $CaCO_3$ Precipitates Using XPS 255
APPENDIX H: Additional Research: Taxis Toward Hydrogen Gas by *Methanococcus maripaludis* 274
APPENDIX I: Additional Research: Struvite Stone Formation by Ureolytic Biofilm Infections 276
APPENDIX J: Experiments and Modeling of Biofilm-Induced Carbonate Precipitation in SU-8 Micromodel Reactors 278

LIST OF TABLES

Table Page

1. Equilibrium reactions and pk ($-\log_{10}(k)$) values for the carbonate system at 25º C. 13

2. Surface reactions on a calcite crystal and their associated solubility constants. ">" indicates surface species and all others are aqueous species. 43

3. Useful relationships for the calculation of the Thiele modulus and effectiveness factor for zero-, first-order and Michaelis–Menten (M-M) rate models assuming boundary conditions $du/d\zeta = 0$ at $\zeta = 0$ and $u = 1$ at $\zeta = 1$. 55

4. Bacterial strains, media and batch growth conditions used in this work. 76

5. Response of different cultures to nickel addition as determined by the relative ability to increase pH in urea broth. Response was determined by measuring the period of time required for the color change reaction to occur in the respective cultures. 86

6. Fitted kinetic parameters along with R2 as a measure of the quality of fit for population growth and ureolysis in batch culture. Values are presented as Mean(±95% Confidence Interval) with n = 3 replicates. 92

7. Average dimensionless parameters for all tube reactors along with their minima and maxima. Da and Pe are calculated for each tube and ϕ is calculated for all L_f measurements. 117

LIST OF TABLES - CONTINUED

Table Page

8. Naming scheme for experiments performed in this study. 136

9. Aqueous species included in the model sorted by charge. Cl^- enforces charge neutrality. 167

10. Equilibrium reactions and pK values included in the model. pK values from the PHREEQC database. 167

LIST OF FIGURES

Figure Page

1. A 3D confocal microscopy reconstruction of a sand grain with attached bacteria (*S. pasteurii*) and calcium carbonate precipitates. The sand grain surface was imaged with reflected light (Blue), calcium carbonate was imaged using auto fluorescence excited by an ultraviolet laser (White), and biomass was imaged using LIVE-DEAD fluorescent staining. Areas containing healthy cells stain green while areas that contain cells with compromised cellular membranes or extracellular nucleic acids stain red. (A) Biomass distribution. (B) Biomass with calcium carbonate overlaid. (C) All components including the sand grain surface shown in blue. 2

2. Fluid flow and reactive processes affecting MICP at the pore network scale. Microbial cells exist either in a freely floating planktonic state or in a biofilm. Precipitation can occur in suspension, in the biofilm or on solid surfaces. Biofilm and precipitates affect local hydrodynamics if they are present in sufficient quantities by blocking pore throats, isolating pores and constricting flow. Stagnant zones and preferential flow pathways develop leading to pore-scale chemical, physical and potentially biological heterogeneity. 11

3. The ratio of the ionic activity versus concentration (also known as an activity coefficient) for monovalent and divalent ions over a range of ionic strengths. For comparison, seawater has an average ionic strength of approximately 0.7 mol/L. The Davies extension of the Debye-Hückel relationship was used (Davies, 1962). The Pitzer equation should be used at ionic strengths above 0.1 mol/L (Pitzer, 1991) but was not shown here because a specific solution chemistry would have to be assumed. 15

LIST OF FIGURES - CONTINUED

Figure Page

4. The theoretical geometry presented in Figure 1 (A) was applied to a 2D, steady-state finite element model to demonstrate the effect of alkalinity production in a biofilm on the pore-scale spatially-resolved saturation state (S). Panels B, C and D show simulations with varied urea hydrolysis rates of 0.5, 1.0 and 2.0 mol/(L·h) respectively and a constant precipitation rate of 0.001 mol/(m^2·h). In this example urea hydrolysis occurs only in the biofilm domains and laminar fluid flow (Re << 1) is restricted to the liquid domain (no flow inside the biofilm domains). Please refer to the 'Modeling Notes' section at the end of this chapter for additional information regarding this model.....27

5. Critical nucleus size behavior due to a maximum in the total free energy (ΔG) based on Equations 20-22. A small nucleus ($r << r_c$) is unstable and is likely to redissolve as relaxation occurs to a lower total free energy. A large nucleus ($r >> r_c$) is likely to grow in order to reduce total free energy (Gibbs, 1948; Mullin, 2001). 32

6. The theoretical geometry presented in Figure 1 (A) applied to a 2D, steady-state finite element model to demonstrate the effect of precipitation rate on pore-scale spatially-resolved saturation state (S). Panels B, C and D show simulations with varied precipitation rates of 0.001, 0.005 and 0.01 mol/(m^2·h) respectively along with a constant urea hydrolysis rate in biofilm domains of 1.0 mol/(L·h). Precipitation is modeled as a surface flux of both carbonate and calcium ions at the precipitate boundaries and laminar fluid flow (Re << 1) is restricted to the liquid domain (no flow inside the biofilm domains). Please refer to the 'Modeling Notes' section at the end of this chapter for additional information regarding this model. 41

LIST OF FIGURES - CONTINUED

Figure Page

7. Expected volume-averaged system behavior in the context of kinetic and transport rate limits. As solute transport is increased the overall reaction rate will increase until reactions are limited by the reaction kinetics of the system. The shape of an actual system curve is highly dependent on factors such as pore size distribution and concentration dependence on reaction rates but generally bulk reaction rates will increase with increasing transport rates (i.e. Darcy velocity) until a kinetic limitation is reached. This behavior was shown through pore-scale modeling by Molins et al. (2012). 50

8. The assumed biofilm profile geometry for Thiele modulus calculations. The biofilm is assumed to be of a slab geometry with $C = C_{bulk}$ at $z = L_f$. A reaction, r_c is occurring in the biofilm domain only and the problem is nondimensionalized such that $u = C/C_{bulk}$ and $\zeta = z/L_f$. The assumed profile is put into context of an assumed pore geometry where L_f can be highly variable highlighting the importance of using caution when using volume-averaged parameters. 52

9. Linearized map of the new vector pMK001 (pJN105 with cloned fragment of DH5α(pURE14.8) inserted). Short arrows *ureDABC* and *ureFG* represent previously sequenced sections of *E. coli* DH5α(pURE14.8). The longer arrow 'urease insert' is the entire section of cloned genes transferred into pJN105. Restriction sites *PstI* and *SpeI* were added by primers and PCR to the insert to facilitate ligation into the vector pJN105. *araC* ^{P}*BAD* is the promoter, *rep* encodes trans-acting replication protein, *aacC1* imparts gentamicin resistance, *mob* encodes the plasmid mobilization functions. 83

LIST OF FIGURES - CONTINUED

Figure Page

10. *P. aeruginosa* MJK1 and *E. coli* MJK2 were constructed by excising the urease operon (*Ure*) from the pUC19 plasmid previously contained in *E. coli* DH5α(pURE14.8). The urease operon was ligated into plasmid pJN105 to construct plasmid pMK001, which was then transferred to *P. aeruginosa* AH298 and *E. coli* AF504*gfp*. The resulting bacterial strains, MJK1 and MJK2, respectively, express both active urease and constitutive GFP. Amp^r and Gm^r refer to ampicillin and gentamicin resistance genes, respectively. 84

11. Ureolytic batch study results for both transformed organisms (MJK1 and MJK2) and the common ureolytic model organism, *S. pasteurii*. OD is reported after correction to a 1.0 cm path length and GFP fluorescence is in arbitrary units from a bulk fluorescent intensity measurement. Both OD and GFP are normalized to inoculated media. Error bars represent 95% confidence intervals with n = 3 replicates. Lines connecting the data points were added to indicate trends and facilitate distinction of the different treatments in the graphs. 89

12. Experimental data (symbols) and model fits (lines) for growth and ureolysis studies. (A,B,C) Population growth was modeled by a Gompertz expression and (D,E,F) ureolysis rates were modeled using Michaelis-Menten (M-M), first order, and zero order rate models. 91

LIST OF FIGURES - CONTINUED

Figure Page

13. Time lapse CLSM images of a *P. aeruginosa* MJK1 biofilm colony (green) during calcium injection under laminar flow in a 1.0 mm square glass capillary flow cell (flow direction is from bottom to top). Calcium carbonate precipitates (white) are shown to accumulate on the downstream side of the biofilm colony (green GFP fluorescence). Biomass was imaged based on the fluorescence of the constitutively expressed GFP and the precipitates were imaged using reflected light microscopy. T = 0 corresponds to the beginning of the imaging session. The total time that the biofilm colony was exposed to calcium was about 15 hours. Please refer to the methods section (2.6) for the image processing associated with this figure. 96

14. A schematic for the tube reactor assembly. Sterile LB medium is pumped through a 10 cm long, 1.6 mm inside diameter (ID) silicon tube with biofilm growing on the walls. Small ID influent tubing was used to connect the syringe to the tube reactor. A 3-way valve was used to take influent samples and the downstream end of the tube reactor was disconnected to take effluent samples. 106

15. A representative example of a thin section image. (A) A transmitted light image shows a qualitative representation of the biofilm. (B) The fluorescence image, showing the GFP signal, is used for quantification. (C) The GFP fluorescence image is thresholded to differentiate between biofilm (white) and background (black), forming a binary image. The area of the biofilm signal is quantified and divided by the calculated visible arc length (0.923 mm) to calculate a representative average biofilm thickness. 109

16. COMSOL model overview with boundary conditions. 110

LIST OF FIGURES - CONTINUED

Figure Page

17. Local urea concentration as predicted from the finite element model for each tube reactor used in the analysis. Concentration is not constant within each tube however when the same color scale is used, as in this figure, it is evident that each tube represents a narrow concentration range within the range of concentrations that exist within this study. Biofilm profiles are shown as white lines in each panel.....120

18. Average urea concentration within the biofilm volume versus estimated urea hydrolysis rate. The modeled points correspond to the rate calculated by the finite element models versus the average urea concentration in the biofilm volume, $C_{Urea,BF}$. Error bars represent the range of urea concentration within the biofilm volume as estimated by the finite element models. Points are labeled with the tube reactor numbers from which they were obtained (see Figure 4).....122

19. Porous media micromodel geometry. The micromodels were etched in silicon wafers to a depth of 18.1 μm and sealed with a 200 μm Pyrex cover slip. 132

20. A representative scanning electron micrograph of the edge of the porous media region of a micromodel without cover glass.....134

21. A schematic of the experimental setup. After inoculation flow of sterile medium was maintained by a syringe pump through a 0.2 μm filter to prevent contamination of the media reservoir. One three-way valve was used to direct flow directly to waste for flushing the influent tubing and the other two three-way valves were used to make the connection to the differential pressure transducer. The micromodel, valves and the pressure transducer were mounted to a polycarbonate microscope stage adaptor (not shown) for ease of imaging. 138

LIST OF FIGURES - CONTINUED

Figure Page

22. A representative section of porous media from reactor run 9-24 near the middle of the porous media region. The porous media elements are 100 μm square and flow is from top to bottom. (A) Reflected light image. (B) GFP biofilm fluorescence image. (C) Precipitation autofluorescence image. (D) Composite thresholded image showing the signal from gas, biofilm and precipitation. (E) Digitized surfaces used in the reactive transport modeling with porous media elements in black and the other phases in shades of gray. 143

23. Volumes of biofilm, precipitate and gas bubbles as determined by the analysis of confocal scanning laser microscopy images. 144

24. Porosity and permeability reduction over time from the micromodel experiments. Porosity was estimated from the thresholding of confocal microscopy images and permeability was estimated from differential pressure data. 147

25. Porosity vs. permeability for the different conditions with fitted parameters. 150

26. Biofilm, precipitate and gas volumes along with porosity versus time in an extension of experimental run 9 where flow was shut off and the reactor was imaged at 72 and 216 hours. 154

27. Modeled urea concentration maps (in mol/L) at 48 hours for all three 0.5 mL/h experiments (3-48, 6-48 and 9-48). The results here are representative of those found in all experiments. We found that “no calcium” and “calcium at inoculation” experiments showed lower urea concentrations and thus higher overall reaction rates than experiments where calcium was added 24 hours after inoculation. Flow is from bottom to top and black represents solid elements (precipitates and porous medium elements). 158

LIST OF FIGURES - CONTINUED

Figure Page

28. Modeled average urea concentration in the porous media section versus time. Note that the two 48-hour time points were excluded from analysis on the far right plot due to plugging (7-48 and 8-48) 158

29. Modeled average and maximum pore fluid velocities the porous media section versus time. 159

30. Carbonate speciation over a range of pH values as calculated by MINTEQ. The top graph shows activity vs. pH and the lower graph shows concentration. 166

31. The main steps of the numerical approach. Flow is from left to right and the axes in the reaction/diffusion step are in µm. 173

32. Model results from the individual-based biofilm and precipitate growth model. Biofilm growth is shown as the expanding dark masses (made up of small particles) and eventually precipitation is predicted at the last time point and represented by the white irregular masses. Axes on each plot are the length scale in µm and urea concentration is in mol/L. Flow is from left to right.....176

ABSTRACT

There are many methods available to decrease permeability in the subsurface but one that has been the subject of much research over the last decade is microbially-induced carbonate precipitation (MICP). In this process, microbial activity is promoted that increases pore water alkalinity. When calcium or other divalent cations are supplied to the system, solid carbonate minerals can form which occupy pore space and can decrease permeability. Permeability reduction can also come from microbial biofilms forming in the pore space. The goal of the work presented in this dissertation is to understand how pore space is affected, both physically and chemically, by biofilms and the precipitates that they can form. Fundamental research presented here is intended to inform ongoing application-based research and development.

Previously it has been a challenge to image MICP at high resolution without the use of destructive techniques. To overcome that obstacle, a fluorescently-tagged bacterium capable of urea hydrolysis-driven MICP was constructed. Biofilms were grown in two-dimensional microscale porous media reactors and allowed to precipitate calcium carbonate under varied conditions. These reactors were imaged noninvasively using confocal microscopy so that both biofilms and carbonate minerals could be resolved at micrometer resolution. Image analysis was utilized to quantify how much pore space was occupied by the biofilm and minerals in order to estimate porosity reduction. Finally, pore-scale reactive transport modeling was utilized in order to estimate local concentrations within the reactors.

The results show that the extent to which the porosity and permeability of the porous medium was decreased depended on when the calcium was added to the system. Also, periods of low flow were found to decrease porosity and permeability to a greater extent. This result adds to the evidence that a pulsed flow injection strategy may be most effective for permeability reduction via MICP in the subsurface. Additionally, reactive transport modeling predicts a heterogeneous mineral saturation environment at the pore-scale which highlights the challenge of predicting precipitation behavior in Darcy-scale reactive transport models.

CHAPTER 1

INTRODUCTION

Background

Controlling and understanding how water, and other fluids, flow in the subsurface is a significant challenge. The resistance to flow in soil, rock or any other porous medium is the primary factor which controls how these fluids flow. The measure of how well a porous medium conducts a fluid is called permeability. It is often desirable to decrease the permeability in regions of the subsurface in order to manipulate ground water transport. For example, this could be to block the flow of pollutants or even potentially to mitigate the effects of hydraulic fracturing to surface water in the oil and gas industry.

The research presented in this dissertation investigates microbially-induced calcium carbonate precipitation (MICP) as a potential method to reduce porosity and permeability in the subsurface. Specifically, urea-hydrolyzing bacterial biofilms and the precipitates that they are capable of forming were focused on. The research presented in this dissertation was conducted in such a manner to have wide applicability across multiple potential applications of MICP by looking at the fundamental processes involved. Figure 1 is an example of the end result of carrying out MICP in a porous medium composed of sand. Calcium carbonate crystals and biofilm form on sand particles, thus taking up pore space and decreasing permeability.

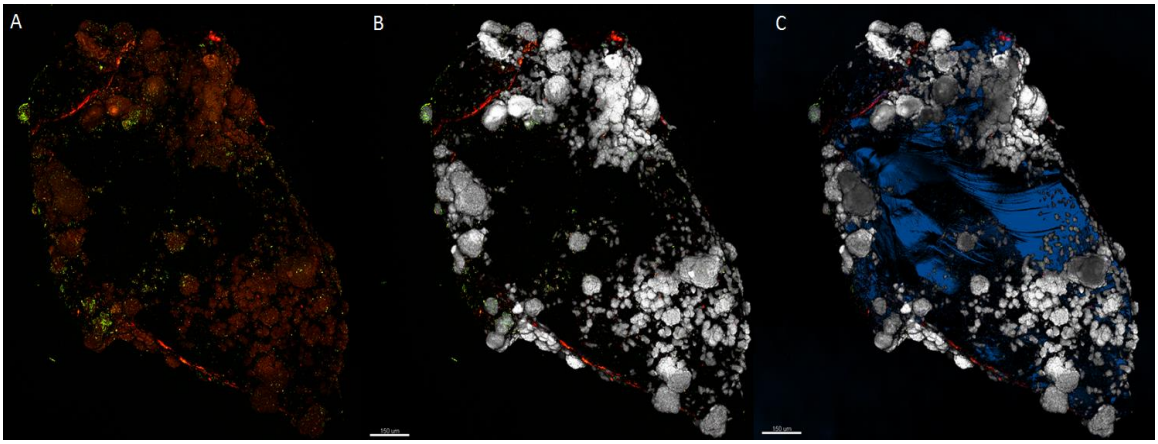


Figure 1. A 3D confocal microscopy reconstruction of a sand grain with attached bacteria (*S. pasteurii*) and calcium carbonate precipitates. The sand grain surface was imaged with reflected light (Blue), calcium carbonate was imaged using auto fluorescence excited by an ultraviolet laser (White), and biomass was imaged using LIVE-DEAD fluorescent staining. Areas containing healthy cells stain green while areas that contain cells with compromised cellular membranes or extracellular nucleic acids stain red. (A) Biomass distribution. (B) Biomass with calcium carbonate overlaid. (C) All components including the sand grain surface shown in blue.

This research was sponsored by the U.S. National Science Foundation (NSF) under CMG award No. DMS-0934696 "Impact of Mineral Precipitating Biofilms on the Physical and Chemical Characteristics of Porous Media." The research was conducted at the Center for Biofilm Engineering (CBE) and the Montana Microfabrication Facility (MMF) at Montana State University (MSU) (Montana, USA). The research described here has been conducted concurrently and in close coordination with other research efforts at CBE-MSU focusing on the scale-up and field application of the MICP technology. These efforts were supported by the US Department of Energy DE-FE0004478, DE-FE000959, DE-FG02-13ER86571, DE-FC26-04NT42262 and DE-FG02-08ER46527.

Research that was supplementary to what is discussed explicitly in this dissertation includes collaboration with Oregon State University (OSU) to validate x-ray computed tomography observations using confocal microscopy. This work was funded by the Office of Science (BER), Subsurface Biogeochemical Research Program, U.S. Department of Energy through Grant Numbers DE-FG-02-09ER64758, DE-FG02-07ER64417 and DE-FG02-09ER64734. Additional support was provided by the NSF IGERT program through a traineeship in "Geomicrobiological Systems" (DGE 0654336) out of which two collaborative projects were born. The first ongoing project is the construction and analysis of a metabolic network model for the sulfate reducing bacterium *Desulfovibrio alaskensis* G20. The second collaboration to come from the IGERT traineeship was a project to observe and model the chemotactic response of the methanogen *Methanococcus maripaludis* to hydrogen gas. The abstract for the chemotaxis work, published in Brileya et al., (2013) can be found in Appendix H. The confocal microscopy equipment used was purchased with funding from the NSF-Major Research Instrumentation Program and the M.J. Murdock Charitable Trust.

Dissertation Overview

This dissertation is organized in a progression from a literature review in Chapter 2 to methods development in Chapters 3 and 4, pore-scale experiments in Chapter 5 and modeling in Chapter 6 where MICP is explored *in silico*. Observations from experimentally motivated chapters inform the model described in Chapter 6 and in turn,

results extracted from the model adds further understanding to the experimental work. Chapter 7 draws conclusions from the work as a whole and proposes future research.

Chapter 2 is a book chapter which serves as a literature review and forms the theoretical basis for the dissertation as a whole. This chapter was accepted and is in press as "Microbially induced carbonate precipitation in the subsurface: Fundamental reaction and transport processes" in the third edition of *The Handbook of Porous Media* (Connolly and Gerlach, 2015). This chapter presents a general introduction to MICP and specifically describes the various alkalinity producing metabolisms, including urea hydrolysis. Biofilm concepts are discussed as well as precipitation theory and the topics are tied together in a discussion of reactive transport concepts and modeling.

In Chapter 3 the description and kinetic characterization of two new model organisms for the study of MICP is presented. The recombinant bacteria constructed in this work are *Pseudomonas aeruginosa* strain MJK1 and *Escherichia coli* strain MJK2 which carry a plasmid-borne urease operon and a chromosomal green fluorescent protein (GFP) construct. The ureolytic activities of the two new strains were compared to the common, non-GFP expressing, model organism *Sporosarcina pasteurii* in planktonic culture under standard laboratory growth conditions. The utility of the new strains was demonstrated with confocal imaging in capillary flow cell reactors with calcium carbonate precipitation occurring. This work was published as "Construction of two ureolytic model organisms for the study of microbially induced calcium carbonate precipitation." in the *Journal of Microbiological Methods* (Connolly et al., 2013).

The biofilm-specific kinetics of urea hydrolysis must be known in order to utilize the new model organism strains for pore-scale reactive transport modeling. If reaction rates were to be left unknown then it would not be possible to predict local concentrations. In Chapter 4 the description of experiments to determine an appropriate kinetic model is described using *E. coli* MJK2. Inverse modeling of the small-scale (mm to cm) plug flow reactors used in these sets of experiments was used to estimate volumetric urea hydrolysis kinetics. The kinetics determined in Chapter 4 are utilized throughout the remaining chapters in reactive transport modeling. This work was submitted and is currently in review as "Estimation of a biofilm-specific reaction rate: Kinetics of bacterial urea hydrolysis in a biofilm." in *npj Biofilms and Microbiomes*.

In Chapter 5 the defined biofilm-specific kinetics of *E. coli* MJK2 and the ease of noninvasive imaging using GFP are utilized in 2D micromodel porous media reactors. MICP was carried out in these 2D micromodel reactors and imaged with confocal microscopy. Imaging allowed for the estimation of porosity reduction due to all pore blocking constituents (biofilm, mineral and gas). Differential pressure measurements also allowed for the estimation of permeability during these experiments. Results of Chapter 5 suggest that the timing of the calcium addition to MICP systems may be important and periods of low flow or no flow lead to more mineral plugging but also may encourage the accumulation of gas bubbles in the pore space. Chapter 5 is currently being prepared in the form of a manuscript titled "Reactive transport and permeability reduction in a synthetic 2D porous medium with biofilm-induced carbonate precipitation" in preparation to be submitted to a peer-reviewed journal.

In Chapter 6, experimental observations are incorporated into an individual-based biofilm model that has been modified to include mineral precipitation. This work is a collaborative effort with Dr. Cristian Picioreanu's research group at Delft Technical University (TU Delft) in the Netherlands who created the original biofilm-only model (Picioreanu et al., 1998). The model agrees well with experimental observations when it is assumed that the model domain is seeded with many mineral nuclei rather than using classical nucleation rate relationships found in the literature. The model also predicts a highly heterogeneous saturation environment in MICP systems that have similar urea hydrolysis kinetics. This is contrasted with a fairly homogeneous urea concentration on the same scale (100 μm)

The appendices contain supplemental information for the main chapters as well as additional work completed during this PhD work that do not fit neatly into the central theme of this dissertation. Additional work contained in the appendices include the surface characterization of microbial precipitates using x-ray photoelectron spectroscopy (Appendices F and G), modeling of microbial chemotaxis (Appendix H) and the discussion of medical struvite stone formation via microbial urea hydrolysis.

CHAPTER 2

MICROBIALLY INDUCED CARBONATE PRECIPITATION IN THE SUBSURFACE: FUNDAMENTAL REACTION AND TRANSPORT PROCESSES

Contribution of Authors and Coauthors

Manuscript in Chapter 2

Author: James M. Connolly

Contributions: Envisioned graphics, table design and major topics of the review. Wrote and revised manuscript.

Co-Author: Robin Gerlach

Contributions: Envisioned major topics of the review. Contributed to the writing, development and revision of the manuscript with comments and feedback.

Manuscript Information Page

James Connolly and Robin Gerlach
Handbook of Porous Media, 3rd Ed.
Status of Manuscript:
____ Prepared for submission to a peer-reviewed journal
____ Officially submitted to a peer-review journal
__x_ Accepted by a peer-reviewed journal
____ Published in a peer-reviewed journal

CRC Press
Submitted: March 2014
Accepted: May 2014
In Press

Introduction

Many microorganisms are capable of inducing carbonate mineral precipitation under certain conditions. Not to be confused with structured biomineralization in eukaryotes for bones and shells, bacteria can indirectly cause precipitation as a byproduct of alkalinity increasing metabolisms, such as photosynthesis, urea hydrolysis, sulfate reduction, nitrate reduction and iron reduction. The geologic record holds many examples of microbially produced carbonates and presently the process is being utilized to manipulate porous media properties (De Muynck et al., 2010; Riding, 2000). Applications in porous media are numerous but can generally be divided into either increasing the material strength or reducing permeability (Phillips et al., 2013a). The microbiology of such systems will be discussed including metabolisms, biofilm concepts and biological reaction rates, followed by mineral precipitation fundamentals and reactive transport modeling approaches.

Microbial activity can induce a cascade of physical and chemical changes, which can include the shift of carbonate equilibrium chemistry, precipitation, and changes to system hydrodynamics. Changes in hydrodynamics in turn can change the reaction and transport in biofilm-and mineral-affected porous media. Both Darcy-scale and pore-scale reactive transport concepts will be discussed and classical porous media methodology will be applied to MICP systems.

In the subsurface, microorganisms have a close association with the surfaces of the porous medium they live in making them potentially sensitive to changes to those

porous media surfaces. Precipitation can cause changes (physical and chemical) to surfaces that the microbes are attached to, and as a result can change the reactive transport behavior in the porous medium. Additionally, precipitation can change the local physical and chemical environments thus altering microbial activity and in mixed microbial communities potentially shifting local populations. As shown in Figure 2, many processes can occur during MICP and affect reactive transport, porous media morphology and biogeochemical conditions. Before precipitation, attached microorganisms can affect flow by the formation of biofilm. Once precipitation commences additional pore space reduction can occur along with the potential for inactivation of biomass through encapsulation in the precipitate (Al Qabany et al., 2012; Cuthbert et al., 2012). Planktonic biomass also has the potential to cause precipitation in the bulk fluid that can be deposited downstream. The deposited precipitates can cause an additional reduction in porosity and permeability.

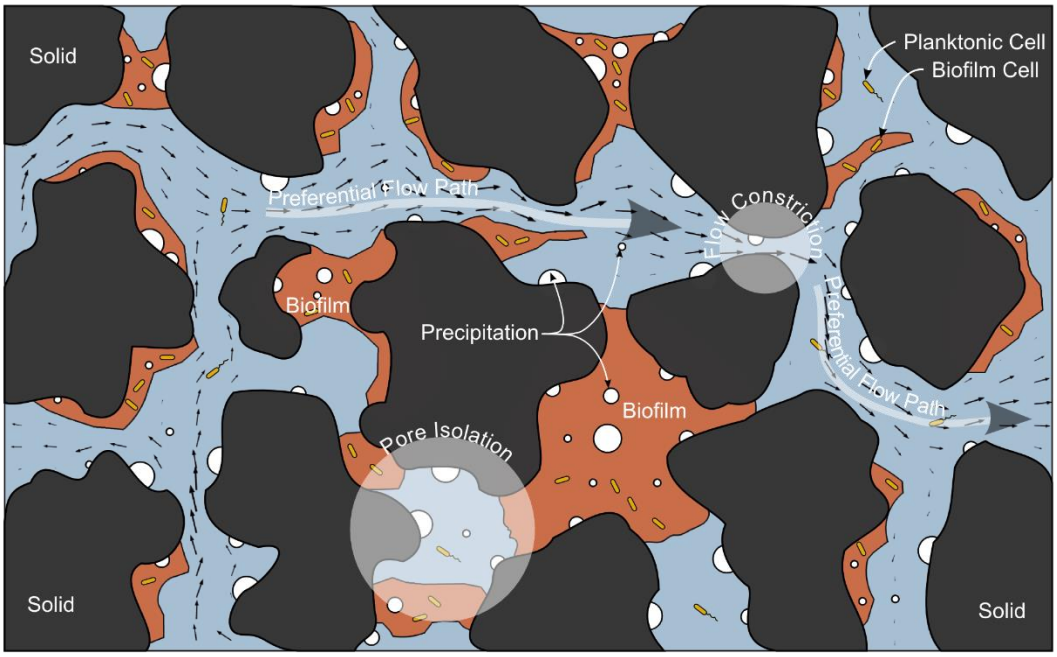


Figure 2. Fluid flow and reactive processes affecting MICP at the pore network scale. Microbial cells exist either in a freely floating planktonic state or in a biofilm. Precipitation can occur in suspension, in the biofilm or on solid surfaces. Biofilm and precipitates affect local hydrodynamics if they are present in sufficient quantities by blocking pore throats, isolating pores and constricting flow. Stagnant zones and preferential flow pathways develop leading to pore-scale chemical, physical and potentially biological heterogeneity.

The aim of this chapter is to describe the major pore-scale processes associated with MICP and put them in the context of porous media reactive transport modeling approaches. First MICP is divided into biological, physical, and geochemical sub processes; their interactions are discussed at the pore-scale, and finally it is discussed how these processes and interactions affect local and system wide reactive transport. The chapter as a whole is intended to serve as an overview of the current knowledge within the MICP field in regards to pore-scale processes. The processes are represented in

equation form where possible to provide mathematical relationships that are useful for modeling.

Biological Processes

Among the known microbial metabolisms there are primarily four types that have been associated with significant mineral precipitation in the subsurface through the generation of alkalinity. These mineral precipitation-inducing metabolisms are urea hydrolysis, nitrate reduction, sulfate reduction and iron reduction (Castanier et al., 1999). Microbial photosynthesis (e.g. in cyanobacteria) is also a significant source of biominerals in nature (e.g. stromatolites (Riding, 2000)). However, the importance of photosynthesis is restricted to the earth's surface because of the requirement for sunlight and will thus not be discussed in this chapter. We do not aim to discuss every type of alkalinity producing metabolism in this chapter; however, the four that are discussed in detail are likely representative of the most effective ones (DeJong et al., 2010; van Paassen et al., 2010).

Alkalinity Producing Metabolisms in the Subsurface

Alkalinity is generally defined as the amount of acid that must be added to a solution to decrease its pH to a given level, or alternatively as the ability of a solution to resist a pH decrease (Crittenden et al., 2012). Where the carbonate buffering system dominates, as is the case in most natural waters, alkalinity can be expressed as

$$\text{Alkalinity} = [HCO_3^-] + 2[CO_3^{2-}] + [OH^-] - [H^+]. \quad (1)$$

Square brackets indicate molar concentrations. Alkalinity production can then be generalized as any process that results in the consumption of acid equivalents (H^+) or production of base equivalents (OH^- or other anions). In the presence of dissolved inorganic carbon (DIC) and certain cations such as calcium (Ca^{2+}), an increase in alkalinity can induce the precipitation of carbonate minerals such as calcium carbonate ($CaCO_{3\,(s)}$):

$$Ca^{2+} + CO_3^{2-} \rightarrow CaCO_{3(s)}. \qquad (2)$$

DIC is the sum of all carbonate species in a solution and can generally be represented as

$$DIC = [H_2CO_3^*] + [HCO_3^-] + [CO_3^{2-}]. \qquad (3)$$

$H_2CO_3^*$ denotes the sum of fully protonated carbonic acid and dissolved CO_2. When other ions such as sodium or calcium are abundant, as is often the case in MICP systems, calcium bicarbonate ions ($CaHCO_3^+$), sodium carbonate ions ($NaCO_3^-$), and other similar species may also have to be included. The relative concentration of each of the three pure carbonate species is pH dependent and is determined by the set of equilibrium equations in Table 1.

Table 1. Equilibrium reactions and pk ($-\log_{10}(k)$) values for the carbonate system at 25° C.

Reaction	Equilibrium Equation	pk
Water dissociation	$H_2O \leftrightarrow OH^- + H^+$	14
Carbonic acid dissociation	$H_2CO_3^* \leftrightarrow HCO_3^- + H^+$	6.35
Bicarbonate dissociation	$HCO_3^- \leftrightarrow CO_3^{2-} + H^+$	10.33

At a pH value between roughly 6.5 and 10, the DIC is dominated by bicarbonate (HCO_3^-). For this reason, most of the biological and geochemical reactions discussed in later sections of this chapter will be written with DIC as bicarbonate. Although bicarbonate generally dominates DIC at biologically relevant pH values, there will still be a small fraction present as carbonate (CO_3^{2-}) which is the species available for precipitation. It should be noted that equilibrium reactions, and thus the pk ($-\log_{10}(k)$) values in Table 2, are dependent on temperature and ionic strength. One example where both ionic strength and temperature must be considered would be a deep brine aquifer that would have elevated temperature and potentially very high ionic strength.

As alkalinity and pH increase, precipitation of carbonate minerals becomes more favorable due to an increase in the carbonate concentration and as a result, the saturation state. The saturation state (S) is defined as

$$S = \frac{IAP}{k_{sp}}, \qquad (4)$$

where IAP is the ion activity product and k_{sp} is the solubility product (Mullin, 2001). The IAP is simply the product of the activities, (here denoted as {x}) of all ions associated with the mineral. Taking calcium carbonate as an example:

$$IAP = \{Ca^{2+}\}\{CO_3^{2-}\}. \qquad (5)$$

When the IAP is greater than k_{sp} (or S > 1) then the solution is supersaturated and precipitation is possible. Increasing the activity of either calcium or carbonate ions can lead to supersaturation. The use of activity rather than concentration is particularly important when calculating the saturation state because depending on the conditions (e.g.

temperature and ionic strength), order of magnitude errors are possible (Zhang and Dawe, 1998). Figure 3 shows the relationship between concentration and activity over a range of ionic strengths for divalent and monovalent species. At low ionic strength the values for ion activity approach the concentrations of the ions (activity coefficient = 1). This approximation cannot be made for high ionic strength solutions such as seawater or high salinity brine systems.

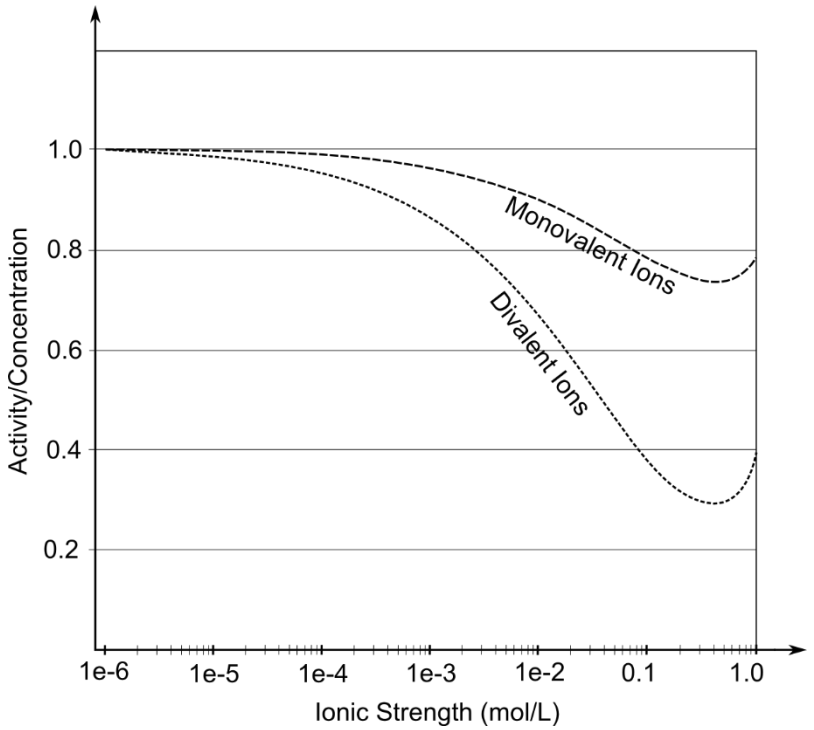


Figure 3. The ratio of the ionic activity versus concentration (also known as an activity coefficient) for monovalent and divalent ions over a range of ionic strengths. For comparison, seawater has an average ionic strength of approximately 0.7 mol/L. The Davies extension of the Debye-Hückel relationship was used (Davies, 1962). The Pitzer equation should be used at ionic strengths above 0.1 mol/L (Pitzer, 1991) but was not shown here because a specific solution chemistry would have to be assumed.

Urea Hydrolysis. Many heterotrophic soil bacteria have the capability to use urea (CO(NH2)2) as a nitrogen source (Mobley and Hausinger, 1989; Morsdorf and Kaltwasser, 1989). Urea can be present in the subsurface from animal waste sources or be added directly to engineered environments. Urea must be hydrolyzed in order to be utilized for biomass growth and many organisms possess enzymes for that purpose. Uncatalyzed urea hydrolysis proceeds slowly but its rate is greatly increased (by orders of magnitude) by the urease enzymes produced by many organisms (Yingjie and Cabral, 2002). Urease (Dixon et al., 1976; Mobley et al., 1995) catalyzes the hydrolysis of urea to form inorganic carbon and ammonia by

$$CO(NH_2)_2 + 2\,H_2O \rightarrow 2\,NH_3 + HCO_3^- + H^+ . \qquad (6)$$

Urea hydrolysis on its own has no effect on alkalinity but at circumneutral pH the ammonia becomes protonated where

$$NH_3 + H^+ \leftrightarrow NH_4^+ . \qquad (7)$$

Combining urea hydrolysis with the subsequent ammonia protonation, the overall reaction becomes

$$CO(NH_2)_2 + 2\,H_2O + H^+ \rightarrow 2\,NH_4^+ + HCO_3^- , \qquad (8)$$

where one proton is consumed and one bicarbonate ion is produced. Thus, at circumneutral pH the hydrolysis of one mole of urea increases the alkalinity by two moles, effectively increasing the saturation state of carbonate minerals.

Microorganisms can utilize urea hydrolysis in an assimilatory fashion by simply incorporating the ammonium or ammonia into their nitrogen metabolism or in a dissimilatory process where the bacteria gain energy through the formation of a

membrane potential (Jahns, 1996). It is also a reasonable theory that dissimilatory urea hydrolysis is a competitive strategy that provides an advantage over non-alkaliphilic organisms. Heterotrophic bacteria in the genera *Sporosarcina* and *Bacillus* have been shown to produce particularly high amounts of urease (Jahns, 1996; Morsdorf and Kaltwasser, 1989). In the case of *Sporosarcina pasteurii*, urease has been shown to comprise approximately 1% of the cell dry weight (Bachmeier et al., 2002), making it a highly effective organism in the context of MICP for engineered purposes in the subsurface where oxygen is present (Al Qabany et al., 2012; Martin et al., 2012; Tobler et al., 2011). Under most conditions, in the presence of sufficient calcium, dissimilatory urea hydrolysis readily induces calcium carbonate precipitation and permeability reduction in a porous medium (De Muynck et al., 2010; Phillips et al., 2013a).

Denitrification. Denitrification is the reduction of oxidized forms of nitrogen, mainly nitrate (NO_3^-), to nitrogen gas (N_2) and is primarily carried out by heterotrophic bacteria. The overall redox half reaction of denitrification is

$$2\,NO_3^- + 10\,e^- + 12\,H^+ \rightarrow 6\,H_2O + N_2. \qquad (9)$$

Denitrification is then coupled to the oxidation of an electron donor such as acetate (CH_3COO^-) and the overall catabolic reaction becomes

$$5\,CH_3COO^- + 8\,NO_3^- + 3\,H^+ \rightarrow 10\,HCO_3^- + 4\,N_2 + 4\,H_2O, \qquad (10)$$

where alkalinity is generated by the consumption of protons and the generation of bicarbonate. The use of acetate as a carbon source in an engineering setting could be particularly useful because the use of calcium acetate and calcium nitrate accomplishes

adding the electron/donor pair necessary for growth and alkalinity production as well as the divalent cation necessary for mineral formation. There are many organic and inorganic electron donors that can be utilized by denitrifying microorganisms. For example, denitrification using hydrogen gas as an electron donor (autohydrogenotrophic denitrification) has been shown to greatly increase alkalinity and to precipitate calcium carbonate in wastewater treatment environments (Lee and Rittmann, 2003).

Mineralization through nitrate reduction has been of recent interest in the bioremediation field as an alternative to urea hydrolysis (Martin et al., 2013) due to concerns concerning growth inhibition of ureolytic bacteria in anaerobic environments and problems with generating large amounts of ammonium in the subsurface (Martin et al., 2012; van Paassen et al., 2010). Denitrification is, however, not without complications due to the potential generation of large amounts nitrogen gas that could cause transient (rather than long lasting) permeability reduction and the potential formation of nitrous oxide, a strong greenhouse gas. Furthermore, the direct injection of nitrate into the subsurface may face regulatory hurdles because it is a regulated pollutant in much of the world although balanced addition of nitrate and electron donor could result in very little nitrate remaining after the treatment. Incomplete oxidation of organic electron donors is also possible, potentially causing unwanted byproducts.

Sulfate Reduction. Bacteria that use sulfate (SO_4^{2-}) as an electron acceptor for respiration, known as sulfate-reducing bacteria (SRB), are capable of increasing alkalinity in anaerobic environments. Sulfate reduction has also been described in

Archaea (Klenk et al., 1997; Muyzer and Stams, 2008) but in this chapter the term SRB refers to the broad class of microorganisms that can use sulfate as an electron acceptor. When oxygen or nitrate is not present, mineralization still can occur in the subsurface via sulfate reduction under the right conditions (Braissant et al., 2007). As a half reaction, sulfate reduction can be written as

$$SO_4^{2-} + 9H^+ + 8e^- \rightarrow HS^- + 4H_2O. \qquad (11)$$

The electron donor could be organic or inorganic depending on the specific organism. The reduced sulfur species equilibrium acts similarly to the inorganic carbon equilibrium in that speciation is dependent on pH. At pH values below 7 the dominant species is hydrogen sulfide gas (H_2S). At pH values between 7 and 13, the dominant species is bisulfide (HS^-), a strong base, and at extremely basic pH values sulfide (S^{2-}) dominates. In this section we will assume that these reactions are taking place in an already alkaline environment where bisulfide is the dominant species.

SRBs are a diverse class of microorganisms, many of which are capable of utilizing multiple electron donors and carbon sources (Lengeler et al., 1998). Some SRB species can produce alkalinity and precipitate carbonate minerals on their own. Others enter into symbiotic relationships that form biominerals and yet others decrease alkalinity and cause corrosive environments (Muyzer and Stams, 2008). Both the metabolic potential of the organism and the biogeochemical conditions that surround them dictate how they will affect the mineral saturation states and this complex interplay cannot be fully covered in this chapter. Rather, this section will primarily deal with the types of systems that are associated with precipitation.

Perhaps the most common example of alkalinity production in nature via sulfate reduction is when it is coupled to anaerobic methane oxidation (Boetius et al., 2000; Milucka et al., 2012). The overall result is the consumption of methane and sulfate and the production of bicarbonate and free sulfides (H_2S or HS^- depending on the pH). At above a pH of 7 the reaction occurs according to

$$CH_4 + SO_4^{2-} \rightarrow HCO_3^- + HS^- + H_2O \cdot \qquad (12)$$

The resulting increase in alkalinity has been shown to cause precipitation, particularly of carbonate minerals and iron sulfides (Wallmann et al., 2006). Anaerobic methane oxidation has been linked to the formation of modern calcium carbonate deposits in marine environments (Glenn et al., 2007) as well as pore-blocking authigenic carbonates in marine sediments (Wallmann et al., 2006).

Alkalinity generation and precipitation can also be facilitated by SRBs in pure culture by the degradation of organic substances such as carbohydrates and organic acids. As an example, the complete oxidation of acetate (CH_3COO^-) increases alkalinity by producing bicarbonate at circumneutral pH where

$$CH_3COO^- + SO_4^{2-} \rightarrow 2\,HCO_3^- + HS^-. \qquad (13)$$

Rather than producing bicarbonate, classes of SRBs, many of which lie in the genus *Desulfovibrio*, are able to gain energy by oxidizing hydrogen gas. Hydrogen oxidation increases alkalinity by consuming a proton where

$$4\,H_2 + SO_4^{2-} + H^+ \rightarrow HS^- + 4\,H_2O. \qquad (14)$$

Iron Reduction. Iron reducing microorganisms represent a potential source of alkalinity production in environments where there is a significant amount of ferric iron (Fe^{3+}). Dissimilatory iron reducers use ferric iron as their terminal electron acceptor reducing it to ferrous iron (Fe^{2+}) coupled with the oxidation of H_2 or organic substrates. Like sulfate reducers, iron reducers are diverse and widely distributed phylogenetically across *Bacteria* and *Archaea* (Fredrickson and Gorby, 1996; Lovley et al., 2004). Species from the genera *Geobacter*, *Desulfuromonas* and *Shewanella* are representative of the metabolisms discussed in this section. Dissimilatory iron reduction is a particularly complex process because ferric iron exists in many forms and is often poorly soluble in the subsurface (Nevin and Lovley, 2002). This section will not cover iron equilibria and how iron reducers can affect it in detail but Nevin and Lovely (2002), as well as others, provide a thorough discussion of this topic.

Iron reduction can be represented by the half reaction

$$Fe^{3+} + e^- \rightarrow Fe^{2+}. \qquad (15)$$

The source of ferric iron and the fate of ferrous iron are highly variable depending on the physical and chemical environment in which the process is taking place. Ferric oxides (Fe_2O_3) and oxyhydroxides (FeOOH) are common in the subsurface but are often not very soluble. Thus, ferric iron reduction requires the use of specialized strategies by the involved microbes, which can include the use of external electron shuttles, chelators, Fe^{3+} solubilizing agents and possibly electron flow by direct electrical contact to the iron minerals through filaments (Nevin and Lovley, 2002; Pfeffer et al., 2012). Soluble iron could also be added to a system in an engineered setting. The fate of the reduced iron can

be as precipitated pyrite (FeS_2) or magnetite (Fe_3O_4), remain in the soluble form, or be oxidized back to ferric iron by either biotic or abiotic reactions (Fredrickson and Gorby, 1996). Ferrous iron can also be precipitated in the form of iron carbonate (siderite, $FeCO_3$) (Fredrickson et al., 1998).

It has been demonstrated experimentally that iron reduction can increase alkalinity when ferric oxyhydroxide (FeO(OH)) is supplied as the source of soluble oxidized iron (Vile and Wieder, 1993). Using acetate (CH_3COO^-) as the electron donor, net alkalinity will be produced by

$$8\,FeO(OH) + CH_3COO^- + 15\,H^+ \rightarrow 8\,Fe^{2+} + 2\,HCO_3^- + 12\,H_2O, \qquad (16)$$

where protons are consumed and bicarbonate is produced, increasing alkalinity. The formation of bacterial iron carbonates in nature is well documented (e.g. Fredrickson et al., 1998) however its stimulation for engineered purposes remains relatively unstudied and remains undemonstrated as a viable technology (Stephens and Keith, 2008).

Biofilms

A microbial biofilm consists of a consortium of cells held together by a self-produced matrix that is attached to a surface. The matrix typically consists of biopolymers such as polysaccharides, nucleic acids and proteins and is often referred to in general terms as extracellular polymeric substances (EPS) (Characklis and Marshall, 1990; Flemming and Wingender, 2001a). The high surface area of a porous medium can be highly conducive to biofilm growth. Biofilm growth in general, and especially in a porous medium, can be a significant cause of metabolic diversity due to spatially and

temporally heterogeneous mass transport (Cunningham et al., 1991; Shafahi and Vafai, 2009) that can cause microenvironments.

Biofilms and planktonic (freely floating) biomass contribute to carbonate precipitation. The ratio of biofilm biomass to planktonic biomass is entirely system dependent but generally it can be assumed that most of the biomass is acting in an attached state in the subsurface (Costerton et al., 1987; Lappin-Scott and Costerton, 2003; Vandevivere and Baveye, 1992). Even planktonic cells detected in a porous medium will often be detached biofilm clusters (Stoodley et al., 2001). This is in fact an important distinction because at the pore-scale the locations of highest microbial activity and alkalinity generation, thus supersaturation will be most likely localized within biofilm colonies. During the early stages of mineral formation, one would expect nucleation to occur in biofilms but microbial biofilms, and even the EPS alone, have been shown to affect and in some cases inhibit mineral nucleation and growth significantly (Braissant et al., 2003; Decho, 2010; Dhami et al., 2013; Ercole et al., 2012; Kawaguchi and Decho, 2002; Rodriguez-Navarro et al., 2007). For example, the growth of aragonite has been shown to be inhibited by the adsorption of acidic polysaccharides to crystalline surfaces (Wada et al., 1993).

Along with the physical effects of biofilm growth on mineral formation and reactive transport in a porous medium, there are chemical effects. The chemical effects of biofilm and EPS on mineral precipitation are not fully understood and are likely to vary from system to system; however, there are some concepts that have gained general acceptance. Prokaryotic cells and biopolymers generally have exposed negative charges

that are available for crosslinking with divalent cations through electrostatic interaction (Flemming and Wingender, 2001b; Mayer et al., 1999). When divalent cations are present, as they are likely to be in MICP systems, EPS has the tendency to bind these ions potentially affecting crystal nucleation and growth (Kawaguchi and Decho, 2002; Perry et al., 2005). This binding adds structural rigidity to the biofilm by crosslinking the negatively charged EPS polymers (Chen and Stewart, 2002) and lowering diffusivity. Cation binding also affects the polymorphism of minerals. For example, calcite is the most stable form of calcium carbonate at long time scales but when organic molecules are present, specifically biofilm-associated polymers, other polymorphs (aragonite and vaterite) or amorphous precipitates can be stabilized (Dhami et al., 2013; Rodriguez-Navarro et al., 2007).

Kinetics

Until now only the existence of the different biogeochemical processes in MICP has been discussed, but in order to truly understand MICP systems the rates at which these processes take place need to be understood. MICP systems generally have slow, rate limiting biological reactions followed by fast aqueous inorganic equilibrium reactions. The reactions responsible for producing alkalinity are limited by microbial enzyme rates. For modeling purposes it is generally assumed that the biological reactions, including those taking place in biofilm, limit overall reaction rates and all inorganic species equilibrate fast enough to be at equilibrium (Zhang and Klapper, 2010).

The enzyme-catalyzed biological reactions discussed in Section 0 are usually a chain of many reactions. Nitrate reduction for example is a multi-step process with each reaction being carried out by a different enzyme possessing different kinetic properties. Even the apparently simple urea hydrolysis system, with the primary reaction being carried out by a single enzyme can be affected by other reactions that would affect intracellular substrate or product concentrations such as cell membrane transport reactions for urea and ammonia or pH regulation (Jahns, 1996).

Enzymatic reactions are typically a function of reaction substrates, products, temperature and pH. The most common rate expression is the Michaelis–Menten kinetic model with only substrate concentration being taken into account where

$$\frac{dC_s}{dt} = R_s = R_{max} C_E \frac{C_s}{k_m + C_s} . \qquad (17)$$

C_s is the substrate concentration, R_s is the substrate-dependent reaction rate, R_{max} is a theoretical maximum rate and k_m is a half saturation constant ($C_s = k_m$ at $R_s = 0.5R_{max}$) and C_E is the enzyme concentration. For example, if the Michaelis–Menten kinetic model were applied to urea hydrolysis, C_s would be the concentration of urea and the other kinetic constants would need to be determined through experiments or extracted from the literature taking into account potential pH, temperature, pressure, and ionic strength dependencies. C_E is often assumed to be constant or scaled to the microbial population. It should be noted that above certain enzyme-to-substrate concentration ratios saturation kinetics with respect to enzyme concentration can also develop. However, such high enzyme-to-substrate concentration ratios are not very likely to occur in porous media

systems of relevance to engineers. Simplifications can be made for cases with very high and very low substrate concentrations resulting in “zero order” and “first order” relationships with respect to C_s as follows.

$$\text{Zero Order}: R_s = R_{max} \quad \text{for} \quad C_s >> k_m \tag{18}$$

$$\text{First Order}: R_s = \frac{R_{max}}{k_m} C_s \quad \text{and} \quad \frac{R_{max}}{k_m} \equiv k_1 \quad \text{for} \quad C_s << k_m \tag{19}$$

In the first order approximation, R_{max}/k_m is typically combined to form a new variable, the first order reaction rate constant (k_1) leaving a simple linear relationship. Both enzyme specific rates and rates of overall metabolic activity are commonly expressed in any of the three forms above depending on the conditions and application. In substrate-limited systems, it can be more appropriate to use the first order approximation because substrate concentrations are low. In other systems, where the substrate concentrations are expected to be higher, a zero order approximation may be appropriate.

Local reaction rates (and concentrations as a result) are difficult to predict at the pore-scale because biofilm specific rates are not well studied. As discussed previously, the majority of the microbiological activity in the subsurface is likely to be attributed to biofilm. Unfortunately most tabulated kinetic values (R_{max} and k_m) are reported for planktonic systems or for pure enzymes. To accurately predict pore-scale behavior the volumetric reaction rate (rate per volume of biofilm, or per volume of porous medium) must be known and estimating those rates accurately can be difficult since planktonic or pure enzyme characteristics might not hold true in biofilms. Figure 4 shows a calculated saturation state distribution in a pore-scale model with ureolytic alkalinity generation.

The biovolumetric reaction rate is varied and the result is a significant change in the calculated heterogeneity of local saturation states. In general, higher biological reaction rates lead to more heterogeneous local concentrations due to mass flux limitations as illustrated in Figure 4.

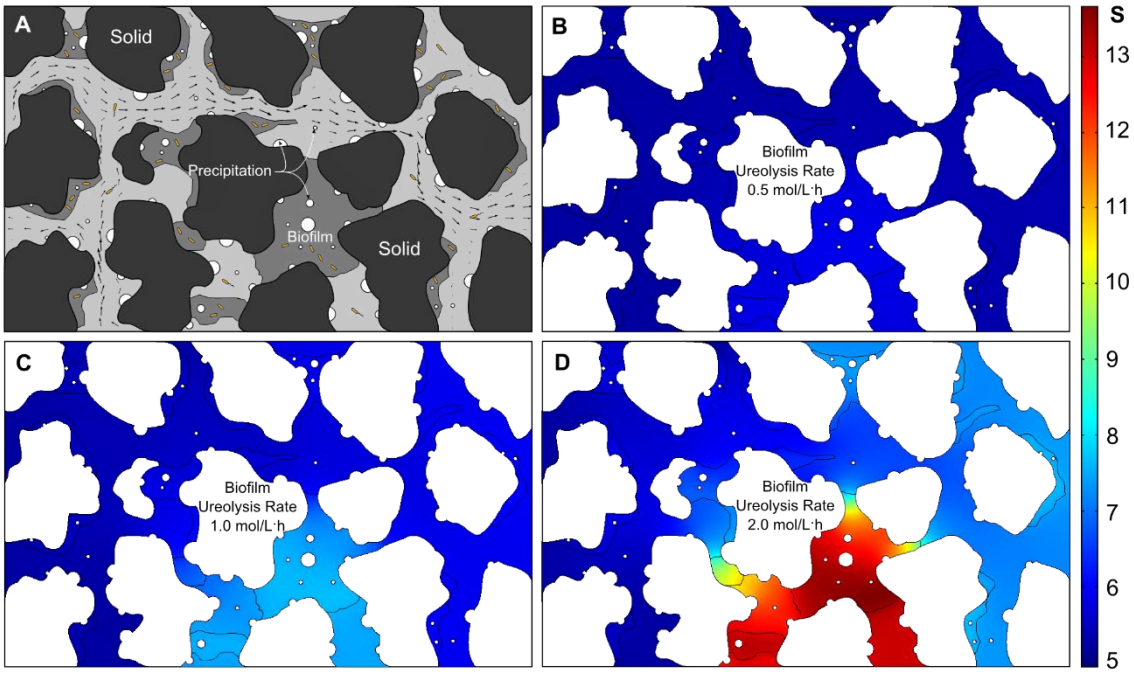


Figure 4. The theoretical geometry presented in Figure 1 (A) was applied to a 2D, steady-state finite element model to demonstrate the effect of alkalinity production in a biofilm on the pore-scale spatially-resolved saturation state (S). Panels B, C and D show simulations with varied urea hydrolysis rates of 0.5, 1.0 and 2.0 mol/(L·h) respectively and a constant precipitation rate of 0.001 mol/(m^2·h). In this example urea hydrolysis occurs only in the biofilm domains and laminar fluid flow (Re << 1) is restricted to the liquid domain (no flow inside the biofilm domains). Please refer to the 'Modeling Notes' section at the end of this chapter for additional information regarding this model.

Mineral Precipitation Theory

Precipitation is very effective at blocking pore space in geologic materials. As opposed to pore blockage with biofilm alone, the precipitation of minerals is an attractive strategy to block pores because the minerals have the potential to be longer lasting (Ebigbo et al., 2010; Mitchell and Ferris, 2006). The precipitation of carbonate minerals can occur in the subsurface abiotically or through the microbial production of alkalinity as discussed in Section 0. Biomolecules, even if they are not directly involved in precipitation have been shown to affect all of the steps involved in precipitation (Decho, 2010; Kawaguchi and Decho, 2002). In order to understand precipitation, and the effect of microbial activity has on it, one must understand abiotic precipitation. The following section presents basic principles of aqueous mineral precipitation processes and theory important in the context of MICP.

Carbonate Minerals and Polymorphs

Carbonate minerals are commonly precipitated when DIC is present in high enough concentration to allow for local, or widespread supersaturation with respect to carbonates. Other minerals, such as iron sulfides, phosphates and silicates can also precipitate but carbonates are generally dominant in natural and engineered systems that produce microbially induced precipitates. This is because many microorganisms produce DIC as a metabolic byproduct and divalent cations can be added easily or may already be present. Carbonate precipitation is also comparatively fast (Palandri and Kharaka, 2004) making it an obvious choice in many engineered applications. Nucleation and crystal

growth behavior varies between particular minerals but the specifics pertaining to carbonates will be the focus here. It should be noted that if phosphate is expected in a system calcium carbonate growth has the potential to be inhibited and if present at a high enough concentration apatite can be precipitated (Plant and House, 2002).

Carbonates can be either crystalline or amorphous (non-crystalline). Of the crystalline carbonates, there are many types depending on the geochemistry of the environment that they are formed in. If only calcium carbonate is considered, there are three possible polymorphs: calcite, aragonite and vaterite. Each polymorph is calcium carbonate but possesses different crystal structure and solubility (Mohamed and Antia, 1998). At room temperature in pure, aqueous environments without microbes, calcite is the most stable polymorph because it has the lowest solubility (Plummer and Busenberg, 1982). The subsurface environment is rarely pure, meaning that trace ions as well as organic and inorganic molecules are present to varying degrees. These impurities change the properties of carbonate minerals that are precipitated. Sparse substitutions by trace metal ions in the crystal lattice of a carbonate crystal can affect the morphology leading to one particular polymorph having many distinct morphologies (Li et al., 2012; Zhang and Dawe, 2000). The precipitation of other carbonate minerals is possible in biologically relevant environments including iron and magnesium carbonates. Carbonates with mixed cationic composition can also form, such as dolomite ($CaMg(CO_3)_2$) (Krause et al., 2012; Sánchez-Román et al., 2011; Vasconcelos et al., 1995).

Polymorphic distribution is affected by biological activity. Multicellular organisms generally control the polymorphism of calcium carbonate shells (e.g. oysters

and egg shells) through the use of scaffolding biopolymers and nucleation control. Although it is not as controlled as in multicellular organisms, it has been shown that microbial biofilms change polymorphic composition in a similar way by stabilizing otherwise metastable polymorphs (Rodriguez-Navarro et al., 2007).

Nucleation

Supersaturation with respect to mineral solubility is required for precipitation, but supersaturation does not guarantee precipitation. The formation of thermodynamically distinct phases in a liquid is usually initiated first by nucleation where the rare phase first appears at discrete points. The formation of a nucleus is associated with the system seeking a point of lowest free energy, as proposed by Gibbs (1948). Classical nucleation theory that arose from the work of Gibbs and others was based on condensation of a vapor to a liquid however it is commonly extended to crystallization from solutions. The energy difference between a small elementary volume of solid precipitate and the same mass of dissolved molecules, ΔG, can be split into two parts. First, there is a free energy associated with the energy difference between the crystal surface and the bulk crystal lattice that is called the surface free energy, ΔG_s. The second part is the free energy between the bulk crystal lattice and the dissolved solute called the volumetric free energy, ΔG_v, analogous to a very large crystal particle of infinite radius. The overall free energy can be written as

$$\Delta G = \Delta G_s + \Delta G_v . \qquad (20)$$

If we assume a spherical crystal geometry of radius r, the total free energy can be written as

$$\Delta G = 4\pi r^2\gamma + \tfrac{4}{3}\pi r^3 \Delta G_{dv} \quad (21)$$

where γ is the unit surface energy and ΔG_{dv} is a unit volumetric free energy. The surface energy is always positive if ΔG_{dv} is negative so there is a maximum ΔG (ΔG_{crit}) occurring at a radius r_{crit} (see Figure 4) such that

$$\Delta G_{crit} = \tfrac{4}{3}\pi\gamma r_{crit}^2 , \quad (22)$$

where r_{crit} is the theoretically minimum stable nucleus radius (Mullin, 2001). A nucleus smaller than r_{crit} is most likely to re-dissolve and nuclei reaching a size larger than r_{crit} are stable and are more likely to nucleate larger crystals.

The free energy treatment of the nucleation shows the importance of heterogeneities. Any localized perturbation (physical or chemical) to bulk conditions can be either a source or inhibitor of nucleation. Local high concentration locations are more likely to be points of nucleation as systems have the tendency to equilibrate.

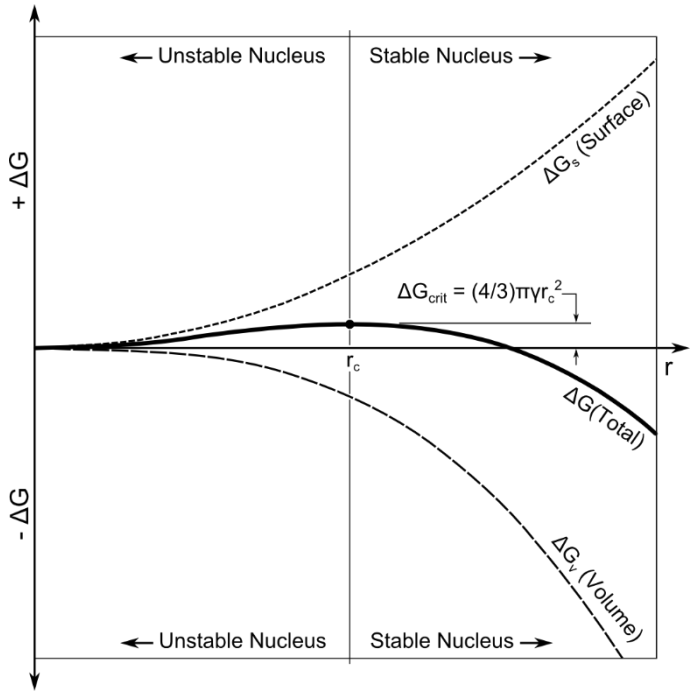


Figure 5. Critical nucleus size behavior due to a maximum in the total free energy (ΔG) based on Equations 20-22. A small nucleus ($r << r_c$) is unstable and is likely to redissolve as relaxation occurs to a lower total free energy. A large nucleus ($r >> r_c$) is likely to grow in order to reduce total free energy (Gibbs, 1948; Mullin, 2001).

Nucleation can happen in two ways. Nucleation can occur on surfaces and as a result of particles in suspension (heterogeneous nucleation) or a nucleus can form randomly in a perfectly homogeneous liquid (homogeneous nucleation). When considering MICP at the pore-scale, the understanding of nucleation is important because it creates the initial conditions for crystal growth. The difficulty for modeling is that nucleation is considered a spatially stochastic process (Gebauer et al., 2008) leading to an uncertainty in the locations and density of nucleation points, and the effects of microbial activity are not well characterized.

The classical approach for homogeneous nucleation is that once a solution is supersaturated, the polymerization of aqueous calcium carbonate occurs randomly and becomes the nucleus precursor (Mullin, 2001). The polymerized aqueous calcium carbonate is termed amorphous calcium carbonate (ACC) and is much different than solid, crystalline phases because it lacks a clear crystal structure. Once an ACC cluster reaches a certain critical size nucleation occurs and ordered crystal growth proceeds (Figure 4) (Yoreo and Vekilov, 2003). This classical view is useful but neglects some detail that is critical to the understanding of the process in biological systems.

A more modern view of calcium carbonate nucleation has three main differences compared to the classical model. First, ACC forms even in under-saturated solutions and can be more stable than was previously thought (Demichelis et al., 2011; Gebauer et al., 2008; Raiteri and Gale, 2010). Second, there is more than one type of ACC that can be ordered such that different calcium carbonate polymorphs are nucleated (Hasse et al., 2000; Politi et al., 2006). Third, ACC can be metastable even in supersaturated conditions, particularly when magnesium ions are present at certain concentrations (Politi et al., 2010; Radha et al., 2012). The overall impact of these more recent discoveries in carbonate nucleation is a change in the assumed energetics of nucleation. The newer view of calcium carbonate nucleation that includes the existence of metastable prenucleation clusters lowers the energetic boundary (free reaction enthalpy) to precipitation relative to what was previously thought under the classical nucleation model (Gebauer and Cölfen, 2011).

The control of the type of ACC that is present during prenucleation in shell-forming multicellular organisms has been shown to be a mechanism for the control of polymorphic composition (Marin et al., 2008; Weiss et al., 2002). Similarly, it is a reasonable hypothesis that biofilms will affect ACC type and cluster size subsequently changing the nucleation characteristics relative to those which would be expected in the bulk fluid. For example, a number of studies have shown that vaterite and ACC are preferentially formed in some MICP systems (Rodriguez-Navarro et al., 2007; Xiao et al., 2010). Vaterite is the least stable crystalline calcium carbonate polymorph at biologically relevant conditions so its occurrence in MICP systems leads to the conclusion that the bacteria are not only inducing precipitation but also affecting polymorphism by stabilizing otherwise unstable intermediate mineral forms (Rodriguez-Navarro et al., 2007). In many MICP systems calcite is the only observed calcium carbonate polymorph, however it is thought that in many cases vaterite is an intermediary and calcite develops through the Ostwald rule of stages where more stable phases form via less stable intermediates (Xiao et al., 2010; Yoreo and Vekilov, 2003). Xiao et al. (2010) also present continued evidence for phospholipid cell walls nucleating carbonate minerals, specifically vaterite as a precursor to calcite (also see: Douglas and Beveridge, 1998).

In the subsurface environment it is reasonable to assume that true homogeneous nucleation is a rare event. Geologic porous media have many of the factors that generally are associated with the existence of heterogeneous nucleation. These factors include the presence of secondary nucleation sites (seed crystals) and rough surfaces (Mullin, 2001). Heterogeneous nucleation requires less free energy change compared to that associated

with homogeneous nucleation, allowing nucleation to happen at a lower saturation state. The concentration and distribution of nucleus-inducing heterogeneities will then also affect precipitation distribution later in the process because nucleation represents the initial condition for precipitation.

There are many factors in nucleation that are difficult to quantitate and even if they are known their effect is difficult to predict. The classical nucleation relationship can be described by the Arrhenius expression where

$$R_{nuc} = B \exp\left[\frac{-16\pi\Gamma^3\nu^2}{3k_B{}^3T^3(\ln S)^2}\right]. \qquad (23)$$

B is equal to 1 nucleus per time per volume and simply contains the units of R_{nuc} as in the Arrhenius form (Kashchiev and van Rosmalen, 2003; Mullin, 2001). Γ is interfacial tension, ν is the molecular volume, k_B is the Boltzmann constant and T is the temperature. Unfortunately Equation 23 does not capture observed nucleation behavior very well leading to a multitude of more complex expressions, many of which are system specific. For a more complete review of mineral nucleation see Yoreo and Vekilov (2003).

One nearly universal example of a situation where observation does not match classical theory in nucleation is the existence of a lag period between critical supersaturation and nucleation. Observable nucleation does not generally occur at precisely the same time at which the critical supersaturation is reached as predicted by Equations 20 and 21. A so called induction time, t_{ind}, is required. Many factors affect t_{ind} however in general shorter induction times are associated with higher nucleation and growth rates (Flaten et al., 2010). Similarly, higher supersaturation and the presence of

heterogeneous nucleation sites will decrease the induction time. Inverse proportionalities between t_{ind} and R_{nuc} have been proposed such that

$$t_{ind} \propto 1/R_{nuc}, \qquad (24)$$

however their use in predicting subsurface behavior is limited because of the unpredictability of heterogeneous nucleation sites.

Crystal Growth Models and Kinetics

Once nucleation occurs, crystals will grow based on the conditions that exist at the crystal/fluid interface. As in nucleation, there are many molecular scale factors that affect crystal growth. There are thermodynamic controls that limit crystal size and polymorphic composition and kinetic controls due to ion diffusion limitations and surface species equilibrium reactions. Many factors affect crystal growth but generally crystal growth is faster with higher supersaturation. The relationship between saturation and crystal growth can be handled a number of ways mathematically. More complete reviews are numerous however a complete discussion of basic crystallization can be found in Mullin (2001).

There is no universally accepted mathematical treatment of crystal growth. The general thermodynamics are understood but the stochastic nature, small scale, and sensitivity to impurities even at extremely low concentration makes the quantitative prediction of crystal growth difficult in many systems, including the subsurface environment. At a fundamental level mineral crystal growth occurs when ions in a supersaturated solution diffuse to a crystal surface and are incorporated into the lattice.

Gibbs is credited with providing the current thermodynamic understanding of crystal growth through the principle of the minimization of system free energy (Gibbs, 1948). Gibbs' theory states that the equilibrium shape of a crystal will be such that it minimizes interfacial energy.

The most basic thermodynamic treatment of crystal growth is the Gibbs-Volmer model where a thin transition phase on the growing crystal surface is assumed (Volmer and Adhikari, 1926). In this thin transition phase adsorbed ions lose a degree of freedom and are only allowed to diffuse along the crystal surface before they are incorporated at points of highest energy (e.g. kinks and steps) and grow via layers. The Gibbs-Volmer model is the basis of a number of other models that are useful in the investigation of structural characteristics and mechanisms however generally these models fall short of being able to make accurate quantitative predictions especially in complex systems.

Recognizing that crystal growth is a diffusion process, with molecules being required to diffuse to the crystal surface before they can be incorporated, classical work by Nernst and Noyes & Whitney in the late 19th and early 20th centuries (Mullin, 2001) suggest a crystal growth rate of the form

$$\frac{dm}{dt} = \frac{D}{\delta} A(C - C^*) . \qquad (25)$$

The mass growth rate (dm/dt) of a crystal, or collection of crystals, is determined by the molecular diffusion coefficient, D, a static boundary layer thickness, δ, the crystal/liquid interfacial area, A, and the bulk solute concentration, C, relative to the theoretical concentration at saturation, C*. Equation 25 is valid for a simple system

containing a single molecule crystal however it requires modification for multicomponent crystals such as carbonates. Equation 25 can be split into two parts: molecular diffusion to the surface and reaction at the crystal surface. This division can be written as

$$\frac{dm}{dt} = k_{diff} A(C - C_i) \qquad (26)$$

and

$$\frac{dm}{dt} = k_{react} A(C_i - C^*) \qquad (27)$$

where k_{diff} and k_{react} are diffusional mass transfer and reaction rate coefficients respectively. C_i is the solute concentration at the interface. Typically reactions 26 and 27 are combined and a reaction order term, n_p, is added resulting in

$$\frac{dm}{dt} = k_p A(C - C^*)^{n_p}, \qquad (28)$$

where k_p is the overall precipitation rate constant. Both k_p and n_p are then determined experimentally. For inorganic salts, n_p is typically between 1 and 2 but should be thought of as a fitting parameter rather than a variable that presents any clear conceptual meaning (Morse et al., 2007). Equation 28 requires further modification in multispecies systems where there are multiple concentrations that would affect the precipitation rate. In this case the saturation, rather than concentration, is used and equation 28 becomes

$$\frac{dm}{dt} = k_p A(S\text{-}1)^{n_p} \qquad (29)$$

and serves as the basis of most empirical crystal growth rate models (e.g. Zhong and Mucci, 1989). Dissolution is commonly treated in an analogous fashion. For calcium carbonate the common rate relationship for dissolution takes the form

$$\frac{dm}{dt} = \left(k_{d1}\{H^+\} + k_{d2}\right)A(1-S)^{n_d} \qquad \text{for} \qquad S<1 \qquad (30)$$

(Chou et al., 1989; Compton et al., 1989). k_{d1}, k_{d2} and n_d are experimentally determined constants. For calcium carbonate dissolution, it was determined that pH plays an important role in addition to the saturation state, S. Thus, an additional rate term is used that is dependent on the bulk proton activity, $\{H^+\}$.

Caution must be used in when using empirical precipitation and dissolution relationships, and published constants therein, for pore-scale modeling purposes. Rate constants are typically determined by measuring bulk concentration changes during desaturation over the course of a precipitation event. These concentration measurements are typically taken in well mixed systems. It may be appropriate to use literature values determined in well mixed systems for a Darcy scale model (e.g. Ebigbo et al., 2012) because both are volume averaged approaches but they might not be appropriate for use in pore-scale models (Miller et al., 2013). The use of Navier-Stokes (rather than Darcy) equations to solve for local pore velocities in pore-scale models allows for the modeling of local concentrations and biofilm reaction kinetics. This calls into question the use of values obtained from well mixed systems for multiple reasons. In a pore-scale model, crystal growth and dissolution might be better predicted from calculated interfacial concentrations, however these are unknown in a volume-averaged system and measured bulk concentrations determine the fitted rate constants. The scarce availability of pore-scale rate constants provides a challenge to using relationships such as Equations 29 and 30 in pore-scale models. Corrections that account for differing mass transfer

characteristics may have to be applied to values that were calculated from experiments in volume-averaged systems in order for them to be used in pore-scale models, potentially reducing their accuracy. Figure 6 illustrates the effect of precipitation rate at the pore-scale thereby highlighting the importance of the use of accurate pore-scale rate constants in systems with precipitation.

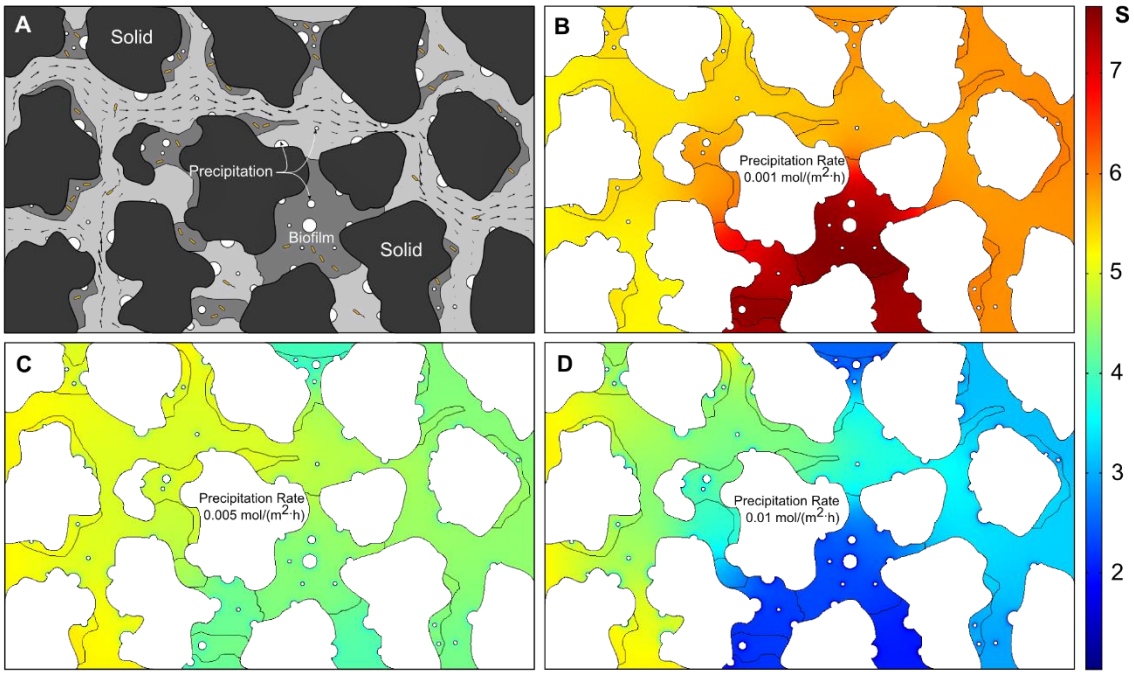


Figure 6. The theoretical geometry presented in Figure 1 (A) applied to a 2D, steady-state finite element model to demonstrate the effect of precipitation rate on pore-scale spatially-resolved saturation state (S). Panels B, C and D show simulations with varied precipitation rates of 0.001, 0.005 and 0.01 mol/(m^2·h) respectively along with a constant urea hydrolysis rate in biofilm domains of 1.0 mol/(L·h). Precipitation is modeled as a surface flux of both carbonate and calcium ions at the precipitate boundaries and laminar fluid flow (Re << 1) is restricted to the liquid domain (no flow inside the biofilm domains). Please refer to the 'Modeling Notes' section at the end of this chapter for additional information regarding this model.

Mechanistic approaches to crystal growth can be found in surface complexation models (Heberling et al., 2011; Ruiz-Agudo et al., 2011; Van Cappellen et al., 1993; Wolthers et al., 2012) that lend themselves well to pore-scale models where interfacial surfaces are known (or assumed) and interfacial concentrations can be calculated. Advances in surface-sensitive spectroscopic analysis that were not available to Gibbs and others in the early 20th century have allowed for an improved understanding of the

surface chemistry involved in crystal growth and dissolution. The basic concept behind surface complexation models is that at the crystal/liquid interface there are water molecules and dissolved ions that form ionic bonds with exposed lattice molecules. These bonded molecules, which are not yet part of the ordered crystal lattice (denoted by > in this text), enter the system of chemical species providing a link between the aqueous chemistry and the crystal surface. Surface complexation has been particularly well studied in carbonates where two classes of hydration species (>CO_3H and >MeOH) have been shown to exist (Morse and Mackenzie, 1990; Nilsson and Sternbeck, 1999; Van Cappellen et al., 1993). Me is any divalent metal such as calcium, magnesium or a transition metal such as iron. Other surface species such as >$MeCO_3^-$ are also present by complexation with dissolved ions rather than water (Pokrovsky et al., 2000; Ruiz-Agudo et al., 2011).

Taking calcite as an example, the reactions occurring at the crystal surface are found in Table 2 which is adapted from Pokrovsky et al. (2000) and Ruiz-Agudo et al. (2011).

Table 2. Surface reactions on a calcite crystal and their associated solubility constants. ">" indicates surface species and all others are aqueous species.

Surface Reaction	pk (25° C)
$>CO_3H \leftrightarrow CO_3^- + H^+$	5.1
$>CO_3H + Ca^{2+} \leftrightarrow >CO_3Ca^+ + H^+$	1.7
$>CaOH \leftrightarrow >CaO^- + H^+$	12.0
$>CaOH + H^+ \leftrightarrow >CaOH_2^+$	-11.5
$>CaOH + CO_3^{2-} + 2H^+ \leftrightarrow >CaHCO_3 + H_2O$	-23.5
$>CaOH + CO_3^{2-} + H^+ \leftrightarrow >CaCO_3^- + H_2O$	-17.1

Precipitation kinetics can be estimated from surface speciation using an approach first proposed by Nilsson and Sternbeck (1999) and later refined by Ruiz-Agudo et al. (2011) where crystal growth occurs through dehydration and incorporation of either aqueous calcium carbonate ($CaCO_{3\,(aq)}$) or calcium ions. The adsorption of lattice ions must happen at dehydrated surface sites $>CO_3Ca^+$, $>CO_3^-$, $>CaHCO_3$, and $>CaCO_3^-$. Under the conditions studied in Nilsson and Sternbeck (1999) and also by Ruiz-Agudo et al. (2011), which are biologically relevant temperatures and pH, it was determined that adsorption to $>CaHCO_3$ would likely be rate-limiting so the two possible rate-limiting precipitation reactions can be written as

$$> CaHCO_3 + CaCO_{3(aq)} \cdot 6\,H_2O \rightarrow\!> CaHCO_3 + 6\,H_2O, \qquad (31)$$

and

$$> CaHCO_3 + Ca^{2+} \cdot 8\,H_2O \rightarrow\!> CO_3Ca^+ + H^+ + 8H_2O. \qquad (32)$$

$CaCO_{3(aq)}$ or calcium ions approach the surface in a hydrated state and when they are incorporated in the crystal lattice they become dehydrated. Equations 31 and 32 are written such that the molecules that were dehydrated disappear on the right hand side indicating a flux out of solution (Ruiz-Agudo et al., 2011). The rates of these precipitation reactions can be treated as first order with respect to the surface concentration of $>CaHCO_3$ (denoted by square brackets in units of mol per surface area) and the activity of the hydrated species being adsorbed. Assuming both reactions from Equations 31 and 32 are happening at the same time the overall precipitation rate can be written as

$$\frac{dm}{dt} = k_1\{CaCO_{3(aq)}\}[>CaHCO_3] + k_2\{Ca^{2+}\}[>CaHCO_3]. \qquad (33)$$

k_1 and k_2 are empirical rate constants and values for calcite have been estimated to be approximately equal and on the order of 10^8 mol/(L·h) when calculated from measured bulk aqueous activities (Ruiz-Agudo et al., 2011).

Reactive Transport

Biofilm and MICP have the potential to affect reactive transport in a porous medium greatly. In a homogeneous porous medium, effects include permeability reduction through a decrease in porosity, the formation of isolated pores and flow channeling that leads to increased dispersion. In a heterogeneous porous medium biologically-mediated effects are less clear and are highly system dependent. The study of pore topology coupled with reaction kinetics and solute transport are essential for a

more complete understanding of how physical and chemical mechanisms interact in MICP systems in the subsurface.

Solute Transport

There is a set of dimensionless parameters that are particularly useful in the study of reactive transport in the subsurface. Here we will discuss them in relation to MICP systems but for a more complete analysis of their meanings many reviews are available in the chemical engineering and porous media literature (e.g. Bird et al., 2006). There are five rates that we are concerned with in MICP systems. These rates are: (1) the solute transport rate due to advection, (2) the solute transport rate due to diffusion, (3) the precipitation rate, (4) the biomass growth rate, and (5) catabolic conversion rates leading to alkalinity production. Note that the biomass growth rate is loosely proportional to the amount of biofilm present in the pore space similarly to high precipitation rates correlating to more blockage due to precipitation. Ratios of these five rates relative to each other or relative to a length scale (such as the pore diameter, biofilm thickness or discretization dimension) describe system behavior and are the basis of some useful dimensionless parameters discussed in this section.

The Reynolds number (Re) is an important parameter in the characterization of the hydrodynamics in a porous medium. Re is the ratio of inertial forces to viscous forces and can be written as

$$\mathrm{Re} = \frac{vL}{\upsilon} \qquad (34)$$

or specifically for a porous medium made up of spherical grains of diameter, d, equation 34 becomes

$$\mathrm{Re} = \frac{v \phi d}{\upsilon(1-\phi)} \qquad (35)$$

where v is the average pore fluid velocity, L is the characteristic length scale, υ the kinematic viscosity, and ϕ is the porosity. Viscous forces generally dominate in the subsurface because of slow velocities and small length scales; however in an engineered setting, areas around injection points may have very high Re depending on the system.

There is an interplay between Re and biofilm growth. In higher Re flow, biofilm is exposed to higher shear forces and is therefore more susceptible to physical detachment (Stoodley et al., 2001). Biofilms grown in high shear environments are generally stronger and thinner, presumably to counteract the higher shear forces. In contrast, biofilms grown in low shear environments are generally less dense and occupy more pore space (Teodósio et al., 2011).

Pore-scale hydrodynamics also affect chemical gradients. Fast fluid flow causes fast convective solute transport which facilitates faster reaction rates. When considering the balance between solute transport (both convective and diffusive) and reaction rates at the pore-scale in MICP systems one must recognize that there are three types of reaction: (1) reactions occurring in mobile pore fluid, (2) reactions occurring within a biofilm or in immobilized pore fluid (3) surface reactions at the precipitate/fluid or precipitate/biofilm interface. Reactions occurring in mobile pore fluid are the most straightforward to quantify. These include reactions for chemical equilibria and planktonic biological

reactions; rates measured in a laboratory setting and found in the literature are likely to be appropriate for direct application. Equilibrium reactions, especially in aqueous carbonate chemistry, are much faster than the biological reactions (Zhang and Klapper, 2010, 2011) so it can be assumed that, for modeling purposes, they occur instantaneously.

Biofilm-Catalyzed Reactions

Reactions that occur in biofilms are more likely to be limited by mass transport for two main reasons. Biofilm limits both advective and diffusive mass transport and high cell densities can lead to locally high rates of reaction. As Stewart (2003) points out, the diffusive time scale of a solute to the base of a biofilm approximately increases with the square of the biofilm thickness. That is to say a 100 μm thick biofilm will be 100 times more diffusion limited than a 10 μm thick biofilm and 10,000 times more diffusion limited than a planktonic cell, assuming a diffusion length scale of 1 μm for a single cell. Literature does support the existence of some advection within biofilms which will increase mass transport but at least some amount of mass transport limitation is inherent in any biofilm system (Pintelon et al., 2012).

Mass transport in precipitation and dissolution surface reactions are often limited by the stagnant layer near the surface often termed the mass transfer resistance layer. In MICP systems the mass transfer resistance layer becomes difficult to predict because of the presence of biofilm can create multiple phase boundaries (biofilm-mineral, mineral-liquid, liquid-biofilm). Pore-scale information, such as the relative abundance of the various phase boundaries, is important for accurate effective rate predictions in MICP

systems because the relative locations of the biofilm that induces precipitation and the growing precipitate become important. Crystals that form and grow within the biofilm matrix may grow at different rates and affect the pore structure differently than crystals attached directly to the porous medium. In MICP systems both of these precipitation processes are likely to be occurring at the same time.

Simplifying the system and taking microbially induced precipitation as one overall reaction, it can be useful to compare a predicted reaction rate with the rate of mass transport in the form the Damköhler number (Da). Generally, Da is defined as a reaction rate divided by the mass transport rate of the rate-limiting compound (usually the substrate) participating in the reaction. Da can also be thought of as the ratio of the time scales of transport and reaction (Fogler, 2005). This allows for an assessment of whether a system is limited by mass transport or by the reaction rate. The convective Damköhler number can be written generically as

$$Da = k_{Da} C_o^{n_{Da}-1} \tau \qquad (36)$$

for a reaction of order n_{Da} where k_{Da} is a kinetic rate constant, C_o is a representative concentration (usually the bulk pore water concentration), and τ is a fluid residence time. Da is a useful parameter to consider for reactions occurring in the bulk pore fluid or when reactions are volume averaged. In more classic chemical engineering reactor design the calculation of Da allows one to quickly decide if a substrate is being fully utilized in a reactor. If the bulk transport is too high relative to the reaction rate ($Da << 1$) most of the reactant will pass through the reactor without time enough to react. In contrast, the entire reactor volume would not be utilized efficiently if the reaction occurs too quickly relative

to bulk transport (Da >> 1). In porous media systems when Da is much greater than one for a precipitation reaction, inlet plugging will be expected. However, if Da is less than one, more uniform precipitate deposition is expected but with a lower conversion efficiency of the reactants supplied to the system. Furthermore, Da is not constant temporally or spatially in systems where the reaction causes a change in porosity or the reaction rate changes in space or time. For instance, as porosity decreases due to precipitation and biofilm growth it is likely that a regime change will occur where the system goes from low Da (reaction rate limited) to high Da (transport limited) behavior (see Figure 7). In engineered systems this transition may mark an important point where control parameters, such as flow rate or reactant concentrations, will need to be adjusted.

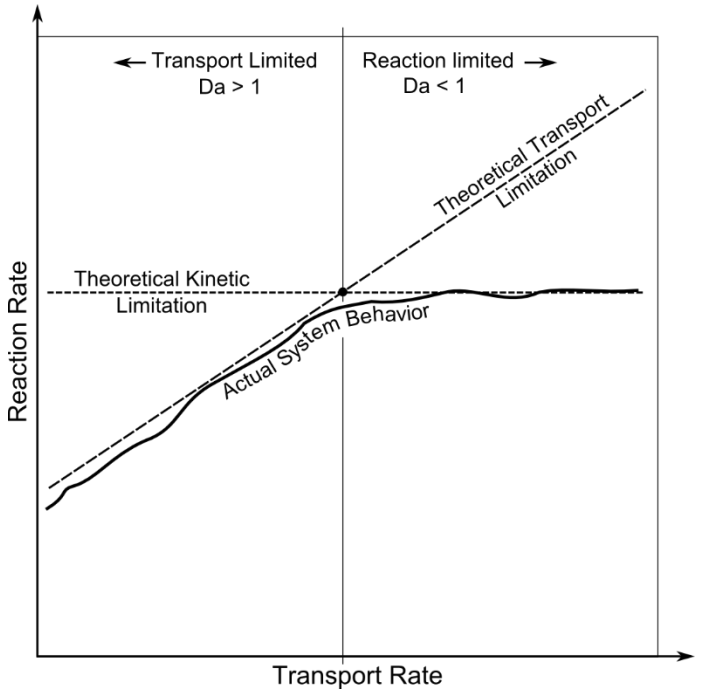


Figure 7. Expected volume-averaged system behavior in the context of kinetic and transport rate limits. As solute transport is increased the overall reaction rate will increase until reactions are limited by the reaction kinetics of the system. The shape of an actual system curve is highly dependent on factors such as pore size distribution and concentration dependence on reaction rates but generally bulk reaction rates will increase with increasing transport rates (i.e. Darcy velocity) until a kinetic limitation is reached. This behavior was shown through pore-scale modeling by Molins et al. (2012).

The use of the convective Damköhler number (Equation 36) is only appropriate if there is minimal diffusion limitation or if effective reaction rates are used, which take into account diffusion limitations. This is because the volume-averaged reaction rates used in the calculation may be inaccurate due to diffusion limitations and locally varying reaction rates. It is reasonable to expect that reactions of interest are limited by diffusion in MICP systems, which are dominated by reactions occurring in biofilms, on surfaces, and in pores with stagnant fluids (potential interfacial mass transport limitations). There

are three primary ways to take the diffusion limitation into account, all of which require the estimation of volume-averaged concentration heterogeneity. Assuming that the reaction rate of interest (i.e. alkalinity production and precipitation) is dependent on substrate or product concentrations, rates cannot be constant at the pore-scale when concentration heterogeneity exists. Taking diffusion limitation and nonconstant reaction rates into account, actual reaction rates can be significantly different than those predicted from models using bulk pore fluid.

The effect of diffusion limitation can be quantified by calculating an effectiveness factor, η, which is defined as the observed mean rate of reaction, R_{obs}, divided by the rate of reaction that would be predicted if there was no mass transfer limitation (Equation 37). The rate predicted as if there was no mass transfer limitation is simply the rate model evaluated at bulk pore fluid conditions, $R_{bulk,}$ so

$$\eta = \frac{R_{obs}}{R_{bulk}}. \qquad (37)$$

The effectiveness factor can be estimated through the use of the Thiele modulus (h_t), a dimensionless number, which relates diffusion and reaction rates. A brief derivation of the Thiele modulus is useful in the understanding of the assumptions that must be made.

First let us consider a section of biofilm that is attached to an inert porous media grain of the geometry presented in Figure 8.

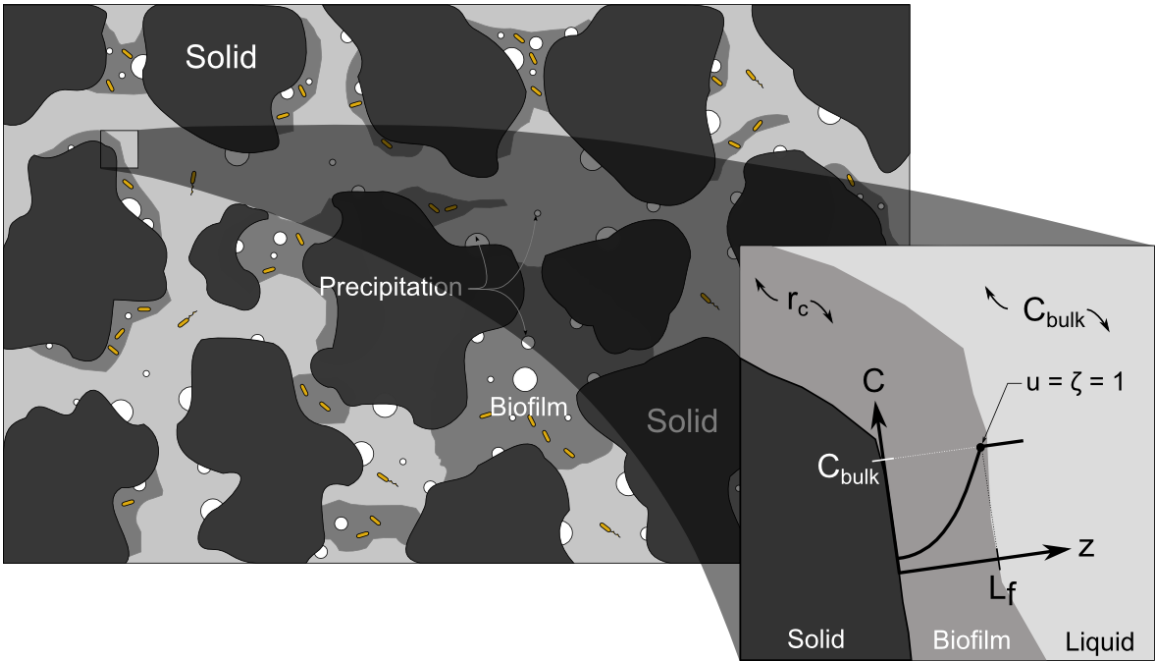


Figure 8. The assumed biofilm profile geometry for Thiele modulus calculations. The biofilm is assumed to be of a slab geometry with $C = C_{bulk}$ at $z = L_f$. A reaction, r_c is occurring in the biofilm domain only and the problem is nondimensionalized such that $u = C/C_{bulk}$ and $\zeta = z/L_f$. The assumed profile is put into context of an assumed pore geometry where L_f can be highly variable highlighting the importance of using caution when using volume-averaged parameters.

It is assumed that a biofilm that is carrying out a reaction R_c in steady-state conditions. R_c is dependent on the concentration of a solute (C). It is also assumed that the biofilm geometry in the system is well approximated by a slab geometry and that the biofilm is homogeneous. Under these conditions we can write a mass balance equation

$$D_e \frac{d^2C}{dz^2} = R_c, \qquad (38)$$

where D_e is the effective diffusion coefficient of solute C within the biofilm and z is the spatial coordinate normal to the biofilm/liquid and biofilm/support interfaces. We can nondimensionalize concentrations within the biofilm by dividing by the bulk pore water

concentration, C_{bulk}, and nondimensionalize the length scale, z, by dividing by the biofilm thickness, L_f, such that $u = C/C_{bulk}$ and $\zeta = z/L_f$.

$$D_e \frac{d^2(uC_{bulk})}{d(\zeta L_f)^2} = R_c . \qquad (39)$$

By rearranging variables the general form of the Thiele modulus (h_t) is derived, where

$$\frac{d^2u}{d\zeta^2} = \frac{L_f^2 R_c}{C_{bulk} D_e} = h_t^2 g(u) , \qquad (40)$$

and

$$h_t^2 \equiv \frac{L_f^2 R_{bulk}}{C_{bulk} D_e} . \qquad (41)$$

g(u) is a function of u (the dimensionless concentration) and is the ratio of the concentration dependent reaction rate expression, R_c, to the reaction rate evaluated at the bulk concentration, R_{bulk}.

$$g(u) = \frac{R_c}{R_{bulk}} . \qquad (42)$$

Mass fluxes and concentration profiles can be obtained by solving Equation 40. Equation 40 is useful in the analysis of h_t for calculating η and characterizing the system with respect to diffusive mass transport.

In order for h_t to be a useful dimensionless descriptor it must be adjusted so that the dimensionless rate is integrated over the concentration profile. A generalized Thiele modulus, h_t^*, is obtained by

$$h_t^* = h_t \left[2 \int_0^1 g(u) du \right]^{-1/2} . \qquad (43)$$

Solutions to Equation 43 can be found in Table 3. If $h_t^* >> 1$ the representative element of biofilm is diffusion limited and if $h_t^* << 1$ it is limited by the reaction rate. Beyond the simple classification of diffusion limitation or reaction rate limitation, h_t^* can also be used to calculate the effectiveness factor, η, of the biofilm element (Gottifredi and Gonzo, 2005) using

$$\eta = \int_0^1 g(u)d\zeta . \qquad (44)$$

The zero-order case is solved easily because $g(u) = 1$ so $\eta = 1$ for $h_t^* \leq 1$. Caution should be used when applying a zero-order model to effectiveness factor calculations. If the biofilm is diffusion-limited ($h_t^* > 1$) it is often the case that a zero-order rate model would not accurately represent the system and another rate model may have to be used. Zero-order rate models are best suited for high substrate concentrations. If a biofilm is limited by diffusion, the deeper region of the biofilm will have very low (or zero) substrate concentration requiring the use of a higher order rate model. Calculating η for a first-order rate model is also straightforward but requires the calculation of a concentration profile (u as a function of ζ) because u is non-constant over the integral space and $g(u) = u$. Equation 38 can be solved with boundary conditions $du/d\zeta = 0$ at $\zeta = 0$ (no flux at the base of the biofilm) and $u = 1$ at $\zeta = 1$ (bulk concentration applied at the liquid/biofilm interface) to obtain

$$u = \frac{\cosh(h_t\zeta)}{\cosh(h_t)}, \qquad (45)$$

and

$$\eta = \frac{\tanh(h_t)}{h_t}, \qquad (46)$$

for a first-order kinetic model.

Calculating h_t^* and η is relatively straightforward for zero- and first-order kinetic models (see Table 3) but is more complex for rate relationships such as Michaelis–Menten. Michaelis–Menten effectiveness factors can be estimated numerically or through approximate solutions that are dependent on h_t^2 being very large or very small (Fang and Govind, 2008; Gonzo et al., 2012; Gottifredi and Gonzo, 2005). Another approach is to employ a weighted average of the fluxes that are calculated from zero- and first-order approximations to provide a smooth transition between the regimes without introducing more complicated mathematics (Pérez et al., 2005).

Table 3. Useful relationships for the calculation of the Thiele modulus and effectiveness factor for zero-, first-order and Michaelis–Menten (M-M) rate models assuming boundary conditions $du/d\zeta = 0$ at $\zeta = 0$ and $u = 1$ at $\zeta = 1$.

Rate Model	$R_c =$	$g(u) =$	$h_t^2 =$	$h_t^* =$	$\eta =$
Zero-Order	R_{max}	1	$\frac{L_f^2 R_{max}}{C_{bulk} D_e}$	$\frac{h_t}{\sqrt{2}}$	$\frac{1}{\text{for } h_t^* \le 1}$
First-Order	$k_1 C$	u	$\frac{L_f^2 k_1}{D_e}$	h_t	$\frac{\tanh(h_t)}{h_t}$
M-M	$R_{max}\frac{C}{k_m + C}$	$\frac{u(\beta+1)}{(\beta+u)}$	$\frac{L_f^2 r_{max}}{(k_m + C_{bulk})D_e}$	$h_t\left[2(\beta+1)[1-\beta\ln(\beta+1)+\beta\ln\beta]\right]^{-1/2}$	No Analytical Solution

$\beta = k_m/C_{bulk}$. Note that if $\beta >> 1$ a first-order approximation is valid and if $\beta << 1$ a zero-order approximation is valid.

Once η is calculated, its use is straightforward if parameters can be estimated and averaged over a representative volume. If an average biofilm thickness and volume fraction can be estimated, bulk pore water concentrations can be used to estimate the

biofilm reaction rate. The correct use of an effectiveness factor can add precision to a volume-averaged model without significantly increasing the computational cost.

Precipitation Reactions

The calculation of an effectiveness factor has been discussed in the context of a biofilm but the other important reaction of the system, namely precipitation, also needs attention. The same principles apply but precipitation reactions occur at a surface rather than within a volume so adjustments must be made. As shown in Figure 1, there can be precipitation in three main forms in a MICP system: Precipitation can occur (1) in the biofilm matrix, (2) suspended in the liquid phase being transported with the bulk pore fluid, or (3) attached to the solid porous media grains in direct contact with the bulk pore fluid. The assumption of which type of precipitation dominates a system affects how it should be modeled because it will dictate the degree of diffusion limitation experienced at the precipitate surfaces.

The precipitation reaction models discussed in Section 0 can be translated into effective rates that can be used in reactive transport modeling similarly to the biofilm-catalyzed reactions however some assumptions must be made. Precipitation is a surface reaction, not a reaction that is well approximated over a volume, so the rate of precipitation is proportional to the surface area of the precipitate. It is often most important to know how much pore space is occupied by the precipitated minerals so additionally, a surface area per volume relationship must be assumed. A surface area (A) to volume (V) ratio can be obtained by approximating individual precipitates as spheres

of radius, r. Equation 27 can then be converted into a volumetric rate where the volume occupied by the number, N, of precipitate particles of radius, r, can be written as

$$\frac{dV}{dt} = \frac{4\pi r^2}{\rho} N k_p (S-1)^{n_p}, \qquad (47)$$

where ρ is the precipitate's density. Equation 47 can be implemented to calculate the porosity reduction over time in volume-averaged numerical simulations where r and N can be updated at each time step according to a mass balance and physical constraints such as a maximum radius. Note that, if attached precipitates dominate a system, Equation 47 still applies but the surface area term must be divided in half to account for a hemispherical geometry. The approach in Equation 47 is best used when discrete (not overlapping) crystals are expected and N (the number of precipitate particles) remains somewhat constant.

The derivation of the precipitation rate model used in Equations 29 and 47 shows that there is already consideration of the diffusive mass transfer resistance inherent to precipitation reactions (see Equation 25). The issue is complicated when additional mass transfer resistance is introduced by the presence of biofilm. k_p is system-dependent because the mass transfer portion depends on variables like biofilm thickness and porosity which can be highly variable from system to system and heterogeneous within a single system. If there is little biofilm in a system, published k_p values, measured in well-mixed batch systems, are more likely to be accurate. When additional mass transfer resistance is expected, it must be taken into account.

Concluding Remarks

Pore-scale behavior in MICP systems is important to understand for the accurate predictions of larger scale process. In this chapter we have discussed the processes that play a role in increasing alkalinity and ultimately the precipitation of carbonate minerals. The biological and abiotic components of the process on their own are relatively well understood but their interactions are complex, particularly in the context of porous media systems, which leaves room for future research in the field. Qualitatively we understand that microorganisms, existing in biofilms, attached cells or as free floating planktonic cells, can increase alkalinity as a byproduct of their metabolisms which can consequently result in carbonate mineral precipitation and porosity reduction. It is known that biologically produced molecules affect the mineralogy of the precipitates however in a reactive transport context this information remains difficult to quantify. The coupled nature of the system where biomass growth and mineral precipitation affect transport, and vice versa, makes it difficult to isolate and study processes independently of each other experimentally. This makes nondestructive analytical techniques important in future research.

Continuing to make progress in this field will benefit from a multidisciplinary approach with novel methods such as microfluidics (Zhang et al., 2010b), confocal microscopy (Connolly et al., 2013; Pitts and Stewart, 2008; Schultz et al., 2011), X-ray microtomography and nanotomography (Wildenschild and Sheppard, 2013), nuclear magnetic resonance imaging (Fridjonsson et al., 2011; Graf von der Schulenburg et al.,

2008; Seymour et al., 2007, 2004), as well as spectroscopic techniques (Dandeu et al., 2006; Nehrke and Nouet, 2011; Ni and Ratner, 2008). Even with quality data from each of these techniques, mathematical models will be essential in order to make predictions about compounds and behavior at spatial and temporal scales currently not observable or measurable. Furthermore, cross validation between techniques is often best done through modeling.

Modeling studies on MICP systems have been done both at the pore-scale (Zhang and Klapper, 2010) and at the continuum scale (Cheng and Cord-Ruwisch, 2014; Ebigbo et al., 2012; Martinez et al., 2014; van Wijngaarden et al., 2010) and the models highlight the need for further experimental characterization and parameter estimation. For example, rate equations can be used to calculate porosity reduction over time but it is unclear how that porosity reduction is best converted into a permeability reduction. Armstrong and Ajo-Franklin (2011) showed that the commonly used Kozeny-Carman relation provides a poor fit when simple raw permeability reduction data is used but could be refined to provide an acceptable fit when geometric factors were taken into account as measured by X-ray microtomography. In continuum modeling there is typically little access to accurate geometric descriptors, especially when the pore topology changes over the course of the simulation. Recent advances in high resolution (≈ 1 μm) 3D imaging techniques in opaque porous media for the biofilm phase of the MICP system will also help to more fully characterize the system, making it possible for accurate field scale modeling (Davit et al., 2011; Iltis et al., 2011).

Acknowledgements

The authors wish to thank Dr. Logan Schultz, Benjamin Jackson and Neerja Zambare for reviewing this chapter. The authors were funded by the National Science Foundation through NSF award No. DMS-0934696 and by the U.S. Department of Energy Grant Numbers DE-FG-02-09ER64758, DE-FE0004478 and DE-FE0009599. J.M.C was also supported by a NSF-IGERT fellowship in Geobiological Systems at Montana State University (DGE-0654336).

Modeling Notes

The pore-scale models shown in Figures 3 and 5 are intended for illustration purposes only however physically relevant equations were solved using tabulated values for chemical constants such as diffusion coefficients and ion dissociation constants. The model was simplified to two dimensions and the system was assumed to be at steady state with respect to fluid flow, reactive transport and ion equilibria. Grain diameters are approximately 20 μm and the pore throats are approximately 5 μm. COMSOL Multiphysics® (Version 4.3a) was used to solve the finite element problem and generate the saturation maps.

Navier–Stokes equations were solved to obtain the flow field with constant velocity defined in the influent region on the left and zero pressure defined at the effluent on the right. Fluid velocities ranged from zero to 0.5 cm/s in the narrowest pore throat (zero at the solid/liquid and biofilm/liquid interfaces and zero inside the biofilm regions).

The average fluid velocity in the fluid domain is 0.024 cm/s. Laminar flow exists throughout the domain. Local ion concentrations were estimated using the Nernst-Planck equation coupled to the Navier-Stokes flow field and ion equilibrium equations were solved for simultaneously. Aqueous equilibrium reactions were modeled with fast forward and reverse reactions (approximately four orders of magnitude faster than ureolysis or precipitation reactions). Uncharged species, such as urea, followed Fickian diffusion. The total influent DIC is 3 mmol/L, which is in the rage of what could typically be found in aqueous environments exposed to the atmosphere. The inlet calcium and urea concentrations were chosen to be equimolar at 100 mmol/L. No chemical species are completely depleted in the domain for this simulation. Precipitation and urea hydrolysis rates are assumed to be constant for illustration purposes; however, they are varied as noted in the figure captions to show the general effect of each.

Chapter 2 Nomenclature

[> X]	Area concentration of a surface species X
{x}	Activity of chemical species x.
A	Crystal/liquid interfacial area
ACC	Amorphous calcium carbonate
B	Unit constant from Arrhenius expression
C	Generic concentration variable
C*	Theoretical solute concentration at saturation
C_{bulk}	Bulk pore water concentration

C_i	Solute/Crystal interfacial concentration
C_s	General substrate concentration variable
D	Molecular diffusion coefficient
d	Pore diameter
Da	Damköhler number
D_e	Effective biofilm diffusion coefficient
DIC	Dissolved inorganic carbon
EPS	Extracellular polymeric substance
ΔG	Total Gibbs free energy (nucleation)
ΔG_{crit}	Total free energy of a critical nucleus
ΔG_{dv}	Unit volumetric free energy
ΔG_s	Precipitate surface free energy
ΔG_v	Precipitate volume free energy
h_t	Thiele modulus
h_t^*	Generalized Thiele modulus
IAP	Ion activity product
k	Chemical equilibrium dissociation constant
k_B	Boltzmann constant
k_{d1} k_{d2}	Disassociation rate constants
k_{Da}	Damköhler reaction rate constant
k_{diff}	Diffusional mass transfer coefficient
k_m	Michaelis–Menten half saturation constant

k_{nuc}	Nucleation rate constant
k_p	Overall precipitation rate constant
k_{react}	Precipitation reaction rate coefficient
k_{sp}	Mineral solubility product
L	Characteristic length
L_f	Biofilm thickness
m	Mass variable
MICP	Microbially induced carbonate precipitation
n_d	Disassociation rate order (fitting parameter)
n_{Da}	Damköhler reaction order
n_{nuc}	Nucleation rate order
n_p	Precipitation rate order (fitting parameter)
pk	$-\log_{10}(k)$
r	Precipitate radius
R_{bulk}	Rate of reaction as evaluated with bulk conditions
R_c	Concentration dependent reaction rate
r_{crit}	Radius of a critical nucleus
Re	Reynolds number
R_{max}	Michaelis–Menten maximum reaction rate
R_{nuc}	Volumetric nucleation rate
R_{obs}	Observed mean rate of reaction
R_s	General substrate-dependent reaction rate

S	Saturation state
S_{crit}	Critical supersaturation where nucleation occurs
SRB	Sulfate reducing bacteria
T	Temperature
t	Time variable
t_{ind}	Nucleation induction time
u	Nondimensionalized concentration variable, C/C_{bulk}
v	Average pore flow velocity
z	Thickness dimension for Thiele modulus calculations
Γ	Interfacial tension
γ	Unit surface free energy
δ	Static boundary layer thickness
ζ	Nondimensionalized spatial variable, z/L_f.
η	Effectiveness factor
ν	molecular volume
τ	Hydraulic residence time
υ	Kinematic viscosity
ϕ	Porosity

CHAPTER 3

CONSTRUCTION OF TWO UREOLYTIC MODEL ORGANISMS FOR THE STUDY OF MICROBIALLY INDUCED CALCIUM CARBONATE PRECIPITATION

Contribution of Authors and Coauthors

Manuscript in Chapter 3

Author: James Connolly

Contributions: Conducted the experimental work, envisioned graphics, table design and major topics of the manuscript. Wrote and revised manuscript.

Author: Megan Kaufman

Contributions: Conducted the genetic manipulations and conducted preliminary experiments. Contributed to the writing, development and revision of the manuscript with comments and feedback.

Author: Adam Rothman

Contributions: Assisted with experimental work.

Author: Rashmi Gupta

Contributions: Envisioned major topics of the manuscript. Contributed to the writing, development and revision of the manuscript with comments and feedback.

Author: George Redden

Contributions: C Envisioned major topics of the manuscript. Contributed to the writing, development and revision of the manuscript with comments and feedback.

Author: Martin Schuster

Contributions: Envisioned major topics of the manuscript. Contributed to the writing, development and revision of the manuscript with comments and feedback.

Author: Frederick Colwell

Contributions: Envisioned major topics of the manuscript. Contributed to the writing, development and revision of the manuscript with comments and feedback.

Contribution of Authors and Coauthors - Continued

Co-Author: Robin Gerlach

Contributions: Envisioned major topics of the manuscript. Contributed to the writing, development and revision of the manuscript with comments and feedback.

Manuscript Information Page

Connolly, James; Kaufman, Megan; Rothman, Adam; Gupta, Rashmi; Redden, George; Schuster, Martin; Colwell, Frederick; Gerlach, Robin
Journal of Microbiological Methods
Status of Manuscript:
____ Prepared for submission to a peer-reviewed journal
____ Officially submitted to a peer-review journal
___ Accepted by a peer-reviewed journal
__x_ Published in a peer-reviewed journal

Elsevier
Submitted: May 2013
Accepted: June 2013
Volume 94, Issue 3, Pages 290-299

Abstract

Two bacterial strains, *Pseudomonas aeruginosa* MJK1 and *Escherichia coli* MJK2, were constructed that both express green fluorescent protein (GFP) and carry out ureolysis. These two novel model organisms are useful for studying bacterial carbonate mineral precipitation processes and specifically ureolysis-driven microbially induced calcium carbonate precipitation (MICP). The strains were constructed by adding plasmid-borne urease genes (*ureABC*, *ureD* and *ureFG*) to the strains *Pseudomonas aeruginosa* AH298 and *Escherichia coli* AF504*gfp*, both of which already carried unstable GFP derivatives. The ureolytic activities of the two new strains were compared to the common, non-GFP expressing, model organism *Sporosarcina pasteurii* in planktonic culture under standard laboratory growth conditions. It was found that the engineered strains exhibited a lower ureolysis rate per cell but were able to grow faster and to a higher population density under the conditions of this study. Both engineered strains were successfully grown as biofilms in capillary flow cell reactors and ureolysis-induced calcium carbonate mineral precipitation was observed microscopically. The undisturbed spatiotemporal distribution of biomass and calcium carbonate minerals were successfully resolved in 3D using confocal laser scanning microscopy. Observations of this nature were not possible previously because no obligate urease producer that expresses GFP had been available. Future observations using these organisms will allow researchers to further improve engineered application of MICP as well as study natural mineralization processes in model systems.

Introduction

Microbially induced calcium carbonate precipitation (MICP) is an important process in many engineered and natural systems including: geologic carbon sequestration, radionuclide remediation, soil stabilization and permeability manipulation (Cunningham et al., 2013; De Muynck et al., 2010; Ferris et al., 1996; Fujita et al., 2000; Lauchnor et al., 2013; Phillips et al., 2013; Whiffin et al., 2007). Natural systems, including the earth's global carbon cycle and ocean chemistry, have been affected by bacterial precipitation of calcium carbonate (Riding and Liang, 2005). Microbial carbonate sediments, including those produced by biofilms, are present throughout the geologic record and are widely distributed, making them important for understanding global carbon cycling (Riding, 2000; Vasconcelos et al., 1995). The medical community is also interested in MICP in the context of kidney stones, and mineral formation in ureteral stents and catheters (Morris et al., 1999). Even with the extensive body of literature and interest in MICP, specific mechanisms and implications of how microbes induce mineral formation spatially and temporally are still not clear. For example, the degree to which micron-scale biomass and mineral formation alter flow paths that translate to centimeter and larger scale processes is not fully understood (Armstrong and Ajo-Franklin, 2011; Graf von der Schulenburg et al., 2009).

Perhaps the most highly studied microbial process that can induce calcium carbonate precipitation is ureolysis. Organisms that produce large amounts of urease, such as *Sporosarcina pasteurii* (formerly known as *Bacillus pasteurii* (Yoon et al.,

2001)), can be extremely efficient at raising the pH of their environment through hydrolyzing urea and subsequently precipitating calcium carbonate as shown in Equations 48-51 (Mitchell and Ferris, 2006).

$CO(NH_2)_2 + 2\ H_2O \rightarrow 2\ NH_3 + H_2CO_3$ Urea Hydrolysis (48)

$2\ NH_3 + 2\ H_2O \leftrightarrow 2\ NH_4^+ + 2\ OH^-$ Ammonia Protonation and pH Increase (49)

$H_2CO_3 + 2\ OH^- \leftrightarrow HCO_3^- + H_2O + OH^- \leftrightarrow CO_3^{2-} + 2\ H_2O$

Shift of Carbonate Equilibrium (50)

$CO_3^{2-} + Ca^{2+} \leftrightarrow CaCO_3(s)$ Calcium Carbonate Precipitation (51)

The urease enzyme hydrolyzes urea ($CO(NH_2)_2$) to produce two ammonia molecules and one carbonic acid molecule (Equation 1). The overall effect of urea hydrolysis is a pH increase and a shift of the carbonic acid equilibrium towards carbonate (Equations 49 and 50). In the presence of calcium, or other divalent cations, precipitation of solid carbonate species takes place once a critical saturation state has been reached (Equation 51). In engineered systems, calcium is typically supplied to the system so calcium carbonate is most often the primary precipitate. Other organic and inorganic compounds are often incorporated into the precipitates, potentially changing their characteristics from those expected from pure forms of calcium carbonate (Bosak and Newman, 2005).

Microscopic observations have been used extensively to study MICP processes but real-time imaging that can differentiate biomass from mineral precipitates has been a significant challenge. Electron microscopy only provides an end-point view of the system with unavoidable sample preparation artifacts (Dohnalkova et al., 2011). In contrast, light

microscopy allows for the direct observation of microorganisms in a fully hydrated environment. Currently, staining is the only way to use light microscopy to definitively differentiate between biomass and the minerals in a hydrated environment (Schultz et al., 2011). However, staining affects biological processes; so long term studies over the course of days using fluorescent stains are not ideal.

The genetic modification of microbes to incorporate a green or other fluorescent protein is a suitable alternative to direct staining (Larrainzar et al., 2005). Organisms that express a fluorescent protein can be imaged over the course of hours and days without the need to introduce potentially inhibitory or toxic stains. Also, expression of the fluorescent protein can potentially be linked to the transcription of a protein of interest thus providing insight into the specific activity of an enzyme.

The goal of this work was to develop bacterial strains that constitutively express green fluorescent protein (GFP) and active urease. This was accomplished through the insertion of plasmid-borne urease genes into bacteria containing a chromosomal *gfp* insert. In addition to the construction of these organisms, their potential to be used in MICP studies was evaluated based on their ability to hydrolyze urea in batch kinetic studies. The growth and ureolysis kinetics of the newly constructed model organisms were compared to *S. pasteurii*, a model organism commonly used for MICP studies. Finally, the model organisms' suitability for studies in microscopic flow cells was demonstrated.

Materials and Methods

Bacterial Strains and Growth Conditions

Appropriate growth medium (100 mL, Table 1) was inoculated with 1.0 µL per mL of frozen stock culture. The baffled 250 mL Erlenmeyer flasks were incubated at the appropriate temperature (Table 1) on horizontal shakers at 200 rpm. Cells from overnight cultures were washed twice by centrifugation at 4200 x g and subsequently resuspended in sterile phosphate buffered saline solution (PBS) to remove spent media. PBS had final concentrations of 8.5 g/L NaCl, 0.61 g/L KH_2PO_4, 0.96 g/L K_2HPO_4 (all Fisher Scientific, NJ, USA) and was adjusted to a pH of 7 with concentrated HCl. The final inoculum for all experiments was diluted to an OD of 1.54 (See Section 0) and inoculated at a volumetric ratio of 1:1000. Experiments were conducted at 37º C for *Escherichia coli* and *Pseudomonas aeruginosa* strains and 30º C for *S. pasteurii*.

Plasmid and Model Organism Construction

To generate urease-producing strains, *Pseudomonas aeruginosa* AH298 (Werner et al., 2004) and *Escherichia coli* AF504*gfp* (Folkesson et al., 2008) were both transformed with plasmid pMK001 carrying the urease operon from *Escherichia coli* DH5α(pURE14.8) (Collins and Falkow, 1990). The pUC19-based plasmid pURE14.8 carries the urease operon that includes structural genes *ureABC* and putative accessory genes *ureD* and *ureFG* used to acquire nickel (Kim et al., 2006). The full-length sequence of this operon was not previously known.

Plasmid pMK001 was generated as follows. To subclone the urease genes, flanking forward and reverse polymerase chain reaction (PCR) primers (Eurofins MWG Operon) were designed with restriction sites *PstI* and *SpeI* added to the respective 5' end. Primer sequences can be found in the Supplemental Information. The PCR-amplified fragment was digested with the appropriate restriction enzymes and ligated into an equally-digested pJN105 vector. This plasmid contains an L-arabinose-inducible promoter and encodes gentamycin resistance (Newman and Fuqua, 1999).

The resulting plasmid construct was used to transform chemically competent *E. coli* cells. Gentamicin-resistant transformants were screened by gel electrophoresis of restriction-digested plasmids. Functional tests for ureolysis were performed in Fluka urea broth (Sigma-Aldrich, MO, USA) containing 100 μg/ml gentamicin and 50 mM L-arabinose (Sigma-Aldrich). Antibiotic pressure was maintained in all subsequent screening and kinetic experiments to ensure plasmid retention.

Plasmid pMK001 was finally transformed into the strains AH298 and AF504*gfp*, resulting in strains MJK1 and MJK2, respectively. Both of these strains already contained a mutant, chromosomal *gfp* variant (Folkesson et al., 2008; Werner et al., 2004). Both GFP variants contain an amino acid sequence at the C-terminal end that is recognized for degradation by proteases within the cell (Andersen et al., 1998). This causes newly produced GFP to have a short half-life resulting in the disappearance of signal over time unless new GFP is created to replace it (Sternberg et al., 1999). In strain AH298 this altered GFP is linked to the growth rate dependent ribosomal promoter $rrnBp_1$ so more

active cells produce more GFP for a relative measure of metabolic activity (Werner et al., 2004).

Urease Gene Sequencing

The urease insert of pMK001 was sequenced in a stepwise manner due to the long sequence length (5,594 bp). First, flanking primers (Eurofins MWG Operon, High Purity Salt Free) were used to sequence across the plasmid backbone junction into the insert from either side. This sequence information then allowed for the design of new primers at the ends of the newly sequenced section. Thus, for each of the newly sequenced sections, primers were designed until the sequencing eventually covered the whole insert. The sequencing was conducted by the Center for Genome Research and Biocomputing at Oregon State University on an ABI Prism® 3730 Genetic Analyzer using ABI Prism® 3730 Data Collection Software v. 3.0 and Prism® DNA Sequencing Analysis Software v. 5.2 and the KB Basecaller algorithm.

Test Tube Screening

Metabolic screening was performed to ensure that the transformed bacteria were ureolytically active. DH5α(pURE14.8) was used as a positive control, and the non-transformed strains, AH298 and AF504*gfp*, were used as negative controls. The screening began by inoculating 15 µL of washed cells into 15mL of fresh media in 15mm x 150mm (23.6mL) glass test tubes in triplicate. The appropriate growth medium for each organism was supplemented with 10 g/L urea (Fisher Scientific) and 1µL/mL phenol red pH indicator (Sigma). At the concentration used in this study, phenol red turns from clear to

bright pink at pH values greater than approximately 8.2, which is qualitatively indicative of the pH increase induced by active urease expression. The time when the media turned pink was used as a measure of relative urease activity between organisms.

Batch Kinetic Studies

Batch cultures were inoculated in 250 mL Erlenmeyer flasks with strains MJK1, MJK2 or *S. pasteurii* for kinetic analysis of urea hydrolysis and population growth. 100 mL of growth media (see Table 1) was supplemented with 10 g/L urea, and flasks were placed on incubated shakers. Samples were taken for a baseline analysis, and the cultures were inoculated. The batch reactors were sampled repeatedly for approximately 30 hours. Samples (1.0 mL) were taken aseptically and placed in 1.5 mL microcentrifuge tubes. Triplicate 100 µL aliquots were transferred into separate wells of a 96 well plate and analyzed for bulk GFP signal and optical density (OD) immediately with the average of the three readings being recorded (see Section 0 and 0). pH was measured, the sample filtered through a 0.2 µm cellulose acetate syringe filter (VWR, NJ, USA) and refrigerated for storage until urea analysis could be performed.

MJK1 and MJK2 were grown in LB medium (see Table 4) with the addition of 10 g/L of urea, 50 mM L-arabinose and 10 µM $NiCl_2$ (Fisher Scientific). It was found that *S. pasteurii* does not grow well in LB medium (data not shown) so batch studies were performed in modified calcite mineralization medium (CMM) after Ferris et al. (1996) by omitting calcium chloride and sodium bicarbonate (CMM- [“CMM minus”]) as well as

adjusting the urea concentration to 10 g/L. *S. pasteurii* starter cultures from frozen stocks were grown in BHI medium (Sigma-Aldrich) containing 20 g/L urea.

Table 4. Bacterial strains, media and batch growth conditions used in this work.

Strain	**Relevant Properties**	**Growth Medium**	**Reference**
***Pseudomonas aeruginosa* AH298**	GFP on chromosome	LB [a]	(Werner et al. 2004)
***Pseudomonas aeruginosa* MJK1**	AH298 with urease operon added on pJN105 plasmid	LB plus 100 µg/mL gentamicin	This Work
***Escherichia coli* DH5α(pURE14.8)**	Urease operon on pUC19 plasmid, source of *Ure* genes for transformations.	LB plus 50 µg/mL ampicillin	(Collins and Falkow 1990)
***Escherichia coli* AF504gfp**	GFP on chromosome	LB plus 100 µg/mL ampicillin	(Folkesson et al. 2008)
***Escherichia coli* MJK2**	AF504*gfp* with urease operon added on pJN105 plasmid	LB plus 10 µg/mL gentamicin	This Work
***Sporosarcina pasteurii* ATCC 11859**	Common urease-positive model organism for MICP studies	BHI [b] plus 20 g/L urea or CMM- [c]	(Larson and Kallio 1954)

[a] 25 g/L Luria-Bertani Medium

[b] 37 g/L Brain Heart Infusion Medium

[c] Modified Calcite Mineralizing Medium (Ferris et al., 1996) without calcium chloride or sodium bicarbonate and modified to 10 g/L urea rather than 20 g/L.

Confocal Microscopy

Confocal microscopy of mature biofilms in capillary flow cell reactors was performed to demonstrate the use of the newly constructed model organisms in MICP experiments. Borosilicate glass capillary flow cells with a 0.9 mm x 0.9 mm square cross section and an approximate length of 10 cm had a wall thickness of 0.17 (±0.1) mm (F&D Glass, NJ, USA). Capillaries were imaged with a Leica DM6000 CS confocal laser scanning microscope (CLSM). Growth media (per Table 1) were infused into capillaries with a calibrated syringe pump connected with size 14 silicone tubing.

Autoclaved capillaries were injected with cell inoculum (per Section 0) and incubated statically for two hours to allow for cell attachment. Flow was initiated and maintained at 0.5 mL/hr for four days at which point biofilm colonies were clearly visible. Capillaries were mounted on the microscope stage and the medium was switched to CMM (containing $CaCl_2$) supplemented with the required antibiotic, 50 mM L-arabinose and 10 µM $NiCl_2$.

Biofilm colonies were located and 3D confocal stacks were collected repeatedly over the course of the observation time. Images presented in this work were collected through a Leica HC PL FLUOTAR 10X/0.30 dry objective. GFP fluorescence was imaged with excitation from a 488 nm laser and detection between 498 and 700 nm. Precipitates were imaged by detecting reflected 488 nm laser light between 483 and 493 nm. Raw CLSM data were processed with Imaris Version 7.6 (Bitplane, Zurich, CH). All confocal slices collected in 3D were projected onto one image for each time point. This

projection provides a view of the sample as though the observer is looking at the specimen from the top.

Analytical Measurements

Biomass Quantification. The optical density (OD) measured at 600 nm was used to quantify the turbidity of liquid cultures as a comparative measure of cell density. Triplicate 100 µL samples were added to separate wells in a polycarbonate 96 well plate and absorbance of 600 nm light was measured by a BioTek Instuments (Winooski, VT, USA) Synergy HT Multi-Mode Microplate Reader and the data were analyzed using Gen5 software. All readings are presented as deviations from the initial time point just before inoculation, or in the case of the inoculum OD to the phosphate-buffered saline solution absorbance. The 96 well plate method results in a light path length of 0.26 cm, so for increased relevance to literature values, the OD values presented herein were adjusted to a standard path length of 1.0 cm using the Beer-Lambert relationship (Anderson et al., 2004).

Bulk GFP. Total culture GFP florescence (bulk GFP) was measured with excitation from a tungsten halogen light source at 485/20 nm and intensity measured through a 528/20 nm band pass filter using a BioTek Instruments Synergy HT Multi-Mode Microplate Reader (Winooski, VT, USA). The bulk GFP measurements represent the total amount of GFP present in the culture at each time point. Values for GFP are

reported in arbitrary fluorescence units relative to the autofluorescence of fresh growth medium.

Urea. Urea was analyzed by high pressure liquid chromatography (HPLC) after 0.2 μm filtration and dilution to within the calibration range of 10-100 mg/L urea (Clark et al., 2007). Urea was derivatized with xanthydrol under acidic conditions to produce a diode array detectable compound at 230 nm. Samples were introduced to a 4.6x150 mm Agilent Zorbax Eclipse XDB-18 analytical column in an Agilent 1100 Series HPLC (Agilent Technologies Inc.) and eluted with a gradient of 20 mM ACS grade sodium acetate (Sigma-Aldrich) and HPLC grade acetonitrile (Fisher Scientific). Peak areas were measured (urea peak at approximately 10.5 min) using Agilent ChemStation software (Rev. A.10.02) and compared to calibration standards.

pH. The pH values of batch cultures were measured using a VWR sympHony meter and a Denver Instruments, Micro Glass-body pH electrode with a 5 mm diameter body. pH values were measured in 0.7 mL samples in 1.5 mL microcentrifuge tubes after the probe was calibrated using pH 7 and 10 buffers.

Kinetic Models

Kinetic rate parameters were established by fitting the experimental results of the batch kinetic studies to models by minimizing the sum of the squared errors between the model and observations. A solution that minimizes the sum of the squared errors was found using the generalized reduced gradient (GRG) nonlinear optimization technique

(Lasdon et al., 1978). A Gompertz function (Equation 5) was chosen to be applied to the population data in the form presented by Zwietering et al. (Gompertz, 1825; Zwietering et al., 1990).

$$\ln\left(\frac{OD}{OD_o}\right) = A\exp\left[-\exp\left[\frac{\mu_{\max}\exp(1)}{A}(\lambda - t) + 1\right]\right] \qquad (52)$$

OD is the optical density at time (t), OD_o is the initial optical density, μ_{max} is the specific growth rate during exponential growth, λ is the lag time and A is equal to $\ln(OD_{st}/OD_o)$. OD_{st} is the optical density at steady state, or in this case OD_{st} was taken to be the maximum OD reached by the culture. OD is the measure of population density throughout this work. The fitted parameters for the population model are μ_{max} and λ. The decrease of OD associated with population decay was not taken into account in this study.

Urea concentration was modeled in three different ways based on techniques from the literature. The general form of the ureolysis model is

$$\frac{dC}{dt} = f(C)\cdot OD\cdot C^n \qquad (53)$$

Where C is the concentration of urea at time (t), f(C) is a function of C and n is a constant describing the reaction order. The rate is scaled by the optical density at time (t) as a measure of the amount of urease present in the reactor.

The simplest ureolysis model is represented with f(C) = - r_0 and n = 0. This is referred to as the zero order model where

$$\frac{dC}{dt} = -r_o\cdot OD \qquad (54)$$

The zero-order model is correctly applied to systems with an excess of urea, or other substrates, where the enzyme is working at a constant maximum rate. The zero-order model is easily solved analytically so its use in complicated models where other processes are taking place is common. dC/dt does not depend on C, so the same ureolysis rate occurs independently of time and concentration. r_0, the zero order rate coefficient, is the fitted parameter in the zero-order model.

The most common ureolysis model in the literature is where f(C) = $-k_1$ and n = 1 so the reaction rate is linearly dependent on concentration. Here we will refer to this model as first order and the following equation applies.

$$\frac{dC}{dt} = -k_1 \cdot OD \cdot C \qquad (55)$$

First order rate models are commonly applied to ureolysis driven calcium carbonate precipitation work (Ferris et al., 2003; Tobler et al., 2011; Zhang and Klapper, 2010), however, only Zhang and Klapper (2010) scale the ureolysis rate to population density as done in this work. The first order rate coefficient, k_1, was fitted to the observed data in the first order model.

The last model that was applied is a Michaelis–Menten (M-M) function where n = 1 and f(C) = $-V_{max}/(k_m+C)$. V_{max} is the maximum reaction velocity and k_m is the half saturation coefficient.

$$\frac{dC}{dt} = \frac{V_{\max}}{k_m + C} \cdot OD \cdot C \qquad (56)$$

M-M models are common for the description of enzyme kinetics in general and have been widely applied to urease and other pure enzymes as well as to systems with

ureolytic bacteria (Bachmeier et al., 2002; Benini et al., 1996; Ciurli et al., 1996; Stocks-Fischer et al., 1999). By using a M-M type expression a more accurate representation of the concentration dependence on the reaction rate is derived. At high concentrations, the reaction rate asymptotically approaches a maximum (V_{max}) and as the urea concentration approaches zero so does the reaction rate. Other, more complex ureolysis models that include pH dependence, ammonium inhibition and temperature relationships have been proposed (Fidaleo and Lavecchia, 2003). More complex models were not used in this work because the large number of fitting parameters require more focused experimentation outside of the scope of this work.

The population growth model is assumed to be independent of the ureolysis models but the ureolysis models are scaled by the population density. As a result, first the Gompertz population growth model was fitted to the experimental optical density data independently of the ureolysis models. The resulting growth curve was then used to estimate ureolysis rate coefficients from experimental data from the same experiment.

Results and Discussion

Construction of Urease Positive GFP Organisms

Two urease-positive GFP-expressing bacteria were successfully constructed and named *Pseudomonas aeruginosa* strain MJK1 and *Escherichia coli* strain MJK2. The initial GFP containing organisms were *P. aeruginosa* AH298 (Werner et al., 2004) and *E. coli* AF504*gfp* (Folkesson et al., 2008), respectively. The previously cloned urease

operon from *E. coli* DH5α(pURE14.8) was inserted into the L-arabinose-inducible plasmid pJN105 and subsequently renamed pMK001 (see Figure 9).

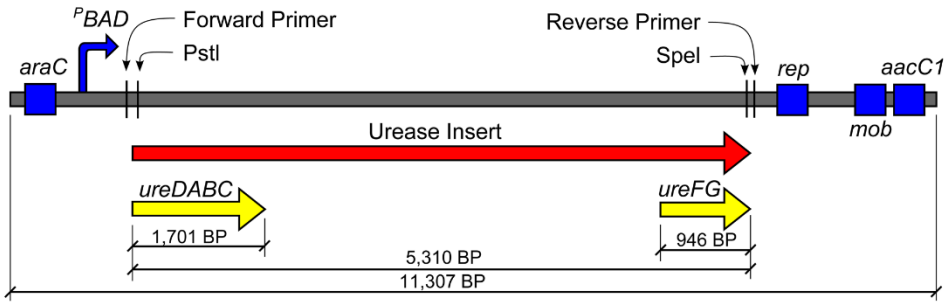


Figure 9. Linearized map of the new vector pMK001 (pJN105 with cloned fragment of DH5α(pURE14.8) inserted). Short arrows *ureDABC* and *ureFG* represent previously sequenced sections of *E. coli* DH5α(pURE14.8). The longer arrow 'urease insert' is the entire section of cloned genes transferred into pJN105. Restriction sites *PstI* and *SpeI* were added by primers and PCR to the insert to facilitate ligation into the vector pJN105. *araC* ^{P}*BAD* is the promoter, *rep* encodes trans-acting replication protein, *aacC1* imparts gentamicin resistance, *mob* encodes the plasmid mobilization functions.

The pMK001 plasmid was introduced into the GFP strains (Figure 10). The urease insert portion of pMK001 was sequenced and compared to the previously sequenced regions that cover the *ureDABC* and *ureFG* in DH5α(pURE14.8). The sequence between *ureDABC* and *ureFG* is not known from previous work and cannot be compared for homology. The DH5α(pURE14.8) *ureDABC* sequence (D'Orazio and Collins, 1993) was found to be identical to the corresponding sequence in pMK001. However, according to the basecalling algorithm used to determine the sequence (KB Basecaller), the insert had two additional nucleotides included near the end of *ureFG* (see supplemental materials). When analyzed with an older an older version of KB Basecaller (3730pop7LR) the two *ureFG* segments were identical. An NCBI BLAST search of the

entire insert region, including insertions, showed segments with high similarity to a *Proteus mirabilis* urease operon (Query cover: 48% E value: 0.0) and *Vibrio fischeri* ES114 chromosome I (Query cover: 43% E value: 0.0). The same BLAST search without the insertions yielded similar results with only the query coverage being reduced slightly. Sequences with and without the insertions were loaded into the NCBI ORF Finder and the insertions were found to have no effect in the predicted open reading frames of the insert. All predicted open reading frames occur before the insertions.

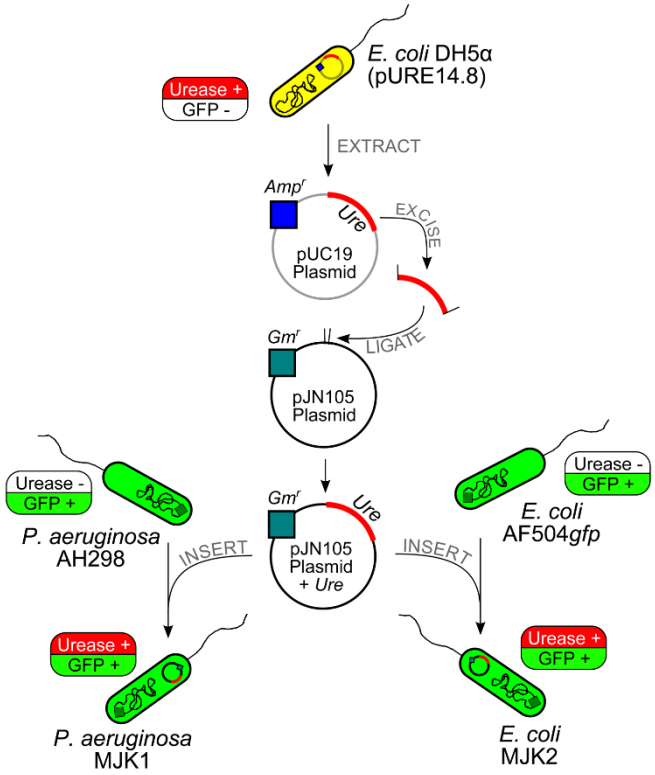


Figure 10. *P. aeruginosa* MJK1 and *E. coli* MJK2 were constructed by excising the urease operon (*Ure*) from the pUC19 plasmid previously contained in *E. coli* DH5α(pURE14.8). The urease operon was ligated into plasmid pJN105 to construct plasmid pMK001, which was then transferred to *P. aeruginosa* AH298 and *E. coli* AF504*gfp*. The resulting bacterial strains, MJK1 and MJK2, respectively, express both active urease and constitutive GFP. Amp^r and Gm^r refer to ampicillin and gentamicin resistance genes, respectively.

The *ureFG* nucleotide insertions are likely due to PCR amplification errors. These insertions may be significant because *ureFG* genes are believed to be involved in acquiring nickel (Kim et al., 2006) and we have shown that both transformed organisms require supplemental nickel to express significant urease activity (see Table 2). There are two possible effects of these insertions. One explanation is that the nickel acquisition genes are somehow incompatible with the organisms into which they have been inserted. The gene is present but potentially not synthesized in a suitable form to function in the context of the native metabolic framework. If this was the case, and the *ureFG* genes were incompatible with the transformant strains, it seems likely that both DH5α(pURE14.8) and MJK2 would exhibit the same behavior towards nickel because they are of the same species. However, these two strains do not behave the same in the presence of nickel (Table 5). A more likely explanation is that these insertions caused a translational difference that was large enough to render nickel acquisition nonfunctional. Based on our data, this seems possible because ureolytic activity in MJK2 was highly dependent on the addition of supplemental nickel (Table 5) while DH5α(pURE14.8) was unaffected by nickel addition.

Table 5. Response of different cultures to nickel addition as determined by the relative ability to increase pH in urea broth. Response was determined by measuring the period of time required for the color change reaction to occur in the respective cultures.

Strain		**No Supplemental Nickel**	**10 µM $NiCl_2$**
***E. coli* DH5α(pURE14.8)**	Positive Control	+++	+++
***P. aeruginosa* AH298**	Untransformed Negative Control	+	+
***E. coli* AF504gfp**	Untransformed Negative Control	-	-
***P. aeruginosa* MJK1**	New Construct	+	+++
***E. coli* MJK2**	New Construct	-	++
Phenol red color change within (10 hr: +++) (12 hr: ++) (24 hr: +) (No Activity: -)			

Test Tube Screening

Transformed strains were screened for ureolytic activity using the phenol red test tube assay. The screening showed positive results for ureolysis in both transformed strains. Non-transformed strains did not exhibit significant ureolysis (see Table 5). L-arabinose, at a concentration of 50 mM, increased the level of urease activity as expected based on plasmid construction (data not shown).

It became evident during preliminary screenings that the addition of nickel is important for the transformed strains to show ureolytic activity. We found that the positive control organism from which urease was extracted, DH5α(pURE14.8), did not require supplemental nickel, whereas the new transformants, MJK1 and MJK2, required additional nickel for urease activity. The addition of 10 µM $NiCl_2$ improved the ability of strains MJK1 and MJK2 to raise the pH similarly to DH5α(pURE14.8). Nickel

concentrations of up to 10 μM did not appear to affect the ability for DH5α(pURE14.8) to increase pH. *S. pasteurii* was not used as a positive control for the initial screening because of differing optimal growth conditions. It is well understood that *S. pasteurii* is highly ureolytically active; however, its population growth characteristics are much different than both *E. coli* and *P. aeruginosa* species making DH5α(pURE14.8) the better positive control for screening purposes.

The activity of urease has been reported to be dependent on nickel concentration (Mobley and Hausinger 1989, Mobley, Island and Hausinger 1995, Benini et al. 1999). The particularly strong nickel dependence in MJK2 has the potential to be utilized as an experimental control in future work, potentially allowing researchers to manipulate ureolysis and growth rates independently.

Although nickel is required for bacterial growth (normally in nanomolar concentrations) micro- or millimolar levels can be toxic to cells (Sar et al. 1998). Supplemental nickel has been added to media for ureolytically constructed organisms in the past. For instance, Zhang et al. found that their recombinant urease strain of *Lactococcus lactis* exhibited the maximum level of urease activity at 250 μM $NiSO_4$. They also reported from the literature that a range of supplemental nickel (from 2.5 μM to 200 μM) has been added to media for growing other urease constructs (Zhang et al., 2009). The 10 μM nickel tested for the transformants created in this work fits within that range.

Kinetic Studies

Growth and Ureolysis Characteristics. Both transformed organisms express measurable urease activity under the conditions tested as demonstrated through a decrease in urea concentrations, and a corresponding increase in pH, OD and bulk GFP signal in batch cultures over time (Figure 11). Urea concentrations decreased to less than 1% of the initial concentration of 10 g/L by 30 hours after inoculation in the presence of strains MJK1, MJK2 or *S. pasteurii*. The transformants began hydrolyzing urea noticeably earlier than *S. pasteurii*, which is attributed to differing lag times. Both transformants showed GFP expression that generally followed the trends in population growth.

The GFP profile during batch growth reveals two differences between the transformants (Figure 3,B). While GFP fluorescence for each of the transformants reaches a maximum very near the time of maximum OD and decays thereafter, the GFP fluorescence for MJK2 decreases more slowly. The faster decrease in GFP fluorescence for MJK1 is expected because of the growth rate dependence of GFP production through control by the growth rate-dependent *rrnBp*$_1$ ribosomal promoter.

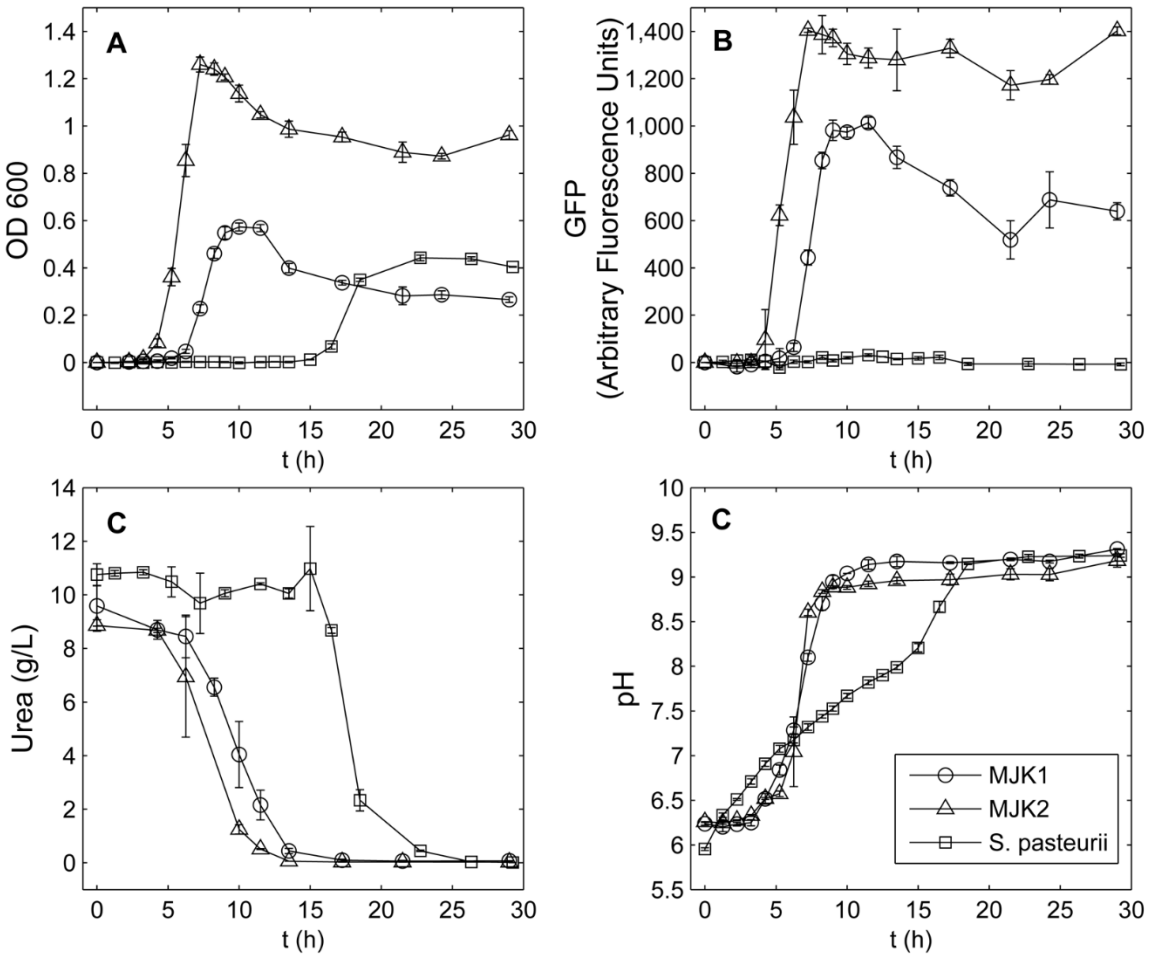


Figure 11. Ureolytic batch study results for both transformed organisms (MJK1 and MJK2) and the common ureolytic model organism, *S. pasteurii*. OD is reported after correction to a 1.0 cm path length and GFP fluorescence is in arbitrary units from a bulk fluorescent intensity measurement. Both OD and GFP are normalized to inoculated media. Error bars represent 95% confidence intervals with n = 3 replicates. Lines connecting the data points were added to indicate trends and facilitate distinction of the different treatments in the graphs.

Despite a significantly longer lag phase, *S. pasteurii* affected the pH such that a maximum was reached over a similar period of time as for both of the transformants. The *S. pasteurii* pH curve has a different shape than for both of the transformants. CMM- has less buffering capacity than LB between pH 6 and 8 (titration data not shown) which

explains the difference in the shape of the *S. pasteurii* pH curve. The maximum pH reached by MJK1 was the highest at 9.31±0.01 followed by *S. pasteurii* at 9.24±0.02 and MJK2 at 9.18±0.08 (± is the 95% confidence interval). Direct comparative conclusions cannot be made about urea hydrolysis based solely on pH because *S. pasteurii* was grown in a different medium. Rather, OD and urea concentration are the primary parameters of interest in this work.

Kinetic Curve Fitting. Kinetic parameters were estimated by fitting the zero, first, and Michaelis-Menten order models to experimental data for both transformed organisms and *S. pasteurii*. MJK2 grew the fastest and had the shortest lag time while *S. pasteurii* exhibited the slowest growth and longest lag time Figure 11; Table 6). Fitted parameters from all three ureolysis models show that, on an OD-normalized basis, *S. pasteurii* is most efficient at hydrolyzing urea. I.e. the cell specific ureolytic activity is the highest for *S. pasteurii*.

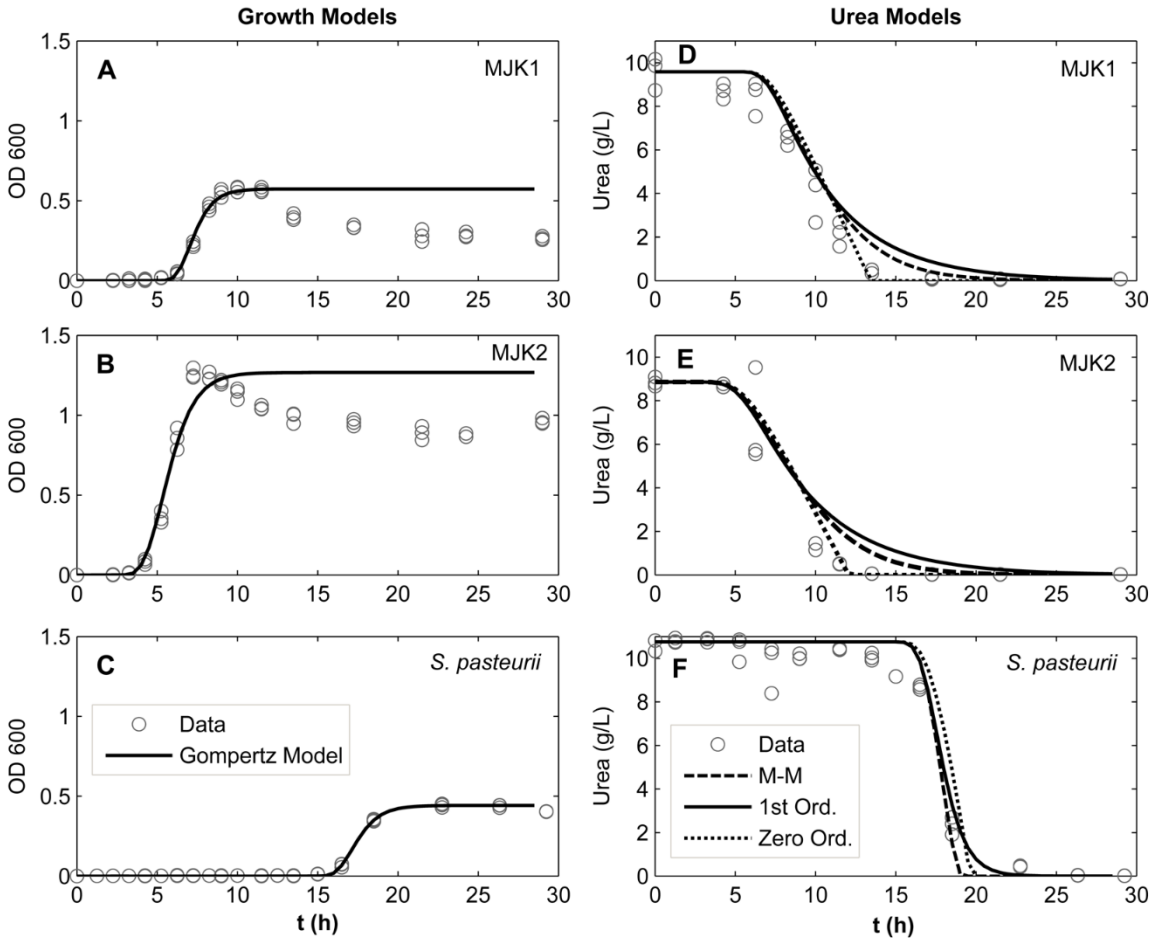


Figure 12. Experimental data (symbols) and model fits (lines) for growth and ureolysis studies. (A,B,C) Population growth was modeled by a Gompertz expression and (D,E,F) ureolysis rates were modeled using Michaelis-Menten (M-M), first order, and zero order rate models.

Table 6. Fitted kinetic parameters along with R2 as a measure of the quality of fit for population growth and ureolysis in batch culture. Values are presented as Mean(±95% Confidence Interval) with n = 3 replicates.

Population Growth Model (Gompertz)

	Parameter	Unit	MJK1	R^2	MJK2	R^2	*S. pasteurii*	R^2
	μ_{max}	1/hr	0.21(±0.01)		0.29(±0.03)		0.15(±0.01)	
	γ	hr	6.12(±0.06)	*0.37*[a]	3.97(±0.08)	*0.89*[a]	16.08(±0.10)	*0.99*
	OD_{max}	OD	0.57(±0.02)		1.27(±0.03)		0.44(±0.01)	

Urea Models

Model	Parameter	Unit	MJK1	R^2	MJK2	R^2	*S. pasteurii*	R^2
M-M	V_{max}	$g\ L^{-1}OD^{-1}\ hr^{-1}$	7.0 (±3.2)	*0.97*	2.5(±0.8)	*0.97*	28.4 (±2.8)	*0.96*
	k_m	g/L	10.6(±7.6)		8.4(±4.0)		4.4(±0.1)	
1st Order	k_1	$OD^{-1}\ hr^{-1}$	0.40(±0.06)	*0.96*	0.17(±0.01)	*0.96*	1.88(±0.15)	*0.96*
Zero Order	r_o	$g\ L^{-1}OD^{-1}\ hr^{-1}$	2.69(±0.64)	*0.96*	1.09(±0.09)	*0.97*	10.66(±0.76)	*0.97*

[a] Low R^2 values are attributed to poor fit at later time points where the decrease in OD due to population decay was not considered in the model. Model characteristics (μ_{max} and γ) still represent the data adequately for the purposes of this comparative study despite the low R^2 value. See Figure 4, A and B for a graphical representation of the model fit.

The population growth model fit the data well from stationary through exponential phases. However, the fit was poor as OD decreased during the stationary phase because there is no decay built into the Gompertz model. This poor fit during stationary phase is acceptable in the context of this work though because the goal was to compare the ureolysis characteristics of the three different strains during the exponential growth phase. Most ureolysis occurs before stationary phase is reached, thus the poor fit at later time points does not significantly affect the results of the ureolysis models.

Zero, first, and M-M order models fit the data at an $R^2 > 0.95$ (Table 6). Parameter estimation for the first and zero order model was highly reproducible with the relative standard deviation of estimates from triplicate treatments being ≤ 7.7%. A larger relative standard deviation was observed with the M-M model at 27.4% for k_m and 18.9% for

V_{max}. The M-M model has more degrees of freedom thus allowing for more variation in the fitted V_{max} and k_m and resulting in a larger deviation of fitted parameters as compared to both of the one-parameter models.

Strain Comparison. MJK1 exhibited a higher specific ureolysis rate, i.e. a higher ureolysis rate per cell; however, MJK2 had a higher specific growth rate resulting in more rapid ureolysis in MJK2 cultures. A number of possibilities may explain these rate differences. pH and ammonium concentration are known to affect urease activity of the pure enzyme (Fidaleo and Lavecchia, 2003). *E. coli* and *P. aeruginosa* species are also known to regulate cytoplasmic and extracellular pH differently. In *E. coli*, cytoplasmic and extracellular pH remain approximately equal when the culture pH is disturbed over a range between approximately pH 6.0 and 7.5 (Wilks and Slonczewski, 2007). To the authors' knowledge, no similar measurement of cytoplasmic pH has been performed for any *P. aeruginosa* strains but it is likely that pH regulation is different due to differing efflux pumps, transporters and metabolic potential.

Native metabolic processes in the transformants may play an important role in their ureolysis kinetics. Many *P. aeruginosa* strains possess urease genes. Currently, all four of the sequenced *P. aeruginosa* strains in the MetaCyc database (Caspi et al., 2012) are annotated for urease structural genes, *ureABC*, and multiple accessory genes. However, native urease in *P. aeruginosa* is thought to be highly regulated. Early ureolysis studies in Pseudomonads even wrongly concluded that all species within the genus *Pseudomonas* were urease negative (Stewart, 1965). In our own work we were

unable to establish growth conditions for *P. aeruginosa* strains that would permit expression of significant ureolysis activity (data not shown). It is known that *P. aeruginosa* strains possess a urea uptake system that is suppressed by the presence of ammonium (Jahns, 1992). *E. coli* is not known to have a similar urea uptake system. Subsequent work by Jahns showed that ATP generation was linked to urea hydrolysis in *S. pasteurii* by cytosolic urease contributing to the membrane potential with cytosol alkalinization and ammonium efflux thought to be the important factors (Jahns, 1996). The mechanism discussed by Jahns (1996) explains the high urease activity in *S. pasteurii* but it could also be argued that some of the same mechanisms allow MJK1 to be more efficient at ureolysis than the *E. coli* strain MJK2 on a population normalized basis.

Additional Parameters. Other factors that influence the kinetics of the urease enzyme are pH, ammonium concentration and temperature. Fidaleo and Lavecchia (2003) constructed a detailed model taking all known major factors into account using purified jack bean urease. Although the Fidaleo and Lavecchia model describes a pure enzyme system very well, constants from the literature for pure enzyme systems do not necessarily apply to systems with microorganisms. The Fidaleo and Lavecchia model was fit to the data with slight modification to scale the rate to OD rather than enzyme concentration and it was found to be a poor fit with the published pH, temperature and product inhibition constants (data not shown). The data collected for this study was not sufficient for the estimation of the large number of parameters associated with such a complex enzyme kinetic model

Application in Flow Cell Reactors

MJK1 and MJK2 are clearly ureolytically active and express GFP under the growth conditions provided during this study but the formation of biofilm must also be considered in order for these strains to be successfully used in the study of MICP. Biofilm formation is an important attribute because it is thought that extracellular biofilm components play an important role in crystal nucleation and calcium carbonate polymorphology (Decho, 2010; Ercole et al., 2012; Rodriguez-Navarro et al., 2007). Preliminary flow-through experiments conducted in 1 mm square glass capillary tubes under continuous laminar flow indicated that both transformants produce thick biofilms and precipitate calcium carbonate. The biofilm characteristics are different between the two transformants with MJK1 forming dense colony biofilms and MJK2 forming a more unstructured, flexible biofilm. In both cases, biomass and minerals were successfully imaged with CLSM. Figure 13 shows MJK1 in a time series of mineral formation associated with a biofilm colony in a square capillary flow cell.

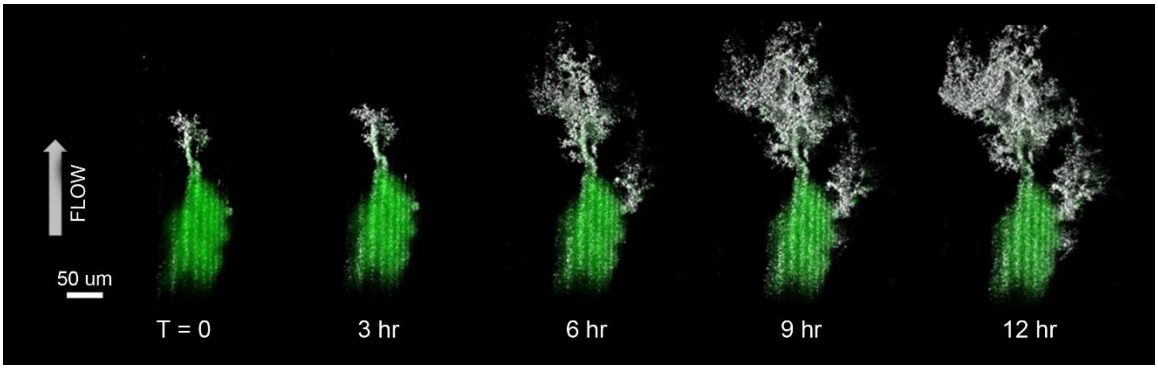


Figure 13. Time lapse CLSM images of a *P. aeruginosa* MJK1 biofilm colony (green) during calcium injection under laminar flow in a 1.0 mm square glass capillary flow cell (flow direction is from bottom to top). Calcium carbonate precipitates (white) are shown to accumulate on the downstream side of the biofilm colony (green GFP fluorescence). Biomass was imaged based on the fluorescence of the constitutively expressed GFP and the precipitates were imaged using reflected light microscopy. T = 0 corresponds to the beginning of the imaging session. The total time that the biofilm colony was exposed to calcium was about 15 hours. Please refer to the methods section (2.6) for the image processing associated with this figure.

Experiments using either MJK1 or MJK2 in flow cells will have to be designed carefully in order to promote and sustain the appropriate metabolism. Both transformants are capable of using metabolic pathways that could potentially counteract the pH increase associated with ureolysis making mineral precipitation impossible even with high ureolytic activity. One example would be if oxygen was depleted in an experimental system and acid-producing fermentation pathways were being utilized. At some point urease might be too inhibited by the low pH values to show significant activity. In addition, even if a low pH-tolerant urease variant is produced, low pH values (often resulting in low saturation indices) might make precipitation not possible and possibly even cause dissolution of previously precipitated calcium carbonate. Metabolic

heterogeneities in biofilm systems could also create multiple environments within an experiment, making results more difficult to interpret.

Conclusions

Two novel model organisms were constructed to conduct pore scale ureolysis-driven MICP experiments, where organism and mineral growth can be visualized continuously and non-invasively. The two new bacterial strains will allow for the research of spatiotemporal physical and biochemical phenomena at the micrometer scale in MICP systems. Previously, it was not possible to observe the spatiotemporal orientation of biomass with respect to newly formed precipitates that were induced by the same biomass. The new strains allow for the visualization of biomass *in situ* without the need for fluorescent staining. The ability to study MICP in this way can be used for the optimization of engineered applications and for the development of an improved fundamental understanding of natural microbial precipitation processes.

Kinetic analysis revealed that the specific ureolytic activity of MJK1 and MJK2 is not as high as for *S. pasteurii*, the most common organism used for MICP experiments. Analysis of batch cultures revealed that all commonly used kinetic models can be fit to the experimental data with limited deviation. The zero order (constant ureolysis rate) model is simple and describes the data well in all cases when its rate is normalized to the population density. The population density was modeled with a Gompertz function, fitting a lag time and maximum specific growth rate to the optical density data. MJK2

exhibited the fastest growth characteristics; however, the other two organisms (MJK1 and *S. pasteurii*) exhibited higher specific (i.e. cell number normalized) ureolysis rates.

Differences in specific growth and ureolysis rates, along with physiological differences, make the potential use of each of the new model organisms unique. The newly constructed strains require supplemental nickel for ureolysis activity. MJK2 urease is particularly well controlled with nickel, introducing a potentially useful system control where ureolysis activity could be regulated independently of growth. The two chromosomal GFP constructs behave differently as well. GFP expression of MJK1 is more closely associated with metabolic activity through its control under the growth rate dependent ribosomal promoter $rrnBp_1$ while MJK2 constitutively expresses GFP. MJK1 will be of more use in studies aimed at determining the spatially resolved metabolic activity whereas MJK2 may be preferred in studies where only the physical location of biomass is important.

Chapter 3 Glossary

A	$\ln(OD_{st}/OD_o)$
C	Urea concentration
CMM	Calcite Mineralizing Medium
GFP	Green Fluorescent Protein
HPLC	High Pressure Liquid Chromatography
k_m	M-M half saturation coefficient
λ	Lag time

LB	Luria-Bertani Medium
MICP	Microbially Induced Calcium Carbonate Precipitation
M-M	Michaelis-Menten enzyme kinetics model
μ_{max}	Maximum specific growth rate
OD	Optical Density
OD_o	Initial Optical Density
OD_{st}	Steady-state Optical Density
R^2	Coefficient of determination
t	Time variable
V_{max}	M-M maximum reaction velocity (rate)

Acknowledgements

We wish to thank Adrienne Phillips for a careful edit as well as Dr. Mike Franklin for thoughtful guidance. This work was funded by the National Science Foundation through NSF award No. DMS-0934696 and by Office of Science (BER), Subsurface Biogeochemical Research Program, U.S. Department of Energy through Grant Numbers DE-FG-02-09ER64758, DE-FG02-07ER64417 and DE-FG02-09ER64734.

CHAPTER 4

ESTIMATION OF A BIOFILM-SPECIFIC REACTION RATE: KINETICS OF BACTERIAL UREA HYDROLYSIS IN A BIOFILM

Contribution of Authors and Coauthors

Author: James M. Connolly

Contributions: Conducted the experimental work, envisioned graphics, table design and major topics of the manuscript. Wrote and revised manuscript.

Author: Benjamin Jackson

Contributions: Envisioned major topics of the manuscript. Contributed to the writing, development and revision of the manuscript with comments and feedback.

Author: Adam P. Rothman

Contributions: Conducted the experimental work.

Author: Isaac Klapper

Contributions: Envisioned major topics of the manuscript. Contributed to the writing, development and revision of the manuscript with comments and feedback.

Co-Author: Robin Gerlach

Contributions: Envisioned major topics of the manuscript. Contributed to the writing, development and revision of the manuscript with comments and feedback.

Manuscript Information Page

James Connolly and Robin Gerlach
npj Biofilms and Microbiomes
Status of Manuscript:
____ Prepared for submission to a peer-reviewed journal
__x_ Officially submitted to a peer-review journal
____ Accepted by a peer-reviewed journal
____ Published in a peer-reviewed journal

Nature Publishing Group

Abstract

Biofilms and specifically urea-hydrolyzing biofilms are of interest to the medical community (e.g. urinary tract infections), scientists and engineers (e.g. microbially induced carbonate precipitation). In order to appropriately model these systems biofilm-specific reaction rates are required. A simple method for determining biofilm-specific reaction rates is described and applied to a urea-hydrolyzing biofilm. Biofilms were grown in small silicon tubes and influent and effluent urea concentrations were determined. Immediately after sampling, the tubes were thin sectioned in order to estimate the biofilm thickness profile along the length of the tube. Urea concentration and biofilm thickness data were used to construct an inverse model for the estimation of the urea hydrolysis rate. It was found that urea hydrolysis in *Escherichia coli* MJK2 biofilms is well approximated by first-order kinetics between urea concentrations of 0.003 and 0.221 mol/L (0.186 and 13.3 g/L). The first-order rate coefficient (k_1) was estimated to be 23.2 ± 6.2 h^{-1}. It was also determined that advection dominated the experimental system rather than diffusion, and that urea hydrolysis within the biofilms was not limited by diffusive transport. Beyond the specific urea-hydrolyzing biofilm discussed in this work, the method has the potential for wide application in cases where biofilm-specific rates must be determined.

Introduction

The hydrolysis of urea by microorganisms has been widely shown as an effective method for the *in situ* production of alkalinity and the subsequent precipitation of carbonate minerals. At circumneutral pH, urea ($CO(NH_2)_2$) hydrolysis can be written as

$$CO(NH_2)_2 + 2H_2O + H^+ \rightarrow 2NH_4^+ + HCO_3^-, \qquad (57)$$

where two ammonium ions and one bicarbonate ion are formed for each urea molecule that is hydrolyzed. Additionally, one proton is consumed which raises the pH. When calcium or other divalent cations are present carbonate mineral precipitation can be possible due to an increase in carbonate (CO_3^{2-}) concentration.

Carbonate mineral formation through microbial ureolysis is significant in medicine because of the role ureolytic microorganisms can have in the formation of kidney and urinary tract stones as well as catheter encrustations (Morris et al., 1999; Zhao et al., 1998). Mineral formation through ureolysis has also been studied extensively for engineered applications in building materials (e.g. De Muynck et al., 2010) and in the subsurface for permeability reduction, soil stabilization and contaminant remediation (e.g. Phillips et al., 2013). Microbial urea hydrolysis is also of interest in industrial and agricultural wastewater treatment settings where a significant portion of the total nitrogen is attributed to urea (Yingjie and Cabral, 2002). In all of the systems mentioned above, particularly where the surface area to volume ratio is high, a significant portion of the ureolytic activity is likely to be attributed to biofilms.

A significant obstacle in predicting system behavior in biofilm-containing systems is the lack of quantitative, system-specific reactive transport characterization. This study looks specifically at ureolysis in a model biofilm system in order to shed light on the reactive transport environment that is likely to be present in systems that have, or have been stimulated to have, ureolytic activity. Ureolysis in planktonic cultures has been investigated thoroughly and there have been a number of studies to quantify volume-averaged (Darcy modeling) ureolysis rates in porous media containing microorganisms (Ebigbo et al., 2012; Handley-Sidhu et al., 2013; Tobler et al., 2011; Wu et al., 2011) and immobilized enzyme (Moynihan et al., 1989; Redden et al., 2014).The most applicable studies concentrate on the rate of precipitation in these systems leaving the micro-scale reactive transport characteristics of ureolysis in biofilms largely undiscussed.

Rather than taking a volume-averaged approach, ureolytic biofilms were grown in silicon tubes that mimic the laminar flow environment that would be encountered in a soil pore or urinary tract. The silicon tubes provide an environment that contains similar reaction/diffusion characteristics as our systems of interest but these chericteristics are much easier to quantify in the simple system. No calcium or other cations that would cause mineral precipitation were supplied to the system so that urea hydrolysis could be studied in detail without the complications introduced when precipitation takes place. The silicon tubes were then destructively sampled and thin sectioned in order to obtain an accurate biofilm thickness profile over the length of the tube. Biofilm thickness profiles were combined with influent and effluent urea measurements to obtain a ureolysis rate per biofilm volume (here referred to as a biofilm-specific rate). This chapter provides a

method for the measurement of effective reaction rates in biofilms and greater insight into the reactive transport environment of biofilm-catalyzed urea hydrolysis through the application of nondimensionalization techniques.

Materials and Methods

Biofilm Growth

Escherichia coli MJK2 (Connolly et al., 2013) biofilms were grown in 10 cm long, size 14 silicon tubes (Masterflex ®, Cole-Parmer, IL, USA) with influent urea concentrations ranging from 0.011 to 0.221 mol/L (0.63 to 13.3 g/L). *E. coli* MJK2 possesses a pJN105 plasmid that has been modified to contain the urease operon from *E. coli* DH5α(pURE14.8) and also carries a mutant chromosomal *gfp* (green fluorescent protein gene) (Collins and Falkow, 1988; Folkesson et al., 2008). Experiments were initiated by the injection of inoculum into an autoclaved reactor assembly and allowing cells to attach for one hour. See the supplementary online material for strain details and preparation of the inoculum. Flow was then started at 1.0 mL per hour (Reynolds number (Re) of 0.1 in a clean tube) and maintained at 1.0 mL/min for 10 days with a KDS220 multichannel syringe pump (KD Scientific, MA, USA). Flow was only stopped for short periods to exchange sterile 60 mL plastic syringes filled with sterile medium. The silicon tube was connected to the syringe via small-inside-diameter (0.127 mm) PEEK tubing (see Figure 14). The small-inside-diameter tubing is intended to minimize residence time and cause a high shear environment that is not conducive to biofilm growth in the

influent tubing. Without biofilm growth the average hydraulic residence time is 4.5 seconds in the influent tubing and 12.1 minutes in the silicon tube reactor.

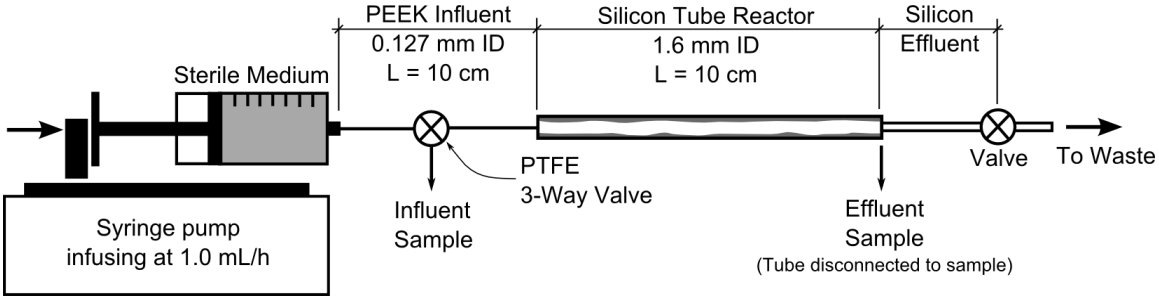


Figure 14. A schematic for the tube reactor assembly. Sterile LB medium is pumped through a 10 cm long, 1.6 mm inside diameter (ID) silicon tube with biofilm growing on the walls. Small ID influent tubing was used to connect the syringe to the tube reactor. A 3-way valve was used to take influent samples and the downstream end of the tube reactor was disconnected to take effluent samples.

After 10 days of biofilm growth three consecutive effluent samples and one influent sample were taken. The three consecutive effluent samples were taken in order to 65demonstrate steady state behavior. Tubes that had at least one consecutive effluent urea concentration deviate from the mean of the three samples by 25% were not used in further analysis. High variation between serial replicates indicates transient behavior such as biofilm detachment events during sampling making the data set unsuitable for modeling. The last effluent sample taken from each tube was taken to be representative and used in all subsequent models because it was taken closest to the end of the experiment when thin section samples were prepared.

Effluent samples were taken by disconnecting the downstream end of the tube and letting media flow into a 1.5 mL microcenterfuge tube at the experimental flow rate for one hour. The influent sample was taken last by directing flow to the sample tube by the

3-way valve as shown in Figure 1. The empty microcentrifuge tubes were weighed, 100 µL of 3.8% HCl was added, weighed, sample added, and weighed again. The final sample pH of approximately 1.5 is effective at stopping ureolysis because the urease enzyme has been shown to loose activity at low pH (Fidaleo and Lavecchia, 2003). Finally, samples were filtered (to remove cells) through a 0.2 µm pore size cellulose acetate syringe filter (VWR, NJ, USA) and refrigerated for later measurement of urea concentrations via HPLC. Immediately after the liquid sample was taken, the silicon tubes were destructively sampled for the determination of biofilm thickness profiles by thin sectioning.

Biofilm Thickness Measurements

Immediately following the liquid sampling, the tubes were dissected in order to determine a biofilm thickness profile along the length of each tube. Each 10 cm tube was cut into five 2 cm long sections. The center 1 cm of each section was cut out and cut in half lengthwise with a surgical scalpel. Remaining liquid was carefully wicked away with tissue paper before Tissue-Tek O.C.T. Compound (Sakura Finetek Inc., CA, USA) was dispensed onto the cross section of each tube and placed on dry ice to freeze. Once the OCT was fully frozen, the cross section of tube was peeled away leaving the biofilm embedded in the OCT. Microscopic investigation showed that no significant biofilm was left behind on the tube. The frozen and embedded biofilm was then completely embedded in OCT in a tissue cryofixation mold. The frozen samples were stored at -20ºC for subsequent thin sectioning.

The frozen biofilm samples were cut into 5 μm thick cross sections and mounted in a Leica CM1850 cryostat. Sections were mounted onto charged microscopy slides (Fisherbrand™ Superfrost™ Plus Stain, Fisher Scientific, NJ, USA) and air-dried. Five sections were taken for each segment of tube. The green fluorescent protein (GFP) produced by the bacteria was imaged via epifluorescence microscopy. Thin sections were imaged on a Nikon E-800 microscope equipped with a CoolSNAP MYO CCD camera (Photometrics, AZ, USA), PhotoFluor LM-75 light source (89 North Inc., VT, USA), Nikon Plan Apo 10X/0.45 DIC L ∞/0.17 WD 4.0 objective and a FITC filter cube (EX 480/30, DM 505 LP, EM 535/40). The raw 16-bit images were 1940 x 1460 pixels with a pixel size of 0.4499 μm. All fluorescence images were obtained with an exposure time of 2 seconds.

Raw images were thresholded in the open source software FIJI (Schindelin et al., 2012) using the automatic triangle method (Zack et al., 1977). The triangle method proved to provide the most representative results over other commonly used methods such as Otsu (1979). The thresholded images were quantified to determine average biofilm thicknesses (L_f). This was done by dividing the calculated ark length of the section of tube shown in the image (0.923 mm) by the area of the biofilm cross section that was obtained from the thresholded image. Images that contained significant defects were excluded from the analysis. Defects included dust particles, bubbles and geometric irregularities that would cause inaccuracy in the thickness measurements. Average thickness from all usable replicates are presented (see Appendix B for thickness calculations and raw data). Images were not taken when samples did not contain any

visible biofilm and the thickness was recorded as zero. Figure 15 shows a typical thin section and the analysis that was performed on it.

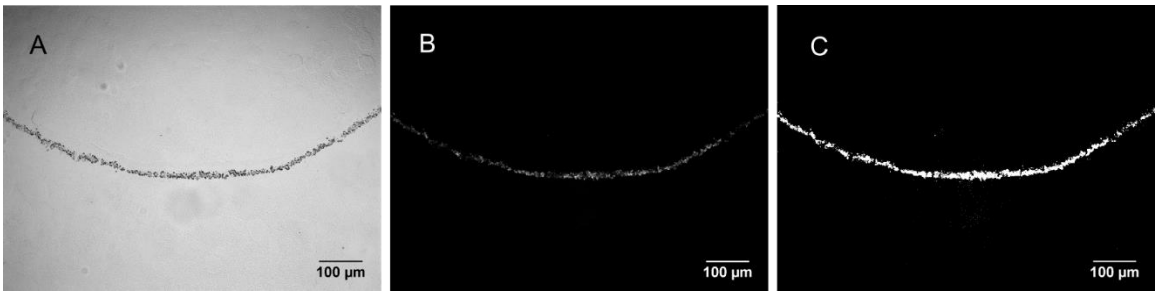


Figure 15. A representative example of a thin section image. (A) A transmitted light image shows a qualitative representation of the biofilm. (B) The fluorescence image, showing the GFP signal, is used for quantification. (C) The GFP fluorescence image is thresholded to differentiate between biofilm (white) and background (black), forming a binary image. The area of the biofilm signal is quantified and divided by the calculated visible arc length (0.923 mm) to calculate a representative average biofilm thickness.

Urea Quantification

Urea was analyzed using high pressure liquid chromatography (HPLC) after the Clark et al. (2007) method with in-autosampler derivatization identically to Connolly et al. (2013).

Urea Hydrolysis Rate Determination

Tube reactors were modeled using COMSOL Multiphysics version 4.3a (COMSOL Inc., USA) in order to fit kinetic parameters to the measured urea consumption over the length of the tube reactors. The tube reactors were modeled as a two-dimensional rotated axisymmetric geometry. Navier-Stokes equations were solved to obtain a flow field and it was assumed that there is zero fluid flow in the biofilm domain. The thin section data were used to reconstruct the biofilm profile for each tube reactor. It

was assumed that the biofilm thickness was constant for discrete values of x (see Figure 3 for model coordinates) and the thickness was linearly interpolated between measured points. Biofilm thickness could not be measured immediately at the influent or effluent of the reactors (x = 0 and 10 cm) due to potential artifacts due to the removal of the silicon tubes from the experimental system, so it was assumed that L_f at x = 0 cm equaled L_f at x = 1 cm and L_f at x = 10 cm equaled L_f at x = 9 cm. Urea transport was calculated with advection by the Navier-Stokes flow field and Fickian diffusion. No reduction in

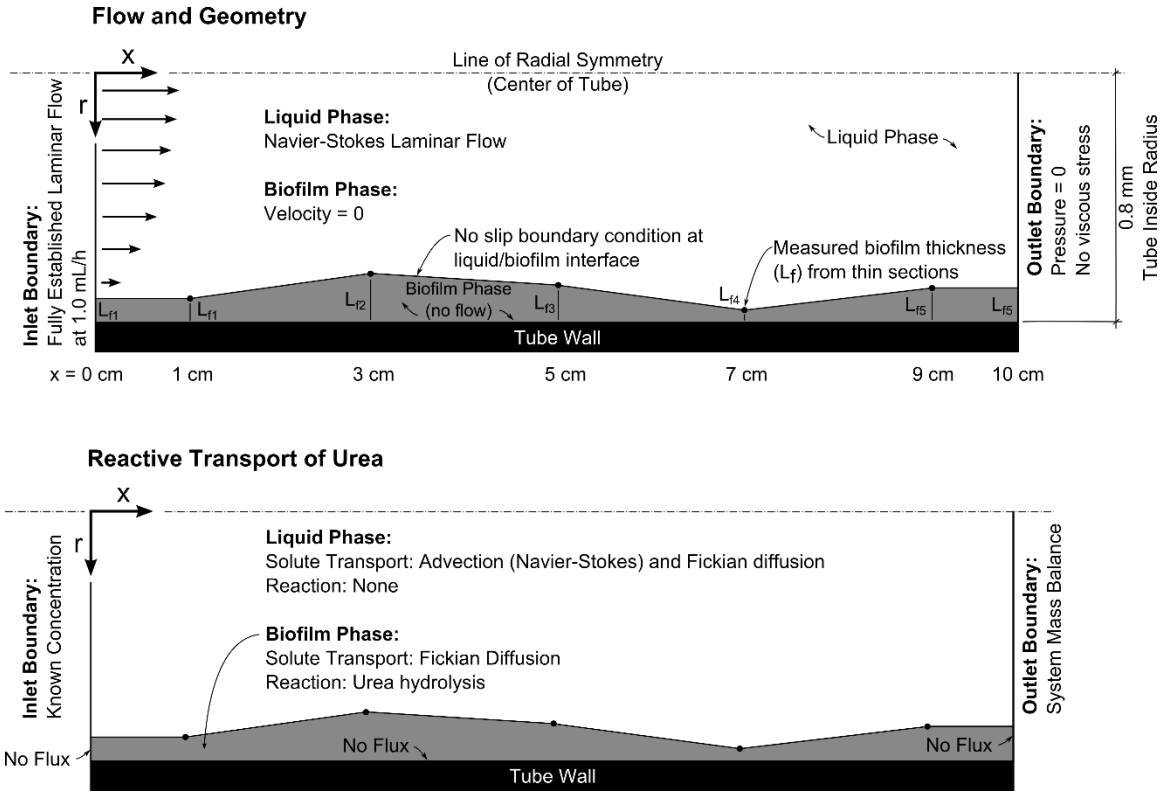


Figure 16. COMSOL model overview with boundary conditions.

diffusive transport in the biofilm domain was considered so diffusion characteristics were assumed to be constant throughout the simulation. Preliminary analysis showed that implementing increased mass transport resistance of solutes in the biofilm as in Stewart (1998) affected the rate fitting minimally (< 1% difference in the thickest biofilms, data not shown). Boundary conditions and modeling assumptions are indicated in Figure 16.

The urea hydrolysis reaction rate, R, was assumed to be constant within the entire biofilm in each tube (independent of concentration) and constrained to the biofilm domain (no reaction in the liquid phase). Justification for the constant reaction rate assumption follows in Section 0. The influent and effluent urea concentrations are known so the urea hydrolysis rate was fitted such that the experimentally determined concentrations fit the model. The urea concentration at the outlet boundary is non-constant so rather than minimizing the difference between modeled and experimental concentrations directly, the difference between the modeled and experimental total effluent urea flux was minimized. The last of the three effluent urea concentrations was taken to be the representative concentration because it was taken closest to the time of destructive sampling. The known effluent urea flux, J_{EF}, can be calculated by multiplying the effluent concentration, C_{EF}, by the volumetric flow rate, Q such that

$$J_{EF} = C_{EF} Q. \qquad (58)$$

C_{EF} is an average and well mixed value. The modeled effluent urea flux, J'_{EF}, was calculated by integrating over the area of the liquid phase at the effluent such that

$$J'_{EF} = 2\pi \int_{0}^{ID/2 - L_f} C\, u\, r\, dr, \qquad (59)$$

where u is the x component of the fluid velocity, C is the local urea concentration and ID is the tube inside diameter (1.6 mm). The model was run iteratively where the biofilm ureolysis rate was varied such that the sum of the squared error between J_{EF} and J'_{EF} is minimized. The COMSOL optimization module was used to find a urea hydrolysis rate, R, that minimizes the squared error, $(J_{EF} - J'_{EF})^2$, using the Nelder-Mead method (Lagarias et al., 1998; Nelder and Mead, 1965) with a nondimensional fitting tolerance of 10^{-6}.

Fitted rate values for each tube were compiled into a data set that represents reaction rates at a range of urea concentrations. An average urea concentration within the biofilm volume, $C_{Urea,BF}$, was calculated for each tube and was taken to be the representative urea concentration corresponding to the rate that was fitted. A Michaelis–Menten (M-M) rate, $R_{m\text{-}m}$, relationship was fitted to the compiled data using the least squares curve fitting tool (cftool) in MATLAB R2012a (The MathWorks, Inc., MA, USA):

$$R_{m-m} = R_{max} \frac{C}{k_m + C}. \qquad (60)$$

R_{max} is the maximum ureolysis rate and k_m is a half saturation coefficient. It was theorized that the M-M relationship would fit the data best but other rate relationships were fit for comparison. For a reaction of order, n, with respect to urea concentration a generalized rate law can be written as

$$R_n = k_n C^n . \qquad (61)$$

First-order (n = 1, linear) and zero-order (n = 0, constant rate) relationships have been used previously to describe microbial ureolysis (Connolly et al., 2013; Ferris et al., 2003; Tobler et al., 2011; Zhang and Klapper, 2010) so they were also included in the regression analysis.

Results and Discussion

Analytical Results

Urea Measurement. Measureable urea hydrolysis was observed in all tube reactors after 10 days of operation. Influent urea concentrations varied between 0.011 and 0.221 mol/L. Effluent concentrations varied between 0.003 and 0.208 mol/L including all serial replicates. Tubes 5, 10, 11 and were eliminated from the analysis because the steady state condition was not met (> 25% deviation from the mean). The reader is referred to Appendix B for all urea measurements.

Biofilm Thickness Profiles. Biofilm profiles were successfully obtained from 11 tube reactor runs. Biofilm thicknesses ranged from 0.6 to 222.0 μm with an average across all observations of 18.7 μm. Assuming zero flow through the biofilm, laminar flow is expected in all tube reactors (a maximum Re = 0.18 was calculated for the reactor with the thickest biofilm observed).

Five replicate biofilm thickness measurements were collected for each profile point. 5.5 % of the measurements were eliminated from the analysis due to apparent

irregularities such as bubbles in the cutting medium, dust particles and deformed sections. All biofilm thickness measurements presented were at least measured in duplicate with an average of 4.7 measurements per thickness value. Raw biofilm measurements can be found in Appendix B and the average profiles used in the model can be found in Figure 17.

Sources of Error. There are some distinct sources of error associated with the tube reactor experiment that must be addressed. The most significant source of error is expected to be in defining the biofilm thickness profile. If the biofilm thickness throughout the tube is not well characterized the calculated rates are not accurate because the rate fitting implicitly depends on the amount of biofilm present. There are four potential sources of error for the estimation of the biofilm thickness profile: (1) Biofilm at the influent and effluent of the tubes cannot be accurately quantified, (2) Biofilm thickness between measurement points may not be well approximated by linear interpolation, (3) Biofilm thickness may not be constant around the entire cross-section of the tube and (4) Significant detachment events have the potential to occur during sampling for aqueous analysis.

In the first three potential sources of error, the problem is that the entire tube, and biofilm within that tube, cannot reasonably be imaged in three dimensions. These errors are directly related to the lack of the ability to sample at a high spatial resolution and can be considered random errors. Random errors in this system can be expected to have the same likelihood for overestimation as for underestimation. In other words, the sampling

regime is just as likely to miss a thick area of biofilm as a thin area. Although more advanced techniques would be required, the low spatial resolution problem can be resolved. 3D imaging techniques such as X-ray microtomography (Davit et al., 2011; Iltis et al., 2011; Wildenschild and Sheppard, 2013), nuclear magnetic resonance imaging (Graf von der Schulenburg et al., 2008; Seymour et al., 2004) and optical coherence tomography (Haisch and Niessner, 2007) have the potential to image simple biofilm systems and better link biofilm geometry to effective reaction rate estimations.

Error associated with detachment events during the sampling process cannot be quantified here but the sign of the error and its effects is known. If a large detachment event were to happen during aqueous sampling or between sampling and thin sectioning, the biofilm profile during aqueous sampling would be unknown but it had to be thicker than would be shown in the thin sections. This would always lead to an overestimation of the effective reaction rate in that particular tube due to the underestimation of biofilm volume. Similarly to the other class of random errors, this problem could be minimized through the use of more advanced 3D imaging techniques. These more advanced techniques would still need to be utilized carefully as to not disturb the biofilm.

Reactive Transport Characterization

The Damköhler number (Da) is defined as the time scale of convective transport divided by the time scale of reaction within a control volume (Fogler, 2005). For a first-order reaction the Damköhler number can be defined as

$$Da = k_1 \tau, \qquad (62)$$

where τ is the average fluid retention time. This standard expression for Da requires modification for a system with rates defined as occurring only in the biofilm phase. Equation 6 assumes that reaction is occurring within the entire volume for which τ is calculated (the liquid volume). In this case the reaction is not occurring in the liquid volume so the transport rate and reaction rates must be normalized for the volumes in which they occur.

Similarly, the Péclet number (Pe) can be defined as the ratio of the advection rate of a solute to the diffusion rate of the same solute (Cussler, 1997). The Péclet number can be expressed as

$$Pe = \frac{vL}{D}, \qquad (63)$$

where D is the diffusion coefficient, which is 1.38×10^{-9} m^2/s for urea in pure water at 25ºC (Cussler, 1997). v is an average fluid velocity and L is a representative length scale. The values of v and L can be chosen based on what is being characterized in the system. In this case both axial and radial behavior is of interest so two Péclet numbers are defined. The first, Pe_x, characterizes axial behavior where the velocity is taken to be the average magnitude of the x component of velocity, v_x. The second, Pe_r, characterizes radial behavior where the velocity is taken to be the average magnitude of the r component of velocity, v_r. The length scales are different for radial and axial behavior. The tube length, l_{tube}, is the length scale for axial flow and the tube diameter d_{tube} is the length scale for radial flow such that

$$Pe_x = \frac{v_x l_{tube}}{D}, \qquad (64)$$

and

$$Pe_r = \frac{v_r d_{tube}}{D}. \qquad (65)$$

The last dimensionless parameter considered is the Thiele modulus (ϕ) which is the ratio of the time scale of reaction to the time scale of diffusion. The Thiele modulus is simple to calculate for first order reactions (Cussler, 1997).

$$\phi^2 = \frac{k_1 L^2}{D}. \qquad (66)$$

The length scale (L) here is a biofilm thickness (L_f) because the Thiele modulus, in this case, is calculated as a metric to quantify potential diffusion limitation of the biofilms in this system. Biofilm thickness is not constant in these systems so average high and low values for each tube are used to bound overall behavior. Table 1 shows the calculated dimensionless parameters (average, minimum and maximum) for each tube reactor in the study. The values used in the calculation of the dimensionless parameters were taken from the finite element model.

Table 7. Average dimensionless parameters for all tube reactors along with their minima and maxima. Da and Pe are calculated for each tube and ϕ is calculated for all L_f measurements.

	Da	Pe_x	Pe_r	ϕ
Average	4.42	1.42×10^{4}	2.31	4.75×10^{-2}
Min	*3.85*	*1.34×10^{4}*	*1.00*	*1.63×10^{-3}*
Max	*4.64*	*1.64×10^{4}*	*6.00*	*3.36×10^{-1}*

In general, the dimensionless parameter analysis shows that advection dominates the system (rather than diffusive transport and urea hydrolysis) and that biofilms are not diffusion limited. The Damköhler number shows that, for this particular system, the time scale of advective transport is larger than the time scale of reaction. In classical chemical engineering terms Da > 1 indicates that not all of the substrate is being utilized in the reactor. The overall reaction rate, within the entire reactor, is limited by high advective transport. Da > 1 is out of necessity in this study because there needs to be measurable urea at the effluent for the quantification of urea hydrolysis within the reactor.

Axial Péclet numbers are all much greater than ($Pe_x >> 1$) one indicating that the system is strongly advection dominated. Only a small fraction of axial urea transport can be contributed to diffusion. The radial Péclet number indicates advective and diffusive urea transport are more balanced with diffusive and advective transport contributing more equally in the radial direction. There are two primary characteristics that control Pe_r assuming a constant diffusion coefficient. First, the bulk flow rate effects Pe_r. A higher overall system flow rate will translate into greater overall velocities, including radial velocities. Second, the heterogeneity of the biofilm profile directly affects radial velocities. As the biofilm profile becomes more constant (i.e. the closest to L_f being equal at all values of x), the average radial velocity will decrease, thus decreasing Pe_r. It can also be expected that flow rate and biofilm thickness heterogeneity could be linked. Although this physiological relationship was not studied here it has been shown that biofilms adapt to their shear and solute transport environments (Stoodley et al., 1999, 1998). *E. coli* biofilms have been shown to adapt their architecture to specific

hydrodynamic and nutrient conditions. Specifically, when nutrients are provided in excess (as is expected in this study due to high Da and low ϕ values) *E. coli* biofilms have been shown to adapt to resist shear stress (Teodósio et al., 2011).

The Thiele modulus was the most variable dimensionless parameter in the system but all values were found to be less than one indicating that the time scale for diffusion is generally shorter than the time scale of reaction. This means that urea hydrolysis within biofilms in this study are not strongly diffusion limited. In other words the bulk liquid concentrations are expected to be approximately equal to the concentrations found within the biofilm (i.e. no steep gradients in urea concentration). This finding is an important validation for the approach that was taken in determining kinetic rate constants where the reaction rate and the corresponding biofilm urea concentration ($C_{Urea,BF}$) in each tube was assumed to be constant. Visual evidence for small Thiele modulus behavior can also be found in Figure 17 where the urea concentration does not appear to change significantly within the biofilms relative to the bulk fluid.

Kinetic Parameter Fitting

Tube reactors that met the steady state criteria were modeled using individual finite element models, and the urea hydrolysis rate, R, was varied until the differences between the modeled and experimental urea fluxes were minimized. The representative concentration corresponding to the calculated reaction rate was assumed to be the average urea concentration within the biofilm volume of each tube.

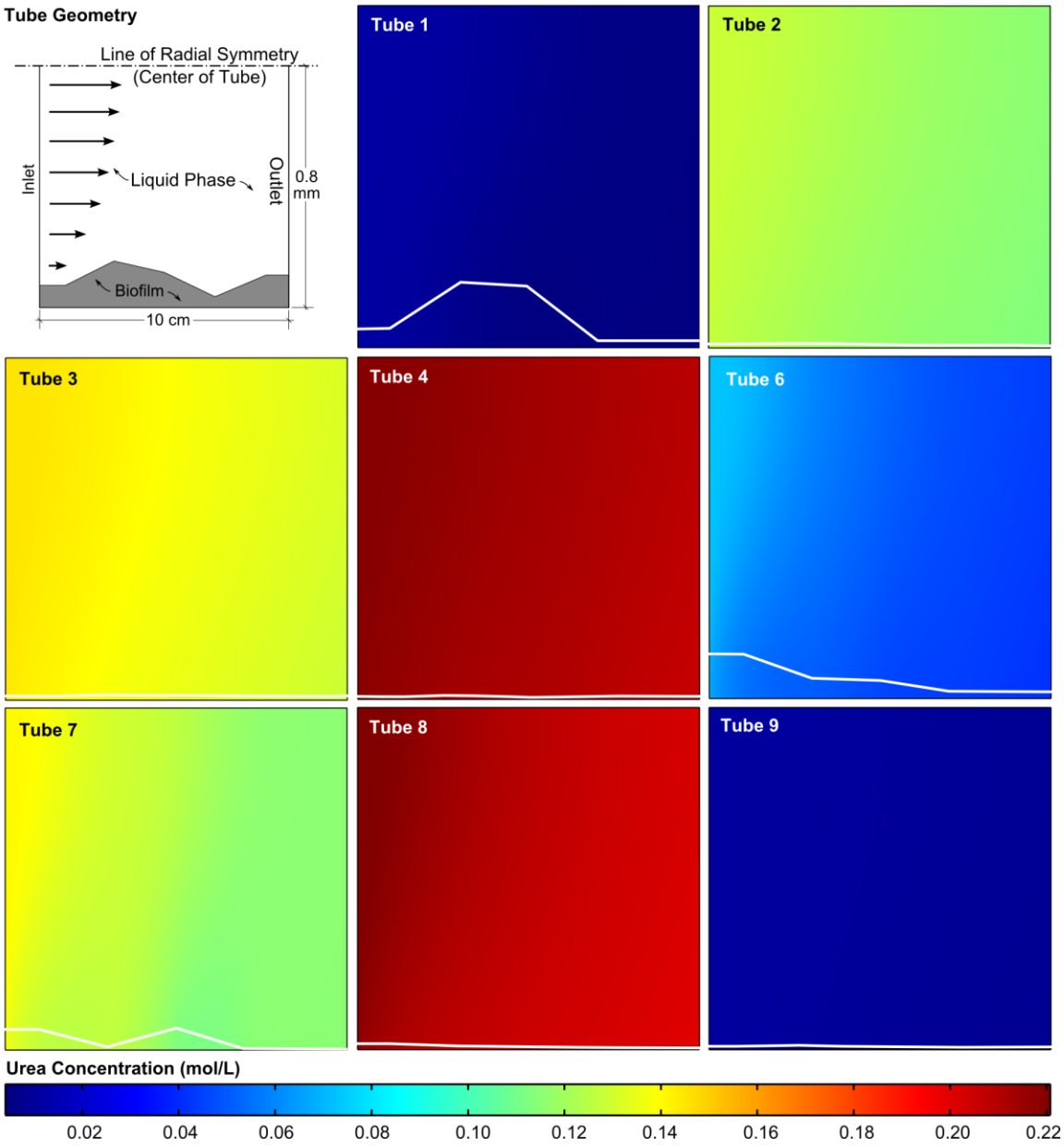


Figure 17. Local urea concentration as predicted from the finite element model for each tube reactor used in the analysis. Concentration is not constant within each tube however when the same color scale is used, as in this figure, it is evident that each tube represents a narrow concentration range within the range of concentrations that exist within this study. Biofilm profiles are shown as white lines in each panel.

The resulting data from the finite element models allowed for regression analysis considering Michaelis–Menten (M-M), first- and zero-order rate models. A plot of urea hydrolysis reaction rate versus representative concentration along with rate model fits can be found in Figure 18. M-M and first-order models fit the data best (root-mean-square error of 1.01 and 0.97 mol/(L·h) respectively) while the zero order was a poor fit compared to the others (root-mean-square error = 1.56 mol/(L·h)). M-M and first-order model fits are not statistically different at 95% confidence over the range of concentrations considered in this study. Rate constants for the M-M model were estimated to be k_m = 0.55 mol/L and r_{max} = 15.9 mol/(L·h) and for the first-order model k_1 = 23.2 ± 6.2 h^{-1} (± is the 95% confidence interval).

The demonstration of first order behavior is important for modeling more complex systems and is a significant finding in this work. Others have used first-order kinetics for ureolysis systems involving ureolysis-driven mineralization (Ferris et al., 2003; Tobler et al., 2011) however the applicability of that model had remained undemonstrated for any biofilm system until now. For reactions obeying M-M kinetics, as has been shown for urea hydrolysis (Ciurli et al., 1996; Fidaleo and Lavecchia, 2003; Moynihan et al., 1989), it is typically assumed that first-order kinetics should only be

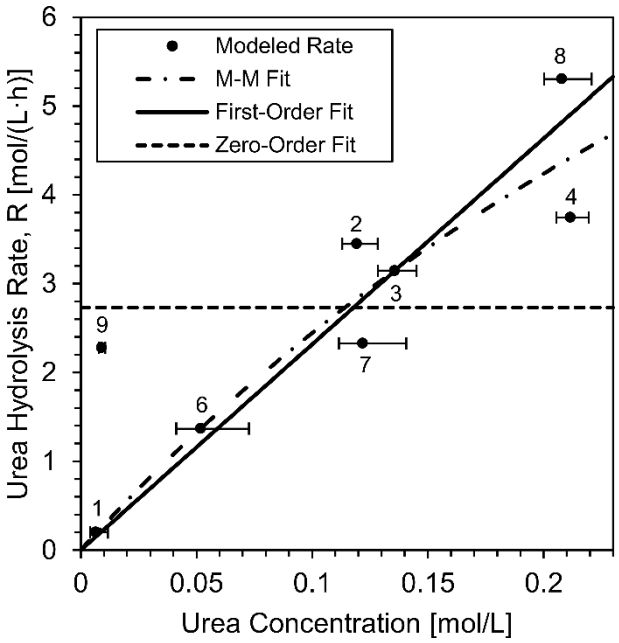


Figure 18. Average urea concentration within the biofilm volume versus estimated urea hydrolysis rate. The modeled points correspond to the rate calculated by the finite element models versus the average urea concentration in the biofilm volume, $C_{Urea,BF}$. Error bars represent the range of urea concentration within the biofilm volume as estimated by the finite element models. Points are labeled with the tube reactor numbers from which they were obtained.

applied to systems where the reaction substrate is at low concentration ($C << k_m$). The results shown here indicate that published kinetic values from pure enzyme or planktonic biological experiments may not be appropriate for use in systems where attached cells and biofilms are the primary catalyst. Diffusion limitation is routinely cited as the reason for different kinetic behavior in biofilms but the results of this work suggest that kinetic differences can occur even without evidence for significant diffusional mass transport limitations.

Practical Applications

The study presented has direct and indirect applications. The most direct application of this work is the continuation of laboratory studies using *E. coli* MJK2. The biofilm-specific kinetic parameters obtained in this study can be used in conjunction with tools such as confocal microscopy, flow cells, and finite element modeling in more complex systems to further investigate local chemical gradients within ureolytic biofilms. Systems that would be particularly well suited include ureteral catheters (Morris et al., 1999) and urea-hydrolysis-driven microbial carbonate precipitation (De Muynck et al., 2010; Phillips et al., 2013a).

Beyond urea hydrolysis systems specifically, this paper presents a robust method for the systematic characterization of effective reaction rates in biofilms in flow systems. The small scale of the tube reactor method has advantages over more common laboratory bench-scale biofilm reactors such as the CDC reactor (ASTM E2562, 2007), annular reactors (Lawrence et al., 2000), or drip flow reactors (Goeres et al., 2009). The main advantages relate to cost and the reduction of waste. The simple tube reactor requires no specialized equipment other than a syringe pump or a similar pump that provides a constant and slow flow. The shear environment can also be easily tailored to the specific requirements of the study by varying the flow rate or tube size. The tube reactor method is also well suited for studies where hazardous materials are used. Studies focusing on quantifying the degradation of hazardous substances by biofilms may find use in small tube reactor studies because experiments could be designed that produce a minimal amount of hazardous waste (e.g. chlorinated aromatics, hydrocarbons, nitroaromatics and

pharmaceuticals). Studies where high cost substrates are used (e.g. stable isotope compounds) may also find use in the tube reactor system. There are also disadvantages to the tube reactor method as compared to larger volume approaches. Some studies may require larger sample volumes for multiple analyses, making the use of such a low-flow-rate system impractical.

Conclusions

The determination of biofilm-specific reaction rates is important for the accurate micro-scale modeling of biofilm systems. In this work biofilm-specific urea hydrolysis rate coefficients were determined (both Michaelis–Menten and first-order rate models) in a tube reactor system. It was found that for the chemical and hydrodynamic conditions present in this study a first-order (linear) rate model fits the reaction rate versus concentration data as well as the Michaelis–Menten model which is more difficult to work with computationally. This work along with the previous characterization of *E. coli* MJK2 in planktonic culture makes the organism a valuable tool for the study of various aspects of ureolysis in biofilms. Applications include medical, environmental science and engineering research topics. Beyond the specific findings related to ureolysis, the method presented in this work has wider applications to other biofilms where a biofilm-specific reaction rate needs to be determined.

Acknowledgements

The authors were funded by the National Science Foundation through NSF award No. DMS-0934696 and by the U.S. Department of Energy Grant Numbers DE-FG-02-09ER64758, DE-FE0004478, DE-FE0009599 and DE-FG02-13ER86571. J.M.C was also supported by a NSF-IGERT fellowship in Geobiological Systems at Montana State University (DGE-0654336).

CHAPTER 5

REACTIVE TRANSPORT AND PERMEABILITY REDUCTION IN A SYNTHETIC 2D POROUS MEDIUM WITH BIOFILM-INDUCED CARBONATE PRECIPITATION

Contribution of Authors and Coauthors

Manuscript in Chapter 5

Author: James M. Connolly

Contributions: Conducted the experimental work, envisioned graphics, table design and major topics of the manuscript. Wrote and revised manuscript.

Co-Author: Johannes Hommel

Contributions: Envisioned major topics of the manuscript. Contributed to the writing, development and revision of the manuscript with comments and feedback.

Co-Author: Robin Gerlach

Contributions: Envisioned major topics of the manuscript. Contributed to the writing, development and revision of the manuscript with comments and feedback.

Manuscript Information Page

James Connolly, Johannes Hommel and Robin Gerlach
Status of Manuscript:
__x_ Prepared for submission to a peer-reviewed journal
____ Officially submitted to a peer-review journal
___ Accepted by a peer-reviewed journal
____ Published in a peer-reviewed journal

Abstract

Microbially- or biofilm-induced carbonate precipitation in the subsurface for permeability reduction has been the subject of many studies in recent years but the particular manner in which pore space is decreased remains largely uncharacterized. This leaves engineers who are eager to apply this technology to the field largely guessing at the most effective ways to carry out the process.

Work presented in this paper describes a set of experiments where a fluorescently-labeled, urease positive bacterium is allowed to form biofilm and precipitate calcium carbonate in a 2D etched silicon and glass porous media micromodel flow cell reactor. The pore blocking constituents were imaged with confocal microscopy at two time points under three different flow rates and with calcium added at varying times during the experiments. Finite element modelling was utilized to predict reactive transport behavior based on the experimental image data. Differential pressure was also recorded which allowed for the estimation of permeability reduction due to the various treatments.

It was found that the greatest permeability and porosity reductions occurred when calcium was added to the system directly after the system was inoculated. A moderate amount of permeability reduction was achieved when no calcium was added to the system, although longer lasting mineral plugging is often seen to be more desirable over only biofilm caused permeability reduction. The least amount of permeability reduction was seen when calcium addition commenced 24 hours after inoculation. Finally, pore space was observed to be occupied by gas bubbles, presumably originating from

microbial activity, during low flow and zero flow periods. With all evidence taken into account, this work provides a case for the pulsed injection of reactants to a system when porosity and permeability reduction is the primary goal.

Introduction

Microbially-induced carbonate precipitation (MICP) has been shown to be an effective method to reduce permeability in geologic porous media (De Muynck et al., 2010; Phillips et al., 2013a). There are multiple microbial metabolisms that are able to precipitate carbonate minerals and block pore space (Connolly and Gerlach, 2015) but the one explicitly studied in this work is urea hydrolysis. In this process urea ($CO(NH_2)_2$) is hydrolyzed, typically by bacteria, to form ammonia (NH_3) and inorganic carbon (Equation 67). In a porous medium it is likely that the majority of the bacteria in the subsurface are present in the attached form known as a biofilm due to the high surface to volume ratio (Characklis and Marshall, 1990). Here we consider a conceptual model where biofilm reduces pore space itself but also catalyzes the precipitation of calcium carbonate, both of which (biofilm and precipitate) occupy pore space and reduce permeability (Phillips et al., 2013b). Urea hydrolysis sets off a series of chemical reactions (Equations 68-70) that have the potential to form solid carbonate minerals when calcium, or other divalent cations are present (Mitchell and Ferris, 2006).

$$CO(NH_2)_2 + 2\ H_2O \rightarrow 2\ NH_3 + H_2CO_3 \qquad \text{Urea Hydrolysis (67)}$$

$$2\ NH_3 + 2\ H_2O \leftrightarrow 2\ NH_4^+ + 2\ OH^- \qquad \text{Ammonia Protonation and pH Increase (68)}$$

$H_2CO_3 + 2\ OH^- \leftrightarrow HCO_3^- + H_2O + OH^- \leftrightarrow CO_3^{2-} + 2\ H_2O$

Shift of Carbonate Equilibrium (69)

$CO_3^{2-} + Ca^{2+} \leftrightarrow CaCO_3(s)$ Calcium Carbonate Precipitation (70)

It has been widely shown that biofilm growth and calcium carbonate precipitation can reduce permeability independently (Armstrong and Ajo-Franklin, 2011; Cunningham et al., 1991). Unfortunately the established methods for measuring the location, volumes and morphological characteristics of both constituents are quite different. Porosity reduction due to carbonate precipitates is often estimated with x-ray computed tomography due to the high x-ray contrast that the dense precipitate provides (Armstrong and Ajo-Franklin, 2011; Wildenschild and Sheppard, 2013). Biofilm provides little x-ray contrast making it difficult to image. It is not impossible to image biofilm using x-ray computed tomography (Davit et al., 2011; Iltis et al., 2011) but techniques to image both biofilm and precipitates are not yet developed. The most common method for the characterization of intact biofilms continues to be confocal laser scanning microscopy (CLSM) (Beyenal et al., 2004; Heydorn et al., 2000; Pitts and Stewart, 2008).

Here we chose to utilize micromodel reactors that mimic a two-dimensional slice of a porous medium in order to observe, at high resolution using CLSM, the porosity change over time due to a green fluorescent protein (GFP) tagged, urease-producing biofilm and the carbonate minerals that the biofilm precipitates. The two-dimensional geometry of the micromodel flow cell allows us to image the entire reactor and resolve all pore-occupying constituents using CLSM. Similar work has been done for biofilm (Dupin and McCarty, 1999; Kirk et al., 2012; Knutson et al., 2005; Nambi et al., 2003;

Zhang et al., 2010b) and mineral precipitation (Dawe and Zhang, 1997; Ghaderi et al., 2009; Zhang et al., 2010a) separately but we were able to combine them in one experiment for a more complete look at the behavior in MICP systems. Specifically, in this work we investigate the degree to which biofilms and the minerals they can precipitate block pore space. This reduction in pore space is accompanied by changes in the reactive transport characteristics of the porous medium which are estimated using a pore scale finite element model that uses experimentally gathered geometric data.

Materials and Methods

Micromodel Fabrication

The micromodel features were etched into a silicon wafer using cryogenic deep reactive-ion etching (cryo-DRIE) under a SF_6/O_2 environment and sealed by anodically bonding a piece of glass to the etched surface. All photolithography was conducted in the class 1000 clean room at the Montana Microfabrication Facility at Montana State University. The micromodel and influent/effluent hole patterns (Figure 19) were drawn electronically and sent to the University of Minnesota Nanofabrication Center for the construction of a photolithography mask constructed of soda lime glass with the pattern in chrome.

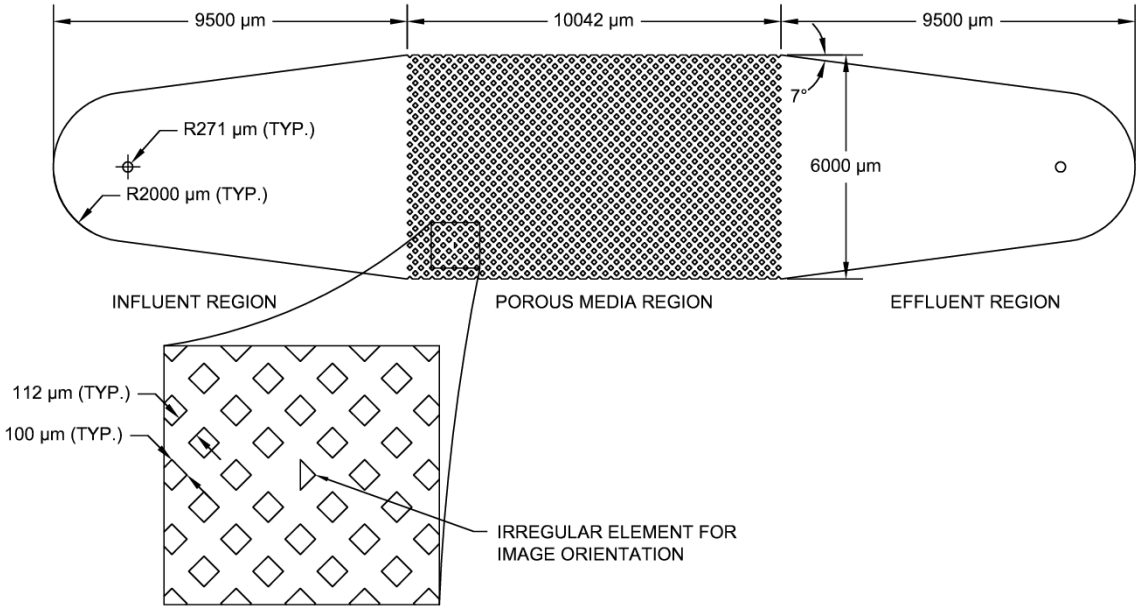


Figure 19. Porous media micromodel geometry. The micromodels were etched in silicon wafers to a depth of 18.1 µm and sealed with a 200 µm Pyrex cover slip.

The lithography process started by coating a P-type silicon wafer with a layer of aluminum (≈ 200 nm) using a MODU-LAB thermal evaporation physical vapor deposition system. The wafers were polished on both sides, 100 mm in diameter and 0.5 mm thick. NR9-1500PY negative photoresist (Futurrex, Inc., NJ, USA) was spin-coated onto the wafer at 2000 rpm for 40 s followed by a 150ºC, 60 s hotplate softbake (1805-1995 nm thickness). The wafer was then exposed for 40 s using a contact aligner (ABM-USA, Inc., CA, USA) emitting 15 mW/cm^2 light at a wavelength of 365 nm. The wafer was hardbaked on a 100ºC hotplate for 60 s, let to cool to room temperature and then developed for 30 s with RD6 developer (Futurrex, Inc., USA). The wafer was rinsed thoroughly in deionized water and dried with nitrogen. The remaining photoresist then served as the mask for patterning the aluminum layer. The exposed aluminum was

dissolved with surfactant-containing aluminum etch 16-1-1-2 (J.T. Baker, USA) at 70ºC for approximately 2 min. The remaining photoresist was dissolved with acetone and the wafer was washed with deionized water and dried with nitrogen.

The wafer was loaded into an inductively-coupled plasma (ICP) reactive ion etcher (Plasmalab System 100, Oxford Instruments, UK) with the wafer chuck cooled to -110ºC. Wafers were etched with an ICP power of 1000 W and an RF power of 3 W at a pressure of 10 mTorr under a mixed gas flow of SF_6 at 40 sccm and O_2 at 3 sccm. Etching under these conditions produced an etch rate of 4.56 µm/min at the center of the wafer as measured by a XP2 stylus profilometer (Ambios Technology, Inc., USA). The total etch depth was measured to be 18.137 µm. After etching the micromodel features, the process was repeated on the reverse side to obtain influent and effluent holes by etching through the wafer completely. Once all of the features were complete the wafer was stripped of the remaining aluminum with aluminum etch, rinsed with deionized water, then immersed into an 80ºC piranha solution bath (three parts concentrated H_2SO_4, one part H_2O_2) for 20 min to completely strip the wafer of organics. 100 mm diameter, 200 µm thick, fully polished Pyrex wafers were stripped in the same piranha bath. Both silicon and Pyrex wafers were rinsed with deionized water and dried with nitrogen. 200 µm Pyrex was chosen because it is the closest commercially-available thickness to standard No. 1.5 microscope coverslips which are 170 µm.

The cleaned wafers were anodically bonded together to form the flow channels. Anodic bonding was completed at Utah Nanofab at the University of Utah with an EVG®501 bonder (EV Group, Inc., AT) at 350ºC, 2000 N and 1000 V. Individual

micromodels were cut apart using a dicing saw and influent and effluent connections were made with NanoPorts (IDEX Corporation, USA). The micromodel used in this study had a measured channel depth of 18.1 µm and a porosity of 0.78. A scanning electron micrograph of the porous media features can be found in Figure 20.

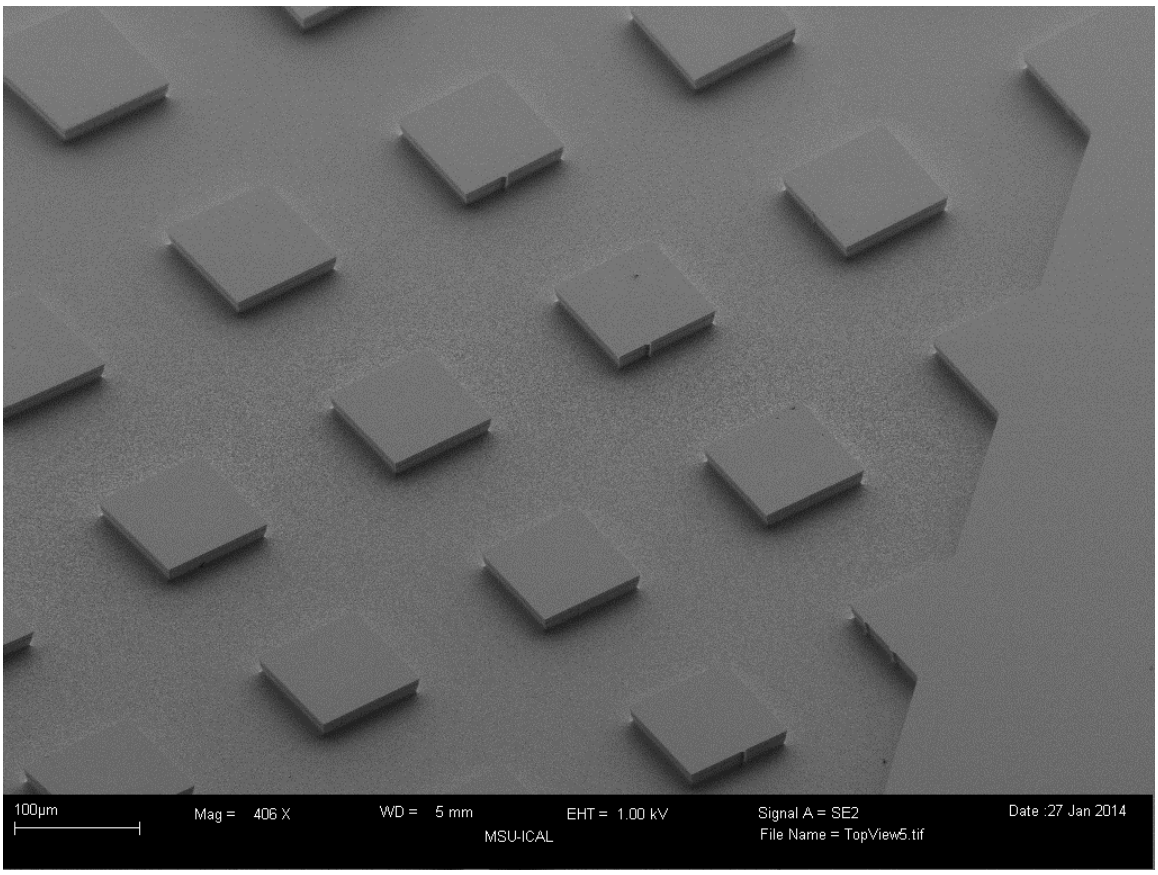


Figure 20. A representative scanning electron micrograph of the edge of the porous media region of a micromodel without cover glass.

Strain and Growth Conditions

Escherichia coli MJK2 was the model organism used in this study. MJK2 is a recombinant bacterium that contains a plasmid-borne urease operon (Collins and Falkow,

1988; Connolly et al., 2013) and a mutant chromosomal green fluorescent protein (GFP) gene (Folkesson et al., 2008). MJK2 was used in this study because it can be imaged noninvasively using the GFP and is a biofilm former for which biofilm-specific ureolysis kinetics have been characterized (Connolly et al., 2015). The growth medium for MJK2 was a supplemented Luria–Bertani (LB) medium which contains 10 g/L tryptone, 10 g/L NaCl, 5 g/L yeast extract, 50 mM L-arabinose (7.5 g/L, for the plasmid promoter), 10 μg/mL gentamycin (to force plasmid retention), 10 μM Ni^{2+} (to increase urease activity) and 0.1 M urea (6.0 g/L). The medium was supplemented with 0.1 M Ca^{2+} when desired and filter sterilized. All experiments were conducted at room temperature (20ºC).

The inoculum for the micromodel experiments was prepared by inoculating 100 mL calcium-free medium with 100 μL of frozen stock. The culture was incubated on a 150 rpm shaker table at room temperature in a 250 mL Erlenmeyer flask for 12 h, which resulted in an optical density of 0.26 for a 1 cm path length measured with 600 nm light. The resulting culture was used directly as the inoculum for micromodel experiments.

Micromodel Experiment

1.0 mL of *E. coli* MJK2 inoculum was introduced into the sterile micromodel at a flow rate of 1.0 mL/h; medium flow was stopped for 1 h to allow cells to attach. Immediately following the attachment period, influent lines were disinfected with a 10% v/v bleach solution for 10 min, influent lines were flushed with sterile growth medium, and then flow was directed through the micromodel at the experimental flow rate. Experiments were conducted at 0.1, 0.25 and 0.5 mL/h. With each flow rate, one

experiment was conducted entirely with calcium-free medium, one experiment where calcium-containing medium flow was started 24 h after inoculation (after imaging), and one in which the flow of calcium-containing medium was started immediately following the cell attachment period. This results in a set of nine experiments with independently varying flow rate and calcium addition timing. See Table 8 for a matrix of experimental treatments. Tiled confocal microscopy images of the entire porous media region of each micromodel were taken 24 and 48 hours after inoculation. Table 1 shows the experiments that were conducted along with the naming scheme that is followed. Experiments 7 and 8 experienced permeability reductions greater than what could be measured with the differential pressure transducer and were terminated early so the 48 hour time points for these experiments (7-48 and 8-48) were excluded from the analysis. In order to observe longer time scale behavior, experiment 9 was taken out to longer time points with zero flow.

Table 8. Naming scheme for experiments performed in this study.

Ca Addition	**Flow Rate**			**Time Point**
	0.1 mL/h	0.25 mL/h	0.5 mL/h	
No Ca	1-24	2-24	3-24	**24 h**
	1-48	2-48	3-48	**48 h**
Ca at 24 h	4-24	5-24	6-24	**24 h**
	4-48	5-48	6-48	**48 h**
Ca	7-24	8-24	9-24	**24 h**
at Inoculation	7-48*	8-48*	9-48**	**48 h**

** Maximum measureable differential pressure exceeded.*

*** Longer time point data collected.*

Differential pressure across the micromodel was directly measured with a 26PCAFA6D differential pressure transducer (Honeywell International, Inc., USA) and a DATAQ DI-718B-U data logger system equipped with a DI-8B30-01 voltage input module (DATAQ Instruments, Inc., USA) at a time resolution of 1 s. The pressure transducer was calibrated between 0 and 30 cm H_2O. Total differential pressure was recorded immediately before each imaging session by recording 15 minutes of data, stopping flow, and recording 15 more minutes of data. The middle 10 minutes of each recording was averaged in order to eliminate start and stop artifacts and then subtracted in order to get the reported differential pressure for each time point. Calibrating to the zero flow state (known zero differential pressure) at each time point was necessary in order to account for the observed systematic drift in the pressure data that occurred over longer time scales (tens of hours).

After each experiment the flow cell was flushed with 10 mL of 10% v/v bleach solution at 1.0 mL/h and precipitates were dissolved with a 10% (v/v from concentrated HCl) HCl solution at 1.0 mL/h until the precipitates had dissolved (approximately 24 h). The bleach solution was effective at removing biofilm as confirmed by microscopy and the precipitates readily dissolved in the acid solution. All parts of the experimental system were flushed with deionized water as the final step. A diagram of the experimental system can be found in Figure 21.

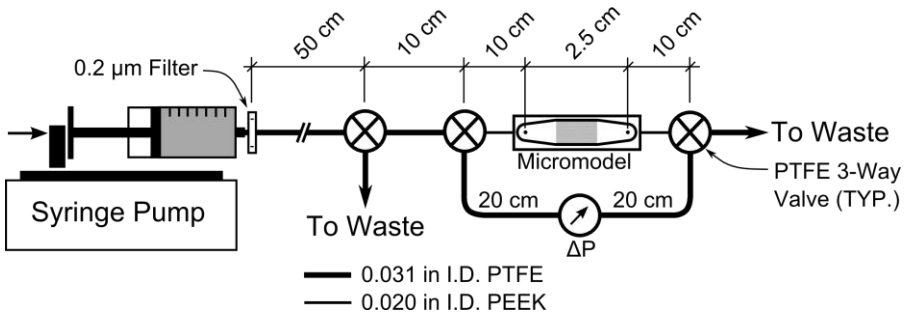


Figure 21. A schematic of the experimental setup. After inoculation flow of sterile medium was maintained by a syringe pump through a 0.2 µm filter to prevent contamination of the media reservoir. One three-way valve was used to direct flow directly to waste for flushing the influent tubing and the other two three-way valves were used to make the connection to the differential pressure transducer. The micromodel, valves and the pressure transducer were mounted to a polycarbonate microscope stage adaptor (not shown) for ease of imaging.

Confocal Microscopy and Image Analysis

Biofilm and mineral deposits were imaged using a Leica TCS SP5 II DM6000 CS upright confocal microscope (Leica Microsystems, DE). Images were collected through a Leica HC PL FLUOTAR 10×/0.30 dry objective and 3D confocal stacks were taken at each location. 40 stacks (8 frames by 5 frames) were taken to image the entire porous media section of the micromodel with a 10% horizontal overlap. Stacks were collected with a vertical slice thickness of 11.066 µm. The individual stacks were merged into a single large dataset automatically by the microscope software. The resulting voxel dimensions were 3.027 µm × 3.027 µm × 5.533 µm.

The GFP signal of cells within the biofilms was imaged using the excitation from the 488 nm laser and photomultiplier tube (PMT) detection between 500 and 700 nm. The natural autofluorescence of calcium carbonate (Yoshida et al., 2010) was utilized to image the precipitates with excitation from a 405 nm diode laser and PMT detection

between 415 and 550 nm. Overlapping signal was addressed by image subtraction. When gas bubbles were present (their presence was obvious by qualitative inspection), reflection images were also collected with illumination with the 488 nm laser line and detection between 478 and 498 nm. Images were collected with 3x frame averaging to eliminate signal from moving (unattached) objects and the channels were collected sequentially.

The 3D datasets were imported to the open source software FIJI (Schindelin et al., 2012). The data was flattened in the vertical (z) dimension by performing a maximum intensity projection, which transformed the data into two dimensions. The 2D images were rotated if required using bilinear interpolation and the image was cropped to only contain the porous media region. The cropped and rotated images were thresholded using the automatic triangle method (Zack et al., 1977) to separate signal (GFP or precipitate) from the background (porous media features and liquid). The precipitate also fluoresces under the same imaging method as the GFP so the precipitate channel image was subtracted from the GFP channel image to eliminate redundant signal. This asserts the assumption that precipitate and biofilm are discrete phases and that any location where there is precipitate signal cannot be occupied by biofilm. Gas bubbles were extracted from the reflected light image by thresholding and any redundant signal was eliminated by image subtraction. Binarized images were quantified for the volume occupied by biofilm, precipitate and gas assuming that pixel containing signal occupied the entire micromodel depth.

The binarized images were translated into 2D isosurfaces (surfaces composed of adjacent triangles) using the FIJI plugin BoneJ version 1.3.14 (Doube et al., 2010) with a subsampling factor of 6 to reduce geometric complexity. The reduction of geometric complexity was found to be required for reactive transport model stability. The surfaces from the BoneJ analysis were exported to AutoCAD 2103 (Autodesk, USA), where they were aligned to the pore structure of the micromodel so that the image containing porous media, precipitate, biofilm and gas phases could be imported to the reactive transport model.

Reactive Transport Simulations

A steady state, 2D, pore-scale reactive transport model was constructed in COMSOL Multiphysics version 4.3a (COMSOL Inc., USA). The purpose of the model was to provide insight into the chemical and physical conditions within the reactor; specifically, the local urea concentrations and hydrodynamics. The surfaces obtained from the image analysis were imported into the model and boundary conditions were imposed. Incompressible Navier-Stokes equations were solved in the liquid and biofilm domains using a shallow channel approximation. The conservation of momentum equation then becomes

$$\rho(\mathbf{u}\cdot\nabla)\mathbf{u} = \nabla\cdot\left[-p\mathbf{I} + \mu\left(\nabla\mathbf{u} + (\nabla\mathbf{u})^{T}\right)\right] - 12\frac{\mu\mathbf{u}}{d_z^2}, \qquad (71)$$

and the conservation of mass equation remains as normal ($\rho\nabla\cdot\mathbf{u} = 0$). $\boldsymbol{u}$ denotes the 2D velocity vector, p is the pressure, μ is the dynamic viscosity, ρ is the fluid density, $\mathbf{I}$ is the identity tensor and d_z is the channel thickness, which is the etched micromodel thickness

of 18.137 μm. Here, the "T" superscript indicates a transpose. The viscosity of the biofilm domains was chosen to be six orders of magnitude higher than water. This effectively made the biofilm phase immobile and non-porous with only diffusive solute transport taking place. It was assumed that trapped gas was immobile as well (i.e. no two phase flow was considered), and that there was no flow in the precipitation domains. Urea transport was calculated by advection due to the Navier-Stokes flow field and Fickian diffusion such that

$$\nabla \cdot \left(-D_{urea} \nabla C_{urea} \right) + \boldsymbol{u} \cdot \nabla C_{urea} = r_{urea}, \qquad (72)$$

where D_{urea} is the diffusion coefficient for urea which is 1.38×10^{-9} m^2/s in pure water at 25ºC (Cussler, 1997). C_{urea} is the local urea concentration and r_{urea} is the urea hydrolysis rate. Urea hydrolysis follows a first-order rate relationship where

$$r_{urea} = -k_{urea} C_{urea}. \qquad (73)$$

The urea hydrolysis rate is linearly proportional to urea concentration for the concentration range considered here. The rate constant k_{urea} has been estimated to be 23.2 ± 6.2 h^{-1} for MJK2 biofilms (Connolly et al., 2015).

For flow, inlet and outlet boundary conditions are fixed flow rate and fixed pressure, respectively. All other boundaries are no-slip and no flux with respect to flow. For solute transport, C_{urea} was held constant at the inlet and flux conservation is maintained at the outlet. The entire reactor was modeled (as opposed to just the porous media section) in order to ensure that the proper hydrodynamics are represented but the following results focus on only the porous media section. Significant biofilm,

precipitation or gas accumulation was not observed in the influent or effluent regions of the reactor during these experiments.

Results and Discussion

Imaging and Image Processing

The images collected in this study were successfully thresholded, quantified and transformed into a form that was suitable for importing into reactive transport modeling software. Figure 22 shows images obtained from a representative section of porous medium along with a visual representation of the processing that was carried out. The processing illustrated in Figure 4 was done for the entire porous media section for each experiment. All raw and thresholded images can be found in Appendix C.

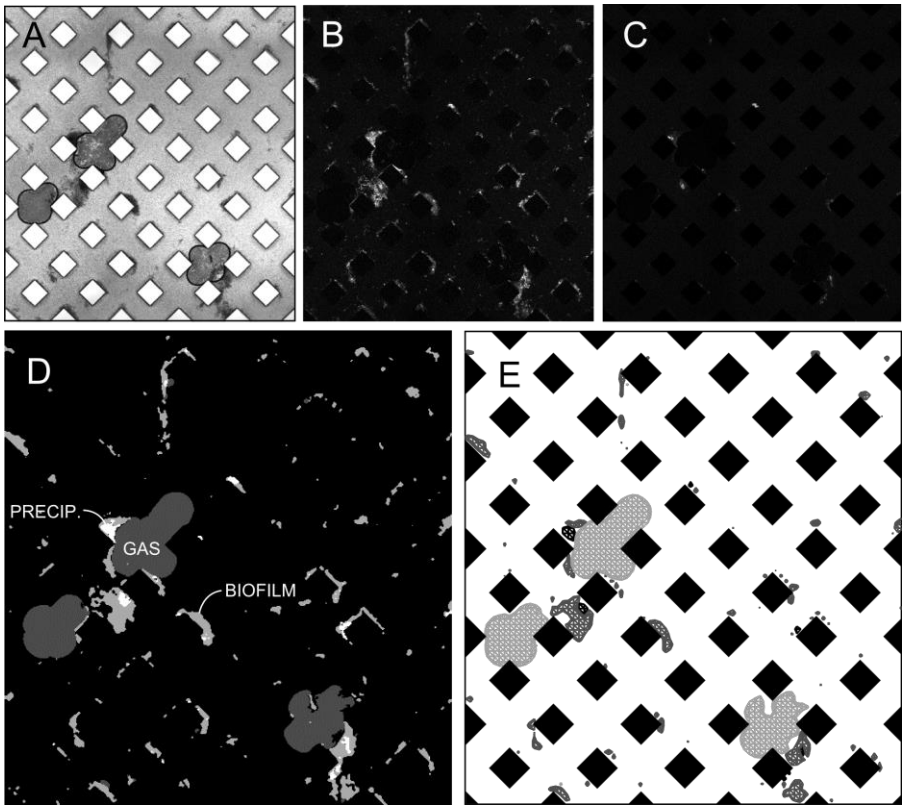


Figure 22. A representative section of porous media from reactor run 9-24 near the middle of the porous media region. The porous media elements are 100 µm square and flow is from top to bottom. (A) Reflected light image. (B) GFP biofilm fluorescence image. (C) Precipitation autofluorescence image. (D) Composite thresholded image showing the signal from gas, biofilm and precipitation. (E) Digitized surfaces used in the reactive transport modeling with porous media elements in black and the other phases in shades of gray.

Porosity and Permeability Reduction

The extent of permeability and porosity reduction varied strongly with calcium injection timing rather than with flow rate. The greatest porosity and permeability reduction occurred when calcium was introduced directly after inoculation and the least occurred when calcium was added starting 24 hours after inoculation. The experiments where calcium was absent had a moderate amount of plugging due to biofilm

accumulation alone. Gas bubbles only appeared in the flow experiments, in which calcium was added to the system at inoculation at the lowest flow rate. Figure 23 shows the volumes occupied by each component as determined from the thresholded confocal microscopy images.

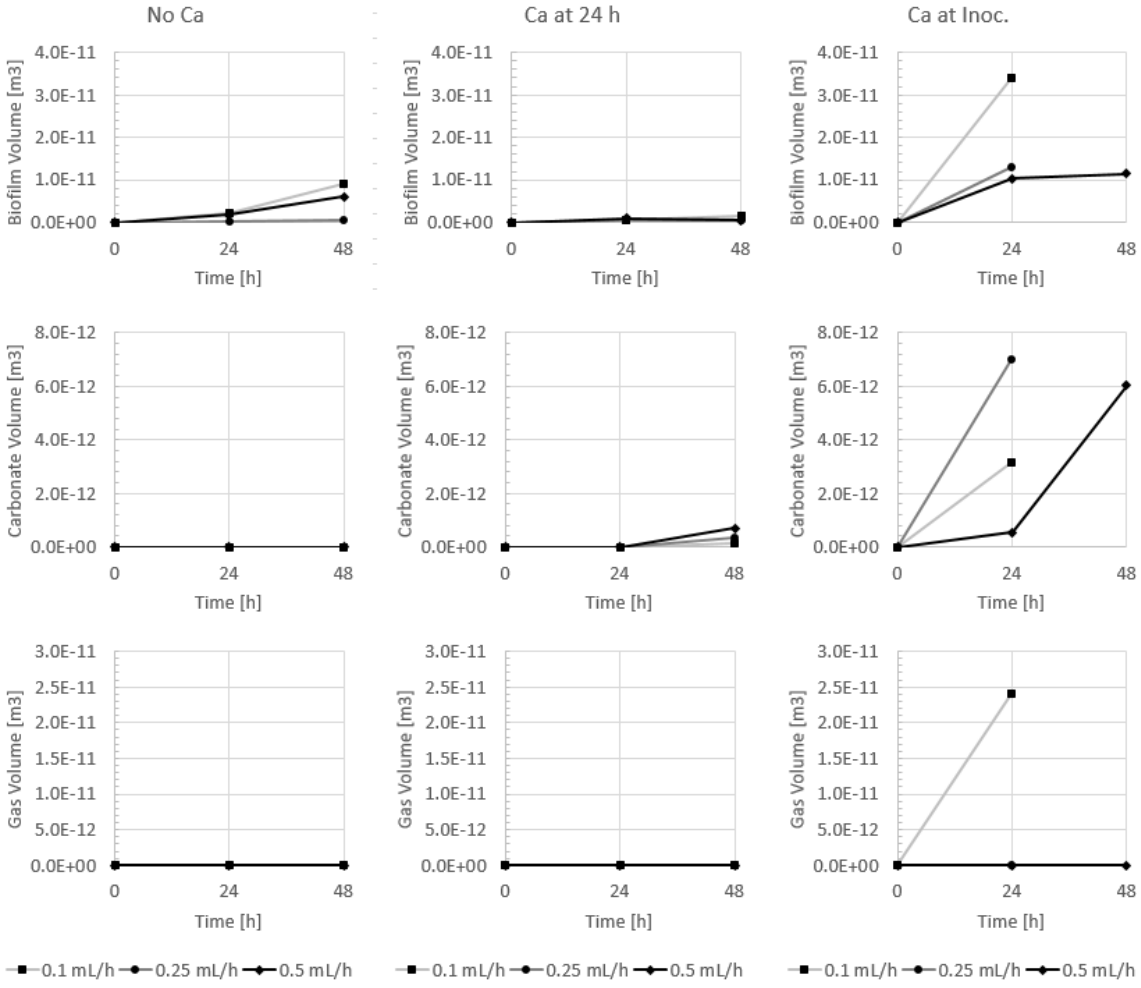


Figure 23. Volumes of biofilm, precipitate and gas bubbles as determined by the analysis of confocal scanning laser microscopy images.

The reason for more pore blockage when calcium is added directly after inoculation is likely to be from two factors. First, the inoculum has a high pH and

generally has chemical conditions that are conducive for carbonate precipitation so when a medium containing calcium replaces the inoculum in the reactor rapid precipitation is expected. The second factor is that the presence of calcium is likely to make biofilm EPS more resistant to detachment by crosslinking polysaccharides, making for a stronger biofilm (Chen and Stewart, 2002).

There are two distinct methods available for the determination of differential pressure across the porous media section of the micromodel so that permeability reduction could be quantified; we chose to use a combination of the two. The tools available are the reactive transport model and the direct measurement using the differential pressure transducer. The reactive transport model can be utilized by extracting an average pressure at the influent and effluent ends of the porous media section and subtracting the two numbers yielding a differential pressure. The differential pressure just due to the porous media can also be determined by the transducer reading but corrections due to pressure losses in tubing and the influent and effluent regions must be applied. Here we chose to estimate the differential pressure across the porous media section of the micromodels using a combination of modeling and the experimental observations.

First, the pressure drop was measured in the clean reactor at each of the experimental flow rates of 0.1, 0.25 and 0.5 mL/h of sterile medium. The pressure drop across the porous media section of the micromodel was then calculated using the finite element model of the clean reactor. Line averages at the influent and effluent sides the porous media section were used to calculate the pressure drop in the model. The

experimental dataset had a higher pressure drop at all flow rates because of the additional pressure loss occurring in tubing, the influent and effluent regions of the micromodel. The difference between the two differential pressures was then assumed to be the pressure loss due to non-porous media elements of the system. The pressure loss in the non-porous medium sections was determined to be 367, 917 and 1834 Pa for 0.1, 0.25 and 0.5 mL/h respectively.

The pressure drop was used to calculate permeability (k) according to Darcy's law where

$$Q = \frac{-kA\left(P_{eff} - P_{in}\right)}{\mu L}, \qquad (74)$$

and Q is the volumetric flow rate, A is the cross-sectional area of flow, μ is the dynamic viscosity, P_{eff} and P_{in} are the effluent and influent pressures respectively. L is the linear distance over which the pressure drop occurs. Permeability reduction was observed in all experiments and generally followed the same trend as the porosity data with greater porosity reduction correlating to greater permeability reduction. Figure 24 shows porosity and permeability reduction over time for all the treatments.

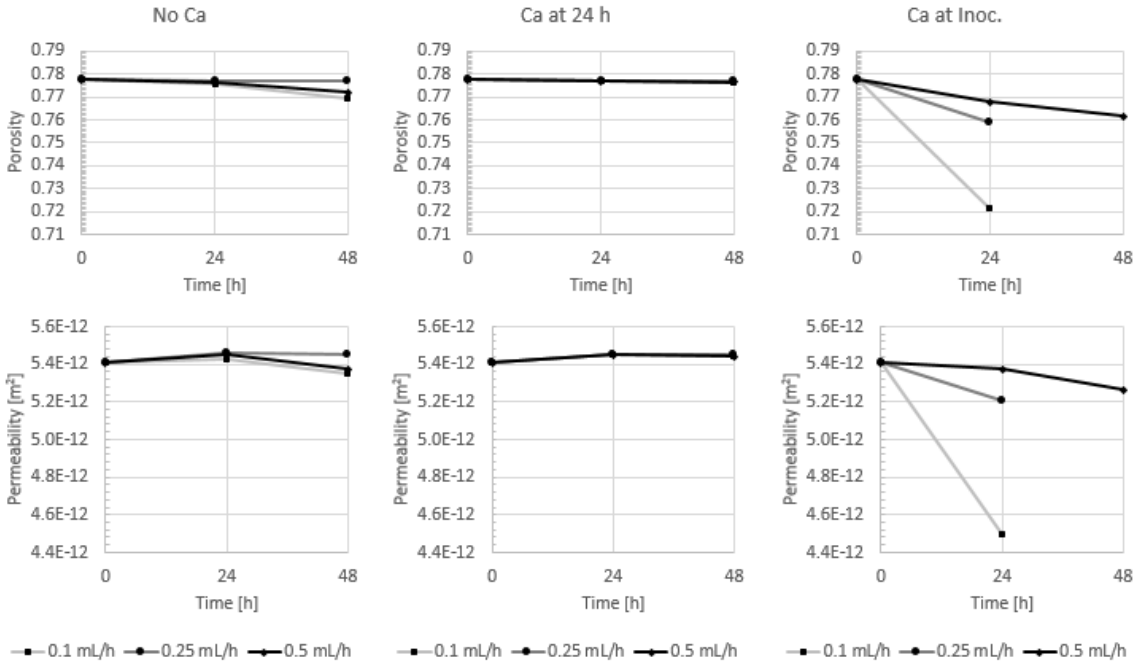


Figure 24. Porosity and permeability reduction over time from the micromodel experiments. Porosity was estimated from the thresholding of confocal microscopy images and permeability was estimated from differential pressure data.

Porosity-permeability relationships have been explored for carbonate containing materials in relation to petroleum extraction (Ehrenberg and Nadeau, 2005) and carbon sequestration (Zhang et al., 2010a). Relationships have also been explored that relate pore space occupied by biofilm (Cunningham et al., 1991) or precipitation (Armstrong and Ajo-Franklin, 2011) to permeability reduction independently. The aim of this analysis was to explore the behavior of the porosity-permeability curve when both biofilm and mineral formation is occurring, which to the authors' knowledge has not been investigated before explicitly. Such a relation between porosity and permeability is of great interest for both models and applications of microbially induced calcite

precipitation, since it is often researched as a leakage mitigation technology, where the reduction of permeability is the main goal.

A common porosity-permeability relationship is the Kozeny-Carman (K-C) model that represents permeability as a function of porosity from first principles (Carman, 1937; Carrier, 2003; Kozeny, 1927). Although there are other relationships used for the same purpose, Kozeny-Carman often serves as the basis for those relationships (e.g. Costa, 2006) so it will be the basis for the analysis here. In its most general form, Kozeny-Carman can be written as

$$k = C_{K-C}\frac{n^3}{1+n}, \qquad (75)$$

where $C_{K\text{-}C}$, is an empirical coefficient and n is porosity. In the form presented in Equation 75, $C_{K\text{-}C}$ is a multi-factor variable that is a function of fluid properties (density and viscosity predominantly) and physical properties of the porous medium including the specific surface area, tortuosity and other factors which have been the topic of much research over the last century (Carrier, 2003; Costa, 2006; Ehrenberg and Nadeau, 2005). More often the change in porosity needs to be related to the change in permeability. Reaction rates (precipitation or dissolution of carbonates in this case) can be estimated and translated into a net change in porosity. Reactive transport models must be able to translate this porosity change to a permeability change at each time step because the two parameters are strongly linked. An inaccurate estimation of permeability change leads to inaccurate solute transport and hydrodynamic calculations, thus potentially leading to an inaccurate estimation of reaction rates in subsequent time steps. Error is then

compounded in each time step that can lead to a significant amount of error a later time steps.

A convenient relationship can be written if all parameters in Equation 75 are assumed to be constant except for porosity:

$$k = k_0\left(\frac{n - n_{crit}}{n_0 - n_{crit}}\right)^{i_{K-C}} \quad \text{if} \quad n > n_{crit},\ k = 0 \text{ otherwise,} \qquad (76)$$

where k_0 and n_0 are the initial permeability and porosity, n_{crit} is the critical porosity where the medium becomes impermeable and $i_{K\text{-}C}$ is a parameter which is dependent on both the fluid and porous medium properties (Ebigbo et al., 2012; Xu et al., 2004). The initial porosity and permeability are generally known leaving n_{crit} and $i_{K\text{-}C}$ to be estimated. n_{crit} can be difficult to estimate but in many cases, and in these experiments, it will be much lower than the range of expected porosities and can be assumed to be zero (Ebigbo et al., 2012). The exponent, $i_{K\text{-}C}$, is generally used as a fitting parameter. It has the effect of making permeability more sensitive to porosity changes. Literature values for $i_{K\text{-}C}$ are not widely available but for geologic materials values between 1 and 10 have generally been estimated (Xu et al., 2004) with $i_{K\text{-}C} = 3$ being the most common value used in Darcy-scale models (Ebigbo et al., 2012).

Figure 25 shows a plot of porosity versus permeability for all data points collected in this study. A K-C relationship was fitted to all of the data. Taking all data points into account, the best fit was achieved with $i_{K\text{-}C} = 62.0$ (and $n_{crit} = 0$) by minimizing the sum of the squared errors using the generalized reduced gradient (GRG) nonlinear optimization technique (Lasdon et al., 1978).

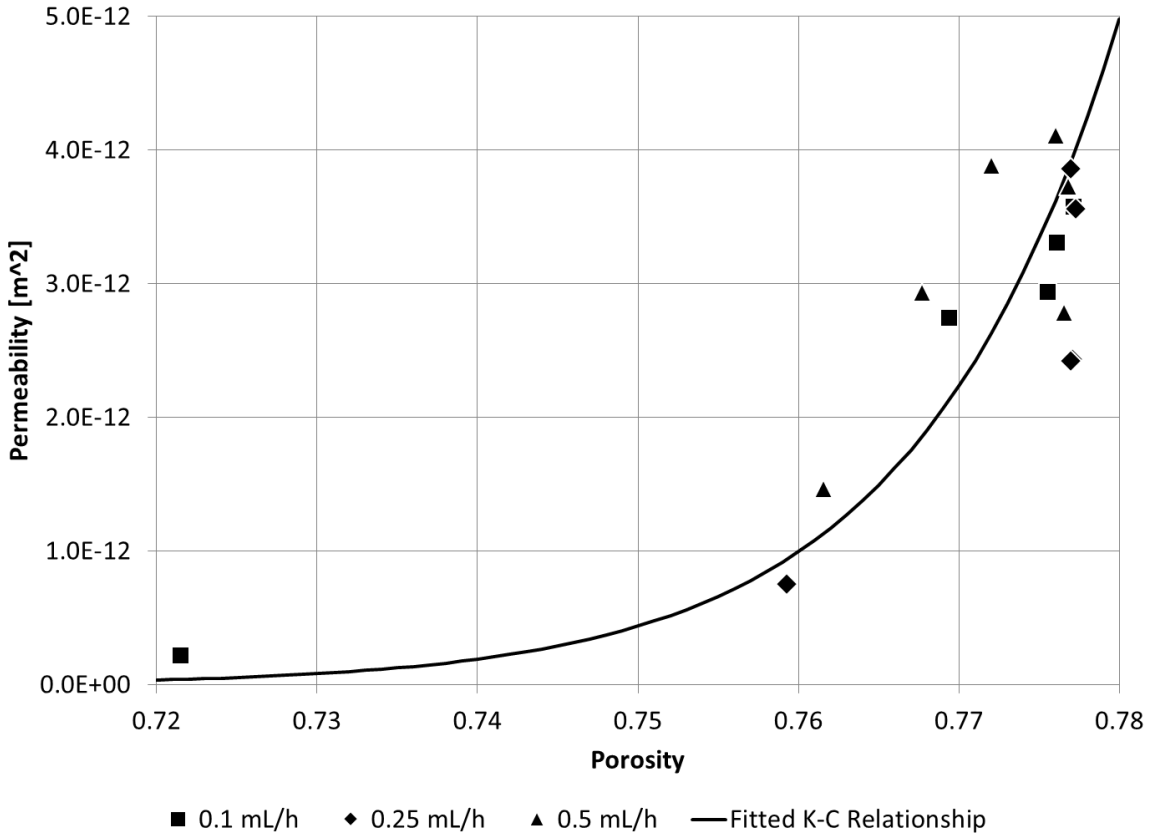


Figure 25. Porosity vs. permeability for the different conditions with fitted parameters.

The fitted $i_{K\text{-}C}$ is larger than was expected and this could be due to a number of factors. The K-C model has been shown to underestimate permeability reduction in geologic porous media with permeability being highly dependent on small porosity changes (Pape et al., 2012). This is, however, usually explained by small-scale heterogeneity where small changes in porosity causes pore isolation and changes in tortuosity. In this study, there is no evidence of such behavior because no channeling was observed.

In this study, the net volumes of each pore-occupying component are calculated and used to estimate total porosity changes. The estimation of gas and precipitate volume are relatively straightforward but biofilm volume is not. Biofilm is generally heterogeneous (Stoodley et al., 1999). In this study, GFP fluorescence was used as a marker for the presence of biofilm. This has two inherent assumptions: (1) all bacterial cells within the biofilm are active and producing GFP and (2) the entire biofilm volume contains cells. Precautions have been made to ensure that these assumptions apply by using bacteria with a relatively high growth rate and the experiments were not conducted over a long period of time. The high growth rate and short experiment time reduces the likelihood of extracellular polymeric substances (EPS) being transported away from the cells that excreted them. This is because cells are expected to be dividing quickly rather than producing large amounts of EPS on the experimental time scale.

Another assumption that must be investigated is that the micromodels are well approximated in two dimensions. The two-dimensional assumption is made routinely for experiments done in micromodels (Karadimitriou and Hassanizadeh, 2012; Knutson et al., 2005; Willingham et al., 2008; Zhang et al., 2011) but here, neglecting the third dimension has the potential to affect the results considerably. The existence of flow over and under pore blocking constituents rather than around them is the primary factor that would contribute to inaccuracy. To investigate the possibility, high-resolution three-dimensional confocal microscopy images were taken to see whether the entire depth of the micromodel was being filled with pore blocking constituents. These images showed full z-dimension occupation of pore space which adds to the evidence that dimensional

compression is not a significant source of inaccuracy. These results are consistent with the findings of Zhang et al. (2010) who conducted similar experiments with precipitation only and found the z dimension to be fully occupied. It is possible that some areas of the micromodel are fully occupied in the z-dimension, as discussed above, while other areas are not; but, qualitative observations predict that the majority of the data agrees with the assumption that was made.

The effect of physical boundaries on the analysis (edge effects) must also be considered as a source of error. In the third (z) dimension, the experimental volume is bounded by two flat plates, causing resistance to flow. This resistance to flow is inherently included in the differential pressure measurement. In typical 2D analyses the domain is assumed to be infinite in the third dimension. Here the third dimension is finite and known. The top and bottom boundaries may not allow for the Darcy-scale analysis conducted here. In order for exact parameter estimation, an experimental control volume must be bounded such that the boundaries of the volume do not affect the behavior within the volume. Taking a column experiment as an example, the column should be of sufficient diameter such that the impermeable outer radius does not affect the flow in the porous media. A higher volume to boundary area ratio is desirable in order to achieve accurate results as long as correct inlet and outlet conditions can be maintained.

Consider a typical triaxial chamber commonly used to test soil permeability. A typical sample diameter is 6.35 cm (2.5 inches). This results in a volume to outer boundary area ratio of 1.59 cm. This can be compared to the volume to outer boundary ratio for the micromodel in this work which is 9.01×10^{-4} cm. It is likely that this is the

reason for the higher than expected sensitivity of the K-C model fit (high $i_{K\text{-}C}$). For this reason, the correlations made between porosity and permeability should be considered relative rather than absolute. In order for an accurate field-relevant relationship a similar set of experiments would have to be conducted in larger systems. Currently high resolution images of such larger systems are difficult to collect but as technology progresses high resolution 3D data may become attainable for systems containing biofilm. Discrepancies between permeabilities calculated from 2D and 3D data have also been described elsewhere (Beckingham et al., 2013) so this is indeed an important consideration.

Preliminary Study of Long-Term Behavior

In order to explore the behavior of MICP over longer time periods, the last experiment in this set of experiments was observed for 7 days after the flow was stopped. A common question to the efficacy of MICP in the subsurface is the possibility of dissolution. It is also of interest what happens to the quantities of pore blocking constituents over time and when flow has stopped. Figure 26 shows the volumes of biofilm, precipitation and gas over time along with total porosity change in an extension of experiment 9-48.

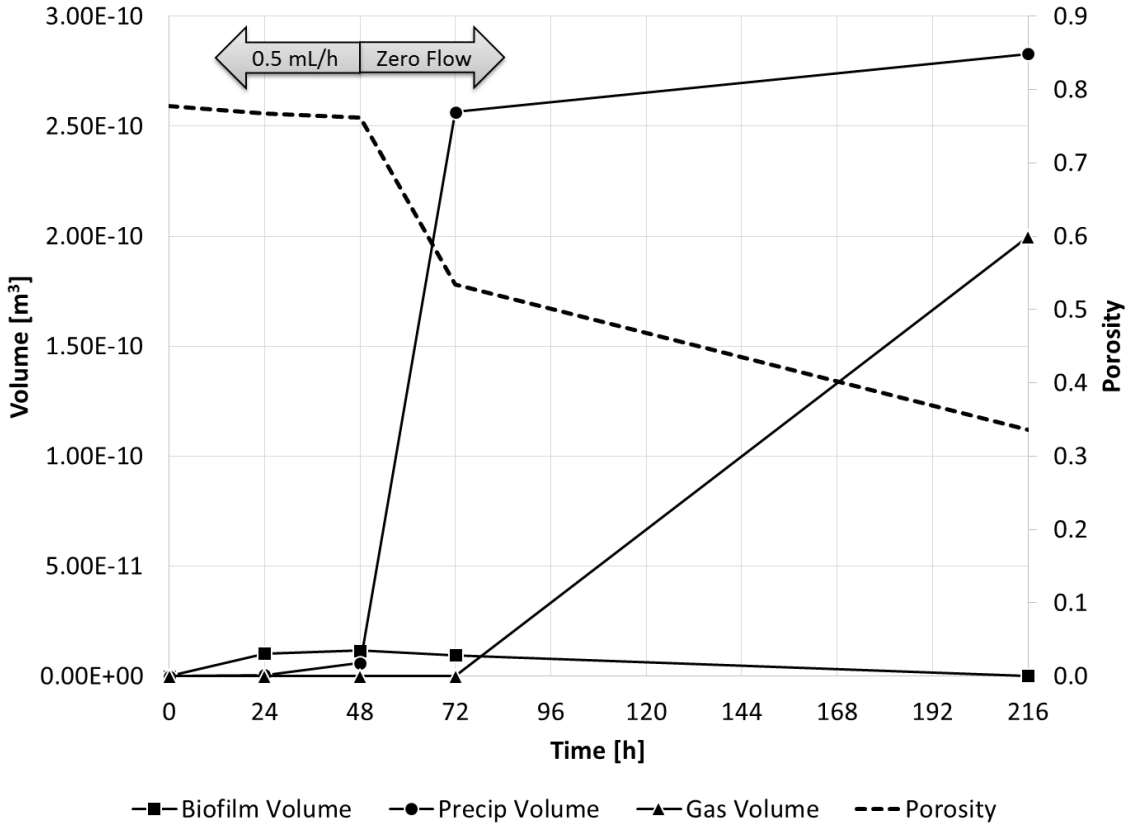


Figure 26. Biofilm, precipitate and gas volumes along with porosity versus time in an extension of experimental run 9 where flow was shut off and the reactor was imaged at 72 and 216 hours.

After flow was stopped biofilm volume decreased, precipitation volume increased and gas bubbles appeared, blocking a significant amount of pore space. Each of these results fit with conceptual models proposed by others (Cuthbert et al., 2012; Ferris et al., 1996; Tobler et al., 2011). In this longer term experiment (9 days), calcium was always supplied to the system but the most precipitation only occurred after flow was stopped. The significant precipitation during the no flow period was accompanied by a steady decrease in the GFP signal detected from the biofilm. This decrease in signal is likely to

be due to inactivation of the biofilm rather than its disappearance. Biomass inactivation has two probably mechanisms here. The first is inactivation due to cell encapsulation where precipitates encase cells (Cuthbert et al., 2012). The cells cannot exchange metabolites with their environment so they can be considered inactive and can then be included in the precipitate volume. The second biomass inactivation mechanism is simple starvation. In this study it is likely that oxygen is depleted soon after flow is stopped. GFP also requires oxygen to produce a fluorescent signal (Hansen et al., 2001) and it has also been shown that urease activity also decreases when oxygen is unavailable (Whiffin et al., 2007) although urea hydrolysis can carry over for a period after oxygen depleted (Tobler et al., 2011).

The explanation of the appearance of gas bubbles in the pore space is less obvious. The origin of the gasses is most likely microbial metabolism and thus is likely consisting of CO_2 or NH_3. Here, gas bubbles were observed only in the zero flow and low flow rate experiments. The simplest explanation is that during low mass transport experiments, the solubility of gaseous metabolic products is exceeded and gas bubbles form. Another possible explanation for the appearance of gas bubbles is through the system of inorganic chemical reactions taking place. This was investigated through the use of a PHREEQC equilibrium model (Parkhurst and Appelo, 1999) which did not predict super-saturation of any gasses for the conditions present in this study (see Appendix D for model output).

It is possible that non-equilibrium behavior (both organic and inorganic) might be responsible for gas bubble formation but this possibility has yet to be explored in detail.

Qualitatively we can expect gas bubble formation during stagnation due to the production of inorganic carbon from microbial activity coupled to pH decrease from organic acid production if the biofilm is anaerobic and carrying out fermentation. The decrease in pH would favor CO_2 outgassing. The system would be buffered by the carbonate system but low pH CO_2 outgassing would be possible theoretically.

A detailed kinetic analysis of inorganic carbon speciation for MICP systems would be very useful here leaving room for others to contribute to this topic. A model similar to that of Mitchell et al. (2009) would be useful where CO_2 is not being dissolved but rather being generated by microorganisms and allowed to precipitate. It should be noted here that in the Mitchell et al. (2009) model one of the slower kinetic steps in the system of reactions is the hydration of dissolved CO_2 to form carbonic acid. If CO_2 bubbles form, they are likely to be slow to redissolve. It is typically assumed that the inorganic reactions happen quickly in relation to the microbially mediated reactions (e.g. Radu et al., 2014; Zhang and Klapper, 2011) but if enough CO_2 is generated by microbial processes it may be possible that the relatively slow dissolution of CO_2 into solution may have to be taken into account for the accurate estimation of porosity in MICP systems. The behavior observed in the zero flow experiment points to the promise of pulsed injection strategies for field applications (Ebigbo et al., 2012; Lauchnor et al., 2013) but this study shows that the formation of gas bubbles may need to be considered if the resting phase is long (on the order of 24 hours).

Pore-Scale Reactive Transport

The pore-scale reactive transport model was able to predict how the flow rate and calcium addition timing affects urea concentration, reaction rate and pore velocities within the reactor. The predicted average urea concentration varied inversely with pore fluid velocity and both of these factors (urea concentration and pore fluid velocity) appear to be correlated with the timing of the calcium addition rather than flow rate. Figure 28 shows data extracted from all of the modeled experimental runs with average urea concentration in the porous media section of each micromodel over time. The model does not predict that urea would be depleted locally within the biofilm for the conditions tested. The reactor in the study was small so it is reasonable to expect that the local urea concentrations do not vary greatly (see Chapter 4). Despite geometric heterogeneity caused by biofilm and precipitates within the micromodels, urea concentrations remain rather homogeneous (for example ≈ 5% variation in urea concentration in Figure 27).

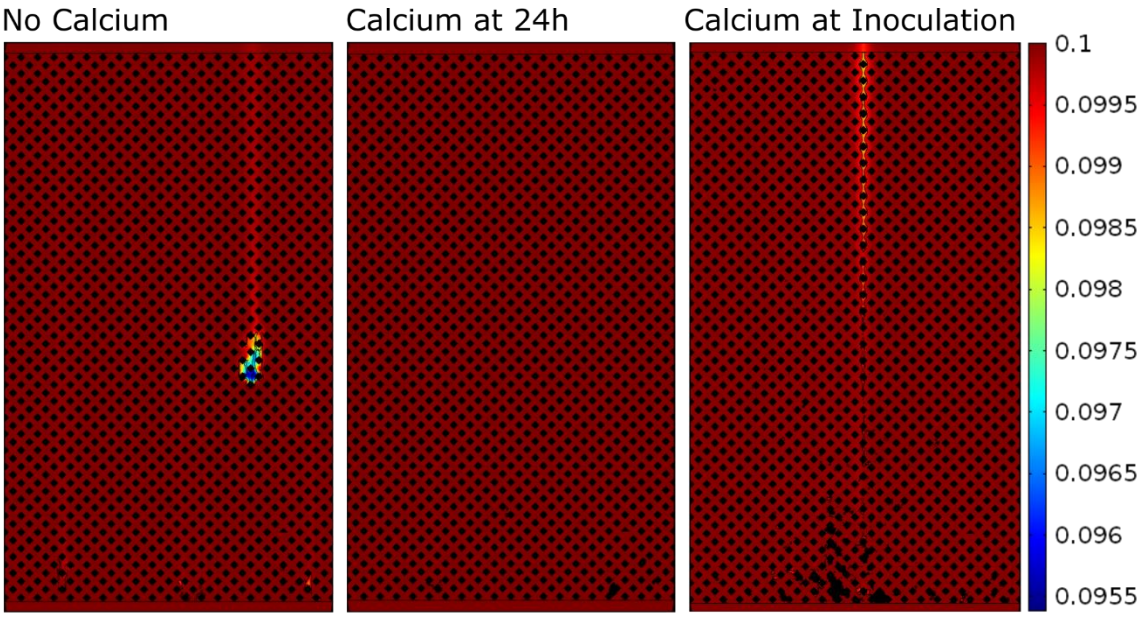


Figure 27. Modeled urea concentration maps (in mol/L) at 48 hours for all three 0.5 mL/h experiments (3-48, 6-48 and 9-48). The results here are representative of those found in all experiments. We found that "no calcium" and "calcium at inoculation" experiments showed lower urea concentrations and thus higher overall reaction rates than experiments where calcium was added 24 hours after inoculation. Flow is from bottom to top and black represents solid elements (precipitates and porous medium elements).

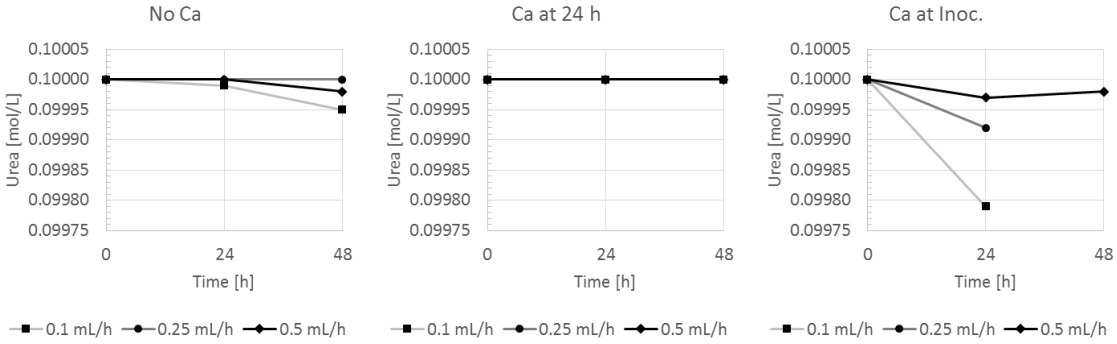


Figure 28. Modeled average urea concentration in the porous media section versus time. Note that the two 48-hour time points were excluded from analysis on the far right plot due to plugging (7-48 and 8-48)

Figure 29 shows the average and maximum pore velocities predicted in this work. Average pore velocities are predicted to change little for the conditions tested however maximum pore velocity is predicted to change significantly. This is likely due to heterogeneous pore blockage where large areas remain largely unchanged but others have significant blockage. Figure 27 shows evidence of such behavior with the majority of the observed porosity reduction concentrated locally rather than dispersed throughout the experimental domain. Note that the values reported here calculated from averages and maxima of element by element absolute velocity magnitudes within the porous medium region of the micromodel.

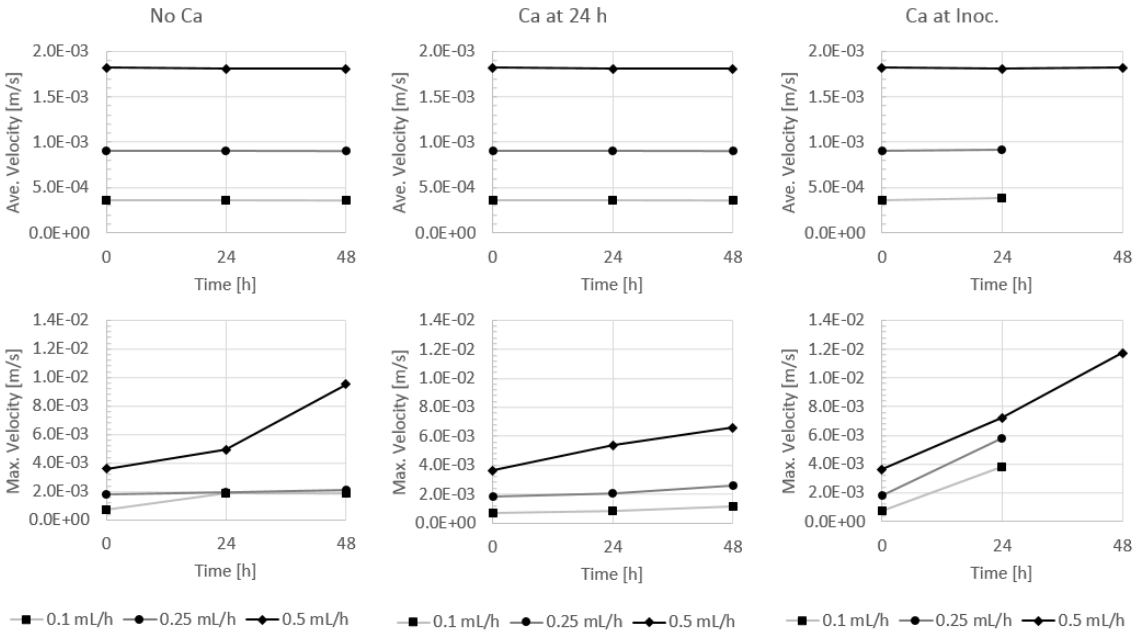


Figure 29. Modeled average and maximum pore fluid velocities the porous media section versus time.

Conclusions

In this work we have been able to provide pore scale observations of biofilm-induced calcium carbonate precipitation and link those observations to behavioral trends that would be useful in field applications. The porous media micromodels allowed for the collection of high resolution images of pore blocking constituents (biofilm, mineral precipitation and gas bubbles) and estimate the porosity reduction due to differences in biofilm, precipitate and gas bubble accumulation in the porous media micromodels. Additionally, direct differential pressure measurements, along with a finite element model, allowed us to observe permeability reduction in the same set of experiments. Biofilm-specific urea hydrolysis kinetics were incorporated into the finite element model in order to predict how homogeneous solute concentrations are likely to be in MICP systems.

The two variables that were investigated were (1) flow rate and (2) the time at which calcium was added to the system. Results show that the timing of the calcium addition had the greatest effect on permeability and porosity reduction and as a result also had the greatest effect on the reactive transport environment in the reactor (see Figures 5,6 and 10). Results varied with flow rate but no definitive correlation can be made (i.e. higher flow rates did not correlate to more pore blockage and vice versa). One useful qualitative observation was made regarding flow rate and the appearance of gas bubbles. Gas bubbles appeared only during low flow or zero flow time points. This suggests that the accumulation of gaseous metabolic byproducts may play an important role, in

addition to the transport of reactants to the system. Permeability reduction via gas bubbles is not long term in most cases and should therefore be avoided when permanent permeability reduction is desired. Until now, to the authors' knowledge the possibility of gas formation in ureolytic MICP has not been directly observed.

The results shown here have important implications for field applications of urea-hydrolysis-driven MICP for permeability reduction. If a section of the subsurface needs to be hydraulically isolated, and it is determined that MICP will be used, there are many design parameters that must be considered. Among these parameters are the flow rate at which injection fluids are introduced and the timing of these additions. The analysis conducted here suggests that the timing of the calcium addition is likely to be the most important parameter tested in this study. Here we have shown that if calcium was added 24 hours after inoculation little permeability reduction would be achieved. If a pulsed injection strategy is chosen, the timing between zero flow and low flow events may also be of high importance due to the possibility of stagnation causing the formation of gas bubbles. Gas bubbles are undesirable if a quickly-established and long-lasting barrier is the goal. Gas bubbles can block pore spaces, thus decreasing the permeability, but potentially only transiently. The work presented here indicates that when permeability reduction is the primary goal, calcium injection at a moderate flow rate followed by a resting period of less than 24 hours is advised assuming that the microbial kinetics are similar to those in this study.

CHAPTER 6

INDIVIDUAL-BASED MODELING OF BIOFILM-INDUCED CALCIUM CARBONATE PRECIPITATION

Background, Rationale and Objectives

Background

Microbially-induced carbonate precipitation (MICP) is a relevant process in many engineered and natural systems. MICP has been researched for its use in engineered systems including, geologic carbon sequestration, radionuclide remediation, soil stabilization, permeability manipulation and a number more (De Muynck et al., 2010; Ferris et al., 1996; Fujita et al., 2000; Whiffin et al., 2007). Natural systems, including the earth's global carbon cycle and ocean chemistry have been affected by bacterial precipitation of calcium carbonate (Riding and Liang, 2005). Microbial carbonates, including those prodiced by biofilms, have a consistent presence throughout the geologic record and are widely distributed, making them important for the understanding global carbon cycling (Riding, 2000; Vasconcelos et al., 1995). The medical community is also interested in MICP in the context of kidney stones, ureteral stents and catheters (Morris et al., 1999). Even with the extensive body of literature and interest in MICP, specific mechanisms of how microbes induce mineral formation spatially and temporally are still unclear and are of interest to the field.

There are many microbial metabolisms that are able to induce the precipitation of carbonate minerals but urea hydrolysis is the specific metabolism targeted in this work.

See Chapter 2 of this dissertation for additional background information regarding MICP via urea hydrolysis. The dominance of biofilm in these systems, as discussed throughout this dissertation, was also a primary factor in the construction of the model presented in this work.

Rationale and Objectives

The main goal of the model described in this chapter is to investigate the chemical environment that would be likely to develop over time under conditions that are similar to those found in the experiments described in Chapter 5. There are numerous modeling approaches that could have been utilized here but based on the experimental observations that are available an individual-based model (IBM) was the obvious choice. IBMs represent biofilms as masses of individual mobile elements which interact with each other by growing and dividing much like individual microbial cells would in a biofilm (Lardon et al., 2011; Picioreanu, 1996). The modular nature of the "cells" in IBMs also allows for different rules to be enforced for multiple types of biofilm constituents. In this case two types of "cells" are defined: biofilm and precipitate. It has been shown that IBMs can predict biofilm and precipitate behavior in similar systems (Radu et al., 2014, 2010) at reasonable computational expense so this approach was chosen. Experimental observations in Chapter 5 allowed for the high-resolution imaging of biofilm and precipitate geometries so model parameters and constitutive relationships can be tuned to fit the model to physical observations. Additionally a comprehensive reactive transport

component can be added so that the local mineral saturation environment of similar MICP systems could be estimated.

Pore-scale modeling of MICP systems will allow for the asking of more informed questions about local chemical gradients that may play important roles in long-term stability of precipitates in engineered systems. For example, one pore-scale MICP model has been developed recently at MSU (Zhang and Klapper, 2010) for simple geometries. Construction of the Zhang-Klapper model revealed a previously unknown effect in that the model predicted the presence of a self-induced electric field caused by differential diffusivities between positive and negative ions in the system (Zhang and Klapper, 2011). The effect of this electric field is thought to be faster precipitation than would be estimated if electrochemistry was neglected, as is done in most biofilm models.

Theoretical Basis

Carbonate Equilibrium

The overall effect of urea hydrolysis is pH increase from circum-neutral conditions and a shift of the carbonic acid equilibrium to carbonate (see Chapter 1). In the presence of calcium, or other divalent cations, precipitation of solid carbonate species takes place once a critical saturation state has been exceeded. The carbonate equilibrium chemistry is extremely important to the precipitation process. Most typically, only carbonic acid, carbonate, bicarbonate and solid calcium carbonate are considered in equilibrium chemistry models and lower abundance carbonate species are neglected (e.g. Ebigbo et al., 2012; Zhang and Klapper, 2010). It was hypothesized that these other,

lower abundance, carbonate species play an important role. To investigate this issue, a more complex carbonate equilibrium model was developed to be used in the model presented in this chapter.

The high ionic strength of the growth media used in these experiments also requires the use of an activity correction. The Davies equation was used to calculate activity coefficients. Figure 30 shows the predicted carbonate speciation using PHREEQC equilibrium model (Parkhurst and Appelo, 1999) with all standard thermodynamic coefficients in the native database. Figure 30 shows both the difference between concentration and activity in this particular simulation and also the importance of $CaCO_3$(aq). Precipitation is not allowed in the Figure 30 simulation so at pH above approximately 8 the solution becomes highly oversaturated and precipitation would be very likely, making it unlikely to see the concentration of $CaCO_3$(aq) that high as it is a precursor to crystal nucleation and growth (Nilsson and Sternbeck, 1999).

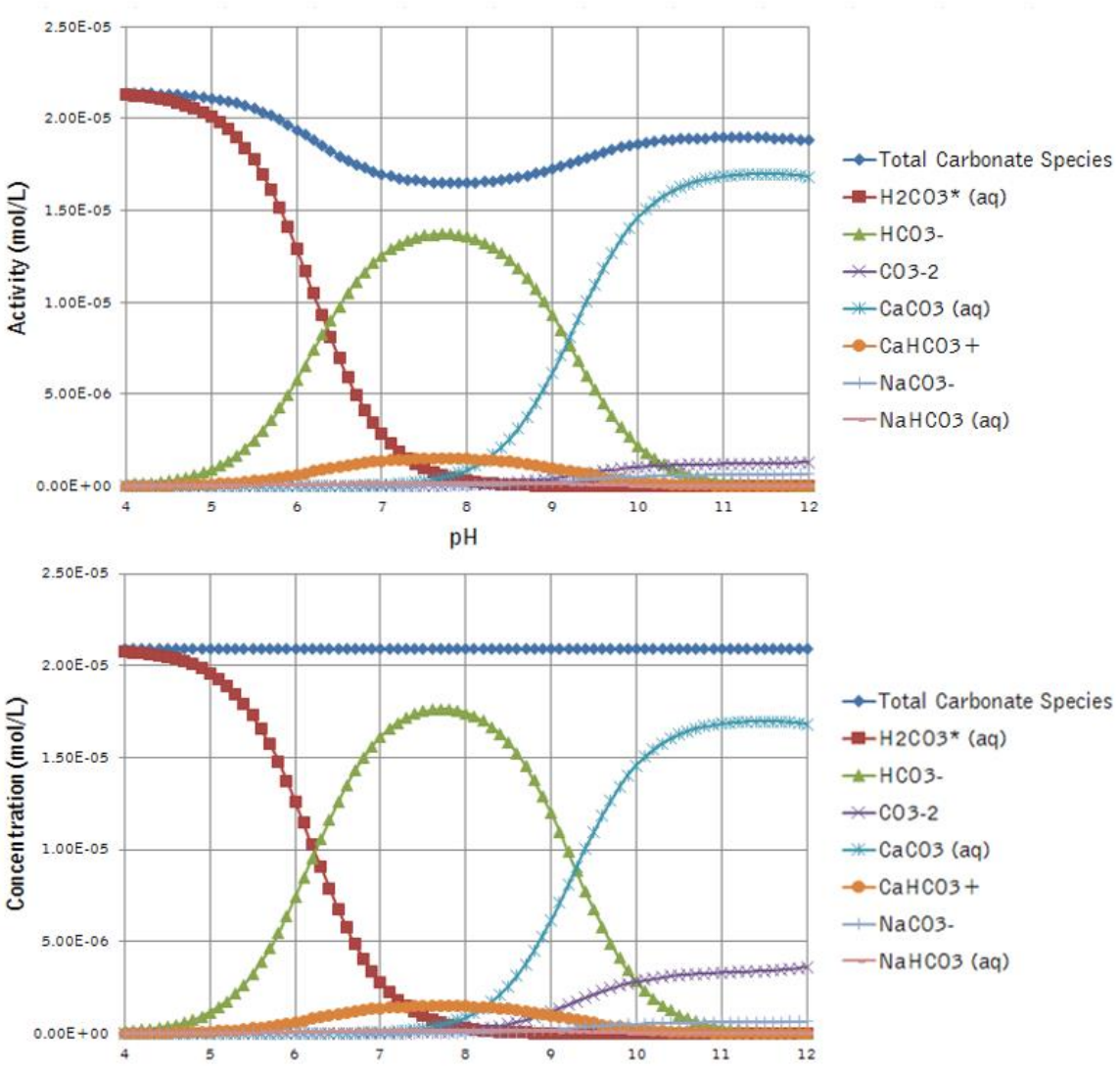


Figure 30. Carbonate speciation over a range of pH values as calculated by PHREEQC. The top graph shows activity vs. pH and the lower graph shows concentration.

This steady state aqueous equilibrium analysis showed that, at a minimum, aqueous calcium carbonate, $CaCO_{3(aq)}$, and calcium bicarbonate, $CaHCO_3^+$, needed to be included (i.e. they cannot be neglected because they are predicted to be at high enough concentration to affect the concentrations of other carbonate species). Sodium species

could likely be neglected because they do not make up a significant fraction of the total carbonate concentration or activity at typical experimental pH values (< 9.5). Therefore, in total, the carbonate speciation model used in this work includes 12 species, shown in Table 9 and 10.

Table 9. Aqueous species included in the model sorted by charge. Cl^- enforces charge neutrality.

-2	-1	0	+1	+2
CO_3^{2-}	Cl^-	$CO(NH_2)_2$	H^+	Ca^{2+}
	HCO_3^-	H_2CO_3*	$CaHCO_3^+$	
	OH^-	$CaCO_3$(aq)	NH_4^+	
		NH_3		

Table 10. Equilibrium reactions and pK values included in the model. pK values from the PHREEQC database.

Reaction	Equilibrium Equation	pK
Water dissociation	$H_2O \leftrightarrow OH^- + H^+$	14
Carbonic acid dissociation	$H_2CO_3^* \leftrightarrow HCO_3^- + H^+$	6.35
Bicarbonate dissociation	$HCO_3^- \leftrightarrow CO_3^{2-} + H^+$	10.33
Calcium bicarbonate dissociation	$CaHCO_3^+ \leftrightarrow HCO_3^- + Ca^+$	3.22
Aqueous calcium carbonate dissociation	$CaCO_3(aq) \leftrightarrow CO_3^{2-} + Ca^+$	11.44
Ammonium dissociation	$NH_4^+ \leftrightarrow NH_3 + H^+$	9.25

Finite Element Model

COMSOL Multiphysics 4.3a was used in this work for modeling fluid flow, solute transport, carbonate speciation, urea hydrolysis and the chemistry which controls

the rate of calcium carbonate precipitation. The system contains four phases: liquid, biofilm, nonreactive solid and calcium carbonate. The method in which these phases were defined is discussed later in this chapter. A gas phase was not considered in this model but may be important under some conditions (see Chapter 5).

The incompressible 2D Navier-Stokes equations were used to describe the flow (see Chapter 5), ion transport is modeled using Nernst-Planck equations and non-charged species follow Fickian diffusion. Flow only occurs in the liquid phase with no slip boundary conditions at all interfaces except for the inlet (constant velocity) and the outlet (pressure equal to zero). Solute transport is allowed in both the biofilm and liquid phases. It is assumed that diffusion is the dominant transport mechanism in the biofilm so convection only takes place in the liquid phase. The entrance boundary condition for all solutes is a known concentration based on equilibrium for the desired pH, and solute mass conservation is enforced as the boundary condition at the outlet. Commonly used, semi empirical saturation (S) dependent precipitation (Zhong and Mucci, 1989) and dissolution (Chou et al., 1989; Compton et al., 1989) rate models are used as follows.

$$S = \frac{a_{Ca^{2+}} a_{CO_3^{2-}}}{k_{sp}}, \qquad (77)$$

$$r_{precip} = k_{precip}(S-1)^{n_{precip}} \quad for \;\; S \geq 1, \qquad (78)$$

$$r_{diss} = (k_{diss,1} a_{H^+} + k_{diss,2})(1-S)^{n_{diss}} \qquad for \;\; S < 1. \qquad (79)$$

r_{precip} and r_{diss} are the precipitation and dissolution rates respectively. a_x denotes the activity of species x, in this case calcium or bicarbonate. K_{precip}, n_{precip}, $k_{diss,1}$, $k_{diss,2}$ and

n_{diss} are all kinetic constants that have been experimentally determined by others. See Appendix E for values used in this work. It should be noted that these relationships were developed to fit results from well-mixed batch experiments that do not consider local concentrations (i.e. at the crystal surface). In this work local concentrations are considered such that $a_{Ca^{2+}}$ and $a_{CO_3^{2-}}$ at the precipitate boundary govern the crystal growth rate. Moving crystal boundaries were not considered however the effect of crystal growth or dissolution on local activities was modeled by a flux (J) of ions so

$$J_{Ca^{2+}} = J_{CO_3^{2-}} = r_{diss} - r_{precip}, \qquad (80)$$

with positive flux defined as mass entering the liquid domain.

The other rate-limited reaction in the system is urea hydrolysis (see Chapter 2). A Michaelis–Menten rate equation was used where

$$r_{urea} = \frac{r_{\max} a_{urea}}{k_m + a_{urea}}. \qquad (81)$$

r_{urea} is the volumetric biofilm urea hydrolysis rate, r_{max} is the maximum rate and k_m is the half saturation constant. Michaelis–Menten was used here in order to make the model most applicable at a wide range of concentrations but it has been shown in Chapters 4 and 5 that a first-order relationship would also be acceptable for typical urea concentrations found in MICP systems. Rate constants determined in Chapter 4 are used to calculate r_{urea} locally in each finite element. All other reactions are assumed to occur at a much faster rate. The numerical technique used does not allow for instantaneous reactions to take place because it creates a numerically stiff solution space. All equilibrium reactions were set to be fast enough to maintain equilibrium conditions, but

not fast enough to cause numerical instability. As an example, we take the carbonate/bicarbonate equilibrium reaction rate that can be written as

$$r_{HCO_3^-} = k_{HCO_3^-}\left(a_{CO_3^{2-}} a_{H^+} - a_{HCO_3^-} 10^{pK}\right) \qquad (82)$$

where k is a rate constant. Typical k values in carbonate equilibrium are on the order of 10^{12} s^{-1} however, all carbonate equilibrium rate constants were set to much lower values to avoid problem stiffness in this model. The lowered values, typically around 100 s^{-1}, were still much higher than the rate limited reactions (ureolysis, precipitation and dilution) so solution equilibrium was still maintained. All rate constants and rate equations used but not native to COMSOL can be found in Appendix E.

Individual-Based Biofilm and Precipitate Growth Model

A combined MATLAB R2012a, COMSOL- and Java-coded model was constructed that simulates biofilm and calcium carbonate crystal growth in a simple, theoretical 2D porous medium domain. This discrete model simulates biofilm and precipitation growth as collections of particles that can grow and exert force on each other, similar to previous work by Picioreanu et al. (Picioreanu et al., 1998; Radu et al., 2010). This approach allows a discrete representation of solid phases while still using continuum methods for solutes discussed in the previous section of this chapter.

For the IBM portion of the simulation, the computational domain was divided into 2 μm square elements in which discrete properties were defined. These properties are defined on a grid of square cells that either contain liquid, biofilm, precipitate or nonreactive solids. The definition of boundaries is avoided by the use of matrices

containing the representative properties of that phase. With respect to flow, the water phase has its typical viscosity, but all other solid phases have extremely high viscosities (six orders of magnitude higher) such that effectively no flow occurs in those domains over the course of the simulations. Diffusive transport is similar where diffusion coefficients are reduced by 50% in the biofilm domains (Stewart, 2003).

Grid cell classification depends on the location of precipitate and biofilm in the computational domain, which are represented by round particles. These particles grow and then once they reach a certain size, they divide. If a grid cell contains the center of one of these spheres it takes on the properties associated with either biofilm or precipitate. If a grid cell contains both particle types, a random classification is made. These particles should not be thought of as individual microbial cells or calcium carbonate crystals but rather a form of discretization.

Computational Procedure

First, the computational domain is randomly seeded with biofilm and precipitate particles. Biofilm particles are seeded at a radius similar to that of a single microbial cell (0.5 μm) and precipitate particles are seeded at a much smaller radius, similar to a crystal nucleus (5 nm). Precipitation kinetics govern crystal growth (Equation 6) and microbial growth kinetics govern the growth of biofilm particles. Microbial growth kinetics were qualitatively fitted to match biofilm growth at the time scale of the experiments discussed in previous chapters of this dissertation (Chapters 3, 5 and 5 specifically). Both types of particles grow based on local solute concentrations, as calculated by the reactive transport

model contained in COMSOL. It was assumed that the biofilm grows according to Monod kinetics with oxygen as the limiting substrate. The precipitate particles grow by the rate model in equations 5-8 and only participate in hydrodynamics (blocking flow) once they reach a critical size. The model does not account for dissolution which limits its application to precipitating systems only (see Chapter 7 for significance).

The time-dependent problem is solved assuming that the system behaves in a quasi-steady state manner (i.e. concentrations do not change significantly over the course of a time step). In the first time step, particles are seeded and a steady-state problem is solved (Navier-Stokes, Nernst-Plank). Then particles grow and divide based on local concentrations that are assumed constant over the time step. The new geometry caused by growing and dividing particles is then used in the next steady-state solution at the next time step. Figure 31 illustrates the solution scheme. Appendix E includes the main model script. Note that the code in Appendix E is only the main part of the model. That main script calls many other MATLAB and Java scripts which are not included. The use of the full model code would require explicit permission from Dr. Picioreanu who is the rightful owner.

This model was developed using a simplified geometry consisting of round porous media elements in a small rectangular flow channel. This geometry is purely theoretical and was chosen based on numerical simplicity.

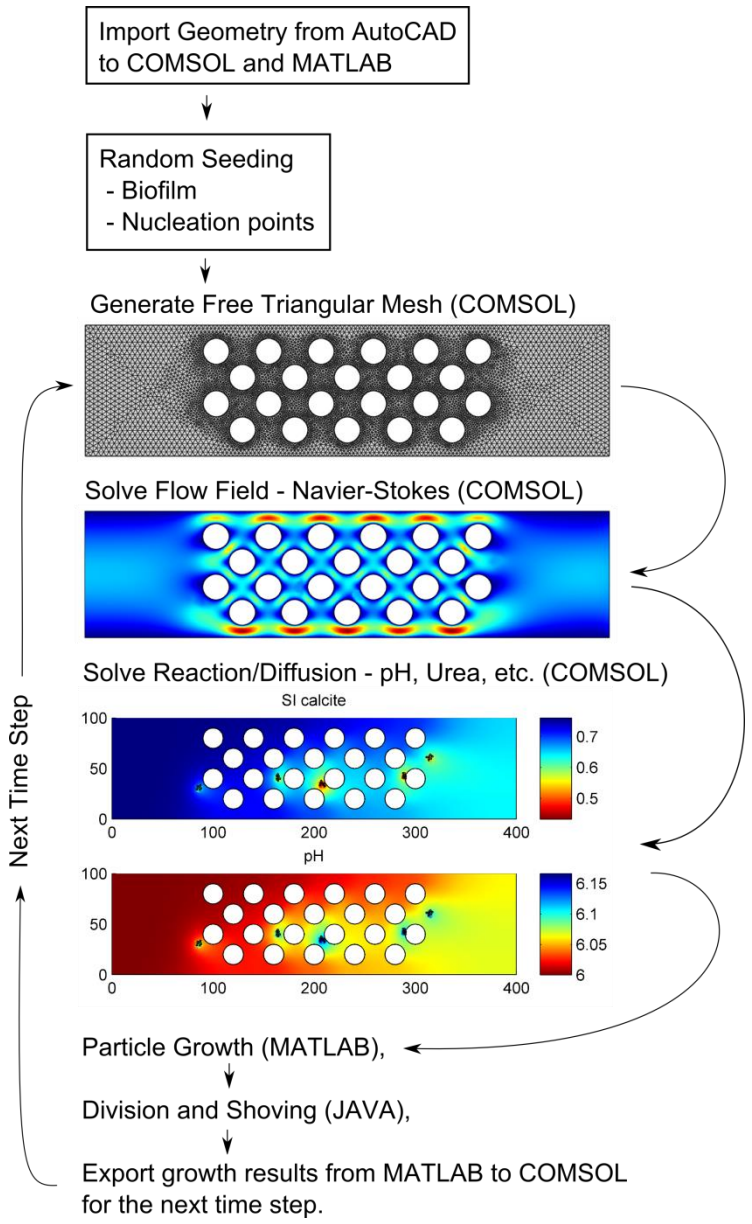


Figure 31. The main steps of the numerical approach. Flow is from left to right and the axes in the reaction/diffusion step are in μm.

2D Approximation

2D models are most commonly applied to problems that can be considered to be infinite in the third dimension (z). This allows one to neglect any forces in that third

dimension, and in the case of fluid flow, assume that the velocity is constant with respect to z. The micromodel reactors modeled in this work are, in contrast, thin in the third dimension so a different 2D approximation is made. An additional force term is added to the Navier-Stokes equation assuming that there is a fully developed laminar flow profile in the third dimension. Neglecting the inertial term (often called Stokes flow or, creeping flow), the laminar flow equations become

$$0 = \nabla \cdot \left[- p\vec{I} + \mu\left(\nabla\vec{u} + (\nabla\vec{u})^T\right)\right] + \vec{F} - 12\frac{\mu\vec{u}}{d_z^{\,2}} \quad \text{and} \qquad (83)$$

$$0 = \rho\Delta \cdot \vec{u}\,. \qquad (84)$$

where u is the average velocity, p is the pressure, I is the identity matrix, μ is the dynamic viscosity, and d_z is the thickness in the z direction. F represents general body forces (gravity) and the last term in equation 5 is the resistive force due to the assumed, fully-developed laminar flow profile between the parallel plates that enclose the reactor. This force can be thought of as a total viscous drag force on each finite element in the 2D model. Equation 6 enforces incompressibility. Equations 5 and 6 together are simple Stokes flow with the additional force due to the narrow z dimension. The major source of inaccuracy using this approximation is anticipated to be the presence of biofilm and mineral features that do not span the entire thickness of the reactor however experimental observations do not predict a significant amount of this behavior (see Chapter 5).

Results and Discussion

Figure 32 shows a time progression for the growing biofilm (dark circles) and precipitate (small white dots at t = 9 hours). Although it is impossible to completely validate this model at this point in time, the results generally follow expectations with the biofilm growing and eventually causing precipitation over the same time scale as typically expected in other flow cell experiments.

The interplay between physical and chemical heterogeneity is the most notable result from the simulation. The results show that, like the experimental observations in Chapter 5, the physical heterogeneity caused by biofilm growth and mineral precipitation does not necessarily translate into heterogeneous urea concentrations. This indicates that when urea is supplied in excess the effect of pore-scale heterogeneity in urea concentration may be neglected. The implications for continuum (Darcy-scale) models is that simple urea hydrolysis rate relationships that use pore water urea concentrations may be used.

The pH and calcium carbonate saturation were found to be heterogeneous, especially at later time points. Seeing as how precipitation kinetics are highly dependent on saturation it would become important to incorporate pore scale saturation heterogeneity in to continuum models. This can be accomplished by either using more complex models or accounting for heterogeneity in precipitation rate models. Chapter 2 provides one example of how heterogeneity cause by mass transport limitations can be accounted for with the use of a Thiele modulus. Precipitation kinetics are usually

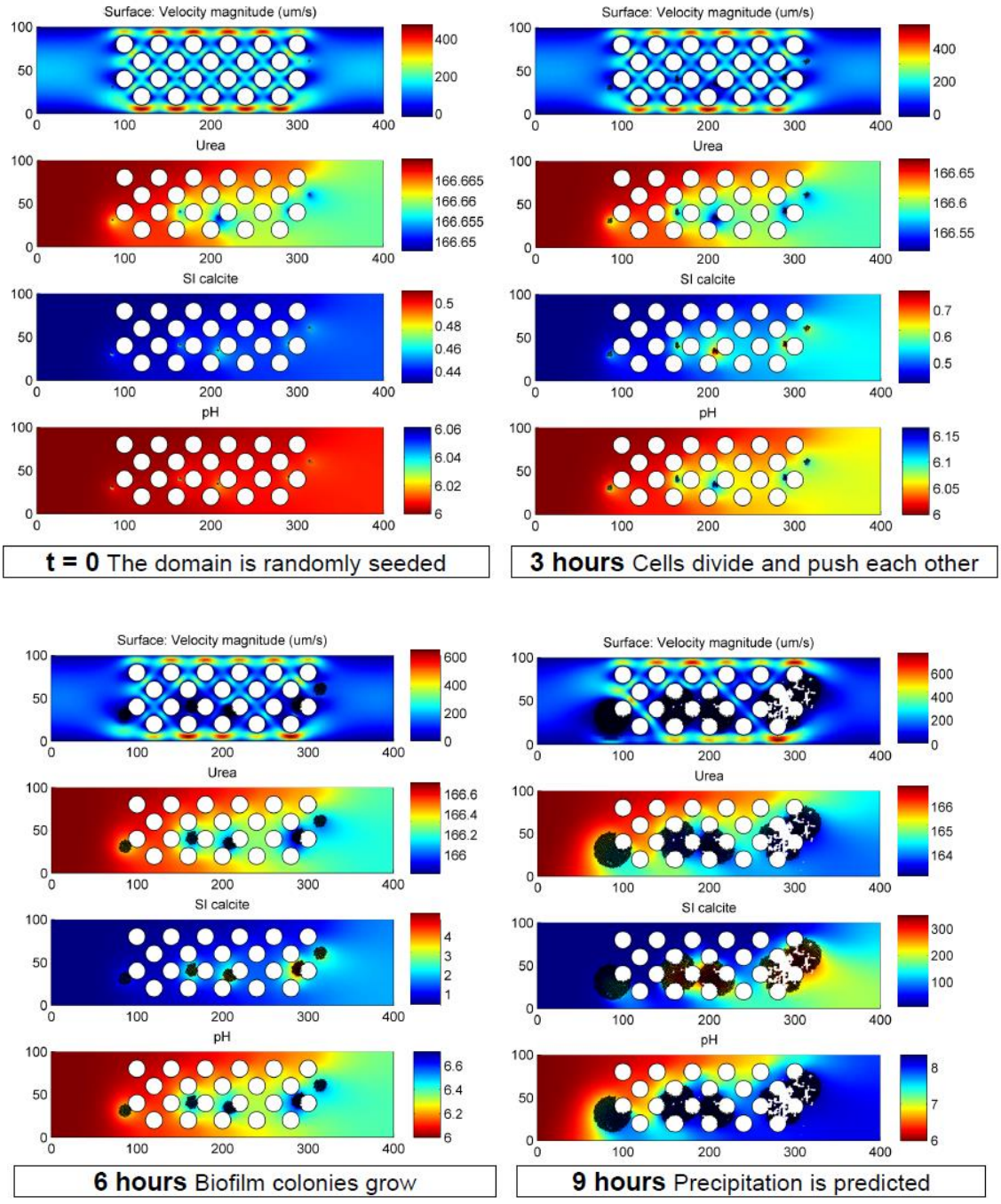


Figure 32. Model results from the individual-based biofilm and precipitate growth model. Biofilm growth is shown as the expanding dark masses (made up of small particles) and eventually precipitation is predicted at the last time point and represented by the white irregular masses. Axes on each plot are the length scale in µm and urea concentration is in mmol/L. Flow is from left to right.

determined by analyzing data from well mixed batch experiments so perhaps rather than using more complex modeling techniques effective kinetic constants from MICP systems should specifically be determined. It has been shown that pH can affect the urea hydrolysis rate in pure enzyme systems but recent research indicates that pH dependence is not significant in systems where living bacteria are the catalysts (Lauchnor et al., 2015).

Conclusions and Outlook

First, by taking a closer look at the carbonate chemistry, it was shown that $CaHCO_3^+$ and $CaCO_{3\,(aq)}$ may be important species to consider in equilibrium calculations at higher pH. This also prompted a closer look into the precipitation rate models that are typically used. When $CaCO_{3\,(aq)}$ is included in the model, it reduces the CO_3^{2-} activity. The saturation-based crystal growth expression is inherently linked to CO_3^{2-} activity so this is an important subject of future work. For example, we will investigate the use of crystal surface complexes for crystal growth rather than relying on saturation. Such mechanistic surface complexation models have crystal growth as dependent on $CaCO_{3\,(aq)}$ and Ca^{2+} (Ruiz-Agudo et al., 2011) which makes conceptual sense for discrete models where local concentrations are solved for and crystal boundaries are calculated.

Biofilm growth fits expectations, and is consistent with previous work by the Picioreanu group, but mathematically representing crystal nucleation and growth was difficult. The most difficult part was deciding how to handle nucleation. Similar to

precipitation and dissolution, there are multiple nucleation rate models. For the purpose of this model we chose to simply assume that the flow cell will be rich in nucleation sites at randomized locations throughout the domain. The initial nucleation point density in the model should be investigated further. It is known that the presence of microbial cells has an effect on nucleation probability (Mitchell and Ferris, 2006) but microscale special behavior (heterogeneous nucleation) remains poorly studied in biofilm systems. Mitchell and Ferris (2006) showed a decrease in nucleation probability in batch experiments with *Sporosarcina pasteurii* cells present as compared to sterile controls; however, other authors have shown evidence for nucleation of carbonate minerals on *Desulfonatronum lacustre* cell surfaces (Aloisi et al., 2006; van Lith et al., 2003). The apparent difference in nucleation behavior between *S. pasteurii* and *D. lacustre* suggests that the nucleation process cannot be assumed consistent throughout all alkalinity producing metabolisms (e.g. ureolysis vs. sulfate reduction respectively in this example).

The modeling work presented in this chapter should be considered preliminary but the results demonstrate the utility of IBMs for the study of MICP at the pore-scale. Using the model presented here as a starting point, others may be able to build on what was done here and run *in silico* experiments in order to better plan lab work or investigate certain aspects of MICP more closely. The modular, flexible nature of the COMSOL-based model facilitates the exploration of new kinetic relationships and mathematical relationships in MICP that will be useful to others within the Gerlach research group and beyond.

CHAPTER 7

CONCLUSIONS AND OUTLOOK

Conclusions and Impacts

The work presented in in this dissertation adds to the fundamental understanding of MICP at the pore scale through minimally-invasive imaging of biofilms precipitating calcium carbonate in synthetic 2D porous media. Images from these observations were analyzed in order to quantitate porosity reduction due to the various constituents (biofilm, precipitate and gasses). This was achieved through the use of recombinant bacteria that express both green fluorescent protein for imaging and the urease enzyme which was the catalyst for alkalinity increase and carbonate precipitation. The overall effect of biofilm-catalyzed MICP was tied to porosity reduction by direct differential pressure measurements that allowed for the estimation of permeability reduction due to the process. Finite element modeling provided an additional level of understanding to pore scale physical and chemical behavior through the estimation of local concentrations and hydrodynamics.

Model Organism Construction

Two novel model organisms were constructed to conduct pore scale ureolysis-driven MICP experiments, where biofilm and mineral growth can be visualized continuously and non-invasively (Connolly et al., 2013). The two new bacterial strains have allowed for the research of spatiotemporal physical and biochemical phenomena at

the micrometer scale in MICP systems. Kinetic analysis revealed that the specific ureolytic activity of *Pseudomonas aeruginosa* MJK1 and *Escherichia coli* MJK2 is not as high as for *Sporosarcina pasteurii*, the most commonly used organism for MICP experiments, but their utility for use in flow cell experiments was demonstrated. The construction of these model organisms provides a useful tool for the field of MICP research and development. This dissertation provides one example of what can be accomplished with the use of fluorescent model organisms in MICP but one could imagine many experimental applications.

Biofilm Kinetics Analysis

Biofilm-specific urea hydrolysis rate coefficients were determined for *E. coli* MJK2 (both Michaelis–Menten and first-order rate models) in a tube reactor system. Strain MJK2 was chosen for further analysis over the other GFP-expressing bacterium described in Chapter 3 because it proved to form biofilms extremely quickly (on the time scale of 24 hours in flow cell reactors with laminar flow). Additionally, strain MJK2 is a biosafety level 1 (BSL 1) organism so it could be utilized by other research groups that do not have a BSL 2 laboratory available to them.

It was found that for the chemical and hydrodynamic conditions in the study (urea 0-15 g/L and $Re < 1$) a first-order (linear) rate model fits the reaction rate versus concentration data as well as the Michaelis–Menten model which is more difficult to work with computationally. The biofilm-specific reaction kinetics determined in Chapter

4 were used throughout the remainder of the dissertation in pore-scale modeling to estimate local concentrations in porous media micromodel reactors.

MICP in Porous Media Micromodels

The construction and operation of porous media micromodel reactors was described in Chapter 5. The analysis conducted in Chapter 5 suggests that the timing of the calcium addition in MICP systems may be an important parameter that could be manipulated in order to maximize permeability reduction. It was shown that if calcium was added 24 hours after inoculation little permeability reduction would be achieved. When calcium was added soon after inoculation a significantly greater amount of permeability reduction was achieved. Gas production was observed in the micromodel experiments under zero flow or low flow conditions, suggesting that gases produced by microbial activity could be important in MICP systems. Gas production and the temporary permeability reduction that it causes has not been considered in other published studies however this work suggests that it may control short term permeability reduction under some circumstances.

Additionally, micromodel reactors similar to those discussed in Chapter 5 (and appendix J) have the potential for wide application for the visualization of processes in porous media. Filtration phenomena and multiphase flow among other processes have the potential for the use of micromodel reactors for quantitative visualization purposes.

Modeling

Finite element models have been integral to the work presented in this dissertation and have been used in two distinct ways. First, inverse models were used in Chapter 4 to estimate kinetic parameters for urea hydrolysis in biofilms of the model organisms developed in Chapter 3. Experimental observations were used to estimate effective reaction rates that existed within a system with a known and regular biofilm geometry. Results from the inverse modeling in Chapter 4 were used to predict local concentrations in systems with more unpredictable biofilm geometries in Chapter 5 in the 2D micromodel work. Finally, taking all of the inverse modeling, experimental observation and predictive modeling into account, MICP was modeled entirely *in silico* to make predictions about local mineral saturation conditions and determine parameters and mathematical relationships that control system behavior.

It was found that although urea concentrations were homogeneous over the experimental length scales present in this dissertation (μm to cm) the saturation state (S) of calcium carbonate was spatially heterogeneous in comparison. This leads to an interesting series of research questions and important considerations when applying MICP in the field. If biofilms are present, diffusion limitations can develop that both limit reactant transport to areas deeper within biofilms and cause metabolic products to reach higher concentrations. In this case the reactant of interest is urea, which is supplied in excess so spatially homogeneous concentrations are predicted. The species which control calcium carbonate saturation are calcium (Ca^{2+}) and carbonate (CO_3^{2-}, see Chapter 2). Calcium is likely to be supplied in excess, like urea, but when pH is high and urea

hydrolysis is occurring carbonate ions can accumulate in the biofilm at high concentrations relative to the mobile pore water, causing a heterogeneous saturation environment. The prediction of a heterogeneous mineral saturation environment is a significant result for those who wish to represent MICP systems in continuum models because it is likely that the volume-averaged concentration would not be representative of the higher saturation regions where minerals are forming the fastest. This prediction points out the need for the development of precipitation rate models that take heterogeneity into account.

Recommendations for Future Work

In order for MICP to become a widely-used permeability reduction technique there are remaining questions that need to addressed. The work presented in this dissertation focuses on precipitation in 2D porous media at the pore scale. Unfortunately one realizes quickly that most subsurface applications could not be considered 2D, many times both precipitation and dissolution need to be considered and continuum models must be used with large (m to dm) element sizes. Homogeneity, as seen in clean micromodel reactors in this dissertation, is also rare in the subsurface.

The question of how microbial precipitates dissolve over both short and geologic time scales must be better addressed by the MICP research field in order for it to be considered a viable technology. Current research suggests that carbonate minerals can be stabilized by biological substances in MICP systems (Mitchell et al., 2013; Riding, 2000; Rodriguez-Navarro et al., 2007) but the long term behavior remains poorly understood.

Experiments to investigate geologic time scale behavior are difficult so modeling becomes important yet again. Collaborative research into bacterial carbonates that remain in the geologic record could be an additional source of data. The micromodels used in this work are biologically inert and if run correctly could be used in long term experiments. Micromodels that are run for years and even potentially at high pressure (Zuo et al., 2013) would not be out of the question.

Pore structure was held constant in this work but micromodels are able to be fabricated with nearly any 2D pore structure imaginable. Using just one porous media type limited the applicability of the results in this dissertation (Chapter 5 specifically). Additional studies with micromodels that have a range of initial permeabilities and porosities would broaden the applicability of the work presented here. Furthermore, it has been shown that the pore structure, holding other factors constant, affects the behavior of permeability reduction in porous media (Willingham et al., 2008; Zhang et al., 2010b). This invites further investigations into how pore shape and other related factors impact permeability reduction could yield results that affect how MICP is applied in the field. Micromodels that contain solute-sensing fluorophore films can also be manufactured (Grate et al., 2012) in order to image the chemical environment rather than exclusively relying on models for such pore-scale chemical data.

The two dimensional analysis presented in this work is useful in certain aspects of the development of MICP technology but for true quantitative information that is useful in continuum modeling, the three-dimensional nature of transport in porous media must be considered. The oil and gas industry uses 3D x-ray tomography data routinely to

construct pore network models that have been shown to represent permeability appropriately for reservoir-scale permeability models (Wildenschild and Sheppard, 2013; Wildenschild et al., 2005). Industrial and governmental entities expect the same reliability and grounding in 3 dimensional reality that 3D x-ray tomography and pore network models (Fatt, 1956) provide, so these tools must be incorporated into further investigations of MICP permeability manipulation technologies.

Concluding Remarks

Fundamental research must continue. We must not wait for the pressures of war or famine to take a harder look at the world around us. It is impossible to know if the answer to a question will be interesting but let's continue to answer these questions, however small, because otherwise we will never know.

REFERENCES CITED

Al Qabany, A., Soga, K., Santamarina, C., 2012. Factors Affecting Efficiency of Microbially Induced Calcite Precipitation. *Journal of Geotechnical and Geoenvironmental Engineering* 138, 992–1001.

Aloisi, G., Gloter, A., KrOger, M., Wallmann, K., Guyot, F., Zuddas, P., Krüger, M., 2006. Nucleation of calcium carbonate on bacterial nanoglobules. *Geology* 34, 1017–1020.

Applegate, D.H., Bryers, J.D., 1991. Effects of carbon and oxygen limitations and calcium concentrations on biofilm removal processes. *Biotechnology and Bioengineering* 37, 17–25.

Armstrong, R., Ajo-Franklin, J., 2011. Investigating biomineralization using synchrotron based X-ray computed microtomography. *Geophysical Research Letters* 38, L08460.

ASTM E2562, 2007. Standard Test Method for Quantification of *Pseudomonas aeruginosa* Biofilm Grown with High Shear and Continuous Flow using CDC Biofilm Reactor. *ASTM International*.

Bachmeier, K.L., Williams, A.E., Warmington, J.R., Bang, S.S., 2002. Urease activity in microbiologically-induced calcite precipitation. *Journal of Biotechnology* 93, 171–181.

Beckingham, L.E., Peters, C.A., Um, W., Jones, K.W., Lindquist, W.B., 2013. 2D and 3D imaging resolution trade-offs in quantifying pore throats for prediction of permeability. *Advances in Water Resources* 62, 1–12.

Beyenal, H., Donovan, C., Lewandowski, Z., Harkin, G., 2004. Three-dimensional biofilm structure quantification. *Journal of Microbiological Methods* 59, 395–413.

Bird, R.B., Stewart, W.E., Lightfoot, E.N., 2006. *Transport Phenomena*, 2nd ed. John Wiley & Sons, New York.

Boetius, A., Ravenschlag, K., Schubert, C.J., Rickert, D., Widdel, F., Gieseke, A., Amann, R., Jørgensen, B.B., Witte, U., Pfannkuche, O., 2000. A marine microbial consortium apparently mediating anaerobic oxidation of methane. *Nature* 407, 623–626.

Braissant, O., Cailleau, G., Dupraz, C., Verrecchia, E.P., 2003. Bacterially induced mineralization of calcium carbonate in terrestrial environments: The role of exopolysaccharides and amino acids. *Journal of Sedimentary Research* 73, 485–490.

Braissant, O., Decho, A.W., Dupraz, C., Glunk, C., Przekop, K.M., Visscher, P.T., 2007. Exopolymeric substances of sulfate-reducing bacteria: Interactions with calcium at alkaline pH and implication for formation of carbonate minerals. *Geobiology* 5, 401–411.

Brileya, K.A., Connolly, J.M., Downey, C., Gerlach, R., Fields, M.W., 2013. Taxis Toward Hydrogen Gas by *Methanococcus maripaludis*. *Scientific Reports* 3.

Carman, P.C., 1937. Fluid flow through granular beds. *Transactions: Institution of Chemical Engineers* 15, 150–166.

Carrier, W.D., 2003. Goodbye, Hazen; Hello, Kozeny-Carman. *Journal of Geotechnical and Geoenvironmental Engineering* 129, 1054–1056.

Castanier, S., Le Métayer-Levrel, G., Perthuisot, J.-P., 1999. Ca-carbonates precipitation and limestone genesis — the microbiogeologist point of view. *Sedimentary Geology* 126, 9–23.

Characklis, W.G., Marshall, K.C., 1990. *Biofilms*. Wiley, New York.

Chen, X., Stewart, P.S., 2002. Role of electrostatic interactions in cohesion of bacterial biofilms. *Applied Microbiology and Biotechnology* 59, 718–720.

Cheng, L., Cord-Ruwisch, R., 2014. Upscaling Effects of Soil Improvement by Microbially Induced Calcite Precipitation by Surface Percolation. *Geomicrobiology Journal* 31, 396–406.

Chou, L., Garrels, R.M., Wollast, R., 1989. Comparative study of the kinetics and mechanisms of dissolution of carbonate minerals. *Chemical Geology* 78, 269–282.

Ciurli, S., Marzadori, C., Benini, S., Deiana, S., Gessa, C., 1996. Urease from the soil bacterium *Bacillus pasteurii*: Immobilization on Ca-polygalacturonate. *Soil Biology and Biochemistry* 28, 811–817.

Clark, S., Francis, P.S., Conlan, X.A., Barnett, N.W., 2007. Determination of urea using high-performance liquid chromatography with fluorescence detection after automated derivatisation with xanthydrol. *Journal of Chromatography A* 1161, 207–213.

Collins, C.M., Falkow, S., 1988. Genetic Analysis of an *Escherichia coli* Urease Locus: Evidence of DNA Rearrangement. *Journal of Bacteriology* 170, 1041–1045.

Compton, R.G., Pritchard, K.L., Unwin, P.R., 1989. The dissolution of calcite in acid waters: mass transport versus surface control. *Freshwater Biology* 22, 285–288.

Connolly, J., Kaufman, M., Rothman, A., Gupta, R., Redden, G., Schuster, M., Colwell, F., Gerlach, R., 2013. Construction of two ureolytic model organisms for the study of microbially induced calcium carbonate precipitation. *Journal of Microbiological Methods* 94, 290–299.

Connolly, J.M., Gerlach, R., 2015. Microbially induced carbonate precipitation in the subsurface: Fundamental reaction and transport processes. In: Vafai, K. (Ed.), *Handbook of Porous Media*. CRC Press, pp. 891–922.

Connolly, J.M., Jackson, B., Rothman, A.P., Klapper, I., Gerlach, R., 2015. Estimation of a biofilm-specific reaction rate: Kinetics of bacterial urea hydrolysis in a biofilm. *In Review*.

Costa, A., 2006. Permeability-porosity relationship: A reexamination of the Kozeny-Carman equation based on a fractal pore-space geometry assumption. *Geophysical Research Letters* 33, L02318.

Costerton, J.W., Cheng, K.J., Geesey, G.G., Ladd, T.I., Nickel, J.C., Dasgupta, M., Marrie, T.J., 1987. Bacterial biofilms in nature and disease. *Annual Review of Microbiology* 41, 435–464.

Crittenden, J.C., Trussell, R.R., Hand, D.W., Howe, K.J., Tchobanoglous, G., 2012. *MWH's Water Treatment: Principles and Design*, 3rd ed. Wiley.

Cunningham, A.B., Characklis, W.G., Abedeen, F., Crawford, D., 1991. Influence of Biofilm Accumulation on Porous Media Hydrodynamics. *Environmental Science & Technology* 25, 1305–1311.

Cussler, E.L., 1997. *Diffusion, Mass Transfer in Fluid Systems*, 3rd ed, Cambridge Series in Chemical Engineering. Cambridge University Press.

Cuthbert, M.O., Riley, M.S., Handley-Sidhu, S., Renshaw, J.C., Tobler, D.J., Phoenix, V.R., Mackay, R., 2012. Controls on the rate of ureolysis and the morphology of carbonate precipitated by *S. Pasteurii* biofilms and limits due to bacterial encapsulation. *Ecological Engineering* 41, 32–40.

Dandeu, A., Humbert, B., Carteret, C., Muhr, H., Plasari, E., Bossoutrot, J.M., 2006. Raman spectroscopy - A powerful tool for the quantitative determination of the composition of polymorph mixtures: Application to $CaCO_3$ polymorph mixtures. *Chemical Engineering & Technology* 29, 221–225.

Davies, C.W., 1962. *Ion Association*. Butterworths, Washington DC.

Davit, Y., Iltis, G., Debenest, G., Veran-Tissoires, S., Wildenschild, D., Gerino, M., Quintard, M., 2011. Imaging biofilm in porous media using X-ray computed microtomography. *Journal of Microscopy* 242, 15–25.

Dawe, R.A., Zhang, Y.P., 1997. Kinetics of calcium carbonate scaling using observations from glass micromodels. *Journal of Petroleum Science and Engineering* 18, 179–187.

De Muynck, W., De Belie, N., Verstraete, W., 2010. Microbial carbonate precipitation in construction materials: A review. *Ecological Engineering* 36, 118–136.

Decho, A.W., 2010. Overview of biopolymer-induced mineralization: What goes on in biofilms? *Ecological Engineering* 36, 137–144.

DeJong, J.T., Mortensen, B.M., Martinez, B.C., Nelson, D.C., 2010. Bio-mediated soil improvement. *Ecological Engineering* 36, 197–210.

Demichelis, R., Raiteri, P., Gale, J.D., Quigley, D., Gebauer, D., 2011. Stable prenucleation mineral clusters are liquid-like ionic polymers. *Nature Communications* 2, 1–8.

Dhami, N.K., Reddy, M.S., Mukherjee, A., 2013. Biomineralization of calcium carbonate polymorphs by the bacterial strains isolated from calcareous sites. *Journal of Microbiology and Biotechnology* 23, 707–714.

Dixon, N., Gazzola, C., Blakeley, R., Zerner, B., 1976. Metal ions in enzymes using ammonia or amides. *Science* 191, 1144–1150.

Doube, M., Kłosowski, M.M., Arganda-Carreras, I., Cordelières, F.P., Dougherty, R.P., Jackson, J.S., Schmid, B., Hutchinson, J.R., Shefelbine, S.J., 2010. BoneJ: Free and extensible bone image analysis in ImageJ. *Bone* 47, 1076–1079.

Douglas, S., Beveridge, T.J., 1998. Mineral formation by bacteria in natural microbial communities. *FEMS Microbiology Ecology* 26, 79–88.

Dupin, H.J., McCarty, P.L., 1999. Mesoscale and Microscale Observations of Biological Growth in a Silicon Pore Imaging Element. *Environmental Science & Technology* 33, 1230–1236.

Ebigbo, A., Helmig, R., Cunningham, A.B., Class, H., Gerlach, R., 2010. Modelling biofilm growth in the presence of carbon dioxide and water flow in the subsurface. *Advances in Water Resources* 33, 762–781.

Ebigbo, A., Phillips, A., Gerlach, R., Helmig, R., Cunningham, A.B., Class, H., Spangler, L.H., 2012. Darcy-scale modeling of microbially induced carbonate mineral precipitation in sand columns. *Water Resources Research* 48, W07519.

Ehrenberg, S.N., Nadeau, P.H., 2005. Sandstone vs. carbonate petroleum reservoirs: A global perspective on porosity-depth and porosity-permeability relationships. *AAPG Bulletin* 89, 435–445.

Ercole, C., Bozzelli, P., Altieri, F., Cacchio, P., Del Gallo, M., 2012. Calcium Carbonate Mineralization: Involvement of Extracellular Polymeric Materials Isolated from Calcifying Bacteria. *Microscopy and Microanalysis* 18, 829–839.

Fang, Y.X., Govind, R., 2008. A new Thiele's modulus for the Monod biofilm model. *Chinese Journal of Chemical Engineering* 16, 277–286.

Fatt, I., 1956. The Network Model of Porous Media. *Petroleum Transactions, AIME* 207, 144–181.

Ferris, F., Stehmeier, L., Kantzas, A., Mourits, F., 1996. Bacteriogenic mineral plugging. *Jounal of Canadian Petroleum Technology* 35, 56–61.

Ferris, F.G., Phoenix, V., Fujita, Y., Smith, R.W., 2003. Kinetics of calcite precipitation induced by ureolytic bacteria at 10 to 20°C in artificial groundwater. *Geochimica et Cosmochimica Acta* 68, 1701–1710.

Fidaleo, M., Lavecchia, R., 2003. Kinetic study of enzymatic urea hydrolysis in the pH range 4-9. *Chemical and Biochemical Engineering Quarterly* 17, 311–319.

Flaten, E.M., Seiersten, M., Andreassen, J.-P., 2010. Induction time studies of calcium carbonate in ethylene glycol and water. *Chemical Engineering Research and Design* 88, 1659–1668.

Flemming, H.C., Wingender, J., 2001a. Relevance of microbial extracellular polymeric substances (EPSs) - Part I: Structural and ecological aspects. *Water Science and Technology* 43, 1–8.

Flemming, H.C., Wingender, J., 2001b. Relevance of microbial extracellular polymeric substances (EPSs) - Part II: Technical aspects. *Water Science and Technology* 43, 9–16.

Fogler, H.S., 2005. *Elements of Chemical Reaction Engineering*, 4th Editio. ed. Prentice Hall.

Folkesson, A., Haagensen, J.A.J., Zampaloni, C., Sternberg, C., Molin, S., 2008. Biofilm Induced Tolerance towards Antimicrobial Peptides. *Plos One* 3, e1891.

Fredrickson, J.K., Gorby, Y.A., 1996. Environmental processes mediated by iron-reducing bacteria. *Current Opinion in Biotechnology* 7, 287–294.

Fredrickson, J.K., Zachara, J.M., Kennedy, D.W., Dong, H., Onstott, T.C., Hinman, N.W., Li, S., 1998. Biogenic iron mineralization accompanying the dissimilatory reduction of hydrous ferric oxide by a groundwater bacterium. *Geochimica et Cosmochimica Acta* 62, 3239–3257.

Fridjonsson, E.O., Seymour, J.D., Schultz, L.N., Gerlach, R., Cunningham, A.B., Codd, S.L., 2011. NMR measurement of hydrodynamic dispersion in porous media subject to biofilm mediated precipitation reactions. *Journal of Contaminant Hydrology* 120-21, 79–88.

Fujita, Y., Ferris, F.G., Lawson, R.D., Colwell, F.S., Smith, R.W., 2000. Calcium Carbonate Precipitation by Ureolytic Subsurface Bacteria. *Geomicrobiology Journal* 17, 305–318.

Gebauer, D., Cölfen, H., 2011. Prenucleation clusters and non-classical nucleation. *Nano Today* 6, 564–584.

Gebauer, D., Völkel, A., Cölfen, H., 2008. Stable prenucleation calcium carbonate clusters. *Science* 322, 1819–1822.

Ghaderi, S.M., Kharrat, R., Tahmasebi, H.A., 2009. Experimental and Theoretical Study of Calcium Phosphate Precipitation in Porous Media using Glass Micromodel. *Oil & Gas Science and Technology* 64, 489–501.

Gibbs, J.W., 1948. *The Collected Works of J. Willard Gibbs: Thermodynamics*. Yale University Press.

Glenn, C.R., Filippelli, G.M., Gontharet, S., Pierre, C., Blanc-Valleron, M.-M., Rouchy, J.M., Fouquet, Y., Bayon, G., Foucher, J.P., Woodside, J., Mascle, J., 2007. Nature and origin of diagenetic carbonate crusts and concretions from mud volcanoes and pockmarks of the Nile deep-sea fan (eastern Mediterranean Sea). *Deep Sea Research Part II: Topical Studies in Oceanography* 54, 1292–1311.

Goeres, D.M., Hamilton, M.A., Beck, N.A., Buckingham-Meyer, K., Hilyard, J.D., Loetterle, L.R., Lorenz, L.A., Walker, D.K., Stewart, P.S., 2009. A method for growing a biofilm under low shear at the air-liquid interface using the drip flow biofilm reactor. *Nature Protocols* 4, 783–8.

Gonzo, E.E., Wuertz, S., Rajal, V.B., 2012. Continuum heterogeneous biofilm model--a simple and accurate method for effectiveness factor determination. *Biotechnology and Bioengineering* 109, 1779–1790.

Gottifredi, J.C., Gonzo, E.E., 2005. On the effectiveness factor calculation for a reaction – diffusion process in an immobilized biocatalyst pellet. *Biochemical Engineering Journal* 24, 235–242.

Graf von der Schulenburg, D.A., Vrouwenvelderb, J.S., Creber, S.A., van Loosdrecht, M.C.M., Johns, M.L., 2008. Nuclear magnetic resonance microscopy studies of membrane biofouling. *Journal of Membrane Science* 323, 37–44.

Grate, J.W., Kelly, R.T., Suter, J., Anheier, N.C., 2012. Silicon-on-glass pore network micromodels with oxygen-sensing fluorophore films for chemical imaging and defined spatial structure. *Lab on a chip* 12, 4796–801.

Guo, H.X., Qin, Z.P., Qian, P., Yu, P., Cui, S.P., Wang, W., 2011. Crystallization of aragonite CaCO3 with complex structures. *Advanced Powder Technology* 22, 777–783.

Haisch, C., Niessner, R., 2007. Visualisation of transient processes in biofilms by optical coherence tomography. *Water Research* 41, 2467–2472.

Handley-Sidhu, S., Sham, E., Cuthbert, M.O., Nougarol, S., Mantle, M., Johns, M.L., Macaskie, L.E., Renshaw, J.C., 2013. Kinetics of urease mediated calcite precipitation and permeability reduction of porous media evidenced by magnetic resonance imaging. *International Journal of Environmental Science and Technology* 10, 881–890.

Hansen, M.C., Palmer, R.J., Udsen, C., White, D.C., Molin, S., 2001. Assessment of GFP fluorescence in cells of *Streptococcus gordonii* under conditions of low pH and low oxygen concentration. *Microbiology* 147, 1383–1391.

Hasse, B., Ehrenberg, H., Marxen, J.C., Becker, W., Epple, M., 2000. Calcium carbonate modifications in the mineralized shell of the freshwater snail *Biomphalaria glabrata*. *Chemistry: A European Journal* 6, 3679–3685.

Heberling, F., Trainor, T.P., Lützenkirchen, J., Eng, P., Denecke, M. a, Bosbach, D., 2011. Structure and reactivity of the calcite-water interface. *Journal of Colloid and Interface Science* 354, 843–857.

Heydorn, A., Nielsen, a T., Hentzer, M., Sternberg, C., Givskov, M., Ersbøll, B.K., Molin, S., 2000. Quantification of biofilm structures by the novel computer program COMSTAT. *Microbiology* 146, 2395–2407.

Iltis, G.C., Armstrong, R.T., Jansik, D.P., Wood, B.D., Wildenschild, D., 2011. Imaging biofilm architecture within porous media using synchrotron-based X-ray computed microtomography. *Water Resources Research* 47, W02601.

Jahns, T., 1996. Ammonium/urea-dependent generation of a proton electrochemical potential and synthesis of ATP in *Bacillus pasteurii*. *Journal of Bacteriology* 178, 403–409.

Karadimitriou, N.K., Hassanizadeh, S.M., 2012. A Review of Micromodels and Their Use in Two-Phase Flow Studies. *Vadose Zone Journal* 11.

Kashchiev, D., van Rosmalen, G.M., 2003. Review: Nucleation in solutions revisited. *Crystal Research and Technology* 38, 555–574.

Kawaguchi, T., Decho, A.W., 2002. A laboratory investigation of cyanobacterial extracellular polymeric secretions (EPS) in influencing $CaCO_3$ polymorphism. *Journal of Crystal Growth* 240, 230–235.

Kirk, M.F., Santillan, E.F.U., McGrath, L.K., Altman, S.J., 2012. Variation in hydraulic conductivity with decreasing pH in a biologically-clogged porous medium. *International Journal of Greenhouse Gas Control* 11, 133–140.

Klenk, H.P., Clayton, R.A., Tomb, J.F., White, O., Nelson, K.E., Ketchum, K.A., Dodson, R.J., Gwinn, M., Hickey, E.K., Peterson, J.D., Richardson, D.L., Kerlavage, A.R., Graham, D.E., Kyrpides, N.C., Fleischmann, R.D., Quackenbush, J., Lee, N.H., Sutton, G.G., Gill, S., Kirkness, E.F., Dougherty, B.A., McKenney, K., Adams, M.D., Loftus, B., Peterson, S., Reich, C.I., McNeil, L.K., Badger, J.H., Glodek, A., Zhou, L., Overbeek, R., Gocayne, J.D., Weidman, J.F., McDonald, L., Utterback, T., Cotton, M.D., Spriggs, T., Artiach, P., Kaine, B.P., Sykes, S.M., Sadow, P.W., D'Andrea, K.P., Bowman, C., Fujii, C., Garland, S.A., Mason, T.M., Olsen, G.J., Fraser, C.M., Smith, H.O., Woese, C.R., Venter, J.C., 1997. The complete genome sequence of the hyperthermophilic, sulphate-reducing archaeon Archaeoglobus fulgidus. *Nature* 390, 364–370.

Knutson, C.E., Werth, C.J., Valocchi, A.J., 2005. Pore-scale simulation of biomass growth along the transverse mixing zone of a model two-dimensional porous medium. *Water Resources Research* 41, 1–12.

Kozeny, J., 1927. Ueber kapillare Leitung des Wassers im Boden. *Sitzungsber Akad. Wiss.* 136(2a), 271–306.

Krause, S., Liebetrau, V., Gorb, S., Sanchez-Roman, M., McKenzie, J.A., Treude, T., 2012. Microbial nucleation of Mg-rich dolomite in exopolymeric substances under anoxic modern seawater salinity: New insight into an old enigma. *Geology* 40, 587–590.

Lagarias, J.C., Reeds, J.A., Wright, M.H., Wright, P.E., 1998. Convergence Properties of the Nelder-Mead Simplex Method in Low Dimensions. *SIAM Journal on Optimization* 9, 112–147.

Lappin-Scott, H.M., Costerton, J.W. (Eds.), 2003. *Microbial Biofilms*. Cambridge University Press.

Lardon, L.A., Merkey, B. V, Martins, S., Dötsch, A., Picioreanu, C., Kreft, J.-U., Smets, B.F., 2011. iDynoMiCS: next-generation individual-based modelling of biofilms. *Environmental microbiology* 13, 2416–34.

Lasdon, L.S., Waren, A.D., Jain, A., Ratner, M., 1978. Design and Testing of a Generalized Reduced Gradient Code for Nonlinear Programming. *ACM Transactions on Mathematical Software* 4, 34–50.

Lauchnor, E.G., Schultz, L.N., Bugni, S., Mitchell, A.C., Cunningham, A.B., Gerlach, R., 2013. Bacterially induced calcium carbonate precipitation and strontium coprecipitation in a porous media flow system. *Environmental Science & Technology* 47, 1557–64.

Lauchnor, E.G., Topp, D., Parker, A., Gerlach, R., 2015. Whole cell kinetics of ureolysis by *Sporosarcina pasteurii*. *Journal of Applied Microbiology* In Press.

Lawrence, J.R., Swerhone, G.D.W., Neu, T.R., 2000. A simple rotating annular reactor for replicated biofilm studies. *Journal of Microbiological Methods* 42, 215–224.

Lee, K.-C., Rittmann, B.E., 2003. Effects of pH and precipitation on autohydrogenotrophic denitrification using the hollow-fiber membrane-biofilm reactor. *Water Research* 37, 1551–6.

Lengeler, J.W., Drews, G., Schlegel, H.G. (Eds.), 1998. Anaerobic Energy Metabolism. In: *Biology of the Prokaryotes*. Blackwell Science Ltd, Oxford, UK, pp. 278–326.

Li, W., Chen, W.-S., Zhou, P.-P., Cao, L., Yu, L.-J., 2012. Influence of initial pH on the precipitation and crystal morphology of calcium carbonate induced by microbial carbonic anhydrase. *Colloids and Surfaces B: Biointerfaces* 102, 281–287.

Lovley, D.R., Holmes, D.E., Nevin, K.P., 2004. Dissimilatory Fe(III) and Mn(IV) reduction. *Advances in microbial physiology* 49, 219–86.

Marin, F., Luquet, G., Marie, B., Medakovic, D., 2008. Molluscan shell proteins: primary structure, origin, and evolution. *Current Topics in Developmental Biology* 80, 209–276.

Martin, D., Dodds, K., Butler, I.B., Ngwenya, B.T., 2013. Carbonate Precipitation under Pressure for Bioengineering in the Anaerobic Subsurface via Denitrification. *Environmental Science & Technology* 47, 8692–8699.

Martin, D., Dodds, K., Ngwenya, B.T., Butler, I.B., Elphick, S.C., 2012. Inhibition of *Sporosarcina pasteurii* under Anoxic Conditions: Implications for Subsurface Carbonate Precipitation and Remediation via Ureolysis. *Environmental Science & Technology* 46, 8351–8355.

Martinez, B.C., DeJong, J.T., Ginn, T.R., 2014. Bio-geochemical reactive transport modeling of microbial induced calcite precipitation to predict the treatment of sand in one-dimensional flow. *Computers and Geotechnics* 58, 1–13.

Mayer, C., Moritz, R., Kirschner, C., Borchard, W., Maibaum, R., Wingender, J., Flemming, H.-C., 1999. The role of intermolecular interactions: studies on model systems for bacterial biofilms. *International Journal of Biological Macromolecules* 26, 3–16.

Miller, C.T., Barry, D.A., Katul, G., Rinaldo, A., Wood, B.D., Valdés-Parada, F.J., 2013. Volume averaging: Local and nonlocal closures using a Green's function approach. *Advances in Water Resources* 51, 139–167.

Milucka, J., Ferdelman, T.G., Polerecky, L., Franzke, D., Wegener, G., Schmid, M., Lieberwirth, I., Wagner, M., Widdel, F., Kuypers, M.M.M., 2012. Zero-valent sulphur is a key intermediate in marine methane oxidation. *Nature* 491, 541–546.

Mitchell, A.C., Ferris, F.G., 2006. The Influence of *Bacillus pasteurii* on the nucleation and growth of calcium carbonate. *Geomicrobiology Journal* 23, 213–226.

Mitchell, A.C., Phillips, A., Schultz, L., Parks, S., Spangler, L., Cunningham, A.B., Gerlach, R., 2013. Microbial CaCO3 mineral formation and stability in an experimentally simulated high pressure saline aquifer with supercritical CO2. *International Journal of Greenhouse Gas Control* 15, 86–96.

Mitchell, M.J., Jensen, O.E., Cliffe, K. a., Maroto-Valer, M.M., 2009. A model of carbon dioxide dissolution and mineral carbonation kinetics. *Proceedings of the Royal Society A: Mathematical, Physical and Engineering Sciences* 466, 1265–1290.

Mobley, H.L.T., Hausinger, R.P., 1989. Microbial ureases: significance, regulation, and molecular characterization. *Microbiological Reviews* 53, 85–108.

Mobley, H.L.T., Island, M.D., Hausinger, R.P., 1995. Molecular-biology of Microbial Ureases. *Microbiological Reviews* 59, 451–480.

Mohamed, A.M.O., Antia, H.E., 1998. Lining Systems. In: *Geoenvironmental Engineering*. Elsevier, pp. 371–403.

Molins, S., Trebotich, D., Steefel, C.I., Shen, C., 2012. An investigation of the effect of pore scale flow on average geochemical reaction rates using direct numerical simulation. *Water Resources Research* 48, W03527.

Morris, N.S., Stickler, D.J., McLean, R.J., 1999. The development of bacterial biofilms on indwelling urethral catheters. *World Journal of Urology* 17, 345–350.

Morsdorf, G., Kaltwasser, H., 1989. Ammonium assimilation in *Proteus vulgaris*, *Bacillus pasteurii*, and *Sporosarcina ureae*. *Archives of Microbiology* 152, 125–131.

Morse, J.W., Arvidson, R.S., Lüttge, A., 2007. Calcium carbonate formation and dissolution. *Chemical Reviews* 107, 342–381.

Morse, J.W., Mackenzie, F.T., 1990. *Developments in Sededementology 48: Geochemistry of Sedimentary Carbonates*, 1st ed. Elsevier.

Moynihan, H.J., Lee, C.K., Clark, W., Wang, N.H., 1989. Urea hydrolysis by immobilized urease in a fixed-bed reactor: analysis and kinetic parameter estimation. *Biotechnology and bioengineering* 34, 951–63.

Mullin, J.W., 2001. *Crystallization*, 4th ed. Butterworth-Heinemann, Oxford.

Muyzer, G., Stams, A.J.M., 2008. The ecology and biotechnology of sulphate-reducing bacteria. *Nature Reviews Microbiology* 6, 441–454.

Nambi, I.M., Werth, C.J., Sanford, R. a, Valocchi, A.J., 2003. Pore-scale analysis of anaerobic halorespiring bacterial growth along the transverse mixing zone of an etched silicon pore network. *Environmental science & technology* 37, 5617–24.

Nehrke, G., Nouet, J., 2011. Confocal Raman microscope mapping as a tool to describe different mineral and organic phases at high spatial resolution within marine biogenic carbonates: case study on *Nerita undata* (Gastropoda, Neritopsina). *Biogeosciences* 8, 3761–3769.

Nelder, J., Mead, R., 1965. A Simplex-Method for Function Minimization. *Computer Journal* 7, 308–313.

Nevin, K.P., Lovley, D.R., 2002. Mechanisms for Fe(III) Oxide Reduction in Sedimentary Environments. *Geomicrobiology Journal* 19, 141–159.

Ni, M., Ratner, B.D., 2008. Differentiating calcium carbonate polymorphs by surface analysis techniques - an XPS and TOF-SIMS study. *Surface and Interface Analysis* 40, 1356–1361.

Nilsson, Ö., Sternbeck, J., 1999. A mechanistic model for calcite crystal growth using surface speciation. *Geochimica et Cosmochimica Acta* 63, 217–225.

Otsu, N., 1979. Threshold selection method from gray-level histogram. *IEEE Transactions on Systems, Man, and Cybernetics* 9, 62–66.

Palandri, J.L., Kharaka, Y.K., 2004. A compilation of rate parameters of water-mineral interaction kinetics for application to geochemical modeling. *U.S. Geological Survey Open File Report*.

Pape, H., Clauser, C., Iffland, J., 2012. Permeability prediction based on fractal pore-space geometry. *Geophysics* 54, 1447–1460.

Parkhurst, D.L., Appelo, C.A.J., 1999. User's Guide to PHREEQC (version 2) — A Computer Program for speciation, Batch-Reaction, One-Dimensional Transport, and Inverse Geochemical Calculations, U.S. Geological Survey Water-Resources Investigations, Report 99-4259. U.S. Geological Survey.

Pérez, J., Picioreanu, C., van Loosdrecht, M., 2005. Modeling biofilm and floc diffusion processes based on analytical solution of reaction-diffusion equations. *Water Research* 39, 1311–1323.

Perry, T.D., Klepac-Ceraj, V., Zhang, X. V, McNamara, C.J., Polz, M.F., Martin, S.T., Berke, N., Mitchell, R., 2005. Binding of harvested bacterial exopolymers to the surface of calcite. *Environmental Science & Technology* 39, 8770–8775.

Pfeffer, C., Larsen, S., Song, J., Dong, M., Besenbacher, F., Meyer, R.L., Kjeldsen, K.U., Schreiber, L., Gorby, Y. a., El-Naggar, M.Y., Leung, K.M., Schramm, A., Risgaard-Petersen, N., Nielsen, L.P., 2012. Filamentous bacteria transport electrons over centimetre distances. *Nature* 491, 218–221.

Phillips, A.J., Gerlach, R., Lauchnor, E., Mitchell, Andrew C Cunningham, A.B., Spangler, L., 2013a. Engineered applications of ureolytic biomineralization : a review. *Biofouling* 29, 715–733.

Phillips, A.J., Lauchnor, E., Eldring, J.J., Esposito, R., Mitchell, A.C., Gerlach, R., Cunningham, A.B., Spangler, L.H., 2013b. Potential CO_2 Leakage Reduction through Biofilm-Induced Calcium Carbonate Precipitation. *Environmental Science & Technology* 47, 142–9.

Picioreanu, C., 1996. Modelling biofilms with cellular automata.

Picioreanu, C., van Loosdrecht, M., Heijnen, J., 1998. A new combined differential-discrete cellular automaton approach for biofilm modeling: Application for growth in gel beads. *Biotechnology and Bioengineering* 57, 718–731.

Pintelon, T.R.R., Picioreanu, C., Loosdrecht, M.C.M. van, Johns, M.L., 2012. The effect of biofilm permeability on bio-clogging of porous media. *Biotechnology and bioengineering* 109, 1031–1042.

Pitts, B., Stewart, P., 2008. Confocal Laser Microscopy on Biofilms: Successes and Limitations. *Microscopy Today* 16, 18–22.

Pitzer, K.S., 1991. Ion interaction approach: theory and data correlation. In: Pitzer, K.S. (Ed.), *Activity Coefficients in Electrolyte Solutions*. CRC Press, pp. 75–153.

Plant, L.., House, W.., 2002. Precipitation of calcite in the presence of inorganic phosphate. *Colloids and Surfaces A: Physicochemical and Engineering Aspects* 203, 143–153.

Plummer, L.N., Busenberg, E., 1982. The solubilities of calcite, aragonite and vaterite in CO_2-H_2O solutions between 0 and 90° C, and an evaluation of the aqueous model for the system $CaCO_3$-CO_2-H_2O. *Geochimica et Cosmochimica Acta* 46, 1011–1040.

Pokrovsky, O.S., Mielczarski, J.A., Barres, O., Schott, J., 2000. Surface Speciation Models of Calcite and Dolomite / Aqueous Solution Interfaces and Their Spectroscopic Evaluation. *Langmuir* 16, 2677–2688.

Politi, Y., Batchelor, D.R., Zaslansky, P., Chmelka, B.F., Weaver, J.C., Sagi, I., Weiner, S., Addadi, L., 2010. Role of Magnesium Ion in the Stabilization of Biogenic Amorphous Calcium Carbonate: A Structure−Function Investigation. *Chemistry of Materials* 22, 161–166.

Politi, Y., Levi-Kalisman, Y., Raz, S., Wilt, F., Addadi, L., Weiner, S., Sagi, I., 2006. Structural Characterization of the Transient Amorphous Calcium Carbonate Precursor Phase in Sea Urchin Embryos. *Advanced Functional Materials* 16, 1289–1298.

Radha, A.V., Fernandez-Martinez, A., Hu, Y., Jun, Y.-S., Waychunas, G.A., Navrotsky, A., 2012. Energetic and structural studies of amorphous $Ca_{1-x}Mg_xCO_3 \cdot nH_2O$ (0<=x<=1). *Geochimica et Cosmochimica Acta* 90, 83–95.

Radu, A.I., Bergwerff, L., van Loosdrecht, M.C.M., Picioreanu, C., 2014. A two-dimensional mechanistic model for scaling in spiral wound membrane systems. *Chemical Engineering Journal* 241, 77–91.

Radu, A.I., Vrouwenvelder, J.S., van Loosdrecht, M.C.M., Picioreanu, C., 2010. Modeling the effect of biofilm formation on reverse osmosis performance: Flux, feed channel pressure drop and solute passage. *Journal of Membrane Science* 365, 1–15.

Raiteri, P., Gale, J.D., 2010. Water Is the Key to Nonclassical Nucleation of Amorphous Calcium Carbonate. *Journal of the American Chemical Society* 132, 17623–34.

Redden, G., Fox, D., Zhang, C., Fujita, Y., Guo, L., Huang, H., 2014. CaCO3 precipitation, transport and sensing in porous media with in situ generation of reactants. *Environmental science & technology* 48, 542–549.

Reid, G., Tieszer, C., Denstedt, J., Kingston, D., 1995. Examination of bacterial and encrustation deposition on ureteral stents of differing surface properties, after indwelling in humans. *Colloids and Surfaces B-Biointerfaces* 5, 171–179.

Riding, R., 2000. Microbial carbonates: the geological record of calcified bacterial-algal mats and biofilms. *Sedimentology* 47, 179–214.

Riding, R., Liang, L., 2005. Geobiology of microbial carbonates: metazoan and seawater saturation state influences on secular trends during the Phanerozoic. *Palaeogeography, Palaeoclimatology, Palaeoecology* 219, 101–115.

Rodriguez-Navarro, C., Jimenez-Lopez, C., Rodriguez-Navarro, A., Gonzalez-Muñoz, M.T., Rodriguez-Gallego, M., 2007. Bacterially mediated mineralization of vaterite. *Geochimica et Cosmochimica Acta* 71, 1197–1213.

Ruiz-Agudo, E., Putnis, C.V., Rodriguez-Navarro, C., Putnis, A., 2011. Effect of pH on calcite growth at constant a_{Ca2+}/a_{CO32-} ratio and supersaturation. *Geochimica et Cosmochimica Acta* 75, 284–296.

Sánchez-Román, M., McKenzie, J. a., de Luca Rebello Wagener, A., Romanek, C.S., Sánchez-Navas, A., Vasconcelos, C., 2011. Experimentally determined biomediated Sr partition coefficient for dolomite: Significance and implication for natural dolomite. *Geochimica et Cosmochimica Acta* 75, 887–904.

Schindelin, J., Arganda-Carreras, I., Frise, E., Kaynig, V., Longair, M., Pietzsch, T., Preibisch, S., Rueden, C., Saalfeld, S., Schmid, B., Tinevez, J.-Y., White, D.J., Hartenstein, V., Eliceiri, K., Tomancak, P., Cardona, A., 2012. Fiji: an open-source platform for biological-image analysis. *Nature methods* 9, 676–682.

Schultz, L., Pitts, B., Mitchell, A.C., Cunningham, A.B., Gerlach, R., 2011. Imaging Biologically Induced Mineralization in Fully Hydrated Flow Systems. *Microscopy Today* 19, 12–15.

Seymour, J.D., Codd, S.L., Gjersing, E.L., Stewart, P.S., 2004. Magnetic resonance microscopy of biofilm structure and impact on transport in a capillary bioreactor. *Journal of Magnetic Resonance* 167, 322–327.

Seymour, J.D., Gage, J.P., Codd, S.L., Gerlach, R., 2007. Magnetic resonance microscopy of biofouling induced scale dependent transport in porous media. *Advances in Water Resources* 30, 1408–1420.

Shafahi, M., Vafai, K., 2009. Biofilm affected characteristics of porous structures. *International Journal of Heat and Mass Transfer* 52, 574–581.

Stephens, J.C., Keith, D.W., 2008. Assessing geochemical carbon management. *Climatic Change* 90, 217–242.

Stewart, P.S., 1998. A review of experimental measurements of effective diffusive permeabilities and effective diffusion coefficients in biofilms. *Biotechnology and Bioengineering* 59, 261–272.

Stewart, P.S., 2003. Diffusion in Biofilms. *Journal of Bacteriology* 185, 1485–1491.

Stoodley, P., Boyle, J.D., DeBeer, D., Lappin-Scott, H.M., 1999. Evolving perspectives of biofilm structure. *Biofouling* 14, 75–90.

Stoodley, P., Dodds, I., Boyle, J.D., Lappin-Scott, H.M., 1998. Influence of hydrodynamics and nutrients on biofilm structure. *Journal of Applied Microbiology* 85 Suppl 1, 19S–28S.

Stoodley, P., Wilson, S., Hall-Stoodley, L., Boyle, J.D., Lappin-Scott, H.M., Costerton, J.W., 2001. Growth and detachment of cell clusters from mature mixed-species biofilms. *Applied and Environmental Microbiology* 67, 5608–5613.

Teodósio, J.S., Simões, M., Melo, L.F., Mergulhão, F.J., 2011. Flow cell hydrodynamics and their effects on *E. coli* biofilm formation under different nutrient conditions and turbulent flow. *Biofouling* 27, 1–11.

Tobler, D.J., Cuthbert, M.O., Greswell, R.B., Riley, M.S., Renshaw, J.C., Handley-Sidhu, S., Phoenix, V.R., 2011. Comparison of rates of ureolysis between *Sporosarcina pasteurii* and an indigenous groundwater community under conditions required to precipitate large volumes of calcite. *Geochimica et Cosmochimica Acta* 75, 3290–3301.

Van Cappellen, P., Charlet, L., Stumm, W., Wersin, P., 1993. A surface complexation model of the carbonate mineral-aqueous solution interface. *Geochimica et Cosmochimica Acta* 57, 3505–3518.

Van Lith, Y., Warthmann, R., Vasconcelos, C., Mckenzie, J.A., 2003. Sulphate-reducing bacteria induce low-temperature Ca-dolomite and high Mg-calcite formation. *Geobiology* 1, 71–79.

Van Paassen, L.A., Daza, C.M., Staal, M., Sorokin, D.Y., van der Zon, W., van Loosdrecht, M.C.M., 2010. Potential soil reinforcement by biological denitrification. *Ecological Engineering* 36, 168–175.

Van Wijngaarden, W.K., Vermolen, F.J., van Meurs, G.A.M., Vuik, C., 2010. Modelling Biogrout: A New Ground Improvement Method Based on Microbial-Induced Carbonate Precipitation. *Transport in Porous Media* 87, 397–420.

Vandevivere, P., Baveye, P., 1992. Saturated hydraulic conductivity reduction caused by aerobic bacteria in sand columns. *Soil Science Society of America …* 56, 1–13.

Vasconcelos, C., McKenzie, J.A., Bernasconi, S., Grujic, D., Tiens, A.J., 1995. Microbial mediation as a possible mechanism for natural dolomite formation at low temperatures. *Nature* 377, 220–222.

Vile, M.A., Wieder, R.K., 1993. Alkalinity generation by Fe(III) reduction versus sulfate reduction in wetlands constructed for acid mine drainage treatment. *Water, Air and Soil Pollution* 69, 425–441.

Volmer, M., Adhikari, G., 1926. Proof and measurement of the diffusion of adsorbed molecules on surfaces of solid bodies. *Zeitschrift fur Physikalische Chemie-Stochiometrie und Verwandtschaftslehre* 119, 46–52.

Wada, N., Okazaki, M., Tachikawa, S., 1993. Effects of calcium-binding polysaccharides from calcareous algae on calcium carbonate polymorphs under conditions of double diffusion. *Journal of Crystal Growth* 132, 115–121.

Wallmann, K., Aloisi, G., Haeckel, M., Obzhirov, A., Pavlova, G., Tishchenko, P., 2006. Kinetics of organic matter degradation, microbial methane generation, and gas hydrate formation in anoxic marine sediments. *Geochimica et Cosmochimica Acta* 70, 3905–3927.

Weiss, I.M., Tuross, N., Addadi, L., Weiner, S., 2002. Mollusc larval shell formation: amorphous calcium carbonate is a precursor phase for aragonite. *The Journal of Experimental Zoology* 293, 478–491.

Werner, W.S.M., 2001. Electron transport in solids for quantitative surface analysis. *Surface and Interface Analysis* 31, 141–176.

Whiffin, V.S., van Passen, L.A., Harkes, M.P., 2007. Microbial carbonate precipitation as a soil improvement technique. *Geomicrobiology Journal* 24, 417–423.

Wildenschild, D., Hopmans, J.W., Rivers, M.L., Kent, A.J.R., 2005. Quantitative Analysis of Flow Processes in a Sand Using Synchrotron-Based X-ray Microtomography. *Vadose Zone Journal* 4, 112–126.

Wildenschild, D., Sheppard, A.P., 2013. X-ray imaging and analysis techniques for quantifying pore-scale structure and processes in subsurface porous medium systems. *Advances in Water Resources* 51, 217–246.

Willingham, T.W., Werth, C.J., Valocchi, A.J., 2008. Evaluation of the effects of porous media structure on mixing-controlled reactions using pore-scale modeling and micromodel experiments. *Environmental Science & Technology* 42, 3185–3193.

Wolthers, M., Nehrke, G., Gustafsson, J.P., Van Cappellen, P., 2012. Calcite growth kinetics: Modeling the effect of solution stoichiometry. *Geochimica et Cosmochimica Acta* 77, 121–134.

Wu, Y., Ajo-Franklin, J.B., Spycher, N., Hubbard, S.S., Zhang, G., Williams, K.H., Taylor, J., Fujita, Y., Smith, R., 2011. Geophysical monitoring and reactive transport modeling of ureolytically-driven calcium carbonate precipitation. *Geochemical Transactions* 12, 1–20.

Xiao, J., Wang, Z., Tang, Y., Yang, S., 2010. Biomimetic mineralization of $CaCO_3$ on a phospholipid monolayer: from an amorphous calcium carbonate precursor to calcite via vaterite. *Langmuir: The ACS Journal of Surfaces and Colloids* 26, 4977–4983.

Xu, T., Ontoy, Y., Molling, P., Spycher, N., Parini, M., Pruess, K., 2004. Reactive transport modeling of injection well scaling and acidizing at Tiwi field, Philippines. *Geothermics* 33, 477–491.

Yingjie, Q., Cabral, J.M.S., 2002. Properties and Applications of Urease. *Biocatalysis and Biotransformation* 20, 1–14.

Yoreo, J. De, Vekilov, P., 2003. Principles of crystal nucleation and growth. *Reviews in Mineralogy and Geochemistry* 54, 57–93.

Yoshida, N., Higashimura, E., Saeki, Y., 2010. Catalytic biomineralization of fluorescent calcite by the thermophilic bacterium Geobacillus thermoglucosidasius. *Applied and Environmental Microbiology* 76, 7322–7327.

Zack, G.W., Rogers, W.E., Latt, S.A., 1977. Automatic measurement of sister chromatid exchange frequency. *The Journal of Histochemistry and Cytochemistry* 25, 741–753.

Zhang, C., Oostrom, M., Wietsma, T.W., Grate, J.W., Warner, M.G., 2011. Influence of Viscous and Capillary Forces on Immiscible Fluid Displacement: Pore-Scale Experimental Study in a Water-Wet Micromodel Demonstrating Viscous and Capillary Fingering. *Energy & Fuels* 25, 3493–3505.

Zhang, C.Y., Dehoff, K., Hess, N., Oostrom, M., Wietsma, T.W., Valocchi, A.J., Fouke, B.W., Werth, C.J., 2010a. Pore-Scale Study of Transverse Mixing Induced CaCO(3) Precipitation and Permeability Reduction in a Model Subsurface Sedimentary System. *Environmental Science & Technology* 44, 7833–7838.

Zhang, C.Y., Kang, Q.J., Wang, X., Zilles, J.L., Müller, R.H., Werth, C.J., Muller, R.H., 2010b. Effects of Pore-Scale Heterogeneity and Transverse Mixing on Bacterial Growth in Porous Media. *Environmental Science & Technology* 44, 3085–3092.

Zhang, T., Klapper, I., 2010. Mathematical model of biofilm induced calcite precipitation. *Water Science and Technology* 61, 2957–2964.

Zhang, T.Y., Klapper, I., 2011. Mathematical model of the effect of electrodiffusion on biomineralization. *International Journal of Non-Linear Mechanics* 46, 657–666.

Zhang, Y.P., Dawe, R., 1998. The kinetics of calcite precipitation from a high salinity water. *Applied Geochemistry* 13, 177–184.

Zhang, Y.P., Dawe, R. a., 2000. Influence of Mg^{2+} on the kinetics of calcite precipitation and calcite crystal morphology. *Chemical Geology* 163, 129–138.

Zhao, H., Thompson, R., Lockatell, V., Johnson, D.E., Mobley, H.L.T., 1998. Use of green fluorescent protein to assess urease gene expression by uropathogenic Proteus mirabilis during experimental ascending urinary tract infection. *Infection and Immunity* 66, 330–335.

Zhong, S., Mucci, A., 1989. Calcite and aragonite precipitation from seawater solutions of various salinities: Precipitation rates and overgrowth compositions. *Chemical Geology* 78, 283–299.

Zuo, L., Zhang, C., Falta, R.W., Benson, S.M., 2013. Micromodel investigations of CO2 exsolution from carbonated water in sedimentary rocks. *Advances in Water Resources* 53, 188–197.

APPENDICES

APPENDIX A

NUCLEOTIDE SEQUENCES REFERENCED IN CHAPTER 3

Nucleotide Sequences

The sequence of primers used for PCR amplification of the urease operon in *E. coli* DH5α(pURE14.8) were as follows:

Forward: N_6**CTGCAG**TTCATTCACATCCTACCCTAC
Bold underline is *PstI* site.

Reverse: N_6**ACTAGT**CTGAGCAAAAACAAGTCAAATTAG
Bold underline is *SpeI* site.

Table A1. The sequence of the urease operon in pJN105 vector and primers used for sequential sequencing.

Legend:

pJN105 promoter

Restriction sites *PstI* and *SpeI* respectively (Bold Underline)

Match to the known urease sequence of DH5α(pURE14.8) *ureDABC* and *ureFG* respectively

Previously unknown sequence

Primers used for the stepwise sequencing of the insert (Underline)

Insertions from the previously sequenced sections of DH5α(pURE14.8)

```
1    tccatacccg ttttttgggg ctagcgaatt cctgcagttc attcacatcc taccctactt
61   gcattagctt ttacatcaca aacacccaat tttggctggg gtatagctaa acatgttcgc
121  gtatttttag ttgactgagt tgcaggagaa agtatgtctg atttttcagg atcaggctgg
181  ttagctgaaa tcttcttacg atatgaacta aaacgtggcg tcacccgctt aacggataaa
241  caacatatcg gccctttaat ggttcagcgg ccattctacc ccgagcaagg aattgcacac
301  acctatttac ttcatccacc cggtggcgtt gtcgggggg ataaactcct tattaatatt
361  gatgttcaac cacacgccca tgcgttattg accacgcccg gtgcgacaaa attttatcgc
421  agtgcgggcg gtgttgcgcg acaagtacaa acattaactg ttgcgcccaa tgggttctta
481  gaatggctac ctcaagaaaa tatttttttc cctgaggctc aagttcgctt agaaacccac
541  gttcgaatcg ctagttcatc aaaatttatc agctgggaaa tccaatgttt agggcgccca
601  gtattaaacg agcaattcga caacggtgat attcggggcc gcttgcagtt ttatattgat
661  gacaaactca ccttagcgga atccatattt atcgaaggtt cgcaaaaaca atcagccgtc
```

721 atgcgtgaat ttcctatggt cggctccttg tatatctacc ccgccagcga tgagttaaaa
781 gctgaacttc acgagagttt ggccgtgttt ttctctacgg aagtgagacc gcttgaatat
841 gggctaactg atgtagacgg cattttagta ttacggttat taggttctca aaccgagccg
901 atgatggctt gctttgccca tatttggcag gcaacaagac aatattggtt aggttattgc
961 ccagaaccac cgcgtatttg ggcaacttaa acgtttttta ggagcaaaaa atggaattaa
1021 ccccaagaga aaaagataaa ttattgcttt ttacagcagg cctcgttgct gaaaggcgtt
1081 tagcccgtgg gctaaagctc aattaccctg aagccgtcgc gctgatcagt tgtgcgatta
1141 tggaaggcgc acgtgatggt aaaactgtcg cccaattaat gagcgaaggc cgaaccctat
1201 taaccgcaga gcaggtaatg gaaggcgtgc cagaaatgat caaagacatc caagtggaat
1261 gtacatttcc tgatggcaca aaactggttt ctattcacga cccgattgta taggtaacaa
1321 aatgatcccc ggtgaaatta aagtcaacca cgctttgggt gatatcgaac taaatgcagg
1381 ccgagaaacc caaacgatac aagttgccaa ccatggtgac cgcccgattc aaattggctc
1441 tcactatcat ttttatgaag tcaacgacgc cctaaaattt gaacgcgaaa atacactcgg
1501 ttttcgtttg aatatccctg cgggcatggc ggtacgtttt gaaccaggac aaagccgcac
1561 agttgaactt gtggctttta gcggcaagcg agaaatatat ggtttccatg gcaaagtcat
1621 gggtaaatta gagagtgaga attaataatg aaaacaatct ctcgtcaagc gtatgcagat
1681 atgtttggtc caacaacagg tgaccgttta cgcttagctg atacagaatt atttctagag
1741 atcgaaaaag atttcaccac gtatggtgaa gaggtcaaat ttggtggcgg taaagttatt
1801 cgtgacggca tgggccaaag ccaagtcacc agtgacctat gtgtcgatgt gctaatcacc
1861 aacgccatta ttttagacca ttggggcatt gttaaagcgg atatcgggat caaaaatggc
1921 cgtattgcgg ggattggtaa agcaggtaac cctgatgttc aacccaatgt cgatatcgtt
1981 atcggccccg gtaccgaagt ggttgcaggc gaaggtaaaa ttatcaccgc gggtggcgtt
2041 gatacccaca tccattttat ttgcccacag caagcagaag aaggtcttgt ttccggtgtt
2101 accaccttta taggcggtgg aactggccct gtggctggca ctaatgccac taccgtcacc
2161 cccggtattt ggaatatgta ccgcatgtta gaagctgttg atgaactgcc tatcaacgtc
2221 gggctatttg gtaaaggctg cgtcagtagg cccgaagcga ttcgcgaaca aattgaagcg
2281 ggtgccattg gcttaaaaat tcacgaggac tggggcgcta ccccaatggc tattcacaac
2341 tgtttgaatg tggctgatga aatggatgtg caagtggcta tccattcaga tacgttaaat
2401 gaaggcggtt tttatgaaga aaccgtgaag gccattgcag gacgagtgat ccacgtattc
2461 catacagaag gtgctggcgg tggccatgcc cctgacgtca tcaaatccgt cggagaaccg
2521 aatattctgc ctgcatcgac caacccaacg atgccataca ccatcaatac cgttgatgag
2581 cacttggata tgttaatggt ttgccaccat ctcgacccat caattccaga agatgtggct
2641 tttgcggaat ctcgtattcg ccgtgaaacc attgctgcgg agatattttg cggaatctcg
2701 tattcgccgt gaaaccattg ctgcggaaga tattttgcac gatatgggcg caatttctgt
2761 gatgtcttca gactcacaag ccatggggcg cgttggtgaa gttatcactc gcacttggca
2821 gtgcgcccat aaaatgaaat tacagcgcgg aactttagaa ggtgacacac cagaaagcga
2881 taataaccgt atcaaacgtt atgtggcgaa atacaccatt aaccccgcta tcgctcacgg
2941 tatcgcccat gaagtcggtt cgatagaaat aggcaagtta gctgatatcg tattatggga
3001 ccctgcattt tttggcatca aacccgccct aattatgaaa gggggaatgg tcgcctatgc
3061 gccaatgggt gatattaacg ccgcaatccc aacaccacag cctgtacatt accgcccgat
3121 gtttggagca ttaggtaaag caaaatacca tacctcaatg atttttatgt caaaagcagg
3181 tattgaagca ggtgttcctg aaaaattagg cttgcagagc caaataggcc gagttgaagg
3241 ctgccgaagc attagcaaag cctctatggt gcacaacagt tatgtgccac atatcgaact
3301 tgacccgcaa acttatatcg tcaaagccga tggtatccca ctggtatgcg aacctgcgac
3361 tgagttaccg atggcacaac gttacttttt attctgaccc ctaattaaaa gagccagaga
3421 atgaaaaaat ttattaaagt ggttgcccaa caaccccatt caccaagcac attaaccctg
3481 tgcttaacca tggatgagcg caccaaaagc cgtttaaaag ttaccttaag tgatgggcaa
3541 gaagcggggc tatttttgcc gcgcggaacc atcctgaagg aaggcgacgt tttatccact
3601 gaagacggtg agttagtcac aatcgaagcc gcgaaagagc aagtttctac cgtttacagc
3661 gatgacgctc tgttgctcgc ccgcgtttgc tatcacttag gcaaccgcca tgttcctttg
3721 caaattgaag cgggttggtg ccgttatttt catgaccatg tgttagatga tatggcgcgt
3781 gggttaggtg ccacggttag tgtcggtttg gaaaaatacc aaccggaacc gggggcttat
3841 ggcggctcat ccggtggtca tcaccaccat cacggccacg atgatcacca tcactaatca

3901 ggttcaggga gtgtgcttat gttagcagat ctgcgcttat accagttagt tagtccttct
3961 ttacctgttg gctcgtttac ctattcacaa ggcttagaat gggcgattga aaaaggttgg
4021 gtaacaacac cagataccct tgcaggctgg ctaaccgcac aaatgacgca tgccattgca
4081 acattagagc ttcccgtttt acggcaaatt cagacttccc tttcccttgg tgatattgaa
4141 gcggtgaaat attggtgtga atttatgatt gccagccgtg aaaccaaaga actacgccaa
4201 gaagagcggc aacgaggaat tgcttttgca cgattgctac ctcaactagg cattgaactg
4261 gatgctaacc tgcaaacctg cgtgaaacaa acccagctaa tggccttcgc cctcgccgcg
4321 gtaaattggc aaattgacgt tgaaaaattg tgcaccgcgt atgcatgggg ttggctagaa
4381 aacacggtga tgtccggtgt taagcttatc cctttagggc aaagcgcggg gcaaaatatt
4441 ttatttaccc ttgctgagcg catacccgaa gtggttgcgc aatcggcaat ctggccatta
4501 gacgatattg gtagttttac acctgcacaa attattgcca gtagtcggca tgaaacccaa
4561 tacacacgac tttttcgttc atgagaaaat gctatgcaag aatataatca acccttaaga
4621 attggtgtcg gtgggccggt cggctcagga aaaaccgcat tattagaagt gttatgtaaa
4681 gccatgcgcg acacttacca aattgccgtt gtcaccaatg atatttacac ccaagaagat
4741 gccaaaattt taacccgtgc cgaagcacta gatgcagacc gcattattgg tgttgaaact
4801 ggcggctgcc ctcataccgc tattcgtgaa gatgcatcaa tgaacttagc ggccgttgaa
4861 gagttagcta tccgccataa aaaccttgat atcgtgtttg tggaaagcgg cggcgataac
4921 ctcagtgcga cgtttagccc agagctggca gacttaacca tttatgtgat tgatgttgct
4981 gaaggcgaaa aaattccacg taaaggtggg ccagggatca cccattccga tttactggtg
5041 attaacaaaa ttgaccttgc tccgtatgtc ggcgcttcat tagaagtgat ggaagccgat
5101 accgcaagaa tgcgaccagt aaagccctat gttttactaa cttaaagaaa aaagtcggct
5161 tagagaccat tatcgagttt atcatcgata aaggcatgtt aagacgttaa taaatttgga
5221 cgccctatag gtttattta tagggcgttt tcaattaaca aatacggggt aaaggctcgc
5281 tgtgaggcaa atctaataac cttgatgtgc cgaagatccc aactaatttg acttgttttt
5341 gctcag**acta gt**tctagagc ggccgccacc gcggtggagc tccaattcgc ccta

APPENDIX B

SUPPLEMENTAL INFORMATION FOR CHAPTER 4

Strain and Growth Conditions

Escherichia coli MJK2 (Connolly et al., 2013) was used as the model biofilm-producing ureolytically active organism in this study. MJK2 possesses a pJN105 plasmid that has been modified to contain the urease operon from *E. coli* DH5α(pURE14.8) (Collins and Falkow, 1988). The urease-carrying plasmid, pMK001, contains an L-arabinose-inducible promoter and encodes for gentamycin resistance. MJK2 also possesses a mutant chromosomal *gfp* (green fluorescent protein gene) variant that can be used for imaging. The parent strain of MJK2 is *E. coli* AF504 which is a nalidixic acid resistant derivative of *E.coli* K12 strain MG1655 (Folkesson et al., 2008). The growth medium for MJK2 was Luria–Bertani (LB) medium containing 10 g/L tryptone, 5 g/L yeast extract, 10 g/L NaCl, supplemented with 50 mM (7.5 g/L) L-arabinose, 10 µM $NiCl_2$, 10 µg/mL gentamycin and varying amounts of urea. The medium was adjusted to a pH of 6 with HCl.

100 mL liquid cultures were inoculated from frozen stock cultures at a concentration of 1.0 µL per mL in 250 mL Erlenmeyer flasks at 37ºC on horizontal shakers running at approximately 150 rpm. The urea concentration of the starter culture matched the experimental concentration in the tube reactors. 100 µL of culture was transferred into 100 mL of the same media after approximately 24 hours. Cells from the transfer culture were harvested after approximately 12 hours by centrifugation at 4200×g for 10 minutes at 5ºC in 50 mL conical centrifuge tubes containing 40 mL of culture. Cells were suspended in sterile phosphate buffered saline (PBS) by vigorous vortexing.

Cells were washed one more time by centrifugation and resuspension. PBS had final concentrations of 8 g/L NaCl, 0.61 g/L KH_2PO_4, 0.96 g/L K_2HPO_4 and was adjusted to a pH of 7 with HCl. The cell suspension was adjusted to an optical density of 0.6 by diluting with additional PBS after the final cell wash. Optical density was measured on triplicate 100 µL samples in polycarbonate 96-well plates (light path length of 0.26 cm) with a BioTek Instuments (Winooski, VT, USA) Synergy HT Multi-Mode Microplate Reader, and the data were analyzed using Gen5 software. The cell suspensions were used as the inoculum for the biofilm growth experiments.

References Relating to the Strain and Growth Conditions

Collins CM, Falkow S. 1988. Genetic Analysis of an *Escherichia coli* Urease Locus: Evidence of DNA Rearrangement. *Journal of Bacteriology* 170:1041–1045.

Connolly J, Kaufman M, Rothman A, Gupta R, Redden G, Schuster M, Colwell F, Gerlach R. 2013. Construction of two ureolytic model organisms for the study of microbially induced calcium carbonate precipitation. *Journal of Microbiological Methods* 94:290–299.

Folkesson A, Haagensen JAJ, Zampaloni C, Sternberg C, Molin S. 2008. Biofilm Induced Tolerance towards Antimicrobial Peptides. *Plos One* 3:e1891.

Biofilm Thin Section Calculations

The following calculations were applied to the thresholded thin section images (e.g. Figure 2C) in order to estimate a representative biofilm thickness at discrete points within the tube.

Table B1. Constants used in thickness calculations

Pixel Size (p)	0.449965 μm/px
Image Size (X by Y)	1940 by 1460 px
Total Image Area (A)	573471.78 μm^2
Visible Biofilm Arc Length (S)	922.95 μm
Tube Inside Radius (r)	800 μm

The visible biofilm arc length was calculated by first calculating the known chord length (C) of the visible biofilm arc,

$$C = X\,p = 872.61\,\mu m\,. \qquad \text{(B1)}$$

Images were taken such that they were centered in the long dimension (X) of the image. The central angle of the biofilm arc (θ) can then be calculated with a simple trigonometric relationship where

$$\theta = 2\sin^{-1}\left(\frac{0.5\,C}{r}\right) = 1.154\,\text{rad}\,, \qquad \text{(B2)}$$

and finally the biofilm arc length can be calculated by

$$S = r\,\theta = 922.95\,\mu m\,. \qquad \text{(B3)}$$

Images were thresholded as stated in the main article and the image area occupied by biofilm (A_f) was determined in ImageJ. The calculated average biofilm thickness (L_f) for each image, as reported in Tables S2-S9, was then be calculated by

$$L_f = A_f / S . \qquad \text{(B4)}$$

It should be noted that this calculation is only valid for thin biofilms. Thin in this context means that the biofilm thickness is much smaller than the tube radius ($L_f << r$). If the thin condition is not met, the visible area of the biofilm will be dependent on L_f due to the vertically (rather than radially) cut off biofilms at the edges of the image.

Urea Measurements

Table B2 Urea measurements obtained in the study including those that were eliminated from the analysis.

Tube #	Sample		Concentration (mol/L)	Effluent Mean (mol/L)	Variation from Mean	Notes
1	1	Out A	0.00368	0.00422	12.80%	
	1	Out B	0.00438		-3.76%	
	1	Out C	0.00461		-9.04%	
	1	In	0.01168			
2	2	Out A	0.10189	0.10872	6.29%	
	2	Out B	0.10972		-0.92%	
	2	Out C	0.11456		-5.37%	
	2	In	0.12835			
3	3	Out A	0.13588	0.13367	-1.65%	
	3	Out B	0.13435		-0.50%	
	3	Out C	0.13079		2.15%	
	3	In	0.14519			
4	4	Out A	0.20390	0.20637	1.20%	
	4	Out B	0.20741		-0.50%	
	4	Out C	0.20781		-0.70%	
	4	In	0.21952			
5	5	Out A	0.00328	0.00460	28.70%	Excluded due to high effluent variation (> 25%)
	5	Out B	0.00311		32.43%	
	5	Out C	0.00741		-61.13%	
	5	In	0.01220			
6	6	Out A	0.04851	0.04632	-4.72%	
	6	Out B	0.04734		-2.19%	
	6	Out C	0.04312		6.91%	
	6	In	0.07271			
7	7	Out A	0.11966	0.11868	-0.83%	
	7	Out B	0.12087		-1.84%	
	7	Out C	0.11550		2.68%	
	7	In	0.14066			
8	8	Out A	0.19859	0.20216	1.77%	
	8	Out B	0.20585		-1.82%	
	8	Out C	0.20205		0.06%	
	8	In	0.22077			
9	9	Out A	0.00653	0.00722	9.54%	
	9	Out B	0.00686		5.05%	
	9	Out C	0.00828		-14.59%	
	9	In	0.01053			
10	10	Out A	0.03980	0.04933	19.31%	Excluded due to high effluent variation (> 25%)
	10	Out B	0.03969		19.53%	
	10	Out C	0.06848		-38.84%	
	10	In	0.08295			
11	11	Out A	0.08498	0.09962	14.70%	Excluded due to high effluent variation (> 25%)
	11	Out B	0.13257		-33.08%	
	11	Out C	0.08131		18.38%	
	11	In	0.15836			

Note: Samples “Out C” and “In” were taken as the representative concentrations for each tube.

Biofilm Thin Section Data

Table B3. Tube 1 thin section data.

Tube #	x Distance from Inlet	Calculated Thickness (L_f)	Averages from Replicates: x Distance from Inlet	Averages from Replicates: Calculated Thickness(L_f)
	[cm]	[µm]	[cm]	[µm]
1	1	50.07	1	45.74
1	1	44.72	3	155.32
1	1	40.14	5	143.15
1	1	45.63	7	14.90
1	1	48.12	9	16.18
1	3	173.34		
1	3	159.22		
1	3	144.21		
1	3	144.51		
1	5	62.61		
1	5	136.96		
1	5	132.68		
1	5	161.45		
1	5	222.03		
1	7	17.00		
1	7	11.74		
1	7	13.45		
1	7	17.40		
1	9	12.94		
1	9	14.66		
1	9	20.94		

Table B4. Tube 2 thin section data.

Tube #	x Distance from Inlet	Calculated Thickness (L_f)	Averages from Replicates: x Distance from Inlet	Averages from Replicates: Calculated Thickness (L_f)
	[cm]	[μm]	[cm]	[μm]
2	1	9.22	1	9.08
2	1	10.17	3	11.53
2	1	8.66	5	9.09
2	1	8.33	7	7.98
2	1	9.03	9	5.34
2	3	9.15		
2	3	11.42		
2	3	11.26		
2	3	14.30		
2	5	9.87		
2	5	10.47		
2	5	8.99		
2	5	7.97		
2	5	8.14		
2	7	7.56		
2	7	7.93		
2	7	8.46		
2	7	7.80		
2	7	8.14		
2	9	3.94		
2	9	5.75		
2	9	4.92		
2	9	6.51		
2	9	5.56		

Table B5. Tube 3 thin section data.

Tube #	x Distance from Inlet	Calculated Thickness (L_f)	Averages from Replicates: x Distance from Inlet	Averages from Replicates: Calculated Thickness (L_f)
	[cm]	[μm]	[cm]	[μm]
3	1	8.79	1	8.47
3	1	8.08	3	10.91
3	1	9.16	5	9.21
3	1	7.66	7	9.00
3	1	8.66	9	9.00
3	3	7.21		
3	3	10.18		
3	3	11.25		
3	3	11.48		
3	3	14.46		
3	5	9.68		
3	5	9.44		
3	5	7.93		
3	5	8.87		
3	5	10.15		
3	7	9.08		
3	7	8.94		
3	7	8.96		
3	7	9.13		
3	7	8.90		
3	9	8.02		
3	9	9.69		
3	9	9.98		
3	9	8.31		

Table B6. Tube 4 thin section data.

Tube #	x Distance from Inlet	Calculated Thickness (L_f)	Averages from Replicates: x Distance from Inlet	Averages from Replicates: Calculated Thickness (L_f)
	[cm]	[μm]	[cm]	[μm]
4	1	5.22	1	6.25
4	1	6.29	3	8.43
4	1	6.52	5	4.43
4	1	6.01	7	6.93
4	1	7.19	9	6.65
4	3	7.45		
4	3	11.04		
4	3	7.34		
4	3	7.91		
4	3	8.43		
4	5	4.95		
4	5	3.78		
4	5	5.20		
4	5	4.14		
4	5	4.08		
4	7	7.06		
4	7	6.79		
4	9	5.65		
4	9	5.18		
4	9	9.24		
4	9	6.51		

Table B7. Tube 6 thin section data.

Tube #	x Distance from Inlet	Calculated Thickness (L_f)	Averages from Replicates: x Distance from Inlet	Averages from Replicates: Calculated Thickness (L_f)
	[cm]	[μm]	[cm]	[μm]
6	1	160.56	1	101.85
6	1	78.07	3	47.97
6	1	121.03	5	40.93
6	1	75.33	7	7.42
6	1	74.29	9	17.09
6	3	54.88		
6	3	41.51		
6	3	47.37		
6	3	43.13		
6	3	52.98		
6	5	30.17		
6	5	36.47		
6	5	49.37		
6	5	43.09		
6	5	45.54		
6	7	7.90		
6	7	7.06		
6	7	6.56		
6	7	7.40		
6	7	8.20		
6	9	18.24		
6	9	19.96		
6	9	15.88		
6	9	17.07		
6	9	14.28		

Table B8. Tube 7 thin section data.

Tube #	x Distance from Inlet	Calculated Thickness (L_f)	Averages from Replicates: x Distance from Inlet	Averages from Replicates: Calculated Thickness (L_f)
	[cm]	[μm]	[cm]	[μm]
7	1	63.97	1	48.73
7	1	45.92	3	8.13
7	1	45.70	5	51.94
7	1	42.85	7	3.63
7	1	45.18	9	1.26
7	3	7.56		
7	3	7.44		
7	3	7.49		
7	3	10.02		
7	5	52.18		
7	5	43.98		
7	5	49.63		
7	5	61.33		
7	5	52.60		
7	7	3.19		
7	7	3.86		
7	7	2.86		
7	7	2.29		
7	7	5.93		
7	9	1.06		
7	9	1.35		
7	9	1.26		
7	9	1.38		
7	9	1.04		

Table B9. Tube 8 thin section data.

Tube #	x Distance from Inlet	Calculated Thickness (L_f)	Averages from Replicates: x Distance from Inlet	Averages from Replicates: Calculated Thickness (L_f)
	[cm]	[μm]	[cm]	[μm]
8	1	12.01	1	13.34
8	1	14.55	3	8.73
8	1	13.86	5	6.23
8	1	13.92	7	11.04
8	1	12.36	9	3.85
8	3	8.08		
8	3	9.26		
8	3	7.74		
8	3	8.59		
8	3	9.99		
8	5	5.84		
8	5	5.72		
8	5	7.12		
8	7	11.77		
8	7	10.75		
8	7	10.17		
8	7	9.67		
8	7	12.83		
8	9	3.50		
8	9	4.50		
8	9	3.29		
8	9	3.09		
8	9	4.86		

Table B10. Tube 9 thin section data.

Tube #	x Distance from Inlet	Calculated Thickness (L_f)	Averages from Replicates: x Distance from Inlet	Averages from Replicates: Calculated Thickness (L_f)
	[cm]	[μm]	[cm]	[μm]
9	1	0.62	1	0.76
9	1	0.65	3	2.00
9	1	0.92	5	2.84
9	1	0.80	7	2.21
9	1	0.80	9	2.15
9	3	2.06		
9	3	2.00		
9	3	2.85		
9	3	1.47		
9	3	1.64		
9	5	2.75		
9	5	2.99		
9	5	3.40		
9	5	1.98		
9	5	3.11		
9	7	1.35		
9	7	1.90		
9	7	2.44		
9	7	2.10		
9	7	3.27		
9	9	2.14		
9	9	2.53		
9	9	2.08		
9	9	1.87		

APPENDIX C

RAW AND THRESHOLDED IMAGES RELATING TO CHAPTER 5

These data are available online through Montana State University at the following URL.

http://scholarworks.montana.edu/xmlui/handle/1/8980

To request DVD copies, contact your local public or university library to place an interlibrary loan request to Montana State University. Questions call 406-994-3161.

APPENDIX D

STEADY STATE PHREEQC OUTPUT RELATING TO CHAPTER 5

```
 Input file: C:\Users\User\Google Drive\MSU PhD Work\2 - Data Calcs and Modeling\20141120
- CO2 Eq PHREEQC\CompleteUreaolysisEquilibrium_AllUreolysis_WithCa.pqi
  Output file: C:\Users\User\Google Drive\MSU PhD Work\2 - Data Calcs and
Modeling\20141120 - CO2 Eq PHREEQC\CompleteUreaolysisEquilibrium_AllUreolysis_WithCa.pqo
Database file: C:\Program Files (x86)\USGS\Phreeqc Interactive 3.1.1-
8288\database\phreeqc.dat

------------------
Reading data base.
------------------

        SOLUTION_MASTER_SPECIES
        SOLUTION_SPECIES
        PHASES
        EXCHANGE_MASTER_SPECIES
        EXCHANGE_SPECIES
        SURFACE_MASTER_SPECIES
        SURFACE_SPECIES
        RATES
        END
-----------------------------------
Reading input data for simulation 1.
-----------------------------------

        DATABASE C:\Program Files (x86)\USGS\Phreeqc Interactive 3.1.1-
8288\database\phreeqc.dat
        EQUILIBRIUM_PHASES 2
            Calcite   0 0
        SOLUTION 4
            temp      25
            pH        6 charge
            pe        4
            redox     pe
            units     mol/kgw
            density   1
            C         0.1000978
            Cl        0.370940171
            N(-3)     0.2
            Na        0.1709
            O(0)      0.002457
            Ca        0.1
            water    1 # kg
        END
-------------------------------------------
Beginning of initial solution calculations.
-------------------------------------------

Initial solution 4.

-----------------------------Solution composition------------------------------

        Elements            Molality       Moles

        C                 1.001e-001  1.001e-001
        Ca                1.000e-001  1.000e-001
        Cl                3.709e-001  3.709e-001
        N(-3)             2.000e-001  2.000e-001
        Na                1.709e-001  1.709e-001
        O(0)              2.457e-003  2.457e-003

----------------------------Description of solution----------------------------

                                       pH  =   9.069      Charge balance
                                       pe  =   4.000
       Specific Conductance (uS/cm, 25 oC) = 41193
                           Density (g/cm3)  =   1.01696
                                Volume (L)  =   1.01838
                       Activity of water  =   0.985
                          Ionic strength  =  4.962e-001
                      Mass of water (kg)  =  1.000e+000
                 Total alkalinity (eq/kg)  =  2.000e-001
                      Total CO2 (mol/kg)  =  1.001e-001
                     Temperature (deg C)  =  25.00
                  Electrical balance (eq)  = -4.853e-014
 Percent error, 100*(Cat-|An|)/(Cat+|An|)  =  -0.00
```

```
                                Iterations  =  10
                                   Total H  = 1.118126e+002
                                   Total O  = 5.580894e+001

--------------------------------Redox couples--------------------------------

        Redox couple             pe  Eh (volts)

        O(-2)/O(0)          11.7391      0.6944

----------------------------Distribution of species----------------------------

                                                      Log       Log       Log    mole V
   Species          Molality    Activity  Molality  Activity     Gamma   cm3/mol

   OH-            1.845e-005  1.168e-005    -4.734    -4.932    -0.199     -2.93
   H+             1.116e-009  8.531e-010    -8.952    -9.069    -0.117      0.00
   H2O            5.551e+001  9.848e-001     1.744    -0.007     0.000     18.07
C(-4)         0.000e+000
   CH4            0.000e+000  0.000e+000   -84.438   -84.388     0.050     32.22
C(4)          1.001e-001
   HCO3-          4.273e-002  2.958e-002    -1.369    -1.529    -0.160     26.46
   CaCO3          3.578e-002  4.011e-002    -1.446    -1.397     0.050    -14.60
   CaHCO3+        7.835e-003  5.541e-003    -2.106    -2.256    -0.150      9.94
   CO3-2          7.080e-003  1.626e-003    -2.150    -2.789    -0.639     -2.50
   NaCO3-         4.870e-003  3.570e-003    -2.312    -2.447    -0.135      1.93
   NaHCO3         1.749e-003  1.961e-003    -2.757    -2.707     0.050      1.80
   CO2            5.140e-005  5.762e-005    -4.289    -4.239     0.050     29.09
Ca            1.000e-001
   Ca+2           5.638e-002  1.468e-002    -1.249    -1.833    -0.584    -16.85
   CaCO3          3.578e-002  4.011e-002    -1.446    -1.397     0.050    -14.60
   CaHCO3+        7.835e-003  5.541e-003    -2.106    -2.256    -0.150      9.94
   CaOH+          3.837e-006  2.813e-006    -5.416    -5.551    -0.135      (0)
Cl            3.709e-001
   Cl-            3.709e-001  2.413e-001    -0.431    -0.618    -0.187     18.69
H(0)          9.192e-030
   H2             4.596e-030  5.152e-030   -29.338   -29.288     0.050     28.61
N(-3)         2.000e-001
   NH4+           1.478e-001  8.754e-002    -0.830    -1.058    -0.228     18.38
   NH3            5.216e-002  5.847e-002    -1.283    -1.233     0.050     24.42
Na            1.709e-001
   Na+            1.643e-001  1.179e-001    -0.784    -0.929    -0.144     -0.63
   NaCO3-         4.870e-003  3.570e-003    -2.312    -2.447    -0.135      1.93
   NaHCO3         1.749e-003  1.961e-003    -2.757    -2.707     0.050      1.80
   NaOH           1.229e-016  1.377e-016   -15.911   -15.861     0.050      (0)
O(0)          2.457e-003
   O2             1.228e-003  1.377e-003    -2.911    -2.861     0.050     30.40

------------------------------Saturation indices-------------------------------

  Phase               SI** log IAP   log K(298 K,   1 atm)

  Aragonite          3.71     -4.62   -8.34  CaCO3
  Calcite            3.86     -4.62   -8.48  CaCO3
  CH4(g)           -81.54    -84.39   -2.84  CH4
  CO2(g)            -2.78     -4.24   -1.46  CO2
  H2(g)            -26.19    -29.29   -3.10  H2
  H2O(g)            -1.51     -0.01    1.50  H2O
  Halite            -3.12     -1.55    1.57  NaCl
  NH3(g)            -3.03     -1.23    1.80  NH3
  O2(g)              0.03     -2.86   -2.89  O2

**For a gas, SI = log10(fugacity). Fugacity = pressure * phi / 1 atm.
  For ideal gases, phi = 1.

-----------------------------------------
Beginning of batch-reaction calculations.
-----------------------------------------

Reaction step 1.

Using solution 4.
Using pure phase assemblage 2.

-------------------------------Phase assemblage--------------------------------
```

Phase	SI	log IAP	log K(T, P)	Moles in assemblage: Initial	Final	Delta
Calcite	0.00	-8.48	-8.48	0.000e+000	8.500e-002	8.500e-002

----------Solution composition----------

Elements	Molality	Moles
C	1.509e-002	1.510e-002
Ca	1.500e-002	1.500e-002
Cl	3.707e-001	3.709e-001
N	1.999e-001	2.000e-001
Na	1.708e-001	1.709e-001

----------Description of solution----------

pH	= 6.719	Charge balance
pe	= -3.770	Adjusted to redox equilibrium
Specific Conductance (uS/cm, 25 oC)	= 39709	
Density (g/cm3)	= 1.00807	
Volume (L)	= 1.01479	
Activity of water	= 0.987	
Ionic strength	= 3.903e-001	
Mass of water (kg)	= 1.001e+000	
Total alkalinity (eq/kg)	= 5.517e-003	
Total CO2 (mol/kg)	= 6.545e-003	
Temperature (deg C)	= 25.00	
Electrical balance (eq)	= 1.645e-013	
Percent error, 100*(Cat-|An|)/(Cat+|An|)	= 0.00	
Iterations	= 32	
Total H	= 1.118126e+002	
Total O	= 5.555395e+001	

----------Distribution of species----------

Species	Molality	Activity	Log Molality	Log Activity	Log Gamma	mole V cm3/mol
H+	2.470e-007	1.909e-007	-6.607	-6.719	-0.112	0.00
OH-	8.022e-008	5.234e-008	-7.096	-7.281	-0.185	-3.12
H2O	5.551e+001	9.871e-001	1.744	-0.006	0.000	18.07
C(-4)	8.550e-003					
CH4	8.550e-003	9.353e-003	-2.068	-2.029	0.039	32.22
C(4)	6.545e-003					
HCO3-	4.750e-003	3.354e-003	-2.323	-2.474	-0.151	26.14
CO2	1.333e-003	1.458e-003	-2.875	-2.836	0.039	29.09
CaHCO3+	2.390e-004	1.720e-004	-3.622	-3.764	-0.143	9.92
NaHCO3	2.124e-004	2.323e-004	-3.673	-3.634	0.039	1.80
CaCO3	5.087e-006	5.565e-006	-5.294	-5.255	0.039	-14.60
CO3-2	3.315e-006	8.240e-007	-5.480	-6.084	-0.605	-2.85
NaCO3-	2.588e-006	1.890e-006	-5.587	-5.724	-0.136	1.36
Ca	1.500e-002					
Ca+2	1.475e-002	4.020e-003	-1.831	-2.396	-0.565	-16.95
CaHCO3+	2.390e-004	1.720e-004	-3.622	-3.764	-0.143	9.92
CaCO3	5.087e-006	5.565e-006	-5.294	-5.255	0.039	-14.60
CaOH+	4.723e-009	3.450e-009	-8.326	-8.462	-0.136	(0)
Cl	3.707e-001					
Cl-	3.707e-001	2.472e-001	-0.431	-0.607	-0.176	18.62
H(0)	1.635e-009					
H2	8.173e-010	8.941e-010	-9.088	-9.049	0.039	28.61
N(-3)	1.755e-001					
NH4+	1.752e-001	1.079e-001	-0.757	-0.967	-0.211	18.34
NH3	2.944e-004	3.220e-004	-3.531	-3.492	0.039	24.42
N(0)	2.444e-002					
N2	1.222e-002	1.337e-002	-1.913	-1.874	0.039	29.29
N(3)	0.000e+000					
NO2-	0.000e+000	0.000e+000	-60.154	-60.351	-0.197	25.53
N(5)	0.000e+000					
NO3-	0.000e+000	0.000e+000	-82.831	-83.028	-0.197	30.08
Na	1.708e-001					
Na+	1.706e-001	1.232e-001	-0.768	-0.909	-0.141	-0.72
NaHCO3	2.124e-004	2.323e-004	-3.673	-3.634	0.039	1.80
NaCO3-	2.588e-006	1.890e-006	-5.587	-5.724	-0.136	1.36

```
   NaOH           5.894e-019  6.448e-019   -18.230   -18.191     0.039     (0)
O(0)         0.000e+000
   O2             0.000e+000  0.000e+000   -74.333   -74.294     0.039     30.40

------------------------------Saturation indices-------------------------------

  Phase               SI** log IAP   log K(298 K,   1 atm)

  Aragonite         -0.14     -8.48   -8.34  CaCO3
  Calcite            0.00     -8.48   -8.48  CaCO3
  CH4(g)             0.81     -2.03   -2.84  CH4
  CO2(g)            -1.37     -2.84   -1.46  CO2
  H2(g)             -5.95     -9.05   -3.10  H2
  H2O(g)            -1.51     -0.01    1.50  H2O
  Halite            -3.09     -1.52    1.57  NaCl
  N2(g)              1.30     -1.87   -3.18  N2
  NH3(g)            -5.29     -3.49    1.80  NH3
  O2(g)            -71.40    -74.29   -2.89  O2

**For a gas, SI = log10(fugacity). Fugacity = pressure * phi / 1 atm.
  For ideal gases, phi = 1.

------------------
End of simulation.
------------------

-----------------------------------
Reading input data for simulation 2.
-----------------------------------

-------------------------------
End of Run after 0.328 Seconds.
-------------------------------
```

APPENDIX E

MODEL PARAMETERS AND CODE ARCHITECTURE RELATING TO CHAPTER 6

COMSOL Model Parameters and Rate Expressions

Model Parameters

Q	0.25e-3[L/h]	Flow Rate
Vmax_urea	5[mol/(L*h)]	Approx from tube reactor experiment
km_urea	0.1[mol/L]	Approx from tube reactor experiment
Vmax_oxygen	10[mol/(L*h)]	Estimated o2 rate parameter
km_oxygen	0.5[mmol/L]	Estimated o2 rate parameter
D_bio	0.8	Biofilm diffusion reduction
Durea	1.38e-5[cm^2/s]	CRC 25C
Dco2	1.91e-5[cm^2/s]	CRC 25C
Dnh3	1.5e-5[cm^2/s]	CRC 20C
Dca	0.79e-5[cm^2/s]	CRC 25C
Dcl	2.032e-5[cm^2/s]	CRC 25C
Dhco3	1.185e-5[cm^2/s]	CRC 25C
Dco3	0.92e-5[cm^2/s]	Zhang Klapper (2011)
Dcahco3	1e-5[cm^2/s]	Estimation
Dcaco3	1e-5[cm^2/s]	Estimation
Dnh4	1.957e-5[cm^2/s]	CRC 25C
Dh	9.311e-5[cm^2/s]	CRC 25C
Doh	5.273e-5[cm^2/s]	CRC 25C
Doxygen	2.42e-5[cm^2/s]	CRC 25C
Ka_hco3	(10^(-10.33))[mol/L]	PHREEQC Database
Ka_co2	(10^(-6.35))[mol/L]	PHREEQC Database
Ka_nh4	(10^(-9.25))[mol/L]	PHREEQC Database
Ka_h2o	1e-14[mol^2/L^2]	PHREEQC Database
Ka_cahco3	(10^(-11.435))[mol^2/L^2]	PHREEQC Database
Ka_caco3	(10^(-3.224))[mol/L]	PHREEQC Database
Ci_urea	0.16667[mol/L]	10 g/L
Cit_ca	0.16667[mol/L]	Equamolar with urea
Cit_co2	0.003[mol/L]	Assume saturation wrt CO2
Cit_n	0.001[mol/L]	Start with background ammonium/ammonia
Ci_h	ai_h/g_h	Calculated from activity
Ci_cl	[From Equilibrium]	Calculated (for charge balance)
Ci_hco3	[From Equilibrium]	Calculated

Ci_co2	[From Equilibrium]	Calculated
Ci_co3	[From Equilibrium]	Calculated
Ci_cahco3	[From Equilibrium]	Calculated
Ci_ca	[From Equilibrium]	Calculated
Ci_caco3	[From Equilibrium]	Calculated
Ci_nh4	[From Equilibrium]	Calculated
Ci_nh3	[From Equilibrium]	Calculated
Ci_oh	[From Equilibrium]	Calculated
Ci_oxygen	0.3125[mmol/L]	1 mg/L o2 Estimated
khco3	1e2[1/s]	Equilibrium Rate Stiffness
kco2	1e2[1/s]	Equilibrium Rate Stiffness
knh4	1e2[1/s]	Equilibrium Rate Stiffness
kcahco3	1e2[1/s]	Equilibrium Rate Stiffness
kcaco3	1e2[1/s]	Equilibrium Rate Stiffness
kh2o	1e2[mol/s/m^3]	Equilibrium Rate Stiffness
Kso	3.8e-9[(mol^2)/(L^2)]	Calcite solubility product Zhang Klapper (2011)
ISi	0.5	Assumed constant ionic strength (IS) from influent value.
g_h	10^(-0.5*(sqrt(ISi)/(1+sqrt(ISi))-0.3*ISi))	Activity correction (gamma)
g_oh	10^(-0.5*(sqrt(ISi)/(1+sqrt(ISi))-0.3*ISi))	Activity correction (gamma)
g_cl	10^(-0.5*(sqrt(ISi)/(1+sqrt(ISi))-0.3*ISi))	Activity correction (gamma)
g_hco3	10^(-0.5*(sqrt(ISi)/(1+sqrt(ISi))-0.3*ISi))	Activity correction (gamma)
g_cahco3	10^(-0.5*(sqrt(ISi)/(1+sqrt(ISi))-0.3*ISi))	Activity correction (gamma)
g_nh4	10^(-0.5*(sqrt(ISi)/(1+sqrt(ISi))-0.3*ISi))	Activity correction (gamma)
g_ca	10^(-0.5*4*(sqrt(ISi)/(1+sqrt(ISi))-0.3*ISi))	Activity correction (gamma)

g_co3	10^(-0.5*4*(sqrt(ISi)/(1+sqrt(ISi))-0.3*ISi))	Activity correction (gamma)
g_nh3	10^0.05	Activity correction (gamma)
g_caco3	10^0.05	Activity correction (gamma)
g_co2	10^0.05	Activity correction (gamma)
ai_h	10^(-6)[mol/L]	Set influent pH = 6
ai_oh	Ci_oh*g_oh	Calculated influent activity
ai_cl	Ci_cl*g_cl	Calculated influent activity
ai_hco3	Ci_hco3*g_hco3	Calculated influent activity
ai_cahco3	Ci_cahco3*g_cahco3	Calculated influent activity
ai_nh4	Ci_nh4*g_nh4	Calculated influent activity
ai_ca	Ci_ca*g_ca	Calculated influent activity
ai_co3	Ci_co3*g_co3	Calculated influent activity
ai_nh3	Ci_nh3*g_nh3	Calculated influent activity
ai_caco3	Ci_caco3*g_caco3	Calculated influent activity
IAPi	Ci_ca*Ci_co3*g_ca*g_co3	Ionic activity product
SIi	IAPi/Kso	Influent Saturation index
k_precip	1.5e-12[mol/dm^2/s]	Zhong and Mucci (1989)
n_precip	3.27	Zhong and Mucci (1989)
k_diss_1	8.9e-3[L/dm^2/s]	Chou et al. (1989)
k_diss_2	6.5e-9[mol/dm^2/s]	Chou et al. (1989)
n_diss	1	Flukiger and Bernard (2009)

Note: Precipitation and dissolution kinetics are handled the same as Ebigbo et al. (2012)

Aqueous Rate Expressions

Rhyd	((Vmax_urea*Curea)/(km_urea+Curea))*bac
Roxygen	((Vmax_oxygen*Coxygen)/(km_oxygen+Coxygen))*bac
Rhco3	khco3*(Chco3*g_hco3-Cco3*g_co3*Ch*g_h/Ka_hco3)
Rco2	kco2*(Cco2*g_co2-Chco3*g_hco3*Ch*g_h/Ka_co2)
Rcahco3	kcahco3*(Ccahco3*g_cahco3-Cca*g_ca*Cco3*g_co3*Ch*g_h/Ka_cahco3)
Rcaco3	kcaco3*(Ccaco3*g_caco3-Cco3*g_co3*Cca*g_ca/Ka_caco3)
Rnh4	knh4*(Cnh4*g_nh4-Cnh3*g_nh3*Ch*g_h/Ka_nh4)
Rh2o	kh2o*(1-Ch*g_h*Coh*g_oh/Ka_h2o)
rurea	Rhyd
rco2	Rhyd-Rco2
rhco3	-Rhco3+RCO2
rnh4	0
rnh3	2*Rhyd+Rnh4
rh	Rhco3+Rco2+Rnh4+Rh2o+Rcahco3
roh	Rh2o
rco3	Rhco3+Rcahco3+Rcaco3
rca	Rcahco3+Rcaco3
rcahco3	-Rcahco3
rcaco3	-Rcaco3
rcl	0
roxygen	-Roxygen

Precipitation Rate Expressions

R_precip_1	if(SI_calcite>=1, k_precip*(SI_calcite-1)^n_precip, 0)
R_diss_1	if(SI_calcite<1, (k_diss_1*Ch+k_diss_2)*(1-SI_calcite)^n_diss, 0)
density_calcite	36.93[cm^3/mol]
V_calcite	density_calcite*(R_precip_1-R_diss_1)
r_precip_ca	R_diss_1-R_precip_1
r_precip_co3	R_diss_1-R_precip_1
SI_calcite	IAP_calcite/Kso
IS	1e-3*0.5*(Chco3+Cco3*4+Cnh4+Ccl+Cca*4+Coh+Ch+Ccahco3)
IAP_calcite	Cca*Cco3*g_ca*g_co3

Notes: bac = 1 in biofilm domain, 0 elsewhere

Main MATLAB Script for Time Resolved Model

Note: Other MATLAB and Java scripts are called within this code. This was included as an appendix in order to convey the architecture of the solution routine.

```
clc             % clear command window
clear all       % clear all MATLAB variables
close all       % close figures
format compact

% Create paths
nameOutput = 'output_new'; % defines name of output directory
PathInput = cd; % Input is always current directory
PathOutput =[cd filesep nameOutput];
PathOutputFct = ['.' filesep nameOutput];
if ~isdir(PathOutput)
    mkdir(PathOutput);
end;

biomass_obj = shoving.biomass();

% define link comsol-matlab
import com.comsol.model.*
import com.comsol.model.util.*

model = ModelUtil.create('Model');
ModelUtil.showProgress(true); % display the progress bar

niter=0;

if niter==0
    writelog(PathOutput,'a',['Start run']);
else
    writelog(PathOutput,'a',['Re-Start run from iteration '
num2str(niter)]);
end

% initialize the random number generation
randtype = 'mt19937ar';
randseed = 5;

% Geometric parameters
Nx = 201;           % number of discrete elements for x-direction
Ny = 51;            % number of discrete elements for y-direction
Lx = 400e-6;        % m, domain size
Ly = 100e-6;        % m, domain height in y
dx = 2e-6;          % m, grid size
dy = 2e-6;          % m, grid size
dz = 2e-6;          % m, grid size
```

```
Ny2 = Ny + 2;       % buffer lines required in some matrices

x = 0:dx:Lx;        % grid to be used for interpolation functions
y = 0:dy:Ly;        % grid to be used for interpolation functions

% steps and time stepping for growth calculations
max_iter = 100;    % maximum number of iterations
dt = 3600;        % s, time step for biomass growth

% particulate parameters
bac_name    = {'bio',  'cry'};          % names of solids (particulate
matter) in the model
bac_num     = [0,       0];             % initial number of particles
of each type
bac_n       = 0;                        % total number of particles,
will be set in the initial attachment
bac_ns      = length(bac_num);          % number of particulate species
bac_rmax    = [0.5*min([dx dy]),    0.5*min([dx dy])];      % m cell,
maximum radius of a particle for division
bac_rho     = [1.0e6,   2.7e6];         % g/m3 particle, density, old x
bac_rho 1e5
bac_mw      = [22.6,    100];           % molar weight in g mol^-1
bac_mmax    = bac_rho.*pi.*bac_rmax.^2.*dz./bac_mw;     % bac_m will
now be in moles!
nuc_rmax    = 0.3*min([dx dy]);         % Max particle radius where
crystals will in hydrodynamic calcs
nuc_r       = bac_rmax*0.1;            % radius of the nucleation
particle
nuc_n       = 100;                      % number of nucleation sites to
see the domain with

% shoving parameters
allowed_overlap = 0.05; % describes how much the radii may overlap, a
negative number gives space between spheres
maxshoviter = 0.5e4;    % maximum number of shoving iterations

stream = RandStream(randtype, 'Seed', randseed);
writelog(PathOutput,'a',['Randomseed set to ' num2str(randseed) ' of
type ' randtype]); %randomseed is now written in the log

if niter==0
    % initialize particle characteristics vector
    bac_m = [];% mass of each particle
    bac_r = [];% radius
    bac_x = [];% x-coordinate of the particle center
    bac_y = [];% y-coordinate of the particle center
    bac_s = [];% species
else
    % load cell data from previous iteration
```

```
    cells = load([PathOutput filesep 'cells.' num2str(niter,'%03d')
'.txt']);
    % retrive particle characteristics
    bac_x = cells(:,2)';  bac_y = cells(:,3)';
    bac_m = cells(:,5)';  bac_r = cells(:,6)';  bac_s = cells(:,4)';
    bac_n = length(bac_x);
end

% define solids matrix from file
load 'solids_matrix.mat';

% create model node
model.modelNode.create('mod1');

%Generate matrices to be used in comsol for visco, eps and cbio, based
on distribution of particulate matter (biomass/crystals)
solids=solids_only;

if niter==0
%%%%% Model Definition and Solving (Seperate Scripts) %%%%%
Create_interpolation_functions
model_parameters
model_geometry
model_rates
define_physics
build_mesh
create_study_solver
create_plots

model.save([PathOutput  filesep 'biomin' num2str(niter,'%03d')
'.mph']);

% Seed domain with a relatively large number of nucleation sites
update_matrices
nucleation

% Attach some cells just on the first itteration
update_matrices
attachment_cells_only
niter=niter+1;

else
    model= mphload([PathOutput  filesep 'biomin' num2str(niter,'%03d')
'.mph']);
end

while (niter < max_iter)

    % Save particles for  (all cell data: position,species mass,radius)
    file = fopen([PathOutput filesep 'cells.' num2str(niter,'%03d')
'.txt'],'w');
```

```
fprintf(file,'%1s%14s%15s%15s%15s%15s%15s\n','%','index','x[m]','y[m]',
'species','mass[mol]','radius[m]');
    for i=1:bac_n
        fprintf(file,'%15d%15.5e%15.5e%15d%15.5e%15.5e\n', i, bac_x(i),
bac_y(i), bac_s(i), bac_m(i), bac_r(i));
    end
    fclose(file);

    update_matrices

    % update model definition with new interp functions
    Update_interpolation_functions

    % calculate flow and mass transfer => all concentration fields and
flow field
    model.sol('sol1').runAll;   % Solve equations using comsol study as
defined outside the while loop

    export_parameters

    model.save([PathOutput  filesep 'biomin' num2str(niter,'%03d')
'.mph']); % save model file in order to have access later to all the
solution (concentration fields, flow field)

    % Close previous plot
    close all;

    % Plot results and save an image into the current directory
    Plot_concentrations;

    % growth and division of cells function of local substrate
concentration
    solids=solids_only;
    growth;

    % Attach cells randomly in the free domain at each timestep and
nucleate where possible
    % attachment_cells_only

    % Cells that have grown or new cells that have been attached shove
each other out of the way. Direction of shoving is randomized.
    Shoving_2d

    niter=niter+1;
end
```

APPENDIX F

SURFACE CHARACTERIZATION AND DEPTH PROFILING OF BACTERIAL UREOLYSIS-DRIVEN $CaCO_3$ PRECIPITATES USING XPS

Introduction

Crystalline precipitates grow through the addition of molecules to their surfaces therefore surface-associated substances have the potential to greatly alter precipitate characteristics. Microbially induced carbonate precipitation (MICP) systems have the potential to contain surface-associated biomass however it is not clear how the precipitation characteristics (e.g. kinetics and crystal morphology) differ from abiotic systems. It is theorized here that in MICP systems, biofilms and thin layers of biological substances would be present. Precipitate samples were analyzed with x-ray photoelectron spectroscopy (XPS) in order to test for the presence of these thin biological layers.

XPS is a surface-sensitive technique that measures the quantity and kinetic energy of photoelectrons emitted from a material when it is exposed to x-ray radiation. The measured electron kinetic energy is used to calculate the electron binding energy by a mass conservation equation that includes an instrument-specific work function, making spectra collected from different instruments are comparable. XPS spectra can be used to analyze the surface chemistry of a material. The technique's surface sensitivity is due to high electron attenuation in solid materials so photoelectrons are only emitted from the outermost layer, at the scale of tens of nanometers (Werner, 2001). Taking a single XPS spectrum yields information about the surface of the sample but when ion sputter etching is used spectra can be analyzed to determine chemical differences between the surface and interior of samples.

In these systems, polymorphic composition is most commonly determined by powder x-ray diffraction (XRD). XRD is a bulk measurement on a powdered sample. If there is a thin film forming on the outer reactive area of the growing crystal it would likely be undetected by XRD. Additionally, many groups determine polymorphic composition with electron microscopy and comparison to known crystal morphology. Crystal morphology is not conclusive evidence for carbonate minerals. For example, aragonite alone can exhibit many different morphologies depending on the conditions that it is formed in, some of which resemble calcite morphologies (Guo et al., 2011).

This study takes advantage of x-ray photoelectron spectroscopy (XPS) as a tool to determine if differences exist between in reactive surface of carbonate precipitates. XPS is extremely surface-sensitive. Photoelectrons are emitted from only the first <50nm of the sample. Argon ion sputter etching can then be used to ablate layers of the sample away with subsequent XPS spectra collection for comparison to the surface spectra. The ability of XPS to determine surface elemental composition is well accepted but more novel observations can be made based on core level spectra shifts. One abiotic study has been published that attempted to differentiate between calcium carbonate polymorphs using XPS (Ni and Ratner, 2008). Redox state distribution and elemental bonding environment can also be determined by studying XPS core-level spectral shifts.

There are two primary experimental objectives for this study. The first objective is to determine if there is a thin surface layer that forms on calcium carbonate precipitates formed by bacterial ureolysis performed by a model organism. Elemental composition and core level spectra shifts are the primary means of determining the presence of a thin

film. The second objective is to asses core level spectra shifts as documented in the literature (Ni and Ratner, 2008) in biological samples. These core level shifts are expected to be complicated by biological activity but it is unknown how. This study is also a test of the usefulness of XPS data with respect to biological carbonate samples. There is no known literature that discusses XPS analysis of precipitates of this nature. Some work has been done in ureteral stents and catheters but that work is not directly comparable (Reid et al., 1995).

Materials and Methods

Sporosarcina pasteurii ATCC 11859, a gram-positive, spore-forming soil bacterium is used for sample synthesis under constant flow conditions. *S. pasteurii* is extremely ureolytically active and is well known to produce calcium carbonate precipitates (Mitchell and Ferris, 2006). The process was carried out in a two-dimensional porous media reactor (**Error! Reference source not found.**) that is designed for direct observation of observation of microbial processes in porous media.

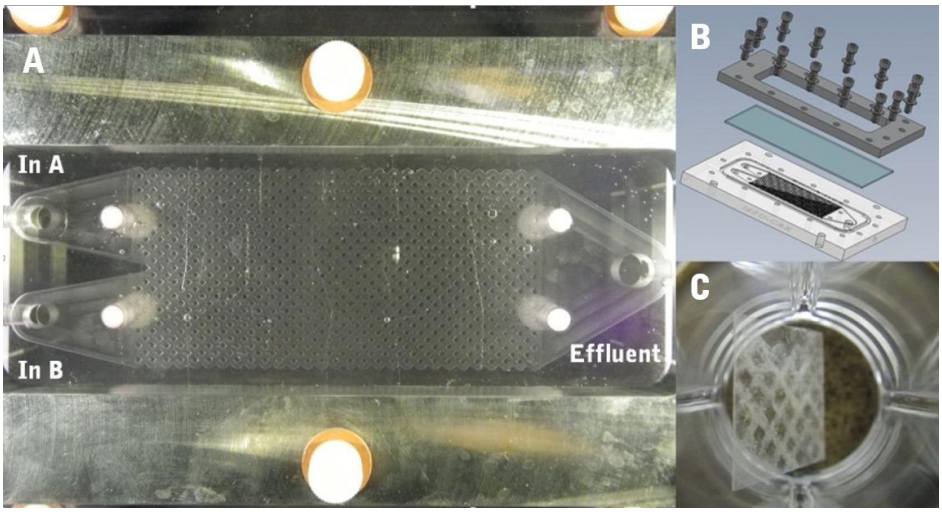


Figure F1. (A) Top view of the two-dimensional porous media reactor where the samples were grown. The artificial porous medium consists of regularly spaced 1.0mm cubic structures. The reactor was run from left to right with two inlets and one outlet. (B) Exploded view of the reactor courtesy of Joe Eldring. (C) Dried precipitates on a square of microscope cover glass that was placed inside of the reactor.

Small squares of microscopy cover glass were placed in the reactor while the precipitation process was taking place. Calcium carbonate precipitates then formed on these pieces of cover glass for easy removal of the sample. The precipitates were rinsed gently by submerging in DI water and stirring gently for approximately 10 seconds. The samples were then covered loosely and allowed to air dry. XPS analysis took place 10 to 30 days after the sampling. Confocal laser scanning microscopy (CLSM) was performed immediately after sampling (see supplemental online material).

XPS analysis was performed using a Physical Electrons 5600 X-ray Photoelectron Spectrometer. Aluminum Kα x-rays were used with a work function of 3.9 eV. Binding energies (BE) were calibrated using the O1s peak at 533 eV. The carbonate samples are subject to charging so sample electrons ejected by the x-rays were replaced with a neutralizer gun at 20.6 mA, e^- energy at 12±3%. All spectra were collected at a pass energy of 46.95 eV with an analysis size of approximately 80 μm in diameter. Survey spectra were collected between 0 and 1000 eV at a resolution of 0.4 eV with 20 ms of electron collection per data point. High resolution spectra of individual peaks of interest were collected identically but with a resolution of 0.2 eV.

Analysis locations on the biological precipitate samples were chosen based on precipitate coverage. Areas were chosen for the most complete precipitate coverage. Due to limitations of the instrument, it is impossible to tell exactly what area was analyzed. In

addition to the biological precipitates, a known calcite sample was analyzed as a control. The calcite is of geologic origin and has impurities that give it a light green color.

Survey spectra were collected from the surfaces of both the biological sample and the calcite control (see supplemental online material). The survey spectra were used to choose peaks of interest for high resolution scans. High resolution scans were then collected for C1s, Ca2p, N1s, O1s and P2p core-level spectra. High resolution spectra were also collected after argon ion sputter etching for a surface versus bulk comparison. Sputtering was done for 30 min at 13.0 mA at a chamber pressure of $\approx 3.5\times10^{-8}$ bar.

The supplemental online material describes the curve deconvolution performed on the C1s, Ca2p and O1s core-level spectra.

Results

Atomic Ratio Analysis

The results from the high resolution multiplex scans were analyzed to determine the atomic percentages of carbon, oxygen, calcium, nitrogen and phosphorus on the sample surface, sputtered sample and the calcite control sample. The results of this analysis are summarized in Table F1 and can be found in the supplemental online material. This analysis showed that there was more C, and N on the sample surface and more Ca, O and P deeper in the sample.

Table F1. Measured and theoretical atomic percentages from XPS multiplex scans.

	Biological Samples		**Calcite Control**		**$CaCO_3$ Theoretical**
	Surface	Sputtered	Measured	Corrected*	
Ca	12.0	15.3	11.6	23.6	20
C	28.7	21.4	43.9	20.0	20
O	49.7	53.4	43.9	55.9	60
N	4.2	2.9	0.6	0.6	0
P	5.4	7.0	0.0	0.0	0

*The hydrocarbon/carbonate C1s peak ratio was applied to the carbon percentage and the residual percentage was added to the Ca and O. This assumes that all hydrocarbon signal is from adventitious carbon adsorbed to the surface.

High Resolution Scans

The high resolution C1s, Ca2p and O1s core-level spectra from the sputtered, unsputtered and calcite control samples were analyzed for comparison to the Ni and Ratner 2008 paper. The results of this comparison can be found in Figure F2 and Table F2.

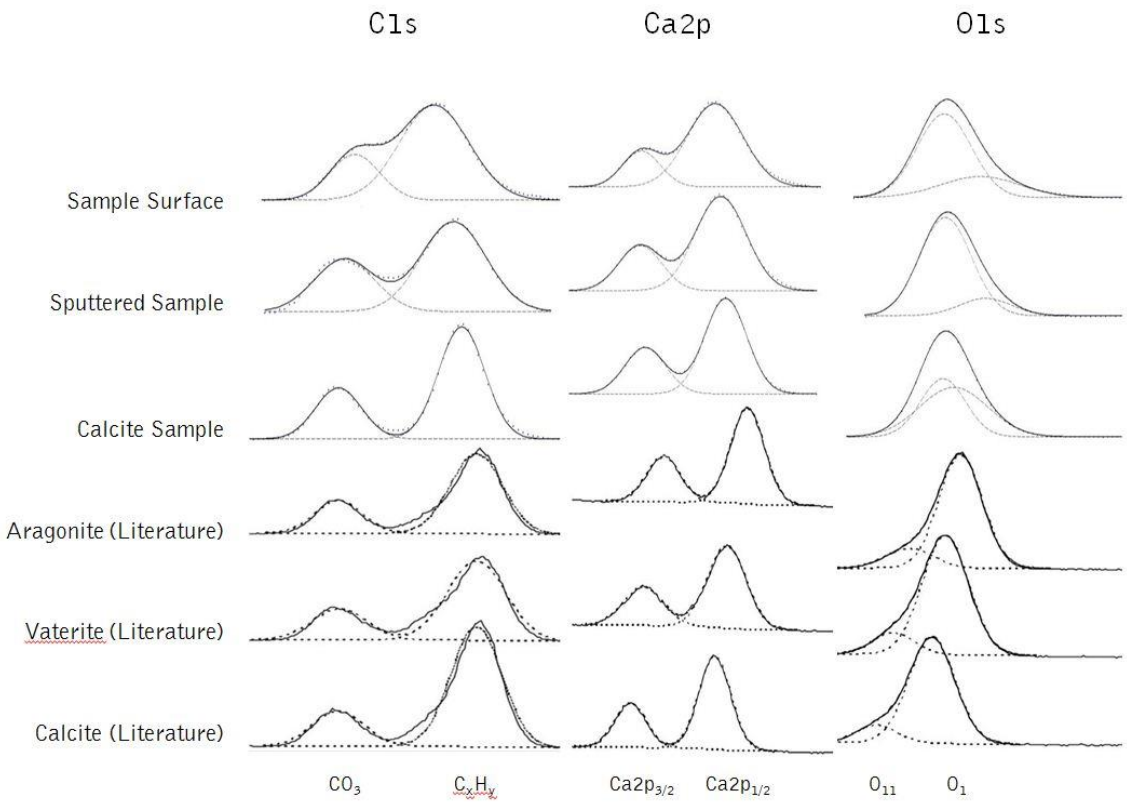


Figure F2. Deconvoluted core level spectra compared to spectra obtained from the abiotic Ni and (Ratner 2008) experiment.

Table F2 Peak locations and peak area ratios from this study compared to literature values.

		Ni and Ratner, 2008			This Study		
		Aragonite	Calcite	Vaterite	Surface	Sputtered	Calcite Control
Ca2p	$Ca2p_{3/2}$	347.9	346.5	347.4	348.2	346.5	346.8
	$Ca2p_{1/2}$	351.5	350.1	350.9	352.0	350.1	350.3
	Peak Area Ratio	2.2	2.1	2.1	3.4	2.5	2.1
C1s	C_xH_y	285.0	285.0	285.0	286.5	284.2	284.3
	CO_3	289.3	289.3	289.3	290.3	288.6	289.2
	Peak Area Ratio	3.5	2.6	2.8	2.9	1.9	2.2
O1s	O_I	534.9	533.9	534.4	530.9	529.2	530.4
	O_{II}	536.7	535.6	536.2	532.6	530.8	530.8
	Peak Area Ratio	7.0	5.2	6.3	0.4	0.2	1.2

The Ca2p peak is well understood and two peaks are always expected at approximately a 2:1 ratio in mineral samples. 2p core-level peaks for all elements have 3/2 and 1/2 components. Shifts in 2p peak location and ratio are typically attributed to differences in electron density, or bonding environment, surrounding the atoms. Here, we see that on average, calcium atoms at the sample surface are likely to be in a different bonding environment than calcium atoms within the precipitates based on the peak area ratio.

Similar observations can be made using the results of C1s and O1s spectra, but there is one key difference. Fundamental XPS theory would only predict one 1s peak for an element. In these, and many other, samples we see multiple 1s peaks for lighter

elements that are visually similar to 3/2 and 1/2 peaks seen in 2p spectra. In the biological samples, it is difficult to say if the hydrocarbon peak is coming from organic material from biological activity or from adventitious carbon adsorbed to the sample surface. It appears that some difference in the carbon bonding environment is present between the surface and deeper layers of the sample.

The O1s peak is subject to the same type of peak speciation due to bonding environment as the C1s. However, the spectra were calibrated based on the same O1s peak so BE shift correlations based on published values for known substances are impossible here. All that can be said is that the average oxygen bonding environment at the sample surface is different than in deeper layers. Also, both surface and sputtered spectra are different than published values for all calcium carbonate polymorphs.

Electron microscopy was performed on the same biological sample presented in this section after XPS analysis (see supplemental online material). The same spot that was sputtered was imaged, although it is unknown if this was the same area of analysis. Two distinct calcium carbonate crystal morphologies were visible. Evidence of the sputter etching was also visible with shadowing due to surface roughness and the angle of the sputter gun. The two crystal structures are indicative calcite and vaterite but there is no clear evidence from XPS or any other technique to definitively determine polymorphic composition. Qualitative estimation of sputter depth form electron micrographs show that on the order of 1 μm of material was removed in sputtered locations. Sputter rates for calcium carbonate do not appear to be present in the literature and a calibration could not be performed as part of this work.

Discussion and Conclusions

The results of this XPS analysis show that it is very likely that the biological samples have a thin film of unknown composition covering the precipitates. Based on the Ca2p core-level peak area ratios, the calcium present at the sample surface is in a very different bonding environment than calcium deeper in the sample. One possible explanation for this is that the calcium at the surface is associated with biomass and bound in dehydrated biofilm residue. It has been shown that divalent cations, and calcium specifically, can be an important constituent in the extracellular polymeric substances of biofilm (Applegate and Bryers, 1991). *S. pasteurii* is not a strong biofilm former but it is difficult to observe biofilms thinner than 100 nm with traditional methods such as light microscopy, more so with mineral formation. This thin layer of biofilm could play an important role in precipitation and dissolution kinetics. The thin biofilm hypothesis is supported by the higher C_xH_y fraction in the C1s spectrum taken from the sample surface. Future studies of the O1s spectrum could illuminate what organic compounds are present in the sample. It does appear that the oxygen bonding environment for samples in this study are very different than those found in the Ni and Ratner 2008 paper. This difference could be due to many things including hydration of the precipitates and organic inclusions.

When the atomic percentage data is investigated, the thin biofilm hypothesis is supported further with more carbon and nitrogen being present at the sample surface, but phosphorus actually increases at inner depths of the sample. This could be due to two

things. First, a mixed calcium carbonate/phosphate mineral could be forming with phosphate making substitutions for carbonate in the crystal lattice. Second, another organic constituent that is high in phosphorus could be incorporated into the crystal.

The sputter gun is oriented at a different angle than the detector so the inherent surface roughness of this sample means that a true surface versus bulk comparison cannot be made due to shadowing. Rather, it must be understood that spectra collected after sputtering are a combination of original surface areas and areas etched away with sputtering. Future studies that utilize instruments with stage rotation during sputter etching could minimize the shadowing effect.

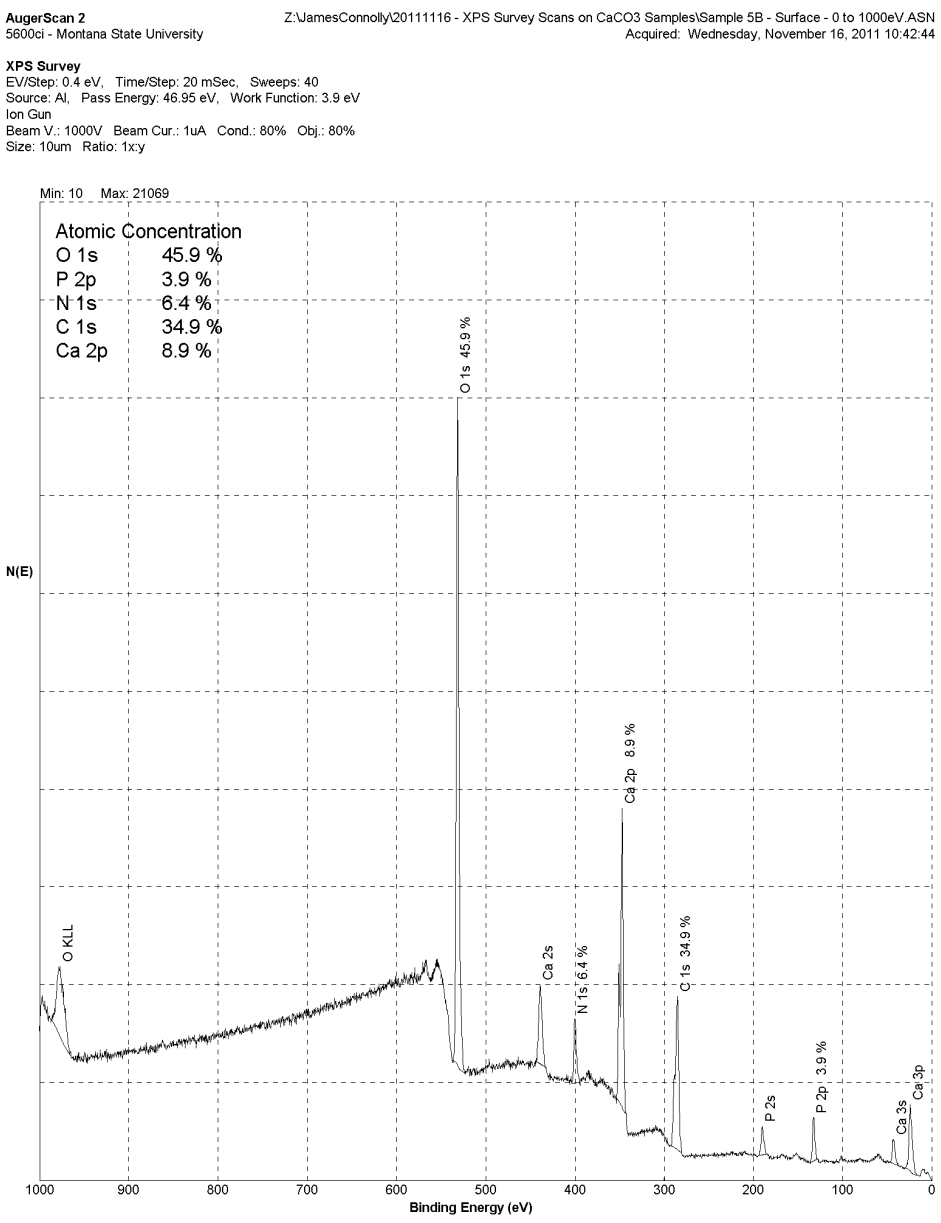
Calcium carbonate polymorph composition could not be determined definitively with data collected for this study. Any shift in core level spectra simply due to crystal structure would be very difficult to isolate from shifts due to organic substances in a biological mineral precipitation experiment. Micro XRD appears to be the best choice for a polymorphic study of this nature.

APPENDIX G

SUPPLEMENTAL DATA AND IMAGES FOR SURFACE CHARACTERIZATION AND DEPTH PROFILING OF BACTERIAL UREOLYSIS-DRIVEN $CaCO_3$ PRECIPITATES USING XPS

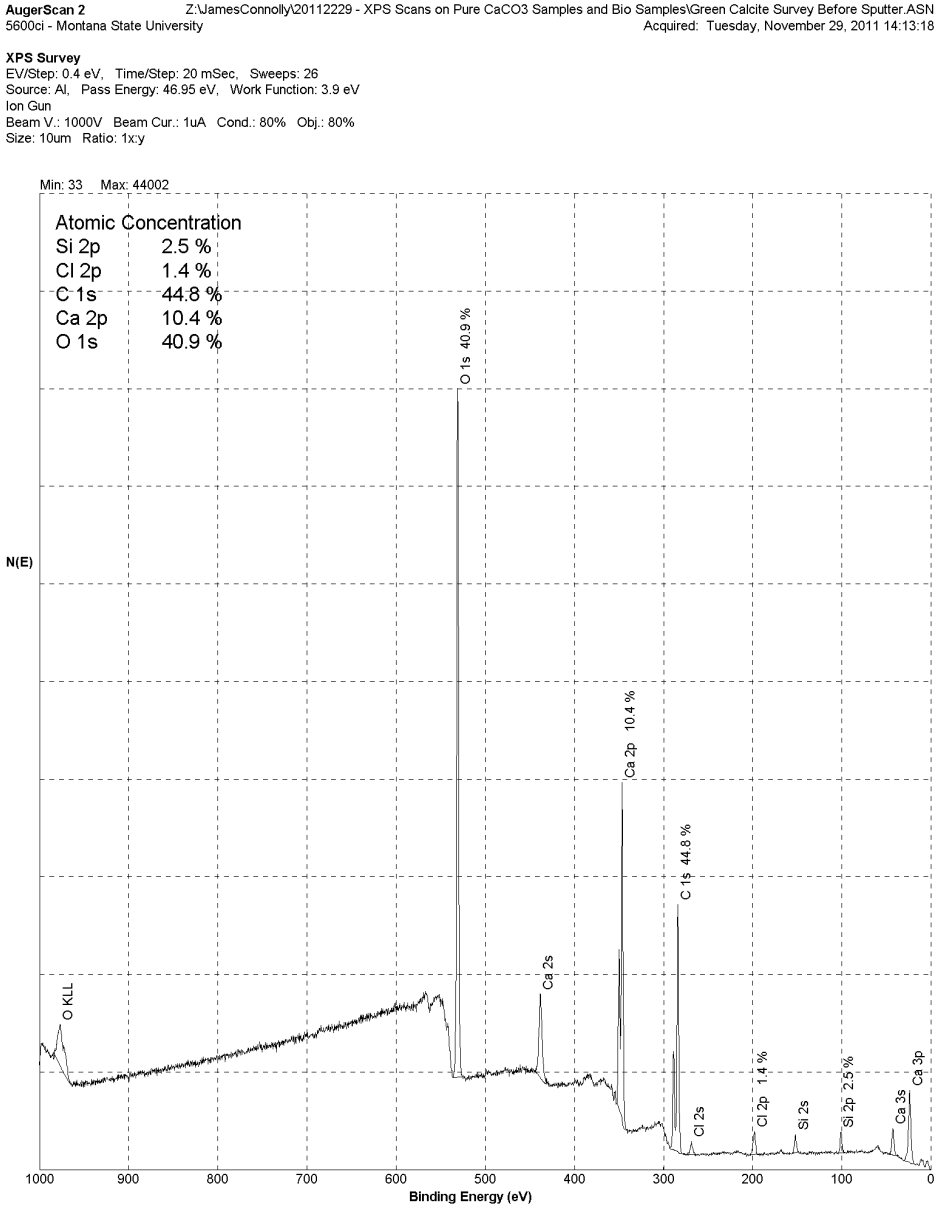
Survey Scan XPS Spectra

Typical Sample Surface (biological, this study)



Calcite from a Geologic Source

Sample: Geologic calcite from an unknown source. The sample had a light green color and was translucent. This sample was scanned as a check for correct instrument operation and for comparison of high resolution scans to both literature and scans performed in this study.

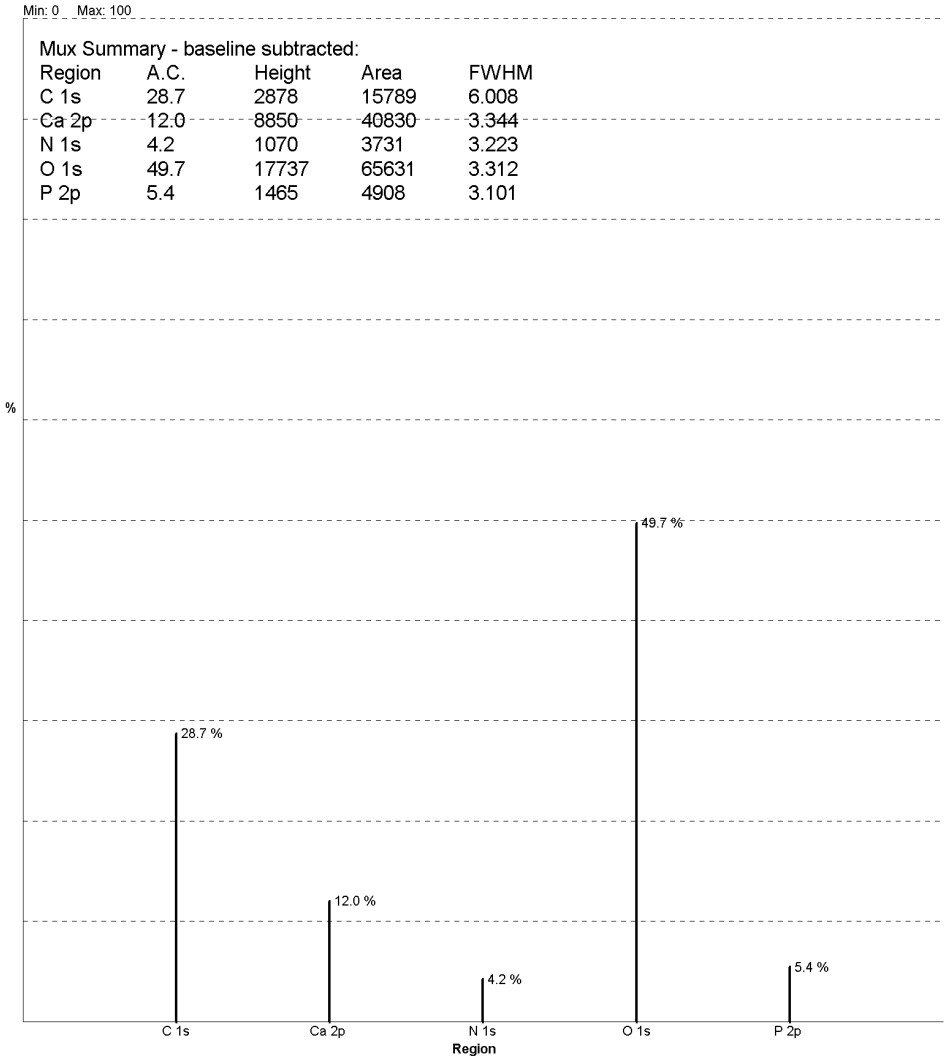


Multiplex XPS Spectra

Sample Surface (biological, this study)

AugerScan 2 Z:\JamesConnolly\20112229 - XPS Scans on Pure CaCO3 Samples and Bio Samples\Sample 2B Multiplex Before Sputter.ASN
5600ci - Montana State University Acquired: Tuesday, November 29, 2011 11:07:51

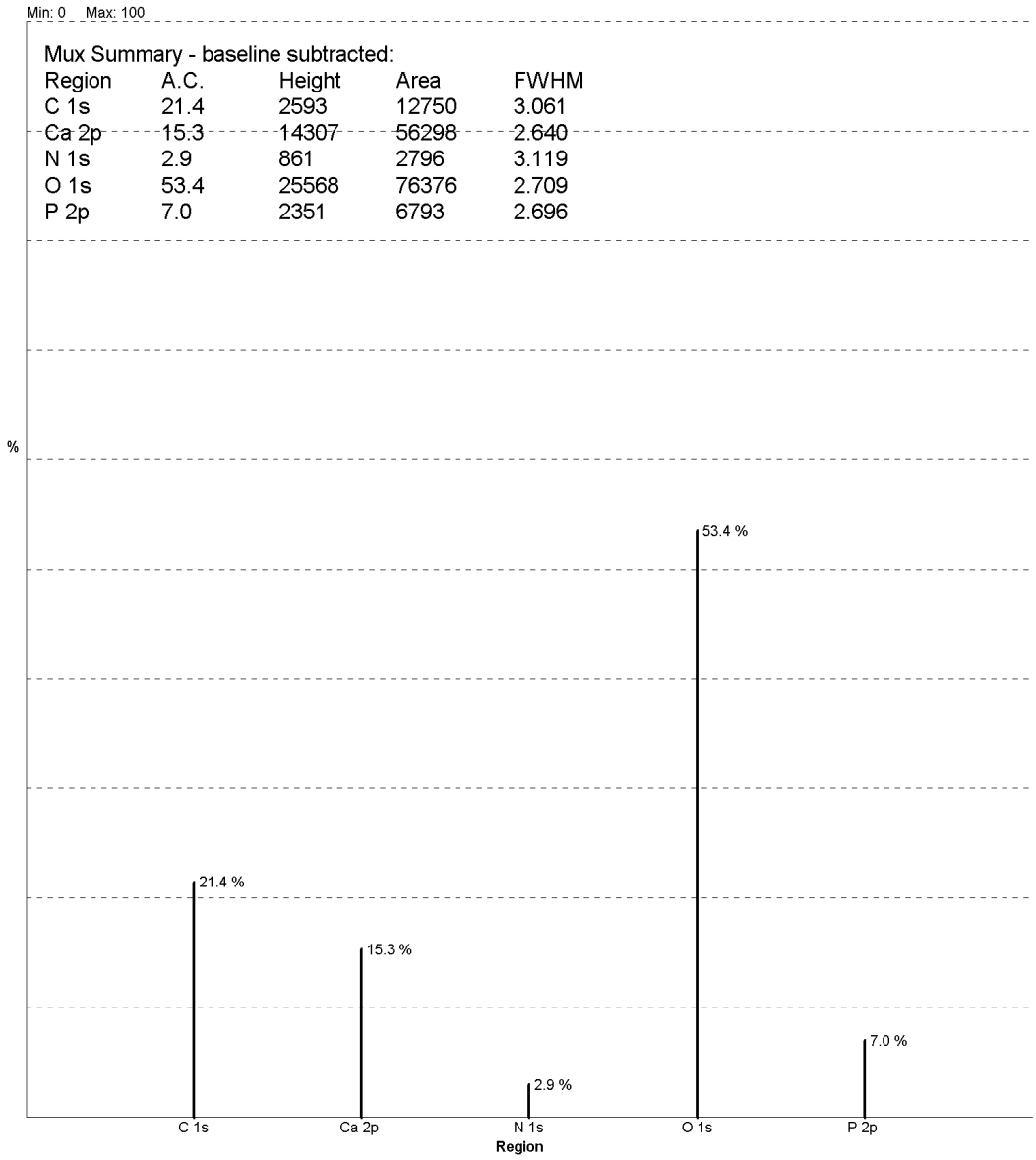
XPS Multiplex
Source: Al, Pass Energy: 46.95 eV, Work Function: 3.9 eV
Ion Gun
Beam V.: 1000V Beam Cur.: 1uA Cond.: 80% Obj.: 80%
Size: 10um Ratio: 1x:y



Sputtered Sample (biological, this study)

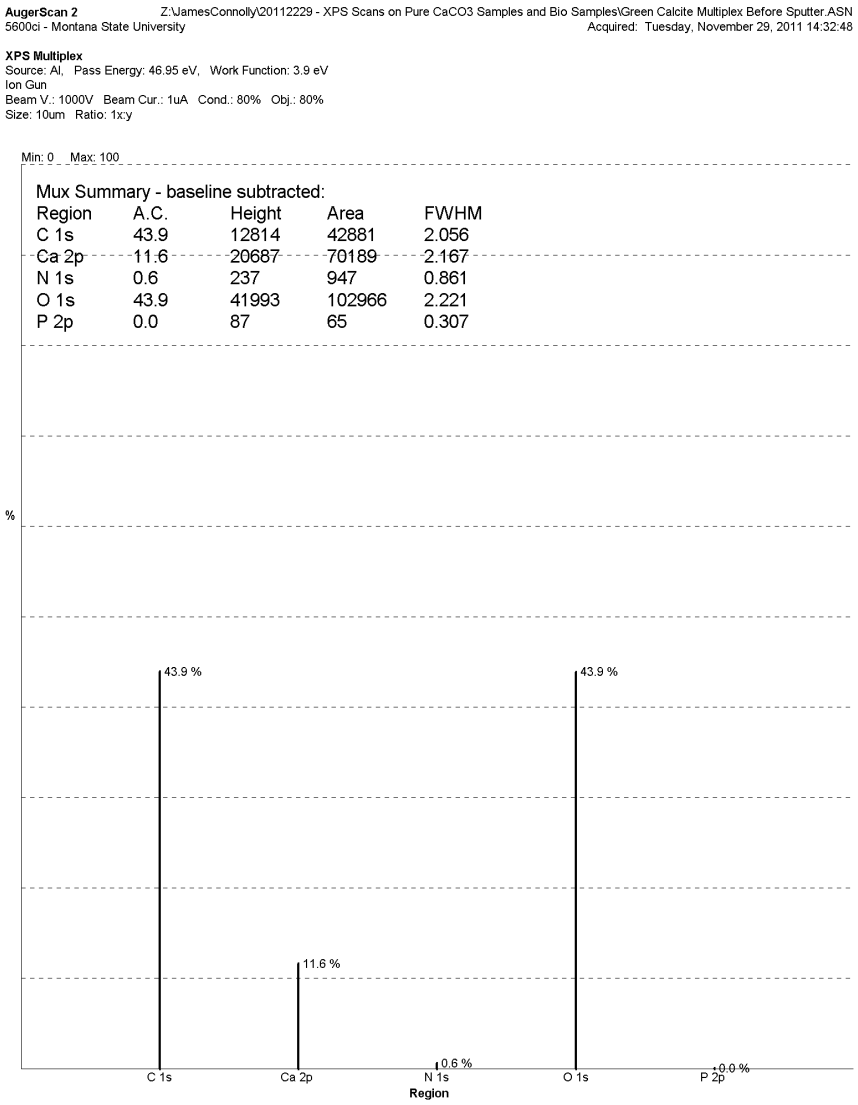
AugerScan 2 Z:\JamesConnolly\20112229 - XPS Scans on Pure CaCO3 Samples and Bio Samples\Sample 2B Multiplex After Sputter.ASN
5600ci - Montana State University Acquired: Tuesday, November 29, 2011 13:22:11

XPS Multiplex
Source: Al, Pass Energy: 46.95 eV, Work Function: 3.9 eV
Ion Gun
Beam V.: 1000V Beam Cur.: 1uA Cond.: 80% Obj.: 80%
Size: 10um Ratio: 1x:y



Calcite from a Geologic Source

Sample: Geologic calcite from an unknown source. The sample had a light green color and was translucent. This sample was scanned as a check for correct instrument operation and for comparison of high resolution scans to both literature and scans performed in this study.



Deconvoluted High Resolution XPS Spectra

The following curve deconvolutions were performed in Matlab using the open-source deconvolution function, Interactive Peak Fitter (Version 7, October 2011). A linear background subtraction was performed on the curves presented here.

Key

Upper Plot: Blue Dot = Raw XPS Data

Green Line = Fitted Gaussian Curves

Red Line = Sum of Fitted Gaussian Curves

X Axes = Binding Energy (eV)

Y Axes = Electron Count N(e)

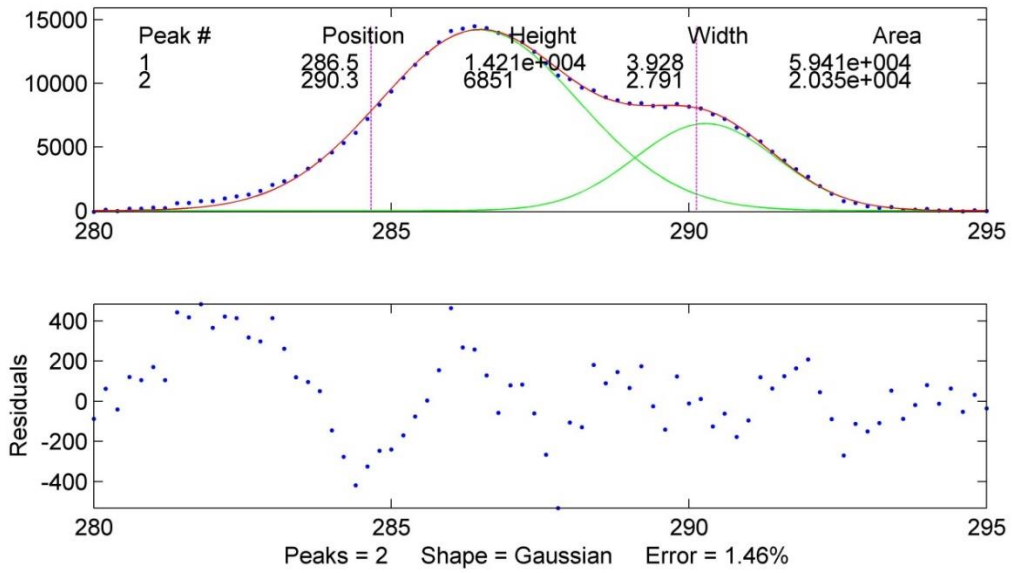
Lower Plot: Blue Dot = Residual from curve fit at each data point (Data – Fitted = Residual)

X Axes = Binding Energy (eV)

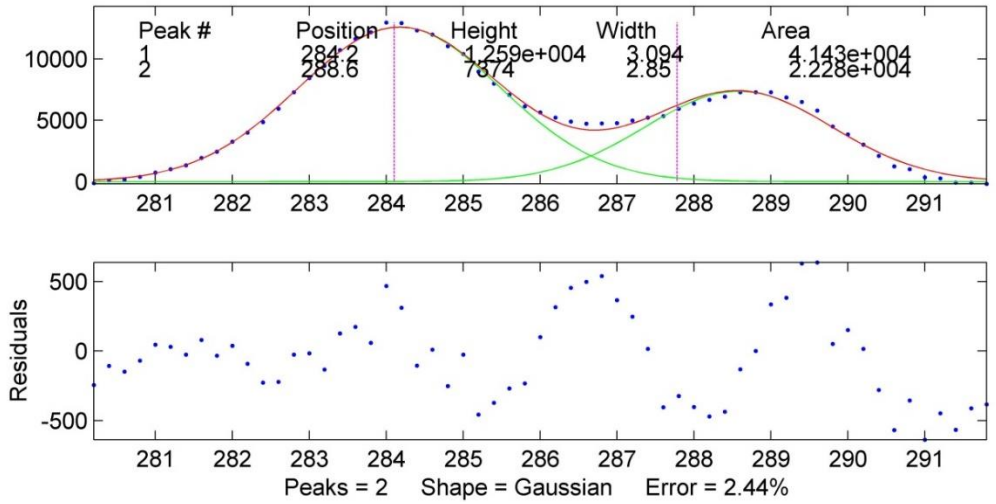
Y Axes = Residuals

Note: Typically, XPS spectra are plotted in decreasing binding energy (high to low). The data presented here is plotted in increasing binding energy (low to high) due to limitations of the deconvolution software. Curves presented in Figure 2 of the report are presented in "high to low" format.

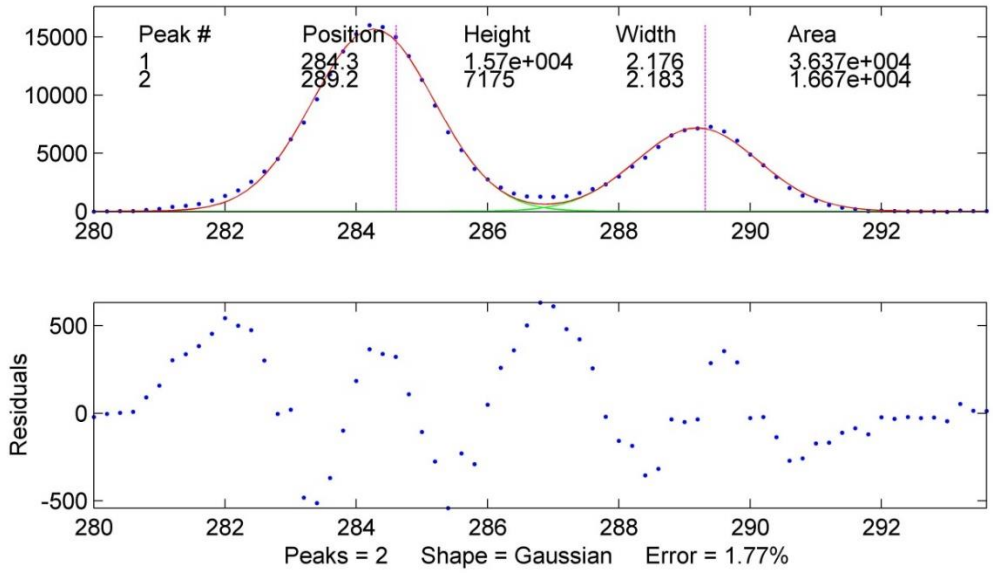
C1s Sample Surface (Biological, this study)



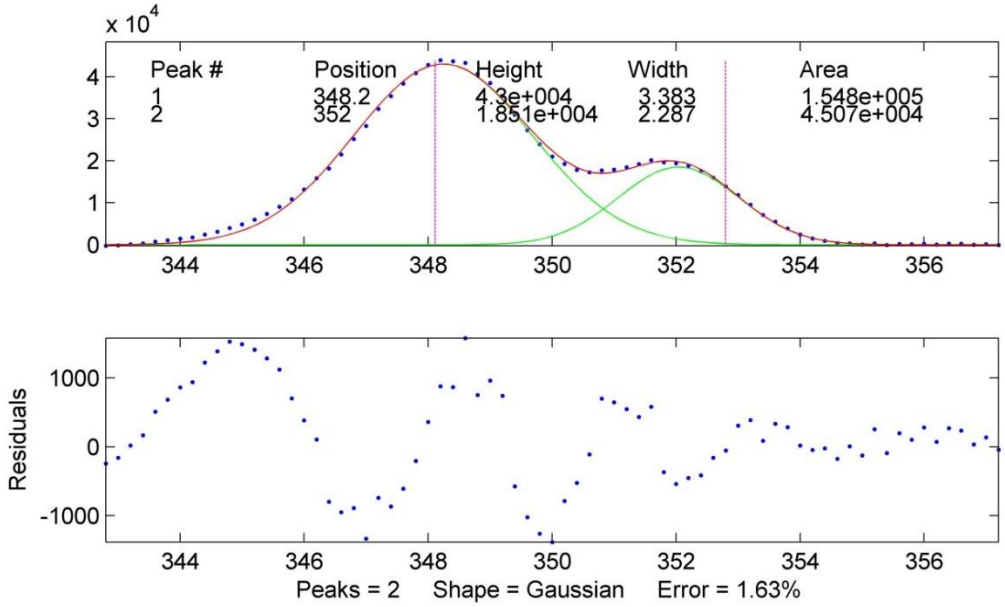
C1s Sputtered Sample (Biological, this study)



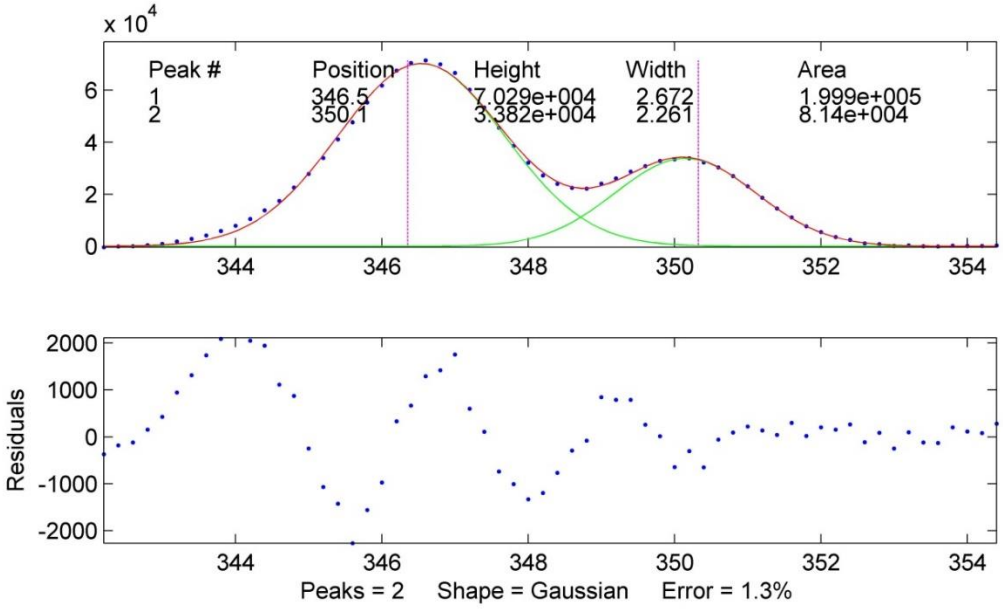
C1s Geologic Calcite Control



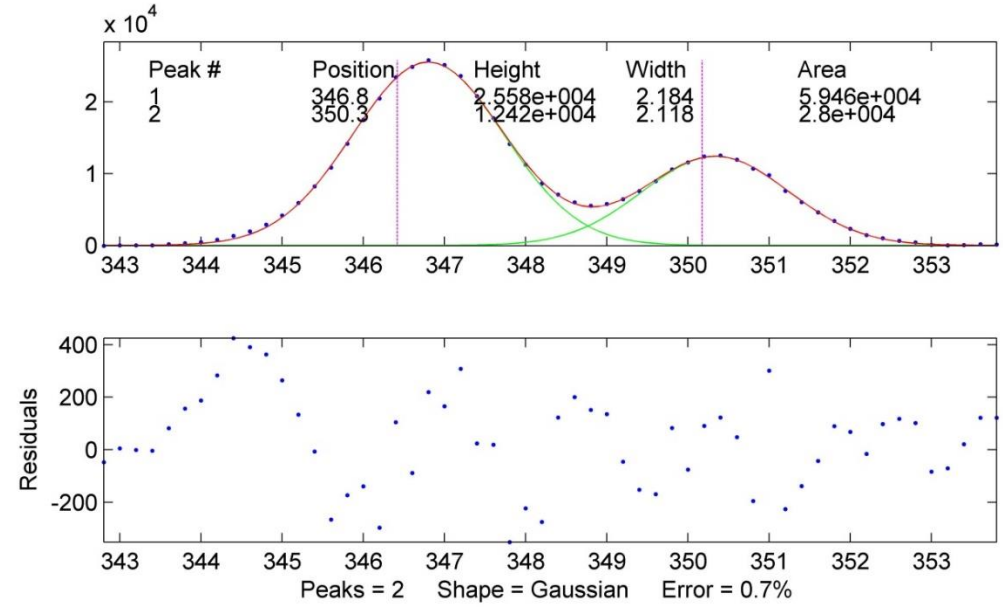
Ca2p Sample Surface (Biological, this study)



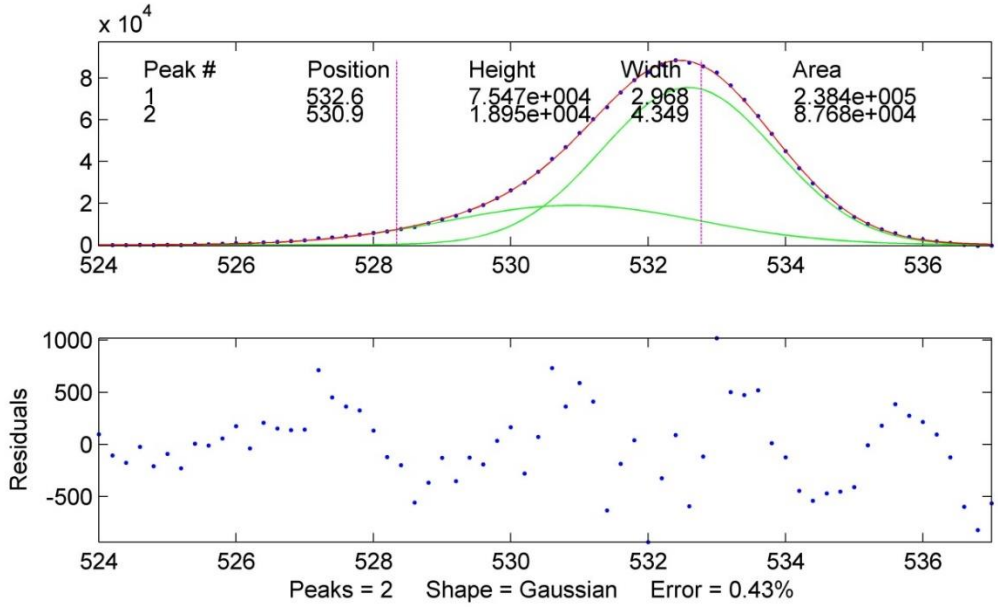
Ca2p Sputtered Sample (Biological, this study)



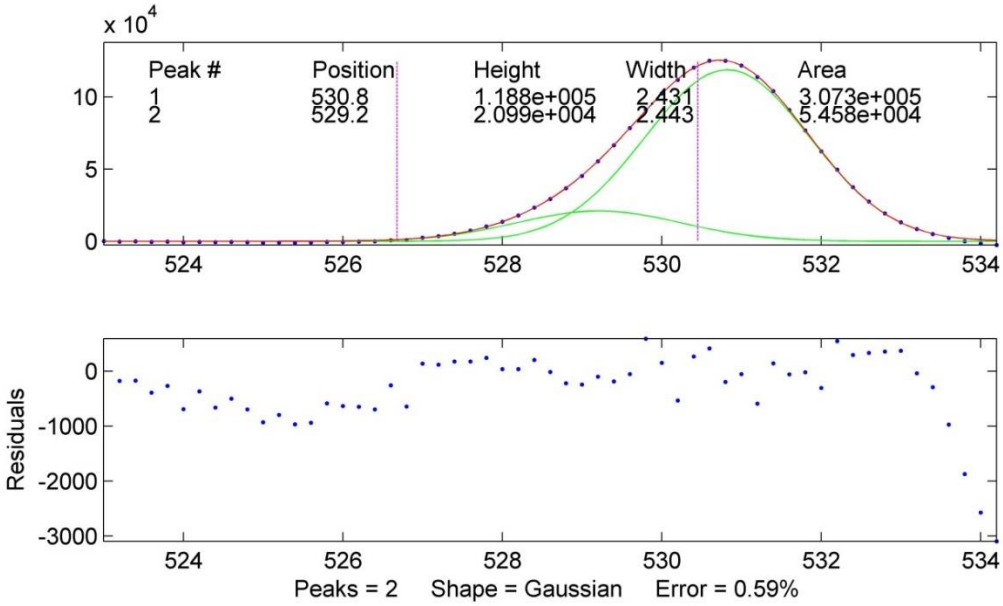
Ca2p Geologic Calcite Control



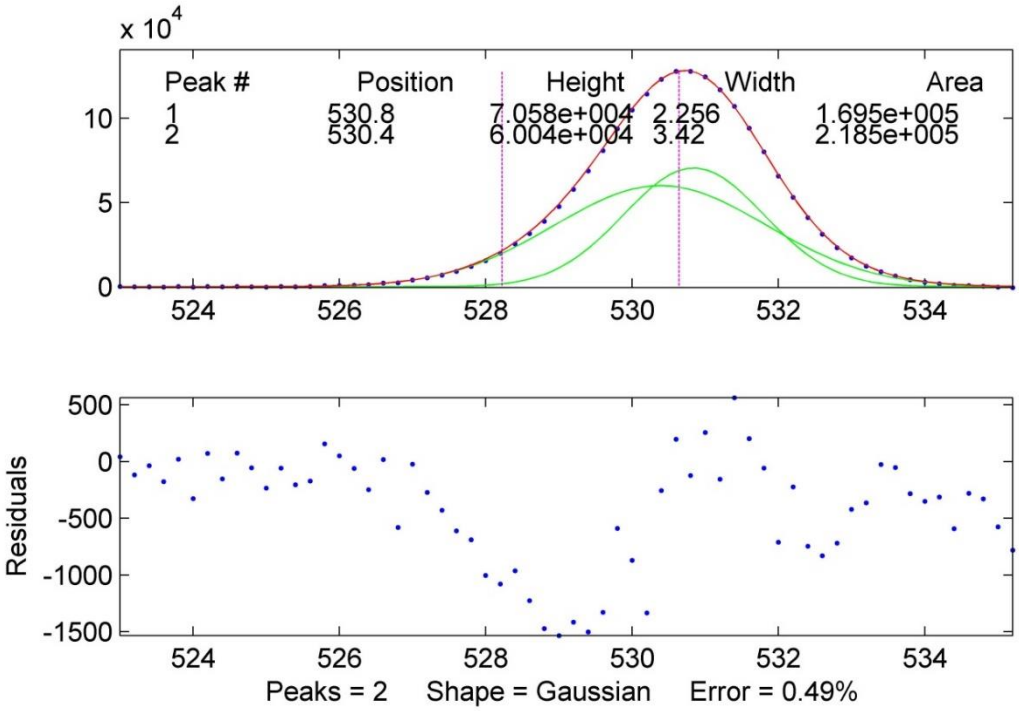
O1s Sample Surface (Biological, this study)



O1s Sputtered Sample (Biological, this study)



O1s Geologic Calcite Control



Microscopy Images

Electron Microscopy

The following images were obtained using the Zeiss SUPRA 55VP Field Emission Scanning Electron Microscope (FEM) housed in the Montana State University Image and Chemical Analysis Laboratory (ICAL)



Figure G1. Wide field of view of a typical biological calcium carbonate precipitate.



Figure G2. Close-up view of the two dominant types of precipitates found in this study. The large, spherical crystals with square or rhombohedral surface elements have morphology matching calcite. The very small spheres with smooth surfaces match vaterite morphology. Smoothing on the lower right of the large spherical crystal is from argon ion sputter etching done in the XPS analysis. The entire crystal is not sputtered due to shadowing.

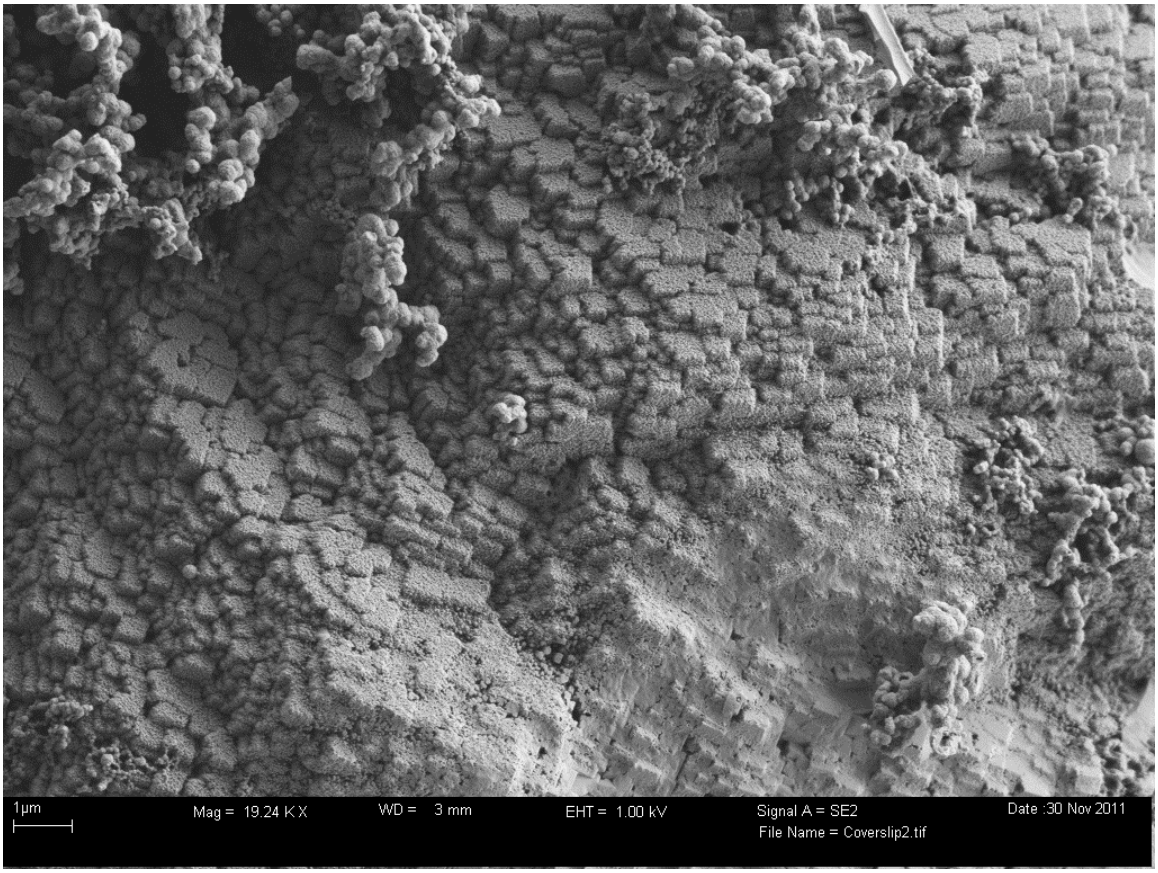


Figure G3 Supposed vaterite in the upper left, supposed calcite in the center and a sputtered area in the lower right.

Confocal Microscopy

The following images were obtained using the Leica TCS SP 5 Inverted Confocal Laser Scanning Microscope housed in the Montana State University Center for Biofilm Engineering. All images in this section are the same field of view of one typical sample from the system.

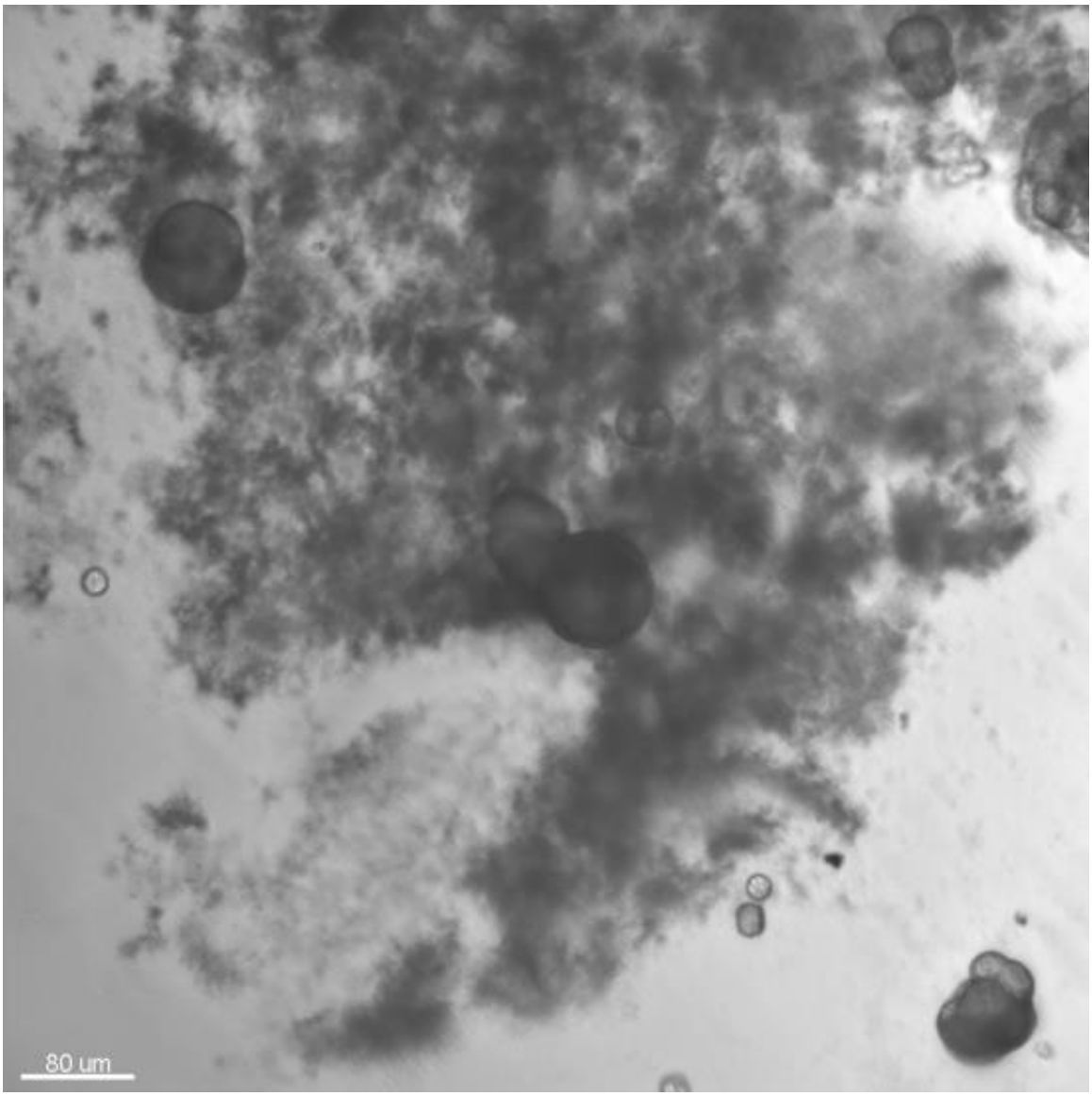


Figure G4. Transmitted light image of a typical biological calcium carbonate precipitate.

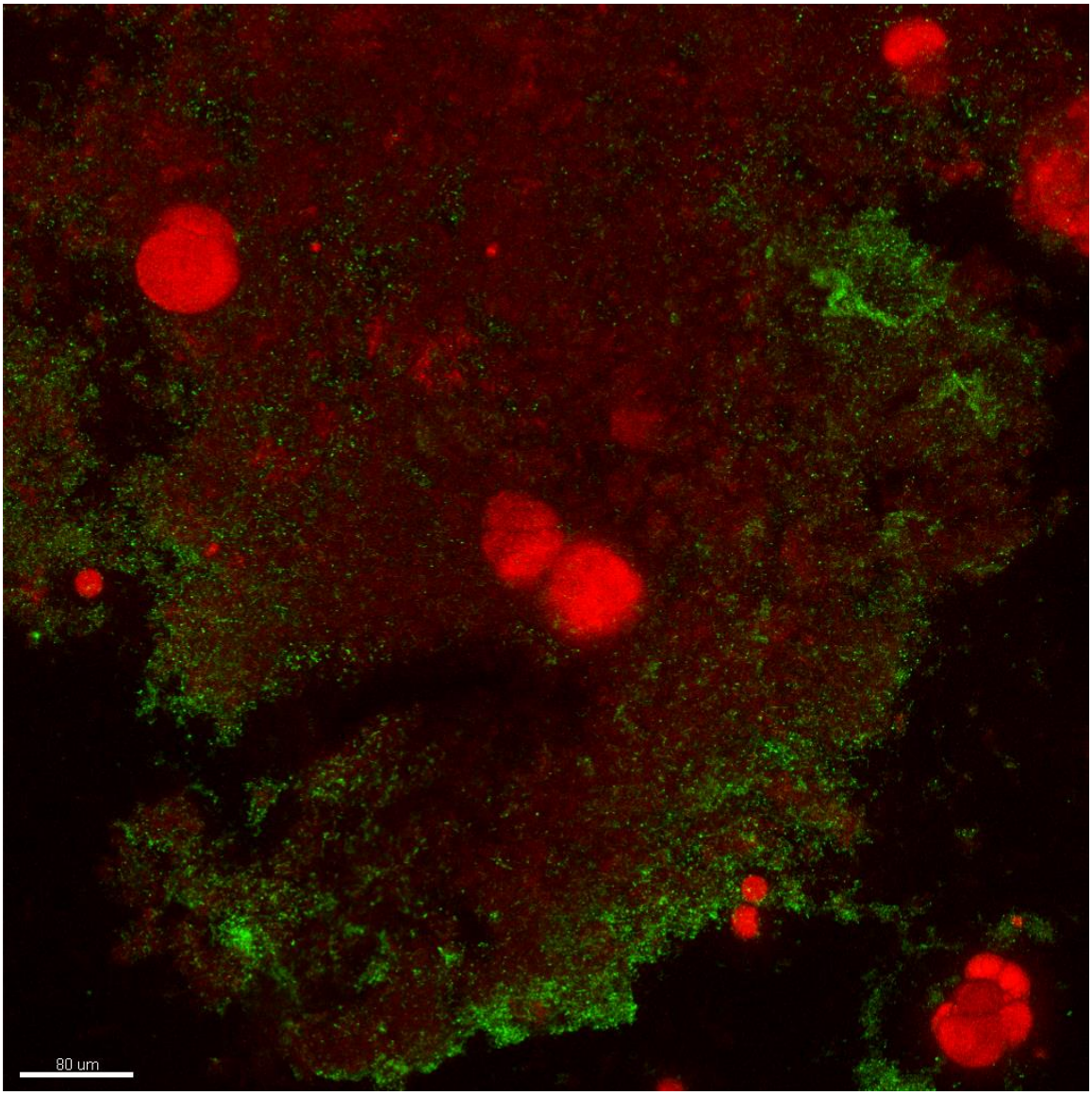


Figure G5. Fluorescence reconstruction (color/stain key below). The general protein stain (red) bound more strongly to the large calcite-like crystals. The nucleic acid stain (green) is stronger on the outer leading edge of the precipitate formation.

Red – Protein stained with Cypro Ruby protein gel stain.

Green – Nucleic acids stained with SYTO 9. Shows cells and extracellular nucleic acids.

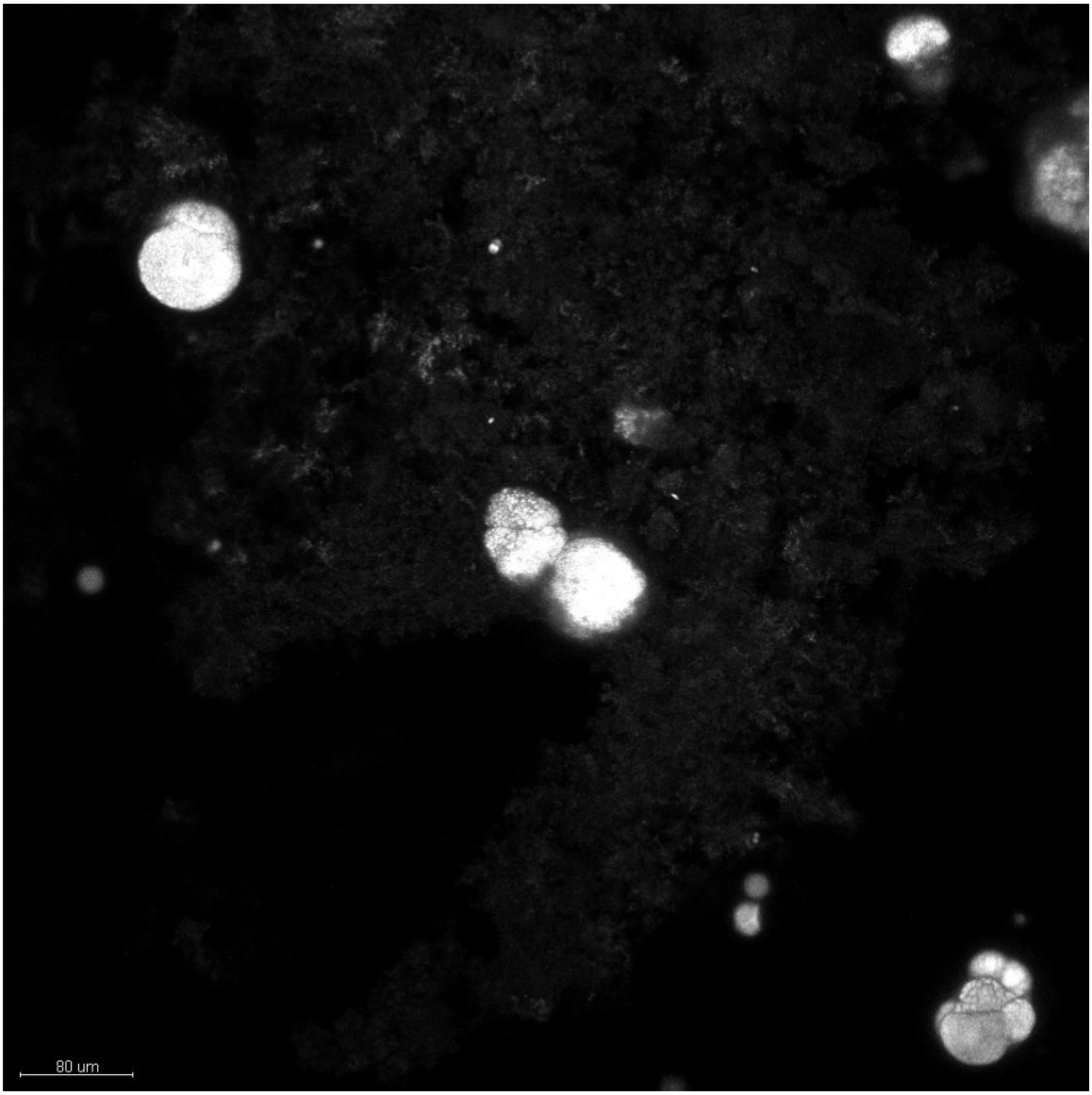


Figure G6. Fluorescence reconstruction of the ultraviolet autofluorescence emitted from the sample. Calcite is known to have to strongest autofluorescence of the calcium carbonate polymorphs so this image supports (but does not prove) that the larger crystals that appear in this study are calcite.

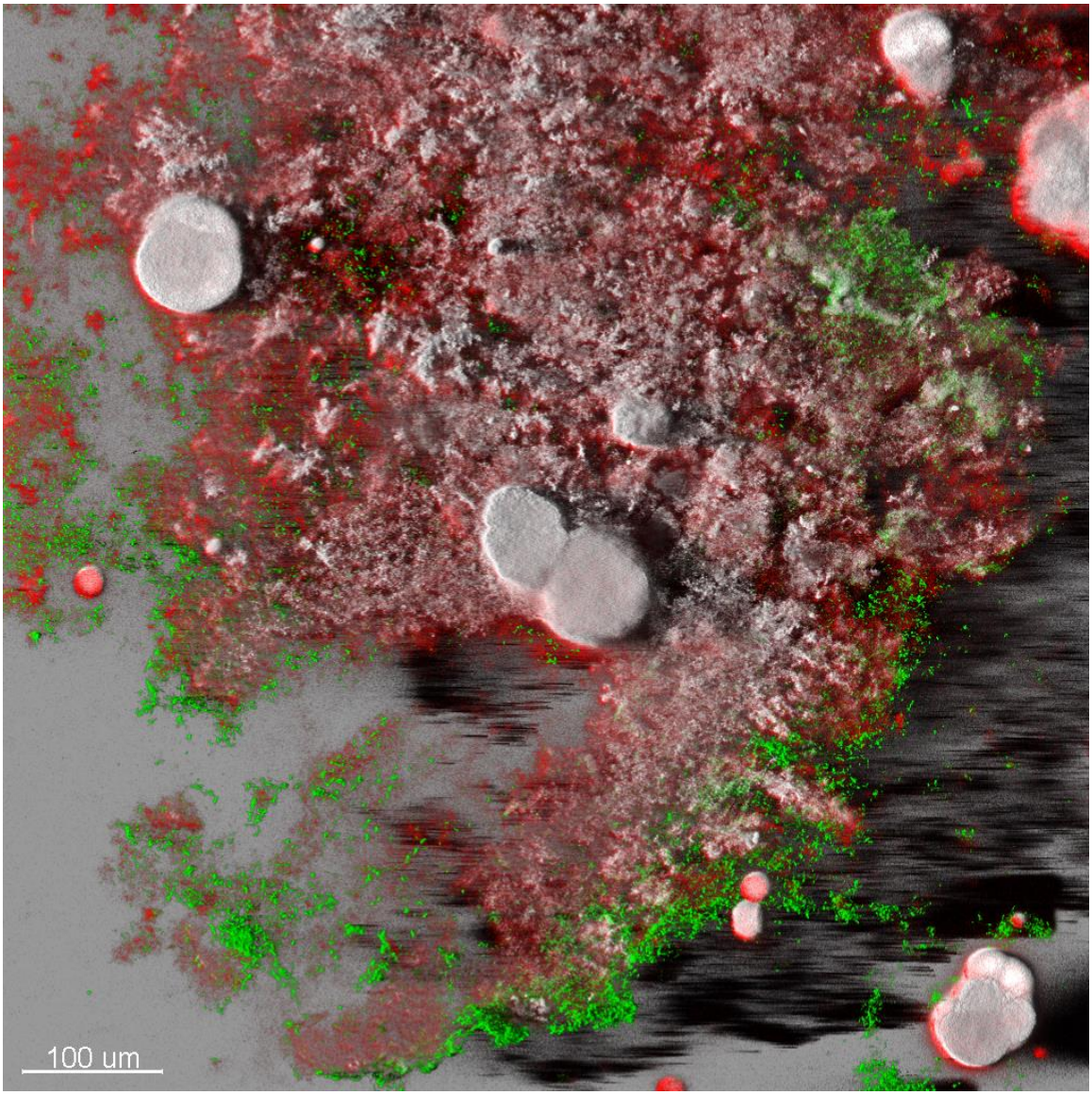


Figure G7. Three-dimensional image of signals from images 5 and 6 combined and rendered using the Imaris software package.

APPENDIX H

ADDITIONAL RESEARCH: TAXIS TOWARD HYDROGEN GAS BY *METHANOCOCCUS MARIPALUDIS*

Abstract

Knowledge of taxis (directed swimming) in the novel receptors, effectors, and proteins involved in signal transduction to the flagellar motor. Although the Archaea is currently expanding through identification of ability for biological cells to sense and swim toward hydrogen gas has been hypothesized for many years, this capacity has yet to be observed and demonstrated. Here we show that the average swimming velocity increases in the direction of a source of hydrogen gas for the methanogen, using a capillary assay with anoxic gas-phase control and time-lapse microscopy. The results indicate that a methanogen couples motility to hydrogen concentration sensing and is the first direct observation of hydrogenotaxis in any domain of life. Hydrogenotaxis represents a strategy that would impart a competitive Methanococcus advantage to motile microorganisms that compete for hydrogen gas and would impact the C, S and N cycles.

Citation

Brileya, K.A., Connolly, J.M., Downey, C., Gerlach, R., Fields, M.W., 2013. Taxis Toward Hydrogen Gas by *Methanococcus maripaludis*. *Scientific Reports* 3.

APPENDIX I

ADDITIONAL RESEARCH: STRUVITE STONE FORMATION BY UREOLYTIC BIOFILM INFECTIONS

Citation

Schultz, L., Connolly, J., Lauchnor, E.L., Hobbs, T., Gerlach, R., 2015. Struvite stone formation by ureolytic biofilm infections. In: Lange, D., Chew, B. (Eds.), *The Role of Bacteria in Urology*. Springer, New York.

APPENDIX J

EXPERIMENTS AND MODELING OF BIOFILM-INDUCED CARBONATE PRECIPITATION IN SU-8 MICROMODEL REACTORS

Materials and Methods

SU-8 Micromodel Fabrication

The micromodels discussed in Appendix J were constructed with SU-8 photoactive polymer on 1 mm Pyrex wafers. This discussion provides an overview of how the micromodels were constructed but for specific details, the laboratory notebooks should be referred to. All photolithography was conducted in the class 1000 clean room at the Montana Microfabrication Facility at Montana State University. The micromodel pattern is identical to that discussed in Chapter 5, Figure 19 and was drawn electronically and sent to the University of Minnesota Nanofabrication Center for the construction of a photolithography mask constructed of soda lime glass with the pattern in chrome.

The lithography process started by spin coating a 100 mm diameter, 1 mm thick polished Pyrex wafer with a 100 µm layer of SU-8 100 negative photoresist. The wafer was then exposed to ultraviolet using a contact aligner (ABM-USA, Inc., CA, USA) emitting 15 mW/cm^2 light at a wavelength of 365 nm. The wafer was hardbaked on a 100ºC hotplate, let to cool to room temperature and then developed with SU-8 developer. The wafer was rinsed thoroughly in deionized water and dried with nitrogen. Influent and effluent holes were drilled with a 1 mm diameter diamond bit on a drill press with soda lime glass backing

A second 4 mm diameter, 200 µm thick Pyrex wafer was spin coated with a 10 µm layer of SU-8 2050 negative photoresist to act as a bonding layer. The 200 µm thick Pyrex wafer was exposed to ultraviolet light in a similar fashion as the first wafer. The

two wafers were pressed together using an aluminum bonding apparatus and baked to allow the two SU-8 layers to heat bond together.

Individual micromodels were cut apart using a dicing saw and influent and effluent connections were made with NanoPorts (IDEX Corporation, USA). The micromodel used in this study had a measured channel depth of 100 µm and a porosity of 0.78. A scanning electron micrograph of the porous media features can be found in Figure J1.

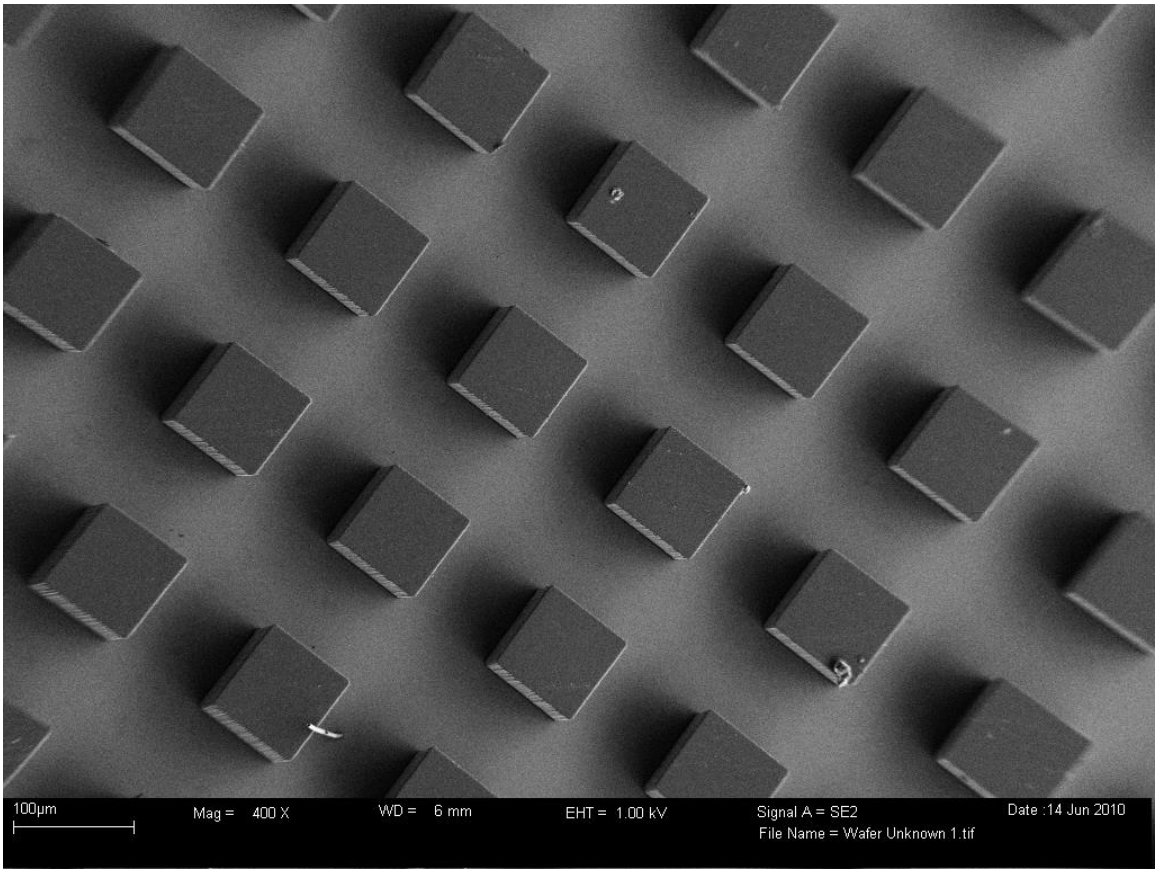


Figure J1. A representative scanning electron micrograph of the porous media region of an SU-8 micromodel without cover glass.

MICP Experiment Overview

This section serves to provide an experimental overview but precise conditions can be found in Connolly et al., (2013) Section 3.4. Although the Connolly et al. (2013) paper describes work done in capillaries, the organism, growth medium and flow conditions are the same. All experimental work referenced herein was conducted under constant laminar flow conditions with Re << 1. The micromodel flow cell pictured in 1J was constructed out of an SU-8 polymer on a Pyrex substrate and enclosed with a 200 µm Pyrex cover slip to allow for confocal microscopy. The flow cells were disinfected with 95% ethanol, flushed with sterile growth medium and then inoculated with *Escherichia coli* MJK2 (Connolly et al., 2013), a recombinant ureolytic bacterium that carries green fluorescent protein (GFP) genes. Cells were allowed to attach, with no flow, for a period of one hour and then flow was started at 0.25 mL/h. The medium used for growth is identical to that used in Connolly et al., (2013) for MJK2 and contains LB broth, 10 g/L urea, 7.5 g/L L-arabinose (as the plasmid promoter) 10 µM nickel and 10 µg/mL gentamycin sulfate. After approximately 48 hours of growth in the micromodel a thick, ureolytic biofilm was present. At this point, the experiment was relocated to an inverted Leica SP5 confocal microscope and the growth medium was amended with 10 g/L $CaCl_2 \cdot 2(H_20)$ to allow for precipitation of $CaCO_3$. Time lapse microscopy images were collected every hour for 12 hours while precipitation occurred. Metabolically active biofilm was imaged with GFP fluorescence from a 488 nm laser light source and precipitation was visualized with transmitted light from the same source.

Steady-state Model

A model was constructed in COMSOL Multiphysics 4.3a with the goal of modeling fluid flow, solute transport, carbonate speciation, ureolysis and calcium carbonate crystal growth. In order to ensure this modeling approach is achievable at an experimentally relevant scale, a data set obtained at MSU was used that has biofilm and crystal growth in a micromodel flow cell shown in J2 (A).

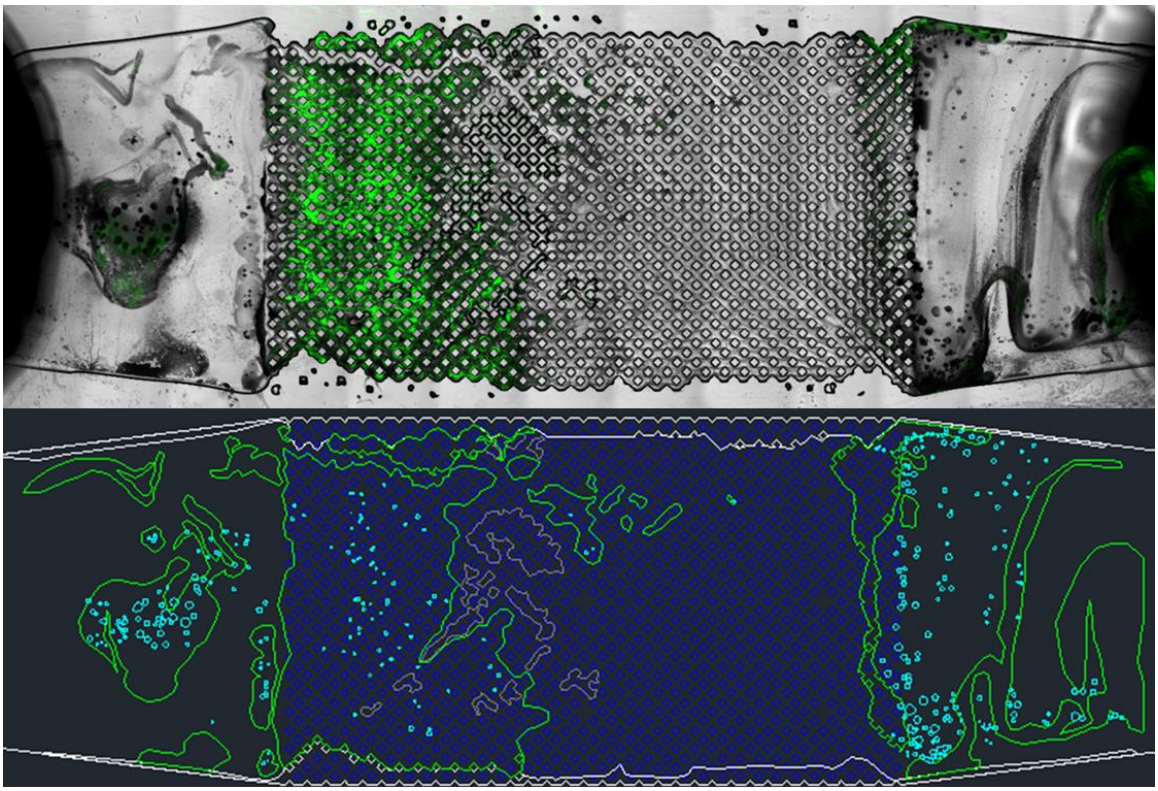


Figure J2. (A) Combined transmitted light and fluorescence microscopy image of a porous media micromodel reactor. Green regions show active biofilm and circular calcium carbonate crystals can be seen in the influent and effluent regions of the reactor. Flow is from left to right. The porous media elements are 100 µm and the reactor is 100 µm deep. (B) 2D digital representation of the boundaries observed in the experimental geometry. Calcium carbonate is in light blue, biofilm in green, air bubbles in gray, porous media elements in light blue, and solid outer boundaries in white.

Biofilm was grown first, under constant flow conditions and then calcium was added to allow for calcium carbonate precipitation. 2D microscopy images were imported to AutoCAD 2013 and interfacial boundaries were drawn by hand. The geometry resulting from this processing is shown in Figure J2 (B). This geometry was directly imported to COMSOL for pore-scale reactive transport modeling.

The system contains five phases: liquid, biofilm, nonreactive solid, calcium carbonate and gas. The gas phase is not intentional however many experiments of this nature do contain gas so its presence needs to be accounted for. In this simulation, the gas phase is simply treated as a nonreactive solid, with the assumption that it is immobile over the time period of interest and that it is in equilibrium with the dissolved gas in the liquid and biofilm regions.

A simplified 2D Navier-Stokes equation is used to solve for the flow field, ion transport is solved for with Nernst-Planck equations and non-charged species are solved for by Fickian diffusion. Generally, flow is restricted to the liquid phase with no slip boundary conditions at all interfaces except for the inlet (constant velocity) and the outlet (pressure equal to zero). Solute transport is allowed in both the biofilm and liquid phases. It is assumed that diffusion is the dominant transport mechanism in the biofilm so convection only takes place in the liquid phase. The entrance boundary condition for all solutes is a known concentration based on equilibrium for the desired pH, and solute mass conservation is enforced as the boundary condition at the outlet. Nonreactive solid boundaries are zero flux with respect to solutes however there is a concentration-based flux at the calcium carbonate boundaries for precipitation and dissolution. Commonly

used, semi empirical saturation index (SI) dependent precipitation (Zhong and Mucci, 1989) and dissolution (Chou et al., 1989; Compton et al., 1989) rate models are used as follows.

$$SI = \frac{a_{Ca^{2+}} a_{CO_3^{2-}}}{k_{sp}}, \qquad \text{(J1)}$$

$$r_{precip} = k_{precip}(SI - 1)^{n_{precip}} \qquad for\ \ SI \geq 1, \qquad \text{(J2)}$$

$$r_{diss} = (k_{diss,1} a_{H^+} + k_{diss,2})(1 - SI)^{n_{diss}} \qquad for\ \ SI < 1. \qquad \text{(J3)}$$

r_{precip} and r_{diss} are the precipitation and dissolution rates respectively. a_x denotes the activity of species x, in this case calcium and bicarbonate. K_{precip}, n_{precip}, $k_{diss,1}$, $k_{diss,2}$ and n_{diss} are all kinetic constants that have been experimentally determined by others. It should be noted that these relationships were developed to fit results from well-mixed batch experiments that do not consider local concentrations (i.e. at the crystal surface). In this work local concentrations are considered such that a_{Ca2+} and a_{CO32-} at the precipitate boundary govern the crystal growth rate. Moving crystal boundaries were not considered however the effect of crystal growth or dissolution on local activities was modeled by a flux (J) of ions so

$$J_{Ca^{2+}} = J_{CO_3^{2-}} = r_{diss} - r_{precip}, \qquad \text{(J4)}$$

with positive flux defined as mass entering the liquid domain.

The other rate-limited reaction in the system is ureolysis. A Michaelis–Menten rate equation was used where

$$r_{urea} = \frac{r_{\max} a_{urea}}{k_m + a_{urea}}. \qquad \text{(J5)}$$

r_{urea} is the volumetric biofilm ureolysis rate (ureolysis is limited to the biofilm), r_{max} is the maximum rate and k_m is the half saturation constant. All other equilibrium reactions are assumed to occur at a much faster rate. The numerical technique used does not allow for instantaneous reactions to take place because it creates a numerically stiff solution space. All equilibrium reactions were set to be fast enough to maintain equilibrium conditions, but not fast enough to cause numerical instability. As an example, we take the carbonate/bicarbonate equilibrium reaction rate that can be written as

$$r_{HCO_3^-} = k_{HCO_3^-}\left(a_{CO_3^{2-}} a_{H^+} - a_{HCO_3^-} 10^{pK}\right) \qquad \text{(J6)}$$

where k is a rate constant. Typical k values in carbonate equilibrium are on the order of 10^{12} s^{-1} however, all carbonate equilibrium rate constants were set to much lower values to avoid problem stiffness in this model. The lowered values, typically around 100 s^{-1}, were still much higher than the rate limited reactions (ureolysis, precipitation and dilution) so solution equilibrium was still maintained.

Results and Discussion

The model was successfully implemented in reproducing the expected hydrodynamics and chemistry of the micro model system. Figure 33 shows the predicted velocity magnitude and Figure 34 shows the predicted pH and SI fields in the model. The results generally agree with the predicted conditions with much higher velocities in the constricted channel region and very slow flow elsewhere. The chemical environment also agrees with predictions with much higher saturation indices and pH deeper in biofilm regions. The model does not agree with one important expectation that more precipitation

would occur in regions of higher pH and SI. In this model, the areas with the most crystal formation and the areas with the highest SI do not correspond. This lack of model agreement leads to the suspicion that either there is an important process missing from the model or that the biofilm inhibits visible crystal formation.

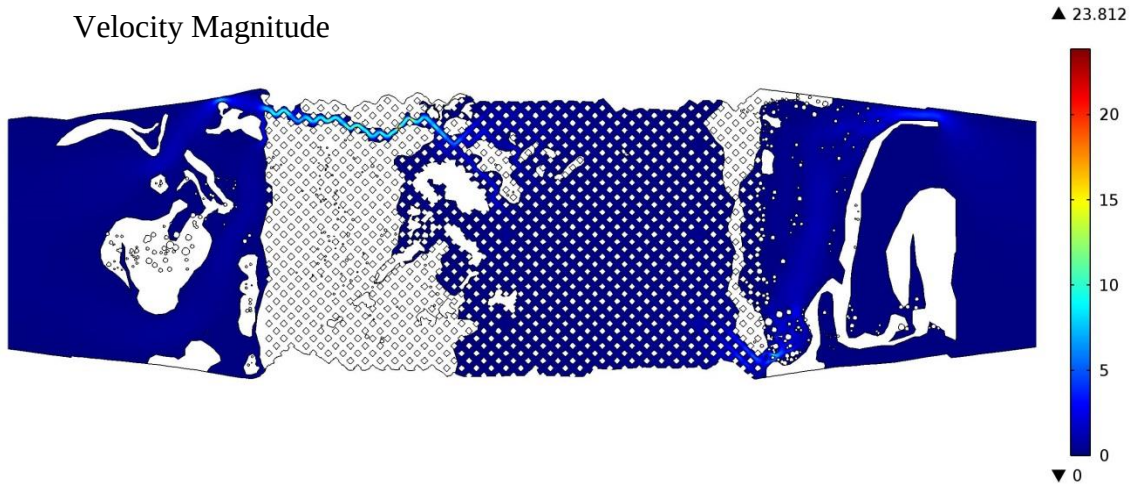


Figure 33. Model results showing the predicted steady state velocity magnitude in the computational domain after approximately 48 hours of biofilm growth and 12 hours of precipitation. It was assumed that there was no flow in the biofilm and precipitate domains.

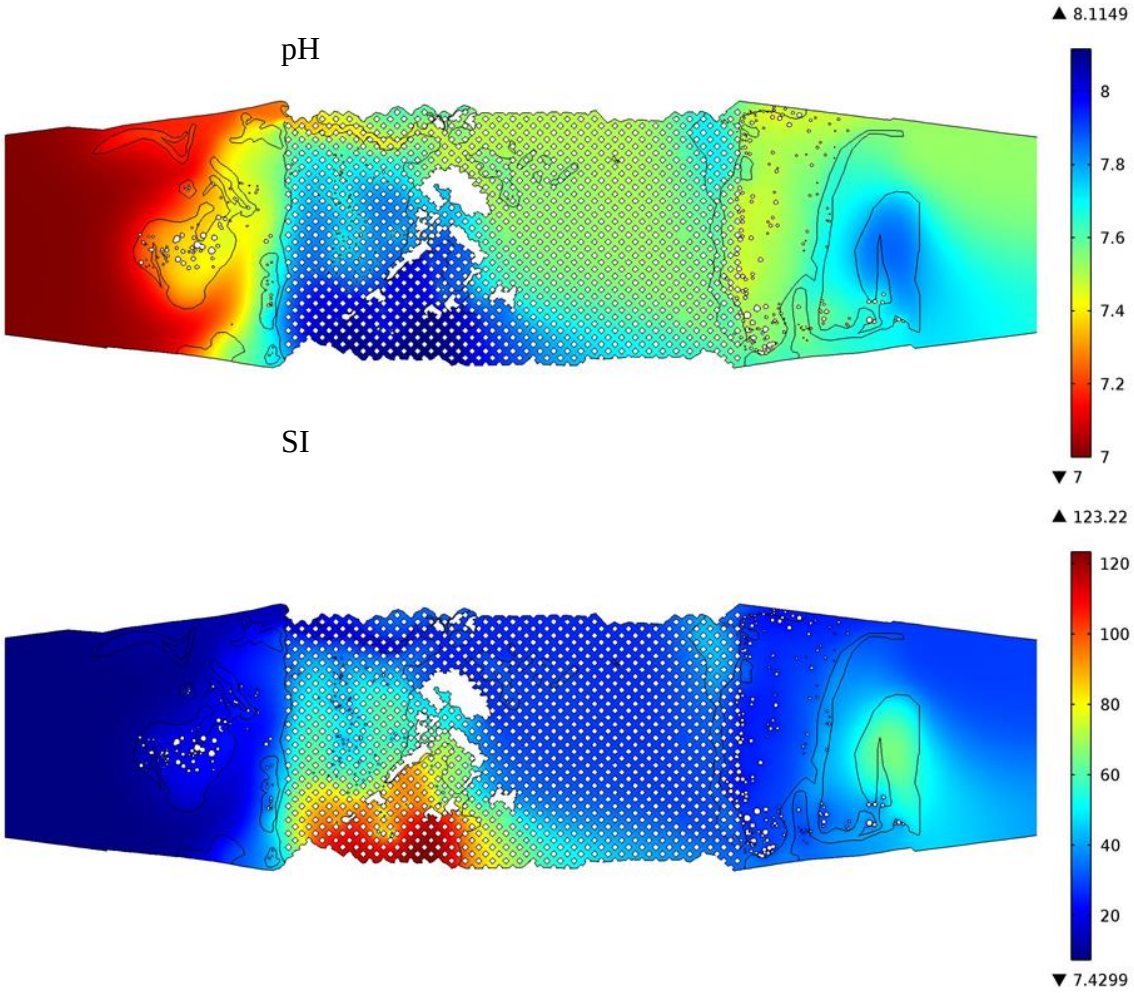


Figure 34. Model results showing the predicted pH (top) and the saturation index with respect to calcite (bottom) with an influent pH of 7. These plots correspond to the flow environment predicted in Figure J2.